Normandie Université

THESE

Pour obtenir le diplôme de doctorat

Spécialité Physique

Préparée au sein de l'INSA de Rouen Normandie

Improving the numerical simulation of soot aerosol formation in flames

Présentée et soutenue par
José C. MORÁN C.

Thèse soutenue publiquement le 15/11/2021 devant le jury composé de		
M. Daniel FERRY	Chargé de recherche au CINaM - Centre Interdisciplinaire de Nanoscience de Marseille, France	Rapporteur
Mme. Laurence LE COQ	Professeur à l'IMT Atlantique, France	Rapportrice
M. Alfred WEBER	Professeur à *Technische Universität Clausthal*, Clausthal-Zellerfeld, Allemagne	Examinateur
M. Andrés FUENTES	Professeur à *Universidad Técnica Federico Santa María*, Valparaíso, Chili	Examinateur
M. Claude ROZÉ	Professeur à l'Université de Rouen Normandie, France	Examinateur / Président du Jury
M. Reza KHOLGHY	Professeur Assistant à *Carleton University*, Ottawa, Canada	Examinateur
M. Jérôme YON	Maître de conférences à l'INSA de Rouen Normandie, France	Directeur de thèse

Thèse dirigée par Jérôme YON du laboratoire CORIA (UMR 6614 CNRS)

Acknowledgments

First of all, thank to my family for their invaluable support with particular mention to my parents. Specially, thanks to my wife for her company and support during these years.

Also, thank to my advisor Jérôme Yon for keeping me focused in my work, supporting me in many important decisions, and teaching me how to do better research. Thank Andrés Fuentes from Chile with whom we have kept a nice collaboration, and also advising me regarding important decisions in my life. Thank to Alexandre Poux for his great help during this thesis and compromise with MCAC project. Thank to Christophe Henry for the nice collaboration during this thesis. Thanks to Felipe Escudero for all the discussions, and exchanges regarding numerical simulations.

Also, thank to my great friends Alejandro Jerez, Francisco Cepeda, and Miguel Valenzuela for those many video-call meetings, constant support, and scientific discussions!

Thank to all the people from CORIA laboratory for receiving me and integrating me to this great work environment. In particular to Clément (Patat and Argentin), Morgan, Marcos, and Dilip for helping me, and sharing this process with me.

Thank to our small Chilean community in Rouen & Le Havre for those many great moments together.

Finally, thank to the Region of Normandy for totally financing my thesis.

Merci beaucoup à tous et à toutes !

Abstract

Soot particles have been identified as the second largest contributor to global warming (just after carbon dioxide). Also, these particles can penetrate deeply into the lungs and may be carcinogenic. In this context, one of the most important properties of soot particles is their morphology which is determined by the interplay between nucleation, surface reactions, and agglomeration in flames. Modeling this process by accurately considering the morphology of particles is currently a big challenge for most numerical codes in the literature. In this thesis, a new and robust approach to simulate the evolution of soot morphology in flames is introduced. It is a Monte Carlo Discrete Element Model, called MCAC, where the trajectories of individual soot particles are accurately solved in flames and detailed particle interactions and morphology are considered. MCAC is adapted to all soot formation mechanisms including nucleation, surface growth, oxidation (including fragmentation), and agglomeration. This code is coupled with continuous CFD simulations solving the flame chemistry, fluid dynamics, and soot aerosol mass transfer leading to realistic soot formation simulations in both premixed and diffusion flames. Based on this approach, the detailed dynamics of soot formation are revealed. Soot aggregation takes place in the transition of both fluid flow and aggregation regimes. This simultaneous change of regimes considerably impacts soot particle size distribution, aggregation kinetics, and particle morphology. Indeed, fractal dimensions below the classical one derived by diffusion-limited approach are found for aggregates formed in the diffusive, and transition flow regime. Agglomeration still leads to self-preserving particle size distribution when this simultaneous change of regimes is considered. This distribution is found to follow a generalized Gamma function that may be expressed based on different equivalent diameters. Aggregation (sticking) of soot particles upon collision is only systematic for soot primary particles larger than 10 nm. New expressions to determine soot collision and sticking probabilities are introduced based on a energy approach based on a coarse-grained description of soot particles. Pure agglomeration leads to agglomerates in some resemblance with those observed experimentally however, soot aggregates are formed under the competition of aggregation and surface reactions. In this context, soot aggregates exhibit a complex morphology which is modeled here as an overlapping spheres approach. Equations take primary particle overlapping effect on aggregates morphology and projected area scaling-laws into account are proposed. Finally, coupling MCAC with CFD simulations revealed the detailed evolution of soot morphology along different trajectories in the flame including the centerline and the wings of a diffusion flame. Marked and robust morphological features of soot aggregates generated under different trajectories in the flame were observed.

Keywords: Soot; Nanoparticles; Discrete Element Modeling; Monte Carlo; Aggregates; Morphology

Résumé

Les particules de suie ont été identifiées comme le second facteur prédominant dans le réchauffement climatique (juste après le CO_2). Par ailleurs, ces particules sont des cancérogènes avérés. Leurs propriétés radiatives et sanitaires sont largement dépendantes de leur morphologie. Aussi, nous constatons que la prise en compte de la morphologie de la suie dans la modélisation des processus liés à sa formation n'est que très peu considérée dans les modèles et codes actuels et représente un véritable défi. La forme des particules de suie résulte de la compétition entre différents mécanismes liés à la formation de la suie au sein même de la flamme. Dans cette thèse, une nouvelle approche est proposée afin de simuler l'évolution de la morphologie des particules de suie dans les flammes. Il s'agit d'un modèle de type Monte Carlo à éléments discrets, appelé MCAC permettant la prise en compte de la variation des conditions thermodynamiques rencontrées par les particules le long de leurs trajectoires dans des flammes. Outre l'agrégation des particules pilotée par le mouvement Brownien, MCAC considère la nucléation, la croissance de surface, l'oxydation et la fragmentation des particules de suie. Ce code est couplé à des simulations CFD résolvant la chimie de la flamme, la dynamique des fluides, et le transfert de masse entre la phase gazeuse et la phase particulaire. Ceci permet une simulation réaliste de la formation des particules de suie dans des flammes de prémélange et de diffusion que ce soit en termes de taille et de morphologie. Cette étude révèle de façon détaillée la dynamique de la formation de la suie en prenant en compte le changement de régime de l'écoulement et de régime d'agrégation. Ces changements de régimes ont un impact considérable sur la distribution de taille, la cinétique d'agrégation et la morphologie des suies. Cependant, on montre que l'agglomération conduit toujours à une distribution de taille auto-préservée répondant à la famille des distributions Gamma généralisées pouvant être exprimées à partir de différents diamètres équivalents. Le recouvrement des monomères a pu être simulé physiquement grâce à la prise en compte des phénomènes de croissance de surface. En outre, ceci a permis l'obtention d'équations prenant en compte l'effet du recouvrement des monomères sur la morphologie des agrégats, leur volume, leur surface ou encore sur les lois de projections 2d utiles à l'analyse de clichés de microscopie électronique. De nouvelles expressions de probabilités de collision et de collage des suies sont introduites à partir d'une approche énergétique prenant en compte le changement de la composition des particules au fur et à mesure de leur maturation. On montre ainsi que le collage des particules de suie lors des collisions n'est systématique que pour les monomères avec un diamètre > 10 nm. Enfin, le couplage de MCAC avec les simulations CFD a révélé l'évolution détaillée de la morphologie des particules pour différentes trajectoires dans une flamme de diffusion. Des signatures morphologiques marquées et robustes des agrégats de suie générés sous différentes trajectoires dans la flamme sont observées.

Mots clés. Suie ; Nanoparticules ; DEM ; Monte Carlo ; Agrégats ; Morphologie

Contents

List of Tables

List of Figures

Nomenclature

Abbreviations

BLCA	Ballistic-limited cluster-cluster agglomeration
BPCA	Ballistic-limited particle-cluster agglomeration
CFD	Computational Fluid Dynamics
DEM	Discrete Element Model
DLCA	Diffusion-limited agglomeration
DMA	Differential Mobility Analysis
GSD	Geometric standard deviation
HACA	Hydrogen-Abstraction and Carbon-Addition mechanism
LD	Langevin Dynamics
LOSA	Line of sight attenuation
MC	Monte Carlo
MCAC	Monte Carlo Aggregation Code
nTEM	Numerical Transmission Electron Microscopy image
PAH	Polycyclic Aromatic Hydrocarbon
PBE	Population Balance Equation
PP	Primary particle
PPSD	Primary particle size distribution
PSD	Particle size distribution
RDG-FA	Rayleigh Debye Gans theory for fractal aggregates
RLCA	Reaction-limited cluster-cluster agglomeration
RPCA	Reaction-limited particle-cluster agglomeration
SEM	Scanning Electron Microscopy
SGE	Surface Growth Efficiency
SM	Supporting Material
SPSD	Self-preserving size distribution
TEM	Transmission Electron Microscopy

Physics constants

κ	Coulomb constant, (kg·m^{3}s^{-2}·C^{-2})
k_B	Boltzmann constant, (m^2·kg·s^{-2}·K^{-1})
K_E	Boltzmann charges distribution constant, (N·m^2·C^{-2})

Variables

α	Projected area scaling-law exponent, (-)
α_s	Aggregate surface area correction factor, (-)
α_v	Aggregate volume correction factor, (-)
β	Stretching exponent, (-)
β_v and β_s	Aggregate volume and surface area correction functions, (-)
Δt	Time step, (s)
η	Fluid viscosity, (Pa·s)
$\Gamma(x)$	Gamma function of x, (-)
Γ_p	Friction coefficient function, (-)
λ	Coagulation homogeneity coefficient, (-)
λ_f/λ_g	Fluid/gas mean free path, (m)
λ_p	Particle's persistent distance, (m)
λ_{Mi}	Coagulation homogeneity coefficient, (-)
$\omega_{Condensation}$	Condensation mass flux, (kg·m^{-3}s^{-1})
ω_{HACA}	HACA surface growth mass flux, (kg·m^{-3}s^{-1})
ω_{nuc}	Nucleation mass flux, (kg·m^{-3}·s^{-1})
$\omega_{Oxidation}$	Oxidation mass flux, (kg·m^{-3}·s^{-1})

ω_{sr}	Surface reaction net mass flux, (kg·m^{-3}s^{-1})	C_c	Cunningham slip correction factor, (-)
ϕ	Packing factor, (-)	C_i	Cunningham slip correction factor i'th parameter, (-)
ρ_g	Gas bulk mass density, (kg·m^{-3})	$C_{ov,p}$	Projected primary particle overlapping coefficient, (-)
ρ_p	Particle bulk mass density, (kg·m^{-3})		
σ_{ab}	Lennard-Jones potential characteristic distance, (-)	C_{ov}	Primary particle overlapping coefficient, (-)
$\sigma_{d,geo}$	Particle geometric standard deviations based on the diameter d, (-)	D	Particle's diffusion coefficient, (m^2·s^{-1})
		d	Generalized gamma Self-Preserving Size Distribution parameter, (-)
$\sigma_{p,geo}$	Primary particle geometric standard deviation, (-)	D_c or d_c	Critical coalescence diameter, (m)
τ	Particle momentum relaxation time, (s)	D_g or d_g	Aggregate gyration diameter, (m)
τ_a	Characteristic time of agglomeration, (s)	D_m or d_m	Aggregate mobility diameter, (m)
τ_{life}	Particle survival (life) time in the system, (s)	D_p or d_p	Primary particle diameter, (m)
τ_{cs}	Characteristic time of coagulation for coalescing spheres, (s)	D_s	Critical sticking diameter, (m)
		D_v or d_v	Aggregate volume equivalent diameter, (m)
τ_{sg}	Characteristic time of surface growth, (s)	$D_{f,i}$	Individual fractal dimension, (-)
Θ	Total number of discretization elements, (-)	$D_{f,p}$ or D_f	Population fractal dimension, (-)
$\tilde{z}$	Kinetic exponent, (-)	D_{fm}	Mobility based fractal dimension, (-)
φ	Surface growth specific flux density, (kg·m^{-2}·s^{-1})	D_{max}	Aggregate maximum diameter, (m)
		$d_{p,ea}$	Volume-surface area equivalent diameter, (m)
ϑ	Arbitrary constant value, (-)		
$\widetilde{x}$	Average particle size parameter for the Self-Preserving Size Distribution, (m)	e	Elementary charge, (C)
		E_{att}	Attractive Lennard-Jones interaction energy, (-)
ξ	Particle's characteristic length, (m)		
A	Pair correlation function, (-)	E_{bar}	Electrostatic barrier, (-)
a	Generalized gamma Self-Preserving Size Distribution parameter, (-)	E_{electro}	Electrostatic interaction energy, (-)
		E_{kin}	Particle kinetic energy, (-)
A_p	Primary particle projected area, (-)	$E_{\text{L-J}}$	Lennard-Jones total interaction energy, (-)
a_v and a_s	Aggregate volume and surface area correction parameters, (-)	E_{rep}	Repulsive Lennard-Jones interaction energy, (-)
A_{13}	Aggregate anisotropy coefficient, (-)		
A_{agg}	Aggregate contribution to pair correlation func., (-)	E_{well}	Lennard-Jones potential well depth, (-)
		f	Agglomerate friction coefficient, (kg·s^{-1})
A_a	Aggregate orientationally averaged projected area, (-)	F_b	Brownian force, (N)
A_{ham}	Hamaker's constant, (J)	F_d	Drag force, (N)
		F_g	Gravitational force, (N)
A_{pp}	Primary particle contribution to pair correlation func., (-)	F_l	Lift force, (N)
		F_t	Thermophoretic force, (N)
b_v and b_s	Aggregate volume and surface area correction parameters, (-)	f_v	Particle volume fraction, (-)

H	Dimensionless coagulation kernel, (-)	R_m or r_m	Particle mobility radius, (m)
h	Distance between primary particle's surfaces, (m)	R_n or r_n	Nearest-neighbor distance, (m)
I	Inertia matrix, (-)	R_p or r_p	Primary particle radius, (m)
J_{nucl}	Nucleation rate, $(\text{m}^{-3}{\cdot}\text{s}^{-1})$	R_{ij}	Eigenvalue number i of the inertia matrix, (-)
$k(i, j)$	Coagulation kernel between ith and jth particles, $(\text{m}^3{\cdot}\text{s}^{-1})$	R_{max} or r_{max}	Aggregate maximum radius, (m)
k_0	Monomer coagulation kernel, $(\text{m}^3{\cdot}\text{s}^{-1})$	R_{pv}	Volume-equivalent average primary particle radius, (m)
k_f or $k_{f,p}$	Population fractal prefactor, (-)	$R_{s,ij}$	Relative collision or Smoluchowski radius, (m)
k_α	Projected area scaling-law prefactor, (-)	S	Total surface area concentration, (m^2-soot/m^3-flame)
$k_{f,i}$	Individual fractal prefactor, (-)	S_a	Aggregate surface area, (m^2)
m_p	Particle mass, (kg)	S_s	Specific surface area, (m^2/kg)
N or n	Particle number concentration, (m^{-3})	T	Absolute temperature, (K)
n_0	Initial particle number concentration, (m^{-3})	t or t_{res}	Residence time, (s)
n_c	Primary particle coordination number, (-)	u_{ox}	Oxidation rate, $(\text{m}{\cdot}\text{s}^{-1})$
N_p	Number of primary particles per agglomerate, (-)	$U_{rep,i}$	Repulsive term of interaction energy, (-)
$n_{c,\text{min}}$	Minimum primary particle coordination number, (-)	u_{sg}	Surface growth rate, $(\text{m}{\cdot}\text{s}^{-1})$
		u_{sr}	Surface reaction rate, $(\text{m}{\cdot}\text{s}^{-1})$
N_{eq}	Equilibrium particle number concentration, (m^{-3})	v	Particle volume, (m^3)
$N_{p,\text{eff}}$	Effective number of primary particles per aggregate, (-)	V_a	Aggregate volume, (m^3)
		V_g	Gas velocity, $(\text{m}{\cdot}\text{s}^{-1})$
$N_{p,\text{eq}}$	Equivalent number of primary particles per aggregate, (-)	V_p	Primary particle volume, (m^3)
		V_{box}	Simulation domain volume, (m^3)
P	Gas pressure, (Pa)	X	Dimensionless particle size parameter for the Self-Preserving Size Distribution, (-)
p	Generalized Gamma Self-Preserving Size Distribution parameter, (-)	x	Particle size parameter for the Self-Preserving Size Distribution, (m)
p_i	Probability of the ith particle displacement, (-)	z	Axial position, (m)
P_{coll}	Collision probability, (-)	$z_{p,i}$	i'th particle electrostatic charge, (-)
P_{stick}	Sticking probability, (-)	Kn_D	Diffusive Knudsen number, (-)
q	Order of the moments of the particle size distribution, (-)	Kn_f/Kn_g	Fluid/gas Knudsen number, (-)
		Kn_n	Nearest-neighbor Knudsen number, (-)
r	Radial position, (m)	PA_{ij}	Relative particle projected area, (m^2)

1 | Introduction

As shown in Fig. 1.1 soot or black carbon particles impact different domains of our life including human health, atmospheric chemistry and air quality. They are also important for the industrial production of nanomaterials, and experimental diagnostics related to industrial particle production, research and development [1–3]. The release of ultra-fine soot particles to the atmosphere can cause detrimental effects on the environment for example by influencing the formation of clouds and/or by changing the radiative properties of the atmosphere [4]. Indeed, soot particles are considered the second most important contributor to global warming just after carbon dioxide [5].
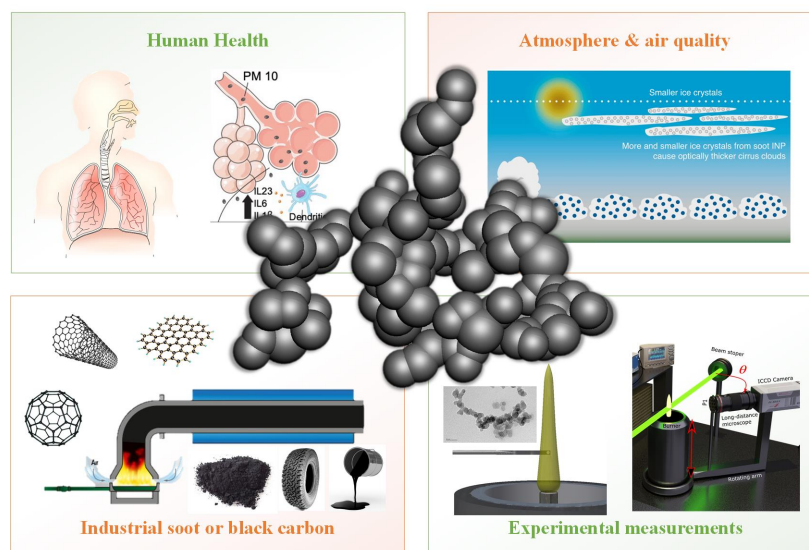
Figure 1.1: Soot and black carbon particles domains of impact. Atmospheric particle image from [4]. Experimental setup and TEM images from [6].

In most numerical works, soot particles are typically considered either spherical in some simulations or fractal aggregates in advanced codes that neglect important details of soot morphology such as primary particle overlapping (see Fig. 1.1). These approximations lead to significant deviations in the surface area and volume of soot particles, which in turn can cause large uncertainties in modeling soot physicochemical processes depending on particle sizes, such as collision and surface reaction rates (both surface growth and

oxidation). In addition, soot particle surface area to mass ratio (specific surface area) has been suggested as one of the most important dose metrics for nanoparticle toxicity by inflammatory response and oxidative stress of pulmonary cells [7–12]. Due to the small size of these particles ($< 1\,\mu$m), they can penetrate deeply into the lungs where the effects mentioned above may exist. Consequently, from this point of view soot particles are considered a threat to human health.

A radically different point of view considers soot as a valuable nanomaterial. The industrial soot or black carbon annual global production has been estimated by 2025 to be ~ 15 Mt [3]. Most of current applications ($\sim 70\%$) involve pigment and tires reinforcers. Morphology and physicochemical properties of soot particles have been highlighted as the most important and promising properties for possible future applications for renewable energy harnessing including CO_2 separation, supercapacitors, batteries, and catalyst support in fuel and solar cells [3]. Flame synthesis of nanoparticles such as soot has gained a great interest compared to other particle synthesis methods due to its availability, no liquid by-products, easier particle collection, high purity products, unique particle morphology, among others [13]. One of the main purposes in the flame synthesis of soot nanoparticles is tailoring their physicochemical properties and morphology, to this end a profound understanding on soot formation dynamics is required.

In addition, better understanding on soot formation dynamics and morphology is required for better predicting their physical properties such as particle-light interaction. Indeed, many experimental diagnostics for soot volume fraction, number concentration, temperature, primary/aggregate size distribution rely on laser-particle interaction [14]. Also, a better description of soot morphology could help improving electron microscopy image analysis techniques such as Transmission Electron Microscopy (TEM) [15].

This thesis aims at numerically simulating soot particles formation in flames with a special focus on their morphological evolution, agglomeration kinetics, and particle size distribution. Soot morphological characterization is one of the principal objectives of the ASTORIA project financed by ANR (*Agence Nationale de Recherche*) to which this thesis is associated to. It is jointly developed between CERFACS (from Toulouse), ONERA (from Paris), RAPSODEE (from Albi), and CORIA laboratories. Also, this thesis is funded by the Normandy Region through the *Gazpropres* project.

Soot particles in flames are generated as a consequence of local richness in terms of hydrocarbon fuels regarding oxygen. Gas-particle conversion (nucleation) is the starting point of the process by creating small soot nuclei, these particles collide and agglomerate. At the same time, they experience surface reactions leading to the increase (surface growth and condensation) or decrease (oxidation) in primary particle mass. Eventually, these particles are released to the atmosphere, consequently becoming a concern for human health and the environment. This thesis is restricted to study the evolution of soot particles within flames. In this context, the work is divided into five steps: (1) modeling soot aggregation by Discrete Element Modeling (DEM); (2) adding surface growth; (3) adding particles oxidation and fragmentation; (4) study the effect of soot maturity evolution; and (5) modeling different laminar flames based on CFD-DEM coupling.

2 | Definitions and state of the art

2.1 Agglomerates and aggregates morphology

Both aggregates (chemically bonded or sintered primary particles), and agglomerates (physically bonded primary particles) are studied in this work. In the following sections, the historical contributions to their morphological characterization are reviewed from an aerosol/colloid perspective. Some numerical and experimental tools to characterize these particles are also described. Finally, the different factors that can potentially impact the morphology of aggregates are described.

2.1.1 Historical contributions

Remarkably, as early as 1967, and without knowledge about fractal geometry (today's fundamental tool in this topic as discussed later in this chapter), Medalia et al. [16, 17, 17–19] are probably the first to quantitatively characterize the morphology of aerosol aggregates. As employees at Cabot Corporation studying carbon black (a special type of soot) particles shows that interest in aerosol aggregates morphology from the very beginning has been linked to flame made nanoparticles. The next big milestone arrived in 1979 when Forrest and Witten [20] used the fractal geometry [21] to characterize the morphology of aerosol aggregates. Aggregates are considered to be fractal when their morphology is self-similar when observed at different scales. Since real aggregates are self-similar only in a statistical sense, they are referred to as fractal-like aggregates/agglomerates. They subsequently introduced the Hausdorff or fractal dimension D_f,

$$N_p = k_f \left(\frac{R_g}{R_{pv}} \right)^{D_f} \tag{2.1.1}$$

where N_p is the number of primary particles belonging to an aggregates, R_{pv} is the volume equivalent average primary particle radius, R_g is the aggregate's radius of gyration (the radius of an sphere having the same inertia moment than the agglomerate), and k_f is the fractal prefactor. This equation is known as the fractal-law and is fundamental for the analysis of colloid or aerosol aggregates morphology both numerically and experimentally. After this work, the subject evolved very fast especially in numerical

modeling of agglomeration [22–24]. However, this progress has been always limited by the computational cost of simulations able to reproduce the morphology of these particles [25]. In parallel, a notable progress was achieved during the 80's decade specially in terms of experimental thermophoretic sampling and electron microscopy images analysis [26], and particle-light interaction modeling [27]. Particularly, the development of the Rayleigh Debye Gans theory for fractal aggregates (RDG-FA) by Dobbins and Megaridis [28] in 1991 is an important achievement for light-scattering techniques to study the morphology, number concentration, and size distribution of nanoparticle aggregates. During the 90's different contributions to electron microscopy images analysis methods and techniques with special mention to Köylü et al. [29] and Brasil et al. [30] were developed. During this decade, the concept of primary particle overlapping, as experimentally observed for soot aggregates, was introduced and numerically simulated [30, 31]. Not commonly recognized and yet notably, in 1994 Nicolai et al. [32] introduced some fundamental equations to characterize fractal aggregates based on the pair-correlation function. This function describes the probability to find particle's mass in space (see section 2.1.4). This work was extended later by [33] who compared different cutoff functions to model the pair-correlation function for finite-sized agglomerates. A remarkable attempt to understand and correlate it to other morphological parameters such as the fractal prefactor were subsequently carried out by [34, 35]. During the last two decades, different attempts to consider the impact of aggregates morphology on for example their mobility [36–38], light-scattering [39, 40], coagulation [41, 42], contact/interaction forces [43], electron microscopy images analysis [30, 44, 45] and electrostatic charging [46] have been carried out. Primary particle overlapping, necking, and coating have been numerically simulated to assess their importance on aggregate radiative properties and bringing corrections to the RDG-FA theory [47, 48]. Aggregates with multi-scale morphology, particularly superaggregates have been studied [49]. Fractal dimension and prefactor are recognized as not enough to characterize the morphology of aggregates and the anisotropy coefficient was introduced [50, 51]. The limitations at small-/large-scales have been considered to model the pair correlation function and structure factor of fractal aggregates [52, 53].

2.1.2 Different equivalent radii

Describing the morphology and physical properties of both agglomerates and aggregates of nanoparticles is challenging. In this context, different equivalent radii can be found in the literature. Some of them are purely geometrical, such as the geometric or maximum radius (R_{max}), corresponding to the radius of the smallest sphere enclosing the aggregate. Also, the volume-equivalent (R_v) is the radius of the sphere having the same value as the aggregate. Some of them are linked to physical properties as described as follows. The already mentioned radius of gyration (R_g) is the radius of a sphere with the same inertia moment (or rotational inertia) as the aggregate. Its value can increase when adding mass to the aggregate or when the same mass is redistributed farther away from its center of mass. Commonly, it is experimentally measured based on light-scattering techniques. Another important parameter is the mobility radius (R_m) which is the radius of a

sphere that feels the same drag force or has the same hydro/aerodynamic mobility as the aggregate under equivalent flow conditions. Different works in the literature have tried to link this parameter to the number of primary particles in an aggregate [38, 54–56]. Providing such a relation is not simple and actually depends on the flow regime (particle-flow interaction) as characterized by the fluid Knudsen number $Kn_f = \lambda_f/R_m$, where λ_f and R_m are the fluid mean free path and the particle's mobility radius, respectively. Here, λ_f is the average distance traveled by fluid molecules between successive collisions. When Kn_f tends toward 0, the relevant hydro/aerodynamic forces result from a continuous process (continuum regime), whereas at large Kn_f they are related to discrete collisions with molecules (free molecular regime). Electrical mobility is the radius of the sphere with the same electric velocity at a constant electric field as the agglomerate. The latter can be experimentally measured based on aerosol measurement devices such as Mobility Particle Size Spectrometer (SMPS) and Differential Mobility Particle Sizer (DMA).

2.1.3 Aggregates size distribution

As discussed in section 2.1.2, nanoparticle aggregates can be characterized based on different equivalent radii such as volume-equivalent, mobility, and gyration. Accurate descriptions of aggregate size distributions such as soot are challenging due to the size range of these particles ranging from one up to hundreds of nanometers (and even micrometer in some extreme cases [49]). Detection capabilities of aerosol devices such as SMPS and DMA are particularly difficult below 2 nm, and high particle concentrations [57]. On the other hand, TEM images can provide the size and morphology of aerosol aggregates. They may even reveal the internal structure (molecular arrangement) of primary soot particles [58]. However, all the aforementioned techniques suffer the uncertainties of intrusiveness and low spatial resolution. Despite these limitations, many important conclusions can be obtained based on recent and improved measurement devices.

Due to strong nucleation, incipient soot particle size distribution may be bimodal as reported by direct sampling and subsequent SMPS measurements of mobility diameter in ethylene premixed flames [59, 60]. As particles evolve, a bimodal or unimodal distribution may be persistently observed. It has been suggested that bimodality is related to flame temperature [60]. Bimodal distributions have been observed in flames with lower temperature where inception is predominant over coagulation (see section 2.4). At higher temperatures inception seems to loss efficiency probably due to PAH dissociation while coagulation becomes faster [60, 61]. However, DMA measurements of soot aggregates have suggested a lower coagulation efficiency at higher temperatures for smaller soot particles, making the explanation of bimodality not evident [62]. The inception mode may be characterized by a power-law function [61], while the coagulation mode may be lognormal or self-preserving as has been observed in ethylene premixed flames [63]. Both geometric mean, and geometric standard deviation of mobility diameter may be a function of the flame richness [63]. TEM image analysis have reported soot aggregate size distributions in diffusion flames to be a broad lognormal distribution [6]. In addition, angular light scattering measurements have shown strong gradient of soot radius of gyration

within the flame with maximum sizes found in the wings of the flame being as large as 220 nm in an ethylene diffusion flame [64].

2.1.3.1   Self-preserving size distribution

The Brownian motion of nanoparticles in flames (e.g., soot) naturally leads to random collisions between particles and therefore to the formation of polydisperse fractal-like aggregates. However, depending on the physico-chemical conditions, this polydispersity may achieve a natural limit where the shape of the normalized particles size distribution becomes invariant in time [65], this is called the self-preserving size distribution (SPSD). It is a fundamental concept allowing to considerably simplify the solution of the Smoluchowski (population balance) equation. It also explains why a limit for the polydispersity of particles size is observed for coagulating colloids. From a numerical point of view, SPSD theoretical expressions exists for aggregates based on some physical properties such as the number of primary particles per aggregate [66] however, a generalized and unified expression is currently missing. This missing expression may be very useful to quantitatively study soot size distribution based on different measurements such as SMPS (mobility radius); light-scattering (gyration radius) and TEM (gyration or maximum projected radius). Also, the numerical study of SPSD for aggregates, especially in the transition regimes (agglomeration/fluid flow), is scarce excepting a few remarkable works [67].

2.1.4   Pair correlation function

As mentioned in section 2.1.1, one of the most important concepts used to describe and model the morphology of aggregates/agglomerates of nanoparticles' is fractal geometry. A self-similar object is termed as fractal, i.e., its structure seems the same when analyzed at different scales [24, 68]. These aggregates/agglomerates are self-similar in a statistical sense so they are referred to as fractal-like. The morphology of fractal-like agglomerates can be characterized based on the pair correlation function. Conceptually, it corresponds to the probability to find particle's material at a location $\vec{r}$ in space from any point belonging to the particle. In other words, it is the probability to find mass elsewhere given there is mass at a reference point. Mathematically, it corresponds to the self-convolution of the aggregates/agglomerate's density function [53],

$$A\left(\vec{r}\right) = \int_{\vec{u}=0}^{\infty} n\left(\vec{r} - \vec{u}\right) n\left(\vec{u}\right) d\vec{u} \tag{2.1.2}$$

where $n\left(\vec{r}\right)$ is 1 if material exists at the location $\vec{r}$ and 0 otherwise. When A is averaged over different orientations i.e., $A\left(\vec{r}\right) = A(r)$, the result becomes a smooth function of r. It can be demonstrated that the aggregate volume V_a and its radius of gyration R_g can be determined based on $A(r)$ as follows [53],

$$V_a^2 = \int 4\pi r^2 A(r)\, dr \tag{2.1.3a}$$

$$R_g^2 = \frac{1}{2} \frac{\int_{r=0}^{\infty} r^4 A(r)\, dr}{\int_{r=0}^{\infty} r^2 A(r)\, dr} \tag{2.1.3b}$$

Please note that the nominator on the right hand side of Eq. (2.1.3b) corresponds to the aggregate's inertia moment. In the case of ideal fractal clusters, the average pair correlation function exhibits a power-law behavior $\left(A(r) \propto r^{D_{f,i}-3}\right)$ whose slope in a log-log plot is related to the cluster individual fractal dimension $D_{f,i}$. However, real agglomerates have a finite size and a cutoff function needs to be added [33, 39, 69, 70],

$$A(r) \propto r^{D_{f,i}-3} \exp\left(-(r/\xi)^{\beta}\right) \tag{2.1.4}$$

The cutoff is determined by a characteristic distance ξ and a stretching exponent β [32]. The latter parameter plays an important role on the scattering properties of agglomerates [39] and, as shown in Ref. [51], it is correlated with the particle shape anisotropy (see Section 2.1.6). The same authors have introduced a packing factor ϕ, related to the local arrangement of primary particles,

$$A(r) = \frac{\phi D_{fi}}{4\pi R_{pv}^{D_{fi}}} r^{D_{fi}-3} \exp\left(-(r/\xi)^{\beta}\right) \tag{2.1.5}$$

However, agglomerates of interest in aerosol science including soot, are commonly small $(N_p \rightarrow 1)$ meaning that primary particles cannot be neglected to describe $A(r)$. In this context, Yon et al. [53] proposed to approximate $A(r)$ as the sum of two components, $A(r) = A_{pp} + A_{agg}$. Where A_{pp} is the contribution of primary particles to the agglomerate morphology (self-correlation of primary particles), and A_{agg} is the contribution of the agglomerate structure by considering the correlation between different neighbor primary particles,

$$A_{pp}(r) = \left(1 + \frac{r}{4R_{pv}}\right)\left(1 - \frac{r}{2R_{pv}}\right)^2, \qquad r \in [0, 2R_{pv}] \tag{2.1.6a}$$

$$A_{agg}(r) = \frac{\phi D_{fi}}{3}\left(\frac{r}{R_{pv}}\right)^{D_{fi}-3}\left[\exp(-(r/\xi_{max})^{\beta}) - \exp(-(r/\xi)^{\beta})\right], \qquad r > 0 \tag{2.1.6b}$$

where Eq. (5.4.7a) is the analytical form of A_{pp} for monodisperse primary particles. The packing factor ϕ, the individual fractal dimension $D_{f,i}$, the maximum and equivalent length scales ξ_{max} and ξ, respectively, and the stretching exponent β are the parameters of this model. It is important to mention that **the author of this thesis contributed to the development of this model [53].**

2.1.5 Local compactness

As mentioned in the previous section, one parameter related to local compactness of primary particles is the packing factor ϕ. It is the inverse of the so-called filling factor [71]. An alternative derivation of this coefficient is described here. For a sphere of radius r centered at any primary particle belonging to the

agglomerate, the following scaling-law is verified [51],

$$N(r) = \phi \left(\frac{r}{R_{pv}} \right)^{D_f}, \qquad R_{pv} \ll r \ll D_{max} \tag{2.1.7}$$

Where $N(r)$ is the number of primary particles within a sphere of radius r, and D_f is the fractal dimension. Heinson et al. [51] derived Eq. (2.1.7) but did not directly use it to obtain ϕ. As can be seen, ϕ is very similar to the fractal prefactor but not the same! Indeed, we can verify that for $r = R_g$ we find $N(R_g) < N_p$, consequently $\phi < k_f$. Another parameter related to local compactness is the fractal prefactor k_f. It has been found to be related to primary particle overlapping [30, 31, 72, 73], polydispersity [74], and fractal dimension [35]. For large agglomerates ($N_p \gg 1$) both parameters are related by the following equation [32],

$$k_{f,\infty} = \left[\frac{2\Gamma(D_f/\beta)}{\Gamma((D_f + 2)/\beta)} \right]^{\frac{D_f}{2}} \frac{\phi D_f \Gamma(D_f/\beta)}{\beta} \tag{2.1.8}$$

where a dependence on the stretching exponent (β) is inferred and where $\Gamma(x) = \int_0^\infty t^{x-1} \exp(-t) \, dt$ is the Gamma function. Actually, for any N_p it may also depend on ξ_{max} and ξ as shown in Ref. [53]. In addition, how both fractal prefactor and packing factor are related to agglomerates local compactness is not evident. So, to make it clearer, Fig. 2.1 shows two chain-like agglomerates. Let's assume the maximum diameter of these agglomerates to be much larger than the primary particle size. Considering that both agglomerates have the same size and number of primary spheres and $D_f \approx 1$. As can be observed, agglomerate 2 has a larger local compactness since monomers are closer to each other. Therefore, based on Eq. (2.1.1) and Eq. (2.1.7) we conclude that agglomerate 2 has a larger fractal prefactor and packing factor than agglomerate 1. Finally, two
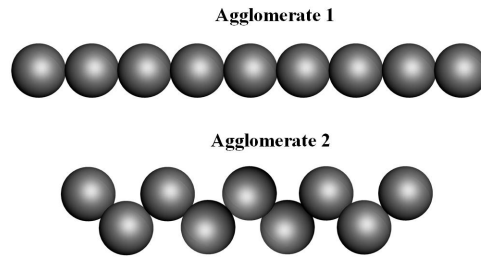
Figure 2.1: Comparison of two chain-like agglomerates with different degree of compactness.

additional important parameters related to local compactness are investigated, namely the primary particle overlapping coefficient and the coordination number. The overlapping coefficient [30, 31] is calculated for each pair of intersecting primary particles of radii r_i and r_j, having a distance between centers d_{ij} as,

$$c_{ov} = \frac{r_i + r_j - d_{ij}}{r_i + r_j} \tag{2.1.9}$$

When primary particles are point-touching then $d_{ij} = r_i + r_j$ and $c_{ov} = 0$. On the other hand, when particles are completely fused then $d_{ij} = 0$ and $c_{ov} = 1$. Also, the coordination number (n_c) is a property defined

for each primary particle as the number of neighbors in contact with it [72]. For example, in a chain-like agglomerate all the primary particles are in contact with two neighbors excepting those located at the extremes that are connected to only one neighbor. The theoretical maximum coordination number of non-overlapping monodisperse spheres in a 3-dimensional configuration is 12 [75] but it has never been observed for aerosol agglomerates [76]. This parameter is commonly overlooked in the literature and its evolution when aggregates experience surface reactions (growth or oxidation), has not been explored.

2.1.6 Shape anisotropy

It is measured based on the anisotropy coefficient (A_{13}) as defined in Ref. [51] for agglomerates. This is generalized here for arbitrary particle morphology by discretizing the particle into Θ cubic volumes of center (x_i, y_i, z_i) in 3-dimensional space, and obtaining the inertia matrix I as,

$$I = \frac{1}{\Theta} \sum_{i=1}^{\Theta} \begin{pmatrix} y_i^2 + z_i^2 & -x_i y_i & -x_i z_i \\ -x_i y_i & x_i^2 + z_i^2 & -y_i z_i \\ -x_i z_i & -y_i z_i & x_i^2 + y_i^2 \end{pmatrix} \qquad (2.1.10)$$

Subsequently, the 3 eigenvalues ($R_1 \leq R_2 \leq R_3$) of the inertia matrix are obtained. Consequently, the anisotropy coefficient A_{13} is determined as,

$$A_{13} = \frac{R_3^2}{R_1^2} \qquad (2.1.11)$$

This anisotropy coefficient represents the propensity of a 3-dimensional shape to have its mass preferentially distributed along one axis (see Fig. 2.2). The eigenvalues of the inertia matrix are related to the aggregate's

Isotropic shape
$R_1 = R_2 = R_3$
$A_{13} = 1$

Anisotropic shape
$R_3 \gg R_1, R_2$
$A_{13} \gg 1$
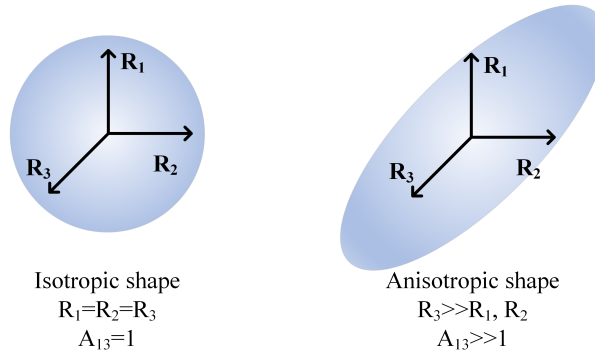
Figure 2.2: Examples of isotropic (left) and anisotropic shapes and the corresponding A_{13}.

radius of gyration as [51],

$$R_g^2 = \frac{1}{2} \left(R_1^2 + R_2^2 + R_3^2 \right) \qquad (2.1.12)$$

2.1.7 Projected area scaling-law

Scaling laws between the number of primary particles per aggregate N_p and the normalized average projected area are highly used to analyze experimental TEM images (see Section 2.1.8.1) to obtain morphological properties of agglomerates of nanoparticles [45, 77] but also in numerical simulations to determine molecule-particle collision frequencies that depends on their projected area [41, 78]. These types of correlations were initially proposed by Medalia et al. [16, 17, 17–19]. For instance, we can consider,

$$N_p = k_\alpha \left(\frac{A_a}{A_p} \right)^\alpha \tag{2.1.13}$$

where A_a and A_p are the orientationally averaged projected area of the aggregate and primary particle, respectively. Also, α and k_α are the power-law exponent and prefactor, respectively. For agglomerates formed in the diffusion-limited regime (see Section 2.2.3.1) for $5 \leq N_p \leq 580$, $k_\alpha = 1.17$ and $\alpha = 1.07$ were obtained by Oh & Sorensen [31]. In addition, for $10 \leq N_p \leq 512$, $k_\alpha = 1.10$ and $\alpha = 1.08$ values were obtained by Brasil et al. [30]. Most of these works neglected the effect of overlapping on the effective number of primary particles per aggregate. Eggersdorfer & Pratsinis studied the dependence of these parameters on the primary particle polydispersity [74]. Both Oh & Sorensen [31] and Brasil et al. [30] evaluated the dependence α and k_α on primary particles overlapping however, their procedure to generate overlapping between primary particles is artificial in the sense that it is not the result of physical phenomena such as surface growth or sintering. For aggregates experiencing sintering, Eggersdorfer et al. [79] proposed to change the definition of N_p and A_p based on a volume/surface equivalent primary particle diameter. Their approach leads to a prefactor of 1 and an exponent of 1.07 independent of the sintering mechanism [79]. However, these results cannot be directly adopted to study surface growth which is currently missing in the literature. Also, the dependence of both α and k_α on the physical properties impacting the morphology of aggregates has not been explored excepting the aforementioned primary particle polydispersity and sintering [74, 79].

2.1.8 Experiments

Not all the aforementioned parameters are currently possible to be experimentally measured, for instance there is no technique allowing a direct measure of the coordination number and packing factor for agglomerates of nanoparticles. It is interesting to note that coordination number has been measured for micrometer-scale granules, produced by spray fluidized bed agglomeration, based on X-ray tomography [80]. However applying this technique to explore nanoparticles such as soot is not evident. This detailed morphological parameter may be measured based on 3-dimensional electron tomography [81–84]. Coordination number may be measured in an indirect way from electron microscopy image analysis (see the sections below) by correlation with other parameters such as aggregate's fractal dimension [76]. Also, it may be measured by correlation with properties visible to Ultra-small angle x-ray scattering [85, 86].

The rest of parameters, and particularly the fractal dimension can be measured by Transmision/Scanning Electron Microscopy (TEM/SEM) image analysis or by Angular light-scattering measurements. Electron microscopy image analysis advantages include the clear and quite accurate soot particles observation and characterization that can go even down to the molecular scale. This technique is considered robust to measure primary particle size. The drawbacks are the intrusiveness [87], point-measurement, and maybe soot collection at different positions along the path of probe insertion in flames [88]. Also, these measurements typically rely on power-laws relating 2d and 3d properties. On the other hand, laser-based techniques are generally non-intrusive, with remarkable spatial and temporal resolution (< 0.001 mm^3, and < 10 ns, respectively) making them specially suitable to study combustion systems such as laminar [89] or turbulent flames [90]. The difficulties of these techniques are the uncertainties on the optical properties of nanoparticles and the complex modeling of particle-light interaction.

(a) Thermophoretic sampling   (b) Light scattering

(c) TEM image [6]   (d) Light scattering power [89]
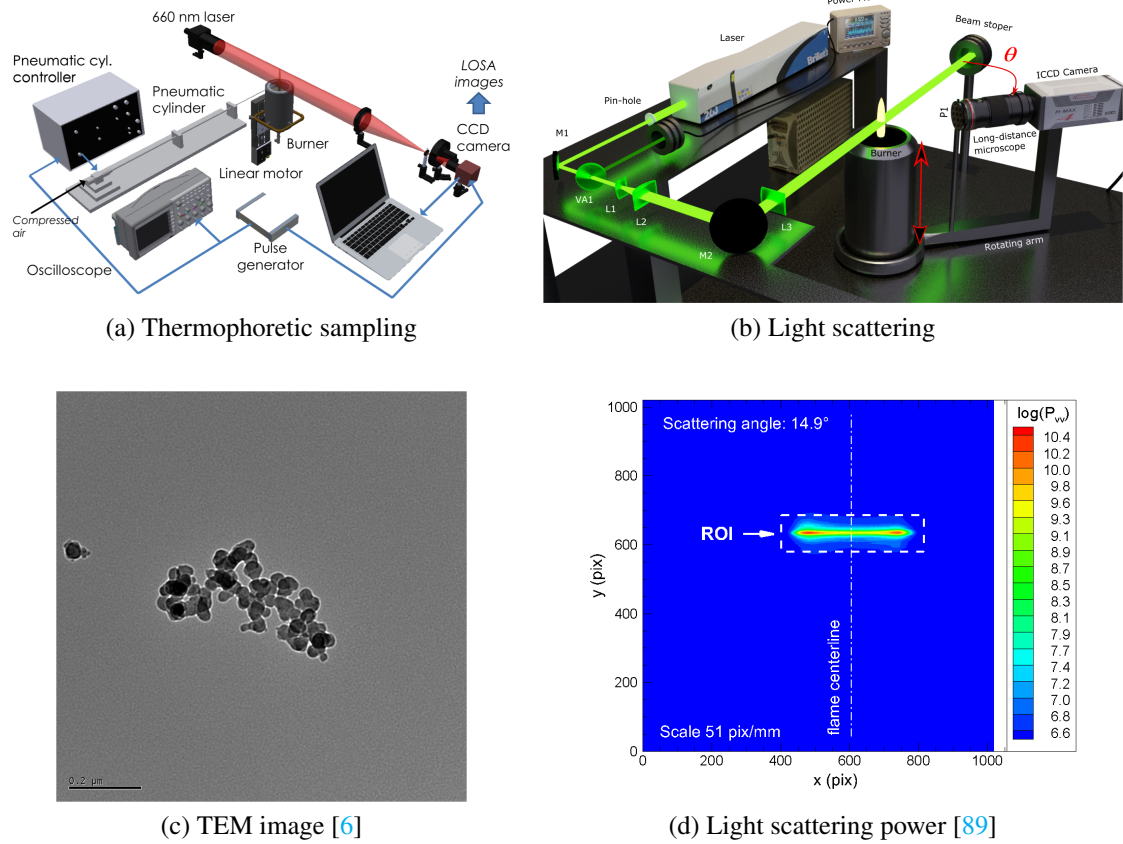
Figure 2.3: Experimental setups and examples of images (rough data) for soot aggregate characterization.

2.1.8.1   Thermophoretic sampling and image analysis

Electron microscopy image analysis requires three steps, namely (1) particle sampling, (2) image obtention, and (3) image processing. As shown in Fig. 2.3a, an example of experimental setup required to conduct

thermophoretic sampling is shown. In this context, the large temperature of soot particles in flames is used to sample them by thermophoretic deposition [26] on a typically 3 mm copper and carbon coated grid. This grid is inserted in the flame thanks to a metallic holder attached to a pneumatic cylinder. The challenge in sampling is the fast insertion (~ 5 ms traveling time), short exposure time (~ 30 − 100 ms), and precise positioning the sampling grid in the flame [88, 91]. Once the sampling is done, TEM or SEM images are obtained. Subsequently, they are analyzed to obtain different morphological properties of soot particles [15] including, primary particle size distribution, aggregate size distribution, fractal dimension/prefactor, and number of primary particles [6, 91]. Figure 2.3c shows an example of TEM image sampled from an ethylene/air diffusion flame [6]. Two aggregates of very different sizes can be observed in this image, the largest has a maximum projected diameter around 400 nm. The complex structure of soot aggregates is observed along with the level of primary particle polydispersity and overlapping.

2.1.8.2 Angular light scattering

This technique allows the aggregate number concentration, size (radius of gyration), and morphology to be assessed *in situ* in the flame. Also, when combined with other measurements such as light absorption, additional parameters such as the number of primary particles per aggregate, and primary particle size can be obtained [89]. As shown in Fig. 2.3b a laser source (in this case 532 nm wavelength) and specific optical devices are needed to direct the beam towards the flame, and (in this case) to produce the desired horizontal planar sheet that will finally traverse the flame. The latter is needed to avoid sampling volume-dependent measurements issues arising when measuring at different scattering angles as thoroughly discussed in Ref. [89]. The scattered signal is collected by an ICCD camera placed at an angle θ from the laser beam direction in the scattering plane as shown in the figure. One of the challenges in conducting angular light scattering is the precise rotation of the camera around the burner axis for angles as small as 5 and as large as 135 degrees. Figure 2.3d shows an example of rough measurement consisting on the power of the scattered light P_{vv} measured at a height above the burner of 30 mm and collected at a scattering angle $\theta = 14.9°$. It exhibits a high gradient of intensity in the highlighted region of interest (ROI) which is quasi-symmetric regarding the centerline of the flame (dash-dotted line). This signal is subsequently vertically averaged in the region of interest to subsequently carrying an Abel deconvolution process. The latter allows the differential scattering coefficient to be measured with radial resolution. This is then related to aggregate's size thanks to RDG-FA theory by assuming particle polydispersity, fractal dimension, and prefactor. In this way, the aggregate radius of gyration for soot particles is accurately measured with radial resolution at different heights above the burner. It is worth mentioning that **the author of this dissertation participated in the experimental campaigns and contributed to the post-processing of light scattering measurements** [89].

2.1.8.3 Other experimental techniques

Primary particle size can also be obtained by time-resolved light induced incandescence [92, 93]. This technique is challenging from an experimental point of view [91] but also from a modeling perspective since it relies on a complex model of soot-gas heat transfer [94], and also requires the flame temperature as an input parameter [95]. Aggregate size distribution can also be measured based on scanning mobility particle sizer (SMPS), however a sampling and dilution line of particles is required to have access to the flame [59, 96]. Also, an alternative to angular light scattering is spectral light scattering to measure soot aggregates' gyration radius distribution [97]. The latter is specially relevant in systems where optical access to the flame at different angles is reduced however it requires the knowledge of spectral dependence of the optical properties of nanoparticles. Many other additional techniques are described elsewhere [14, 98–101].

2.1.9 Factors influencing the morphology of aggregates

In the present section different physical, chemical, thermodynamic or even numerical factors influencing the morphology of fractal-like aggregates are quickly reviewed. When existing, an explanation of how the corresponding aspect actually influences the morphology of aggregates is provided highlighting the current level of understanding. Fig. 2.4 summarizes different aspects influencing the morphology of agglomerates/aggregates of nanoparticles. These factors can be associated with different transport mechanisms, namely mass, momentum or energy. Due to the size of these aggregates ($1 - 1000$ nm) most of these mechanisms are really complex and still not well understood, this is the reason why we typically find in the literature studies only dealing with specific mechanisms such as aggregation (mass transfer) considering the drag force (momentum transfer) caused by the interaction with the surrounding fluid [25, 39]. A review on the morphological influence of some of these factors on colloid aggregates is found in Ref. [102].

2.1.9.1 Momentum transfer

Some of the forces experienced by fractal aggregates generating transfer of momentum are; drag, electrical, magnetic [103], acoustic [104], and gravity [43]. Under the effect of an electrical field, polarizable particles tend to align forming chain-like agglomerates with $D_f \sim 1.2$ [105]. External magnetic fields can be used to induce dipole moments in primary particles and therefore forming chain-like agglomerates with D_f as small as 1.2. This is experimentally possible for particles with sizes between $10 - 500$ nm [106]. The inter-aggregate repulsion barrier (e.g., electrical double layer) reduces the collision probability of aggregates and may increase the fractal dimension up to $D_f \sim 2.1$ for very low collision probabilities ($\sim 10^{-3}$, RLCA) [25, 107, 108]. The latter is not intuitive and the increase in mobility within colliding particles, and the subsequent increase in particles inter-penetration, has been suggested as a possible explanation of the compact morphology of aggregates [108]. Recently, Pankaj et al. [109] proposed a levitation magnetic and inductive heating method
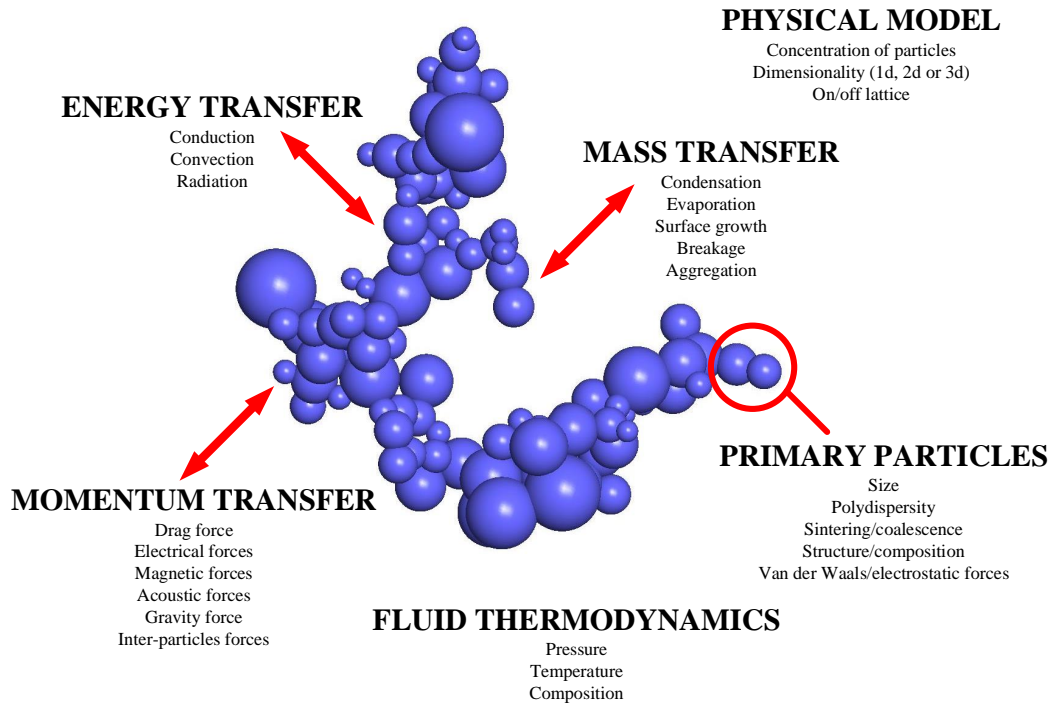
Figure 2.4: The different factors influencing the morphology fractal-like agglomerate/aggregate of nanoparticles.

for ferromagnetic metal nanoparticles assembly resulting in filamentary structures with fractal dimensions as low as 1.3. This work revealed that magnetic field has to be in the order of 200 times the thermal energy of the carrier gas to overcome Brownian fluctuations.

2.1.9.2   Mass transfer

Some mechanisms of mass transfer between aggregates and the surrounding fluid include condensation, evaporation, and surface growth [110–112]. The agglomeration with other suspended primary particles or other aggregates is one of the most important and most studied mechanisms of aggregates growth specially in early numerical works [25]. The morphology of aggregates is determined by the mechanism of aggregation (particle-cluster or cluster-cluster) or the trajectory of particles between collisions (ballistic or diffusion limited). Particle-cluster aggregation leads to denser aggregates with larger fractal dimension due to the larger probability of penetration in comparison with the cluster-cluster mechanism. Analogously, if the trajectory of aggregates between collisions is ballistic it leads to denser aggregates with larger fractal dimensions because they can penetrate deeper other aggregates, in contrast diffusive trajectories between collisions lead to aggregation at the boundary of neighbors structures with less inter-penetration [113]. Due to mechanical stress [114, 115], or oxidation [116, 117], aggregates fragmentation can take place. Sintering may also lead to aggregate fragmentation [42]. Aggregate coating may lead to restructuring depending on the balance between viscous forces, and primary particle binding forces [118].

2.1.9.3   Energy transfer

The three mechanisms of heat transfer, namely conduction, convection and radiation are important for the performance of aggregates. Increasing the temperature of primary particles can have two effects namely, reduce the characteristic times of sintering, and increase primary particle mobility. The latter may lead to aggregates thermal restructuring depending on the strength of bonds between primary particles. Various studies have focused on the radiative properties (energy transfer) of these particles [55], including complex details of aggregates such as primary particles polydispersity, necking, overlapping or coating [47, 119, 120]. However, the morphological change induced by energy mechanisms has received less attention in terms of numerical simulations compared to experiments [93, 121–123]. Recently, Wang et al. [123] found soot particles to be slightly more compact (larger D_f by TEM image analysis) when externally irradiated by a solid-state plasma light applied in the particles inception region of the flame.

2.1.9.4   Primary particles

The structure, composition (including mass density), size, polydispersity and mass transfer between monomers (sintering/coalescence) are key aspects influencing the morphological details of aggregates. Wu et al. [124] reported an inverse relation between the fractal dimension of colloid aggregates and the size of primary particles within the $10 - 200$ nm range. They also mentioned these results actually lack of explanation. On the other hand, for low levels of monomers polydispersity [125, 126] no relevant effect on the morphology of aggregates numerically generated by DLCA was found, however, for large levels of monomers polydispersity the morphology of aggregates characterized by the fractal dimension and prefactor are considerably affected [74, 127]. The latter results currently lack of experimental evidence. Goudeli et al. [127] also found that increasing PP polydispersity also delays the attainment of self-preserving size distribution. However, there are still some fundamental points to be clarified. For example, they reported that the fractal prefactor is strictly increasing with monomers polydispersity leading to values being one order of magnitude larger than typical prefactors measured in experiments [128].

Finally, the degree of sintering between monomers affects the fractal dimension of aggregates and most notably it may lead to the self-preserving size distribution of monomers size [42]. In principle we might predict that increasing the degree of sintering would lead to a larger fractal dimension of DLCA aggregates, however, initially (at low levels of sintering) it actually decreases and after the degree of sintering has long progressed it leads to the formation of more compact aggregates until eventually (depending on particles residence times) finally the aggregates become spherical [42]. The reason of the initial decrease in D_f is that smaller particles sinter faster than the larger ones leading to initially more elongated aggregates.

2.1.9.5   The physical model

The initial concentration of monomers, the dimension (1d, 2d, or 3d) of aggregation and the fact that aggregates are simulated on or off-lattice are factors relevant for the morphological aspects of fractal aggregates. The fractal dimension of aggregates generated by cluster-cluster aggregation has been found to be independent on the the on/off-lattice simulation [129], in contrast, aggregates generated by particle-cluster experience a relevant variation in fractal dimension [25]. In addition, considering nanoparticle rotation may not affect the morphology of aggregates [130] however, more recent studies have found less compact aggregates than the classical DLCA regime when rotation is included [108, 131].

2.1.9.6   Thermodynamics of the surrounding fluid

The temperature, pressure and composition of the surrounding fluid are factors relevant for the interaction with the particle and therefore influencing the dynamics of aggregation. Even more, in the context of colloidal aggregation Xiong et al. [132] studied the effect on aggregation and aggregates morphology due to the evaporation of the surrounding liquid. On the other hand, for soot particles in flames, it has been suggested by experiments that pressure may (at some extent) influence their particle size distribution and morphology [133–136].

2.2   Numerical simulations of nanoparticle formation

The present section aims at bringing a quick overview of the different alternatives currently available in the literature, to simulate the aggregation of nanoparticles highlighting their main strengths and weaknesses in the view of simulating the morphological aspects of fractal aggregates.

The growth of suspended nanoparticles by coagulation (agglomeration and/or coalescence) is found in many industrial, combustion and environmental processes. In this context, particles naturally evolve into polydisperse sizes and, except in the case of total coalescence, they evolve into complex morphologies [42, 102]. Different numerical methods can be found in the literature to simulate different characteristics of this process [25, 102, 137]. As shown in Fig. 2.5, they can be classified into three main groups, i.e. those focused on a single agglomerate such as, diffusion-limited, ballistic and reaction limited particle-cluster agglomeration [138] (abbreviated as DLA, BPCA and RPCA, respectively), purely random algorithms [139], based on Langevin Dynamics [41], and also tunable algorithms [140, 141]. Those focused on many agglomerates, also called DEM or Discrete Element Methods [112] and the Population Balance methods based on the generalized Smoluchowski equation [142, 143].
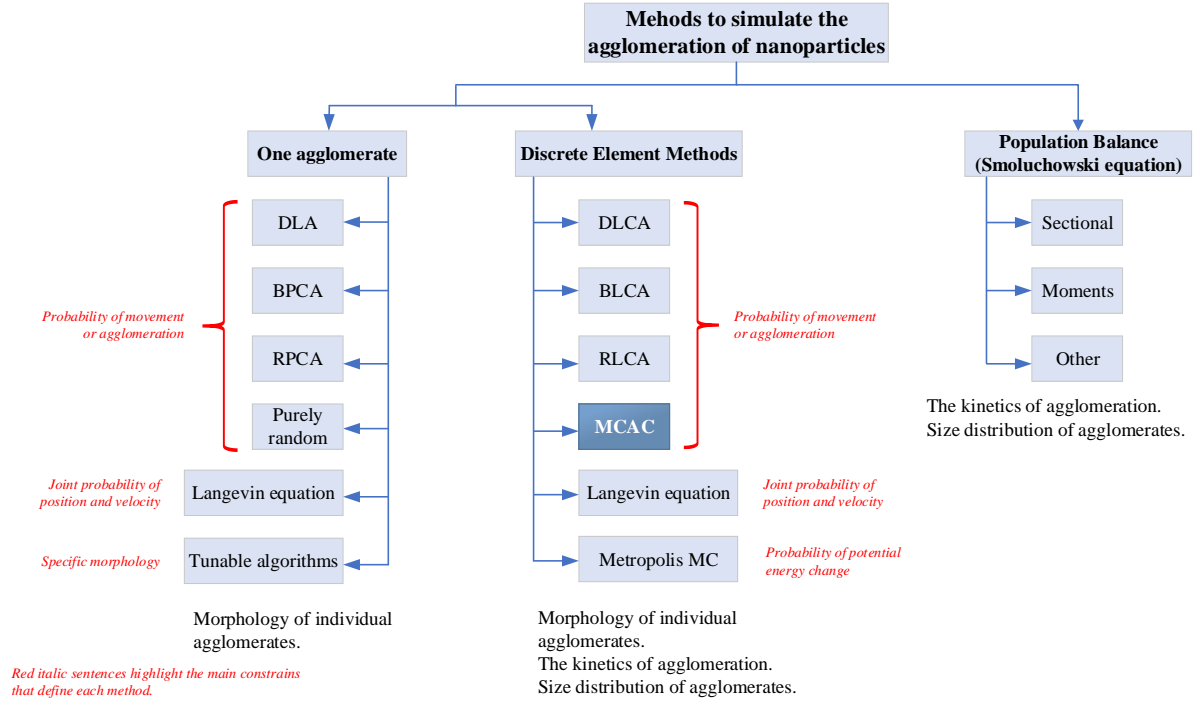
Figure 2.5: The different models to simulate the agglomeration of nanoparticles.

2.2.1 Population balance methods

This method was initially proposed in 1916 by Marian Smoluchowski [144] to actually simulate the coagulation and coalescence of suspended nanoparticles. This method does not deal with the details of particles morphology, it is rather based on a balance of particles of different sizes by considering birth and death terms in a continuum integro-differential equation [142]. This method brings the time evolution of the particle size distribution typically in terms of particle volume and has been adapted to include different mechanisms of particle formation such as surface reactions and fragmentation [42]. Analytical solutions exists for very simplified cases such as the coagulation and coalescence of spherical particles. To study the kinetics of aggregation there are many uncertainties related to collision frequencies, and regimes [42, 143, 145]. As reviewed by Jeldres et al. [143] this method is generally adjusted based on empirical relations to study the dynamics of aggregation and there are many different mathematical expressions to adapt the method to specific aggregation mechanism (e.g., coagulation, and bridging flocculation) and system critical conditions, i.e. flow regime, and particles size. Despite the above mentioned limitations, this method is highly used to study aggregation in industrial-scale problems [146] as well as simulating the aggregation of soot particles in flames [99, 147, 148].

2.2.2 Tunable algorithms

They generate individual fractal aggregates consisting of spherical primary particles by particle-cluster or cluster-cluster agglomeration. In these types of methods the morphology of the growing agglomerate is constrained to respect a constant prescribed fractal dimension and/or prefactor, this is the reason they are called "tunable algorithms". With the aim at fixing the fractal dimension, Thouy and Jullien [149] introduced the first tunable cluster-cluster agglomeration algorithm. Subsequently, several algorithms were developed [150–160]. Filippov et al. [154] introduced a method able to preserve both the fractal dimension and the prefactor. This method has been further improved in very computationally efficient applications for monodisperse [161] and polydisperse primary particles [140]. The latter is named FracVAL and it is accessible on line [140]. Tunable algorithms are widely used to study soot morphology and particle-light interaction properties [45, 162–165]. However, they cannot in principle, be used to study the physics of soot formation in flames. This because they do not take physical properties into account such as flame temperature, and morphology is imposed rather than naturally resulting from the particle formation dynamics. Currently, the accordance of tunable agglomerates compared to those produced by more physical codes is unknown. Also, the selection of couples of fractal parameters (fractal dimension and prefactor) when varying one of these parameters is uncertain. However, tunable algorithms may give enough accuracy depending on the application. Indeed, they may be combined with physical codes to study the agglomeration of particles as done in the context of fluidized bed agglomeration modeling [166].

2.2.3 Discrete element methods

To avoid redundance with previous works, in the following lines some important reviews currently available in the literature are summarized. The focus is on DEM methods due to their ability to simulate the morphological details of aggregates.

- Meakin 1999 [25]: The early work (mainly during the 80s and 90s decades) on aggregation by two mechanisms; particle-cluster and cluster-cluster is reviewed. Special attention is paid to the models and the effect of aggregation by ballistic, diffusion-limited and reaction-limited regimes on aggregates fractal dimension. A complementary work, focused on the very early work in this field, including aggregation and fractal aggregates morphology is the book of Jullien and Botet [24].

- Dickinson 2013 [137]: Despite it is focused on particle gelation and morphology of colloidal gels, many different methods to take into account particle interactions and/or hydrodynamics interaction are reviewed namely, Monte Carlo, Molecular dynamics, Brownian dynamics, Stokesian dynamics, Dissipative particle dynamics, Multiparticle collision dynamics (or stochastic rotation dynamics) and Fluid particle dynamics. Each method is quickly explained and important insights regarding nanoparticles aggregation are given.

- Eggersdorfer and Pratsinis 2014 [42]: It is a wide review, it offers an overview of aerosol particle coagulation, aggregate/agglomerate stability, aggregate characterization and their industrial applications. It is mainly focused on collision frequency functions for population balance equation and sintering.

- Lazzari et al. 2016 [102]: This review fundamentally focuses on the different processes, such as aggregation, breakage or coalescence influencing the fractal dimension of aggregates. Some techniques for simulation of aggregation such as, Monte Carlo, Molecular dynamics, Brownian dynamics, Stokesian dynamics and population balance equations are also discussed. Some techniques to measure the fractal dimension and its importance in colloid science are also discussed.

Other reviews concerning fractal aggregates properties and applications include, aggregate mobility [55], light scattering [39], synthesis and technological applications of these particles [112, 167–169].

2.2.3.1 Diffusion-/Ballistic-/Reaction-limited agglomeration

Depending on the transport mechanism leading to particle collision the agglomeration process is classified into diffusion-limited (DLCA) when particles collide by diffusive motion [170, 171], or ballistic-limited (BLCA) when particle collide ballistically [172]. Both agglomeration mechanisms consider an unitary sticking probability after collision. Some agglomeration processes, especially in colloids are characterized by a non-unitary sticking probability. When the latter is extremely low, in the order of 10^{-3} the agglomeration is termed reaction-limited (RLCA) [108, 173]. As discussed later, soot agglomeration is much more complicated than the above mentioned mechanisms, experiencing a transition between different regimes.

2.2.3.2 Langevin Dynamics

Since the application of Langevin Dynamics (LD) to study soot aggregation by Mountain et al. [174] many studies have used this method to, among other objectives, providing corrections for the coagulation kernels used in the PBE discussed in section 2.2.1 to account for the aggregate morphology [67, 174, 175], particle-cluster aggregation or condensation [176, 177], high particles concentrations [178–180] or different molecular regimes [181]. An introductory tutorial to this method is found in Ref. [182]. This method is very versatile, allowing for example acoustic [104], turbulent [183], or magnetic forces [103] to be taken into account. Many attempts have been made to improve the computational time efficiency of this method by reducing the number of calculations [184], or by coupling with other simulation methods [67, 103, 183, 185].

2.2.3.3   Monte Carlo methods

Monte Carlo (MC) is in fact a general technique of numerical integration for solving problems that may involve too many calculations or do not have an analytical solution, its name comes from the extensive use of random numbers. In the context of agglomeration, one can find Monte Carlo techniques used to solve the population balance equation [186, 187] as well as to simulate aggregation by DEM. For DEM simulations of aggregation one can distinguish between two different types of Monte Carlo methods however, this difference is not clearly made in the literature!. Therefore, they should not be confused. The *Configuration energy or Metropolis Monte Carlo methods*, where the probability of particles displacement is based on their configuration energy. The second one is simply referred to as *Other Monte Carlo methods*. In the latter, the effect of configuration energy is neglected and consequently the particle dynamics is purely determined by their kinetic energy.

Configuration energy or Metropolis Monte Carlo

This method comes originally from the field of fluid modeling by discrete elements and was developed in 1953 by Metropolis [188]. A good introduction in this context is found in the book [189]. Also, a good review on the adaptation of this method in a wider perspective to study the dynamics of colloidal systems was carried out by Dickinson [190] and more recently by Satoh [191, 192]. In these simulations, the physical time is not deterministic and results are usually expressed in terms of time iterations. The probability of movement maximizes the variation in the configuration energy for the system. Satoh [193] discussed about the adaptation of this method to the agglomeration of suspended nanoparticles. It has been used to study agglomeration of nanoparticles [194]. Akhtar et al. [195] used this method to study the effect of sintering on the agglomerate morphology generated in a 2d on-lattice system. Besides the "artificial" description of time, this type of simulations are also limited to processes that can be described by potential energy functions, therefore, including hydrodynamics interactions, or shear induced agglomeration is not trivial [102]. Interestingly, Kikuchi et al. [196] found that actually the Metropolis MC method is consistent with the Fokker-Planck diffusion equation, this means that even when particles are displaced in a canonical ensemble, their movements can be related to a corresponding time of diffusion. Different studies have proposed different approaches to obtain an equivalent physical time for Monte Carlo iterations by comparison with Brownian Dynamics simulations [197–201].

Other Monte Carlo methods

This method has been mathematically and computationally validated to study the dynamics of suspended monodisperse particles based on the theory of probability by demonstrating the convergence with the solution of the generalized Smoluchowski equation (assumed to govern the time evolution of the system of

monodisperse suspended spheres without hydrodynamics interactions) in the limit of small time-steps by Cichocki and Hinsen [202]. However, it has not been formally probed to study the dynamics of agglomeration. To the author's knowledge, the first application of Monte Carlo to the agglomeration of nanoparticles was developed by Kolb et al. [171], and Meakin [170] for 2d on-lattice DLCA. Different applications of MC methods and advances on the technique come from studies of gelation and sol-gel processes [203–206]. Lattuada et al. [206] added a second step of agglomeration by introducing a probability of agglomeration in order to study the transition from DLCA to RLCA. Similar approaches have been considered in other subsequent studies [207–210].

2.3   Premixed and diffusion flames

The combustion process where fuel and oxidizer (typically air) are mixed first and burned later is called premixed flame, for example the flames produced by a Bunsen burner. When combustion and mixing happen simultaneously they are referred to as non-premixed or diffusion flames, e.g., candle flames. This is because molecular diffusion determines the combustion rate. These flames can also be classified according to their fluid flow as laminar or turbulent [211]. Academic, controlled premixed, and diffusion flames represent a fundamental approach to study soot particle formation. Some of the difficulties in measuring (and simulating) diffusion flames are the strong gradients of temperature, and particle concentration [212]. One considerable advantage is their axisymmetry allowing radially resolved measurements thanks to laser-based techniques [14]. Indeed, considerable progress has been achieved in terms of aggregate sizing, and volume fraction measurements, especially in laminar ethylene flames [213, 214]. However, morphology and primary particle characterization remain very challenging. Characterization of incipient soot particles is also currently difficult [14]. For ethylene flames some progress has been achieved in terms of chemical kinetics modeling for different species formation specially for gas hydrocarbon fuels (e.g., methane or ethylene), while for liquid and solid fuels the progress has been much slower. Furthermore, Polycyclic Aromatic Hydrocarbon (PAH) clustering, and soot nucleation are currently not well understood [215, 216].

2.4   Soot formation mechanisms and maturity

This section describes the main mechanisms involved in soot formation process (see Fig. 2.6), and the numerical modeling is emphasized. Under fuel-rich combustion of hydrocarbons the formation of complex Polycyclic Aromatic Hydrocarbon (PAH) has been observed. PAH molecules are typically simulated up to a specific aromatic size in terms of a number of rings. For example [217] simulated soot formation including PAH reaction pathways up to 5-rings. Another approach is to consider a linear lumping technique [218] where aromatic grow without limit.
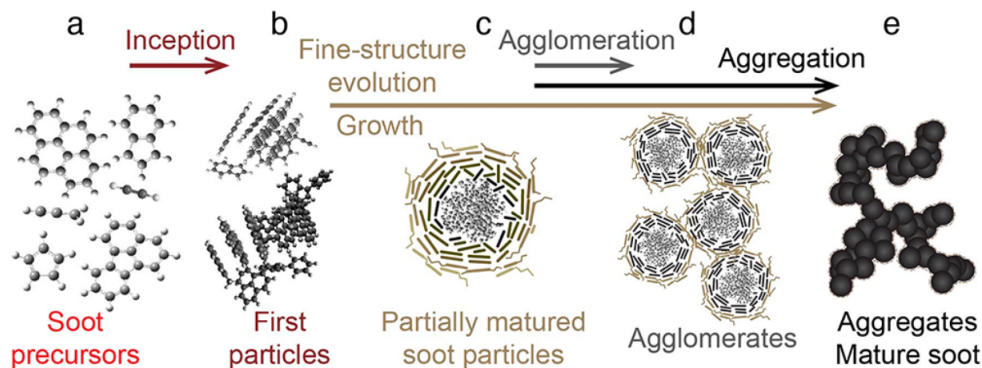
Figure 2.6: Processes and mechanisms influencing soot formation [219].

2.4.1 Nucleation

There is consensus in considering PAH molecules as the precursors for soot formation in flames. However, this has been a topic of intense research and the actual path for gas-particle transition is currently unknown [220]. The collision and clustering (stacking) of PAH molecules such as pyrene, benzene or larger aromatic compounds are typically considered as the nucleation or incipient soot formation. This leads to incipient soot particles of around 2 nm in size [116]. The clustering of these PAH molecules commonly leads to the formation of spheroidal nascent soot primary particles, which can reach sizes around a few nanometers [215, 216, 221–224]. These incipient soot particles can continue growing by surface growth, or decrease in size by oxidation caused (mainly) by oxygen and hydroxyl chemical reactions. These particles may also experience coalescence i.e., collision with subsequent restructuring to minimize surface free energy. Therefore these molecular clusters are considered spherical. This PAH clustering process is very complex to understand (and simulate) from a physical and chemical point of view. Molecular Dynamics simulations have provided important insights into the formation of these nascent soot primary particles. For instance, they have provided an estimation of soot available reactive sites and surface properties [225–227], molecular PAH cluster morphology [222, 228], internal structure [229, 230], detailed PAH molecules interactions and clustering [231]. These simulations have shown that smaller soot particles coalesce faster than larger ones [222, 230]. In this context, it is reasonable to consider a critical time t_2 (corresponding to a limit monomer diameter d_c) after which agglomeration replaces coalescence leading to ramified structures also called fractal-like aggregates (see Fig. 2.7).

2.4.2 Agglomeration

As the molecular clusters grow, their characteristic time of coalescence becomes negligible compared to the characteristic time of collisions [116]. The collision frequency is determined by the particle size and dynamics [232]. At short-distances (in the order of the particle size) the dynamics of these nanoparticles is

characterized by Brownian Motion, and at a macroscopic scale (in the order of the flame size) these particles are carried by the flow. When particles collide, they are commonly considered to agglomerate with an unitary probability, forming random ramified, and self-similar structures referred to as fractal-like agglomerates [233]. Some progress has been achieved in terms of modeling soot agglomerates collision efficiency by considering the change in agglomeration regime ranging from ballistic to diffusive [41, 67]. However, the simultaneous dependency of this property on the flow regime (from free molecular/Epstein to continuum/Stokes) remains a challenge and there is no theoretical approach to model this transition. Pure agglomeration may lead to a self-preserving size distribution under specific agglomeration and flow regimes [67, 234]. Agglomeration kinetics has known asymptotic values for ballistic or diffusive regimes but transition regime is poorly understood [235, 236]. Excepting a few works [112], the above mentioned problems have received little attention in the literature for soot formation in flames, particularly the simultaneous dependence on agglomeration and flow regimes has not been explored. In particular, their impact on particle morphology may be important but they have not been explored.

2.4.3 Surface growth

Soot particle mass increase at the scale of primary particles is referred to as surface growth. This because the chemical mechanisms explaining this phenomena involve soot surface reactions with gas molecules. In this context, surface growth may happen by two mechanisms, namely condensation where a PAH molecule condensates on the surface of soot particles, and Hydrogen-Abstraction-Carbon-Addition (HACA) mechanism. In this mechanism an acetylene molecule coalesces with a soot particle at the same time that hydrogen is removed from the particle [237]. The latter may explain soot dehydrogenation as observed in experiments [238, 239]. At the same time that soot C/H increases, the particle reactivity has been observed to decrease. Indeed, experiments have shown that acetylene depletion is not the reason of surface growth rate decrease as soot particles are ageing in the flame [238]. The heterogeneous reaction between soot particles and gas molecules is commonly based on empirical relationships related with the availability of reaction sites, and Arrhenius-like reaction rates [240]. The effects of surface growth on soot morphology have received little attention in the literature.

2.4.4 Soot maturity

According to Michelsen et al. [219], soot maturity level describes how much it has evolved from inception towards a fully mature graphite-like particle. In this context, soot particles experience changes in internal structure (how molecules arrange within primary particles), and chemical compsition (C/H ratio, and elemental carbon to total carbon ratio). This combination of structural, and chemical evolution produces macroscopic changes as observed in the increasing light absorption coefficient [241], the change on its spectral
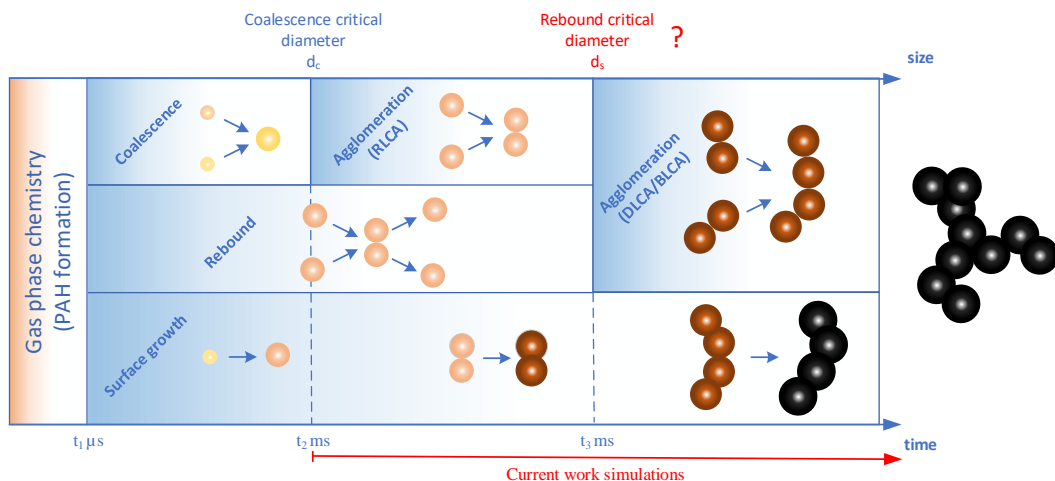
Figure 2.7: Soot formation mechanisms and critical diameters.

dependence [242], and increasing mass bulk density [243]. Incorporating the consequences of soot maturity in numerical simulations is currently a challenge due to the dependence on the atomic resolution of particles for which Molecular Dynamics can give some clues [222, 244]. One remarkable attempt has been done to track soot maturity in PBE-CFD codes for soot formation in academic flames [245]. More recently, soot maturity was suggested to play a quite important role on soot coagulation efficiency as PBE-CFD simulations of soot formation in premixed flames [246, 247].

2.4.5 Oxidation

The chemical reaction of soot particles mainly with oxygen and hydroxyl makes them lose carbon atoms and therefore reducing the mass of primary particles. These carbon atoms may be located on the surface or within primary particles and therefore oxidation can be a surface or volume phenomena [116]. The access to internal soot primary particle structure is determined by their porosity [248]. This mass loss rate may lead to agglomerate fragmentation, and thus decreasing agglomerate size [249].

2.5 Summary and research needs

Different transport mechanism have been studied in the literature as factors influencing the morphology of nanoparticle aggregates/agglomerates. Generally, these studies are limited to specific regimes of particle-fluid (continuum or free molecular), of particle-particle interaction (BLCA or DLCA), and of particle sticking (RLCA). Also, they are typically restricted to study the global structure of aggregates, particularly focusing only on the fractal dimension. Local compactness has received little attention especially in terms of mass

transfer mechanisms such as surface growth. The variation of physical properties (such as temperature or surface growth rate) during the aggregation process may induce morphological changes on particles such as soot. There are a few works reporting physical mechanisms that considerably influence the morphology of aggregates such as external electric or magnetic fields. These fields could be used in purpose for tailoring agglomerate's morphology. The morphological change induced by energy transfer mechanisms such as laser-particle interaction, have received little attention in the literature.

PBE is commonly used to study the kinetics of agglomeration in terms of the time-evolving particle size distribution. This method is based on the probability of particle collisions obtained from the coagulation kernels [250–253]. Although this approach is very practical and widely used for simulating more realistic scenarios of particles agglomeration [250, 252, 253], it relies on a good approximation of the coagulation kernels. These kernels are dependent on the particle's morphology, the flow regime, and agglomeration regime. Only DEM methods are suitable to accurately study the morphology of aggregates/agglomerates [102]. For these methods, the dynamics of individual particles should be simulated. To this end, the most accurate method is Langevin Dynamics however, it is very computationally expensive [23, 102, 254]. On the other hand, the classical DLCA/BLCA and RLCA, here referred as Monte Carlo methods, are faster but, limited by the simplified particle dynamics and to the specific agglomeration/flow regimes. Contrary to LD, MC is usually regarded as a method that relies on an artificial description of time, making it difficult to study the agglomeration of nanoparticles [102]. Despite this, some efforts have been made to obtain a more physical description of time [210, 255]. Unfortunately, as it is shown later, they can lead to incoherent time progress for the ensemble of polydisperse particles and/or they are restricted to a specific agglomeration regimes (BLCA or DLCA). Also, in different studies based on the MC method, the probabilities of particle displacement suffer the same limitation and even for equivalent agglomeration regimes, different definitions of probabilities can be found. For example, Kim et al. [208] compared different alternatives for calculating this probability when the agglomeration takes place in the DLCA regime. One remarkable exception is the work of Heinson et al. [236] who developed an interpolating formula to simulate the transition between BLCA and DLCA regimes. Finally, particles are usually displaced along a constant distance in the order of the monomer's diameter, regardless of their sizes. Not many studies have considered size-dependent displacements [67, 256, 257].

Soot maturity evolution in flames involves a change in both chemical composition and bulk density whose effect on soot morphology and aggregation kinetics has not been explored. Soot particles formed in flames acquire a natural electric charge [258–260]. These electric charges are typically neglected in most numerical simulations though they may influence the particle formation dynamics.

The effects of soot formation mechanisms such as surface growth on aggregates morphology is currently poorly understood. For instance, surface growth may induce relevant changes on aggregates fractal dimension and/or prefactor. How the morphology of this particles, in terms of volume and surface area, depends on the degree of primary particle overlapping lacks of models to predict it.

The effect of soot particles detailed morphology evolution in the flame on the projected area power-laws for the analysis of experimental TEM images has received little attention in the literature. They have been studied only for simplified agglomerates generated by DLCA codes considering an artificial overlapping between primary particles [29, 30]. Their dependence on primary particle size, polydispersity, physically-driven primary particle overlapping is unknown. Since CFD simulations based on the PBE for simulating the aerosol dynamics are not able to simulate the detailed morphology of soot aggregates, they need to be coupled with codes revealing soot morphology.

In this thesis, a new MC method with justified probabilities of particles movement, considering size-dependent displacements and able to bring a validated and consistent physical residence time for individual and for the ensemble of polydisperse particles is introduced. This method is numerically implemented and referred to as MCAC (Monte Carlo Agglomeration Code), this is highlighted as a different method in Fig. 2.5. MCAC allows the transition of agglomeration and flow regimes to be taken into account. This code is coupled with CFD continuum simulations in order to account for the time-evolving flame temperature, nucleation, and surface reaction rates. MCAC is able to simulate all the mechanisms of soot formation including nucleation, surface growth, oxidation (and fragmentation), and agglomeration. In addition, MCAC can take the collision and sticking probabilities into account. therefore, the role played by soot electric charges and maturity can be explored.

2.6 Scope and organization of the dissertation

The main purpose of this dissertation is to numerically simulate soot formation under different laminar flames conditions (premixed and diffusion). To this end, Monte Carlo DEM simulations are carried out to account for the explicit morphology of soot agglomerates/aggregates. This leads to specific objectives as listed below,

1. Develop and validate the MCAC code (Chapter 3).

2. Study soot agglomeration under flame conditions (Chapter 4).

3. Study the simultaneous soot aggregation and surface growth. Adapt MCAC to oxidation and time-evolving nucleation (Chapter 5).

4. Simulate soot aggregation, surface growth, and maturity evolution (Chapter 6).

5. Coupling CFD-MCAC simulations of soot nucleation, aggregation, surface growth, and oxidation (Chapter 7).

The list of objectives is naturally reflected by the organization of the manuscript.

3 | MCAC: Monte Carlo Aggregation Code[1]

As shown in Fig. 3.1, MCAC simulations aims at representing the evolution of soot particles along a given streamline in the flame (cyan continuous line). This streamline will determine a temperature profile, and the gas-particle mass transfer. As shown on the right hand side, at the beginning of the simulation, soot particles are considered spherical with a certain degree of polydispersity in size. These particles are initially randomly distributed in a cubic box domain avoiding overlapping and introducing enough particles to respect a known initial particle volume fraction. The cubic box domain is assumed to be carried by the flow, consequently neglecting inertia effects. The latter is justified by the small size and mass of soot particles (rarely arriving to micrometer range).
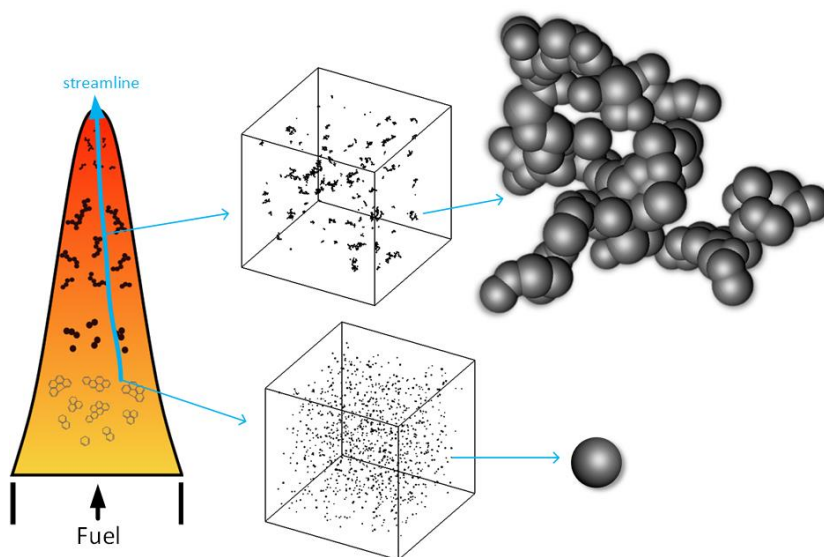
Figure 3.1: MCAC simulation method.

---

[1]Part of this Chapter has been published in: Morán, J., Yon, J., & Poux, A. (2020). Monte carlo aggregation code (MCAC) part 1: Fundamentals. Journal of Colloid and Interface Science, 569, 184-194.

The trajectory of each individual particle within the cubic domain is integrated in time based on a new Monte Carlo DEM approach. Periodic boundary conditions are considered. Particles are allowed to agglomerate with a given probability of collision and sticking (thoroughly discussed in Chapter 6). Additionally, when the number of agglomerates is reduced by a factor of eight then, each side of the box is duplicated and the number of agglomerates is increased by a factor of 8. In this way, the simulation domain remains always cubical. The new agglomerates correspond to periodic images of the existing ones, ensuring a constant particle volume fraction while not influencing the agglomeration process [250, 251]. This method is used to avoid the loss of statistical significance on the physical description of the system due to the reduction of the number of particles (agglomerates) in the box due to agglomeration. At the same time they are displaced, particles experience surface reactions. The latter leads to the formation of aggregates as the one shown in the upper part of Fig. 3.1. These aggregates are accurately simulated in terms of morphology based on the proposed MCAC method as described in the following sections.

3.1 Proposed approach

The proposed Monte Carlo Aggregation Code (MCAC) considers nanoparticle nucleation, coagulation, surface growth, and oxidation. The latter may lead to aggregate fragmentation which is taken into account. The term aggregation is preferred in the name of the code (MCAC) in accordance with previous similar developments (DLCA/BLCA/RLCA/Tunable aggregation codes, as discussed in the previous chapter). This is also explained by its goal of simulating strongly connected/overlapping structures (aggregates, also referred to as hard agglomerates in the literature). The code can be explained in 8 main steps (see the frame below).

The dynamics of nanoparticles simulations (steps 1-3) are described in the following sections of this Chapter. The developments linked to particle agglomeration are given in Chapter 4, those linked to surface reactions and nucleation (essentially steps 6-7) are given in Chapter 5, those linked to collision efficiency (essentially steps 4-5) are given in Chapter 6. Finally, the details of CFD-MCAC coupling (essentially step 8) are described in Chapter 7.

> **Monte Carlo Aggregation Code**
>
> **Step 1:** At the beginning of the simulation, particles are randomly distributed in a cubic box avoiding overlapping.
>
> **Step 2:** One particle is randomly selected with a picking probability p.
>
> **Step 3:** The selected particle is moved in a random orientation (θ) along its persistent distance (λ_p) or less if a collision with a neighbor is detected.
>
> **Step 4:** If no possible collision is detected, then continue to Step 6. In the case of possible collision, a random number (with uniform distribution) $\delta_1 \in [0,1]$ is generated and two possible outcomes exist depending on the collision probability P_{coll},
>
> > **Step 4.1:** The two particles collide when $\delta_1 \leq P_{\text{coll}}$. Continue to Step 5.
> >
> > **Step 4.2:** The process is restarted from Step 3 when $\delta_1 > P_{\text{coll}}$.
>
> **Step 5:** A new random number (with uniform distribution) $\delta_2 \in [0,1]$ is generated and two possible outcomes exist depending on the sticking probability P_{stick},
>
> > **Step 5.1:** The two particles stick together at the first point of contact when $\delta_2 \leq P_{\text{stick}}$. Continue to Step 6.
> >
> > **Step 5.2:** Particle rebound takes place i.e., particle do not stick and collide elastically when $\delta_2 > P_{\text{stick}}$.
>
> **Step 6:** The selected particle experiences surface reactions. This means that its primary particles may increase (surface growth) or decrease (oxidation) in size. The latter involves a subsequent check for aggregate fragmentation.
>
> > **Step 6.1:** If no fragmentation occurred then continue to step 7.
> >
> > **Step 6.2:** Otherwise, the agglomerate is fragmented into smaller pieces.
>
> **Step 7:** Nucleation, where primary particles are randomly introduced in the domain (avoiding overlapping with neighbors) may take place.
>
> **Step 8:** Otherwise, surface reaction rate, nucleation rate, temperature, and particle composition are updated according to MCAC-CFD coupling. When temperature evolve then the gas viscosity, gas mean free path, and the particles friction coefficient are updated. This process is repeated iteratively from Step 2 until an user-defined criterion is met, for example, a limit in residence time is reached.

3.2 MCAC: aerosol particle dynamics

3.2.1 Objectives and methodology

According to MCAC description given in section 3.1, the main purpose of the present section consists in determining for each particle its persistent distance (λ_p), the corresponding time step (Δt), its probability of displacement (p_i) according to its size, morphology and the thermodynamic conditions of the surrounding fluid. It is also necessary to define a coherent physical residence time for the whole population of particles in the system. As discussed before, these correspond to the main principles of MC simulations. Additionally,

to the author's knowledge, there are no studies discussing about the implications on for example λ_p and Δt related to an accurate description of suspended nanoparticle dynamics. Consequently, this dissertation intends to fill this gap of knowledge.

3.2.2 Results

3.2.2.1 The persistent distance λ_p and the corresponding time step Δt

Among the currently available options in the literature is the Fuchs [261] or Dahneke's [262] persistent distances however, the exact corresponding time step (Δt) for conducting MC simulations are missing in the literature. One exception is Hayashi et al. [256] who used the Fuch's persistent distance $\lambda_p = 8D/(\pi\overline{c})$ and considered $\Delta t = \lambda_p/\overline{c}$, where D and $\overline{c}$ are the diffusion coefficient and average Maxwellian velocity of the particle, respectively.

    Fig. 3.2 shows the mean squared displacement of an individual nanoparticle in suspension in a still gas. The couple λ_p and Δt proposed in Ref. [256] is compared with Langevin Dynamics simulations (see Section S1 of the SM A) as well as the Einstein theory of Brownian motion [263]. As observed in this figure, the combination of λ_p and the corresponding Δt proposed in Ref. [256] is biased when compared with both Langevin Dynamics and the theory of Brownian motion by a factor of 0.4. Considering this inconsistency, the objective now is to find a proper persistent distance λ_p and the corresponding time step Δt for MC simulations leading to a correct simulation of Brownian motion.
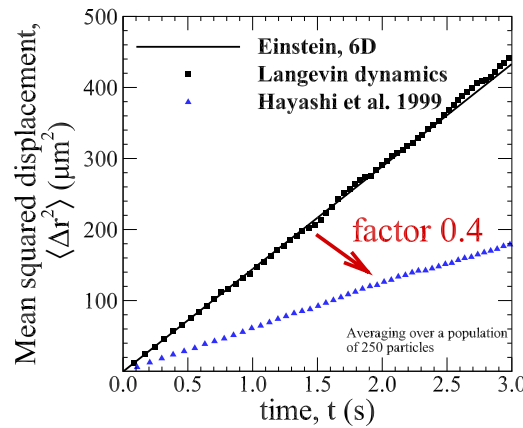
Figure 3.2: Mean squared displacement of a 1 μm spherical particle suspended in air at ambient conditions (fluid mean free path 66 nm) as a function of time. Calculated from Langevin Dynamics simulations, Einstein's theory on Brownian Motion [263] and Hayashi et al. [256] simulations.

3.2.2.2 The asymptotic behavior of Random Walks

A first methodology to find a λ_p and its corresponding time step Δt is to ensure an equality in the asymptotic behavior of random walks obtained from a binomial approach and the asymptotic mean squared displacement predicted by Einstein's theory on Brownian Motion. This asymptotic behavior is also predicted by Langevin Dynamics [264], and it is experimentally proved for particles suspended in fluids [265, 266]. The same binomial approach is used for on-/off-lattice random walks and the results are explained in S2 of the SM A and summarized in Table 3.1. For example, for a 3-dimensional off-lattice random walk of persistent distance λ_p and corresponding time step Δt the following equality should be respected $6D = \lambda_p^2/\Delta t$, where D is the particle's diffusion coefficient. Consequently, by selecting λ_p or Δt, the other can be obtained by using this expression. However, the question now is, how to choose one of these two parameters? To answer this question, a closer comparison between MC particle trajectory and the one simulated by the reference Langevin Dynamics method is carried out. This is explained in the following section.

Table 3.1: Comparison of mean squared displacement for random walks (RW) compared against the generalized Einstein's relation.

Dimensions d	Einstein's relation	On-lattice RW	Off-lattice RW
1	$2Dt$	$[\lambda_p^2/\Delta t]t$	$[\lambda_p^2/\Delta t]t$
2	$4Dt$	$[2\lambda_p^2/\Delta t]t$	$[\lambda_p^2/\Delta t]t$
3	$6Dt$	$[3\lambda_p^2/\Delta t]t$	$[\lambda_p^2/\Delta t]t$
d	$2dDt$	$[d\lambda_p^2/\Delta t]t$	$[\lambda_p^2/\Delta t]t$

3.2.2.3 Comparison with Langevin Dynamics

To mimic a MC simulation, the trajectory followed by a particle suspended in a fluid as numerically simulated by Langevin Dynamics (see Section S1 of the SM A) is discretized. The discretization time step is $n\tau$, where n is a factor and τ is the momentum relaxation time $\tau = m/f_p$ defined as the ratio between particle's mass and friction coefficient. The friction coefficient of a spherical particle is determined as $f_p = 3\pi\eta d_p/C_c(\mathrm{Kn}_g)$, where η is the gas viscosity, d_p is the particle's diameter, and $C_c(\mathrm{Kn}_g)$ is the Cunningham slip correction factor,

$$C_c(\mathrm{Kn}_g) = 1 + \mathrm{Kn}_g \left(C_1 + C_2 \exp\left[-\frac{C_3}{\mathrm{Kn}_g} \right] \right) \tag{3.2.1}$$

where $\mathrm{Kn}_g = 2\lambda_g/d_p$ is the gas Knudsen number, λ_g is the gas mean free path, $C_1 = 1.142$, $C_2 = 0.558$, and $C_3 = 0.999$ are empirical constants for air [267].

As shown in Fig. 3.3, the angle θ between two successive displacements is calculated as $\theta = \mathrm{atan2}(\|a \times b\|/a \cdot b)$, where a and b are the vectors corresponding to two consecutive discretized displacements, the function atan2() corresponds to the typical inverse of tangent function found for example in Matlab avoiding the division by zero when $a \cdot b = 0$. This expression ensures an angle $\theta \in [0, \pi]$ and avoids numerical

issues found for inverse cosine and sine functions [268]. The theory of Brownian motion predicts a rectilinear
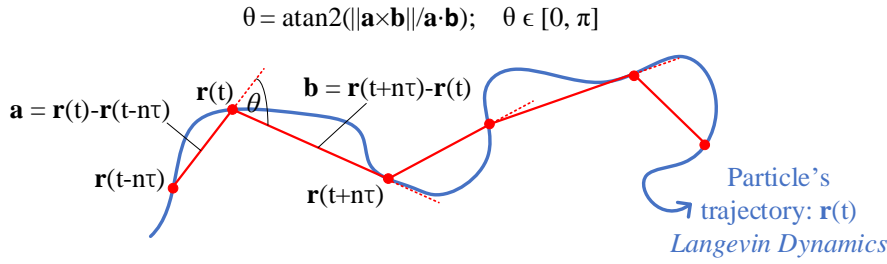
Figure 3.3: Calculation of apparent mean free paths and the angles between succesive displacements from the trajectory of a particle describing a Brownian Motion. The trajectory is calculated based on Langevin Dynamics simulations. $\tau = m/f_p$ stands for the momentum relaxation time.

movement when $t \ll \tau$ meanwhile, for large times $t \gg \tau$ the movement becomes diffusive and therefore, the particle performs movements in random directions [264]. Having this in mind, Fig. 3.4(a) shows the normalized probability density function (pdf) $P(\theta)/P_{uni}(\theta)$ of the angle θ for different values of n. $P_{uni}(\theta)$ corresponds to the asymptotic distribution of angles, calculated based on $\theta = \cos^{-1}(2\varrho - 1)$, where $\varrho \in [0, 1]$ is a random number with uniform distribution [140]. The $P_{uni}(\theta)$ corresponds to a non-biased random polar angle distribution.

On the one hand, for small n, namely $n = 0.01$, the ratio $P(\theta)/P_{uni}(\theta)$ is a narrow distribution with larger probabilities for smaller angles suggesting no significant changes in directions. This is in accordance with theory since the particle is experiencing a ballistic-like motion. On the other hand, for $n = 50$, the normalized angle probability density function $P(\theta)/P_{uni}(\theta)$ is almost flat suggesting random displacements, characteristic of a diffusive motion. Considering these results, a quantitative criteria is needed to select a time step Δt and thus, the corresponding λ_p based on the aforementioned binomial approach. Because the particle's displacement in MC simulations is considered isotropic, here the goal is to determine the minimum Δt, such that, the normalized pdf of θ becomes uniform. To this end, the information entropy $S(n)$ is defined based on the probability density function of θ as follows,

$$S(n) = -\sum_j P_j \log P_j, \qquad P_j = P(\theta_j) \qquad (3.2.2)$$

where θ_j is a discretization of the angle $\theta \in [0, \pi]$. In Fig. 3.4(b) the normalized entropy as a function of n is presented. The selected quantitative criteria consists in finding the minimum Δt to reach 99% in the normalized information entropy of θ. This is based on the idea that $S(n)$ is a monotonically increasing function of n as the kurtosis of the distributions shown and explained before is decreasing. As can be seen in Fig. 3.4(b), this corresponds to $n = 3$, i.e. the movement becomes diffusive when $\Delta t \approx 3\tau$. Finally, considering $\Delta t = 3\tau$ and the asymptotic condition imposed by the binomial approach combined with the

Einstein's theory on Brownian motion, a corresponding persistent distance $\lambda_p = \sqrt{18D\tau}$ is obtained.
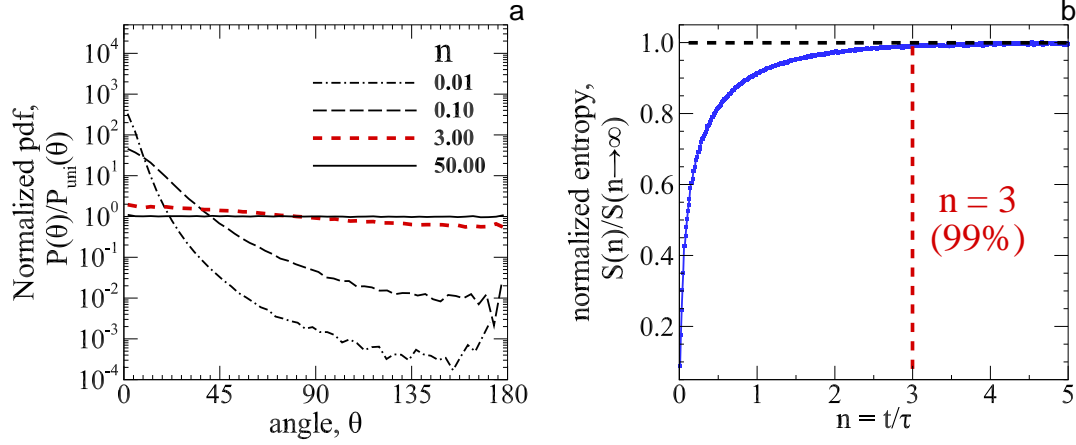
Figure 3.4: Normalized pdf of θ (a) and normalized information entropy of θ (b). Here, θ is the angle between successive displacements of a particle in Brownian Motion calculated by discretized Langevin Dynamics trajectories. The asymptotic distribution of angles $P_{\text{uni}}(\theta)$ is calculated based on $\theta = \cos^{-1}(2\varrho - 1)$, where $\varrho \in [0, 1]$ is a random number with uniform distribution [140]. This definition ensures a flat normalized distribution when $n \to \infty$.

3.2.2.4 How to take into account the change in flow regime

Both the persistent distance and time step introduced in the previous section, strongly depend on the friction coefficient of the suspended nanoparticles. The growth of these particles by coagulation may lead to a change in both the flow regime and agglomeration regime. The flow regime is commonly characterized by the classical gas Knudsen number $\text{Kn}_g = \lambda_g/r_m$ where λ_g is the mean free path of the gas and r_m the mobility radius of the suspended particle. When $\text{Kn}_g \to 0$, the non-slip condition applies for fluid molecules approaching to the surface of the suspended particle (continuum regime) meanwhile, when $\text{Kn}_g \to \infty$, there is slip between the fluid and the surface of the particle (free molecular regime). For spherical particles, it is just necessary to introduce the Cunningham correction factor to the Stokes-Einstein friction factor in order to numerically simulate the transition between both regimes. But, in the case of fractal agglomerates, it is much more challenging and not many options can be found in the literature [37, 38, 55]. However, they are typically limited to a specific regime and/or a constant fractal dimension (commonly $D_f = 1.78$). There are limited options in the literature to evaluate the agglomerate's friction coefficient for all flow regimes, some remarkable exceptions are the expressions proposed by Corson et al. [38] and Zhang et al. [37]. The semi-empirical method proposed by Yon et al. [56] is preferred here due to its simplicity and good agreement with the literature. This method is based on the following power law between the friction coefficient of the agglomerate f and the number of primary particles N_p,

$$f = f_p N_p^{\Gamma_p/D_f}, \qquad \Gamma_p = \Gamma_p\left(\text{Kn}_g\right) \qquad (3.2.3)$$

here f_p stands for the primary particles friction coefficient, and d_p is the mass average primary particle diameter. The method takes into account the morphology of particles by means of the fractal dimension D_f. The function Γ_p is governed by the flow regime of primary particles [56],

$$\Gamma_p(\text{Kn}_g) = 1.378 \left[\frac{1}{2} + \frac{1}{2} \left(\frac{\text{Kn}_g(d_p) + 4.454}{10.628} \right) \right] \tag{3.2.4}$$

giving an important physical role to the primary particles diameter in the agglomeration process as shown in Chapter 4.

3.2.2.5 Probability of particles displacement

In the context of MC simulations, contrary to the DEM approach proposed in the literature [112], particles are iteratively displaced by randomly selecting them with a probability p_i yet to be defined. As mentioned in the previous chapter, this probability is often limited to a given flow regime. Here, an original definition for this probability, valid for all the flow regimes is proposed. Indeed, to ensure a coherent physical time step for a population of polydisperse particles, it is clear that particles moving faster have to be displaced more often than slower ones. This is illustrated in Fig. 3.5 showing a simple set of 3 polydisperse particles where particle 3 has the shortest time step and 1 the largest one. In the time scale of particle 1, particles 2 and 3 should be displaced twice and three times, respectively for the system to have the same residence time after Δt_1.
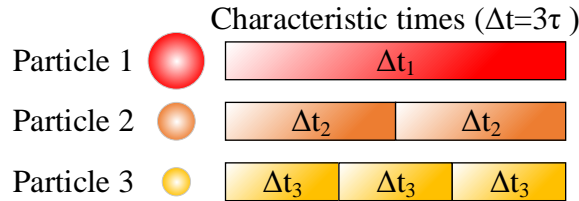
Figure 3.5: Example of 3 different particles under the same thermodynamics conditions and their corresponding characteristics times, corresponding to 3τ, i.e. $3m/f$.

This simple reasoning enables the determination of a general definition of the particle's probability of displacement,

$$p_i \propto \Delta t_{max}/\Delta t_i, \tag{3.2.5}$$

where Δt_i is the characteristic time step of the ith particle and Δt_{max} the maximum one among the whole population of particles in the system (i.e. Δt_1 in Fig. 3.5). Eq. (3.2.5) can be normalized to obtain a probability between 0 and 1 as follows,

$$p_i = \Delta t_i^{-1} / \sum_j \Delta t_j^{-1} \tag{3.2.6}$$

Thus, each time two particles collide forming a new one, the new Δt has to be determined in replacement of

the two colliding particles corresponding Δt's. Consequently, all the probabilities are re-evaluated.

3.2.2.6 Determination of a physical residence time

As discussed in the previous chapter, a physical residence time is often inaccurate or even missing in the MC simulations found in the literature. Now, we show how this key variable can be easily derived in the proposed Monte Carlo agglomeration code. To this end, let's consider again Fig. 3.5. It is clear that the residence time increases in $\Delta t_{max} = \Delta t_1$ when particles 1, 2 and 3 are displaced 1, 2 and 3 times, respectively. Thus, the residence time increases in Δt_{max} after a total of $n_t = 6$ random displacements, corresponding statistically to the following expression,

$$n_t = \sum_i \Delta t_{max}/\Delta t_i \qquad (3.2.7)$$

In this context, the population residence time in the $(k + 1)$ iteration is increased as,

$$t_{res}^{(k+1)} = t_{res}^{(k)} + \frac{\Delta t_{max}}{n_t} \qquad (3.2.8)$$

As shown more rigorously in Section S2 of the SM A, the definition of probability given by Eq. (3.2.6) ensures a consisting residence time for the system of polydisperse particles.

3.2.2.7 Validation

This section aims at showing the ability of MCAC to simulate the Brownian motion of polydisperse particles as a function of a physical residence time. To this end, three spherical particles having very different diameters (in continuum, intermediate and free molecular flow regimes) are considered. To summarize, MCAC considers the redefined persistent distance $\lambda_p = \sqrt{18D\tau}$ and the corresponding time step $\Delta t = 3\tau$ as well as the probabilities of particles displacement given by Eq. (3.2.6). Finally, the residence time is evaluated based on Eq. (3.2.8). Note that collisions and subsequent aggregation/agglomeration are not considered in the present test case. The agglomeration process is studied in more details in Chapter 4. The calculated mean squared displacements of the three mentioned particles are reported in Fig. 3.6. Once again, LD simulations are used to validate the proposed approach, corresponding to the continuous lines in this figure. The excellent agreement highlights the robustness of the proposed MC method to simulate the dynamics of suspended polydisperse particles for any individual flow regime.

3.3 Discussions and conclusions

Langevin dynamics predicts a transition from ballistic (very short times) to diffusive movement [264]. This has been experimentally proved for particles in suspension in fluids [265, 266, 269]. The difficulty for
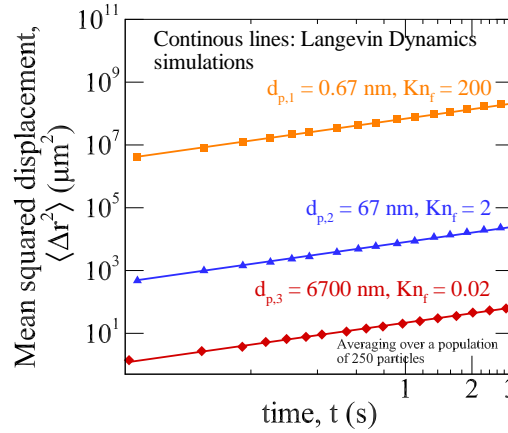
Figure 3.6: Mean squared displacement of particles as a function of time compared against Langevin Dynamics (continuous lines) and Einstein's theory on Brownian Motion, considering the proposed particles persistent distance and the introduced probability of particles displacement.

Monte Carlo simulations is to find a persistent distance or apparent mean free path λ_p to approximate this transition in a single step. For this problem, there is no exact solution and only approximations can be done. In the particular case of numerical simulation of agglomeration λ_p is typically considered equal to the monomer's diameter independent on the agglomerate's size [208, 209, 270]. Camejo et al. [257] proposed a displacement proportional to the agglomerate diffusion coefficient being therefore restricted to the DLCA mechanism. Other options include the Fuchs [261] or Dahneke's [262] persistent distances as can be seen in refs. [256, 271]. Despite the latter options may capture the essential aspects of the underlying physics, there is no corresponding physical time step for each λ_p. Therefore, it is decided to search for a proper persistent distance λ_p for MC simulations and the corresponding time step (Δt). Based on a binomial approach and the discretization of Langevin Dynamics trajectories of individual particles, the $\lambda_p = \sqrt{18D\tau}$ and the $\Delta t = 3\tau$ are proposed, where $\tau = m/f$ is the momentum relaxation time. This couple of persistent distance and time step are recommended for conducting MC simulations.

The probabilities of particles displacement are commonly expressed as a function of the number of primary particles of one agglomerate and the expressions are limited to specific DLCA or BLCA regimes [236, 272]. Many different expressions for the probabilities of particles displacement are found in the literature. Commonly, for DLCA they are assumed proportional to the diffusion coefficient [171, 208, 210, 255, 273] and for BLCA they are assumed proportional to the Maxwellian velocity [236, 272]. However, as showed by Kim et al. [208] for colloidal particles experiencing DLCA, the most consistent results with experiments are found when the individual diffusion coefficient are normalized by the maximum one. One remarkable attempt to simulate the transition BLCA-DLCA is the work of Heinson et al. [236] who proposed an interpolation expression for the probability of particles displacements. In the present thesis, a new probability of particles displacement is introduced which is not constrained to a specific agglomeration or flow regime.

Results of Monte Carlo simulations are commonly expressed in terms of the number of iterations instead of a physical residence time [235, 236]. Another approach is to estimate the time between collisions based on the coagulation kernels as done in Refs. [251, 270]. The latter method is limited to the cases where the morphology of agglomerates and therefore, the coagulation kernels are known. Here, an accurate time step for both individual and for the population of polydisperse particles are proposed. Individual time accuracy is ensured by the definition of the time step associated with the persistent distance and the coherent population time step is achieved based on the definition of the probabilities of particles displacements. The proposed Monte Carlo Aggregation Code is validated. It combines the advantages of MC codes, i.e. the ability to efficiently simulate the agglomerates formation including their complex morphology and the advantages of Langevin Dynamics to respect a physical particles dynamics. The application of this code to simulate soot agglomeration process is presented in Chapter 4.

4 | Soot agglomeration[2]

During the agglomeration of nanoparticles and in particular, soot, a change in both the flow regime (from free molecular to near continuum) as well as the change of agglomeration regime (from ballistic to diffusive) is expected. However, these effects are rarely taken into account in numerical simulations of particle agglomeration and yet, they are suspected to have an important impact on the agglomeration kinetics, particle morphologies, and size distributions. This work intends to study these properties by using MCAC as presented in Chapter 2, focusing on the physical impacts of varying the particle volume fraction and monomers size and polydispersity. The results show an important sensitivity of the kinetics of agglomeration, coagulation homogeneity, and agglomerates' morphology to the size of monomers. First, for smaller monomer diameters, the agglomeration kinetic is enhanced and agglomerates are characterized by larger fractal dimensions. Second, for large monomer diameters, fractal dimensions down to 1.67 can be found being smaller than the classical 1.78 for DLCA mechanism. One important conclusion is that variation in time of both regimes has to be considered for a more accurate simulation of the agglomerate size distribution and morphology.

4.1 Introduction

Particles formed under agglomeration naturally evolve into complex fractal-like morphology of polydisperse size consisting also of polydisperse primary particles. Eventually, depending on the physical conditions, particles may change the way they interact with the surrounding fluid and also the way they interact with each other. In other words, particles may undergo a change of flow regime and/or agglomeration regime, respectively. The flow regime is characterized by the classical fluid Knudsen number $Kn_f = \lambda_f/r_m$, where λ_f and r_m are the fluid mean free path and particle's mobility radius, respectively. As introduced by Pierce et al. [235], the agglomeration regime can be quantified by the nearest-neighbor Knudsen number $Kn_n = \lambda_p/r_n$, where $\lambda_p = \sqrt{18D\tau}$ is the particle persistent distance [274] calculated from the particle diffusion coefficient D and momentum relaxation time $\tau = m/f$. The latter corresponds to the ratio between particle mass and friction

---

[2]Part of this Chapter has been published in: Morán, J., Yon, J., Poux, A., Corbin, F., Ouf, F. X., & Siméon, A. (2020). Monte Carlo Aggregation Code (MCAC) Part 2: Application to soot agglomeration, highlighting the importance of primary particles. Journal of Colloid and Interface Science, 575, 274-285.

coefficient. λ_p is the distance over which particles experience an approximately ballistic movement [235]. r_n is the nearest-neighbor distance given by $r_n = n^{-1/3} - 2r_{max}$ where n is the particle number concentration and r_{max} is the average maximum radius describing the agglomerate. This radius is around 1.5 the gyration radius of agglomerates [30].

When Kn_n is high, cluster agglomeration tends to become ballistically limited (i.e. BLCA) whereas when tending toward 0, it is diffusion-limited (i.e. DLCA). For soot particles generated in premixed or
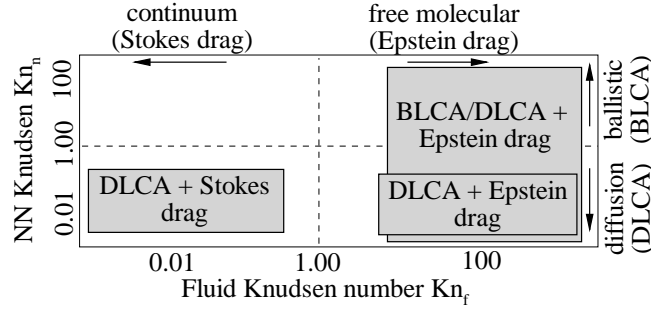
Figure 4.1: Different regimes of agglomeration and fluid flow studied in the literature.

diffusion flames, the fluid Knudsen number has been typically considered to be $Kn_f \gg 1$, i.e. being in the free molecular flow regime [66, 275, 276], meanwhile other studies have shown it can evolve down to $Kn_f \sim 1$ depending on the flame conditions [277]. Moreover, for different aerosol and colloid systems, fluid Knudsen numbers up to $Kn_f \sim 10$ have been found in the transition regime for titania and silica aerosols [278], oleic acid and sodium chloride aerosols [279, 280], di(2-ethylhexyl)sebacate in a rarefied gas [281] and down to $Kn_f \sim 0.1$ by other studies involving different types of particles [282–285].

Fig. 4.1 summarizes most of the current simulations found in the literature as classified based on the above mentioned Knudsen numbers. Agglomeration has been commonly studied in the continuum flow regime for diffusion-limited agglomeration (DLCA + Stokes drag) [210, 286]. Indeed, in this context, the transition from strong inter-particle interactions forces, i.e. DLCA to the weak interactions (reaction limited agglomeration, RLCA) has been studied [210, 286–288]. In this chapter, focused on soot particle agglomeration, strong interaction forces are not considered and therefore the transition towards the RLCA regime is beyond the scope of this chapter. Pierce et al. [235] studied the DLCA with an Epstein drag, i.e., considering a friction coefficient valid for free molecular flow regime $Kn_f \to \infty$ [232]. Transition in the flow regimes (abscissa in Fig. 4.1) is complex due to the lack of models for calculating the friction coefficient of fractal agglomerates. In this context, some studies have treated both continuum and free molecular flow regimes separately [23]. Similarly, BLCA and DLCA are generally treated independently [286]. Notably, only a few studies have considered a transition between both agglomeration regimes (vertical axis in Fig. 4.1) but commonly in the free molecular flow regime, i.e. with an Epstein drag [67, 236]. To the author's knowledge, simultaneous transitions between both agglomeration and flow regimes have not been considered in the past except notably, the work of Thajudeen et al. [289]. The latter is based on Langevin Dynamics simulations by

considering the agglomerate morphology, which is very accurate but computationally expensive. However, the influence of the nearest-neighbor distance, the kinetics of agglomeration, the particle size distribution and particle morphology were not systematically studied. The Monte Carlo Aggregation Code (MCAC), developed and validated in Chapter 2 enables this knowledge gap to be covered with a reduced computational cost. In this context, the focus is on the effect of particle volume fraction, and primary particle size and polydispersity. The present chapter aims at illustrating that caution has to be taken regarding the change in both regimes because they impact the kinetics of agglomeration, particle size distribution, and agglomerate morphology. On the one hand, when increasing the particle volume fraction (f_v), the mean distance between particles decreases and therefore Kn_n increases. Thus, the agglomeration becomes more ballistic and therefore an increase in the fractal dimension of agglomerates has been observed [270]. This is consistent with classical DLCA and BLCA regimes [286], but in the present study, the transition between both regimes is continuous. On the other hand, when the primary particle diameter increases (for example during aggregation or agglomeration and surface growth process), the flow regime evolves. In the context of soot simulation, the agglomeration process is often restricted to the Epstein flow regime because of the high flame temperatures. Nevertheless, from nascent soot typically around 1-4 nm at flame temperatures to the mature primary particles around 30-60 nm eventually released to the atmosphere, the flow regime strongly evolves [91, 96, 290, 291].

Another objective of the present Chapter is to analyze and report the evolution of the coagulation kernels during the agglomeration process. Indeed, the Smoluchowski (or population balance) equation has been proved to be a powerful tool for modeling soot agglomeration [148, 291, 292]. This equation follows the evolution of the particle number concentration as a function of time. To this end, $k(i, j)$ has to be known, i.e. the coagulation kernels determining the rate of collisions between particles i and j. In certain cases, especially for fractal agglomerates, this kernel is a homogeneous function, i.e. $k(\vartheta i, \vartheta j) = \vartheta^\lambda k(i, j)$ where λ is the agglomeration kernel homogeneity parameter. This λ parameter is very important for the kinetics of agglomeration and the resulting particle size distribution qualified as "self-preserving" [65, 66]. It has been proposed that λ depends on both the fluid Knudsen number and the nearest-neighbor Knudsen number [235, 236], however, these relations are not well understood especially in the transition regime. Considering its simplicity, the scaling hypothesis is widely used to obtain λ [278, 286, 293, 294]. However, its accuracy is rarely discussed [295]. In the present work, a robust and more direct method for determining λ is proposed.

4.2 Numerical simulations

MCAC algorithm as introduced in Section 3.1 is used. Pure agglomeration (without time-evolving nucleation, and surface reactions) is simulated. Simulations start with a total of 3200 monodisperse or polydisperse spherical primary particles, ending when the average number of monomers per agglomerate is 100. Particles

systematically and irreversibly stick together upon collisions. Sticking and collision probabilities are assumed unitary, and the consequences of this assumption are discussed later in Chapter 6. In this Chapter, a constant primary particle bulk density $\rho_p = 1.8$ g/cm^3 is considered, corresponding to soot particles with low organic content [296]. Three different monomer diameters are simulated, i.e. 1, 20 and 80 nm. Unless indicated, they all consist of monodisperse monomers ($\sigma_{geo,p} = 1$). For the case of polydisperse monomers, a lognormal distribution is considered ($\sigma_{geo,p} = 2$). Particles are suspended in air at a temperature of 1700 K and pressure of 101.3 kPa, corresponding to flame conditions [297]. Three different volume fractions are simulated: 1, 10, and 10^4 ppm. Under these conditions, the fluid mean free path has a constant value of $\lambda_f = 498$ nm, this value is only dependent on fluid temperature and pressure [56]. On the other hand, the average primary particle persistence distance goes from $\lambda_p = 183$ nm for monomers having $d_p = 20$ nm and $\sigma_{geo,p} = 2$ up to around $\lambda_p = 2000$ nm for monomers having $d_p = 2$ nm. The latter is dependent on the diffusion coefficient and momentum relaxation time of the particles [274].

Except for the highest volume fraction 10^4 ppm (selected for being important for many colloid/aerosol applications [178, 298–300]), these parameters were selected for representing soot particles generated under different combustion systems [6, 91, 96, 297, 301]. All the results are averaged over 10 different simulations and error bars reported in figures correspond to the 95% confidence intervals.
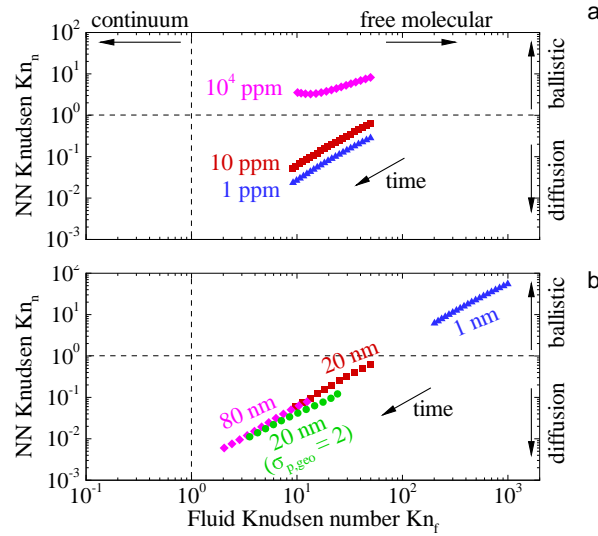
Figure 4.2: Different regimes of agglomeration and fluid flow for (a) different particle volume fraction and (b) different monomer diameters.

4.3 Results and discussion

4.3.1 Agglomeration and fluid flow regimes

Figure 4.2 illustrates the main advantages of MCAC, i.e. to consider both the time-evolving agglomeration regime (nearest-neighbor Knudsen number Kn_n) and time-evolving fluid flow regime (fluid Knudsen number Kn_f). This figure has the same axes as Fig. 4.1, but now illustrates the different cases simulated. It clearly shows the ability of MCAC to simulate the evolution in this bidimensional map, indicating that the transition from ballistic to diffusive and from free molecular to near continuum regimes are well taken into account. This simultaneous transition is not commonly considered in the literature.

Initially, particles consist of isolated primary particles (top right position for each case). The initial primary particle diameter and fluid thermodynamic properties determine the horizontal position of this starting point, whereas particle volume fraction and primary particle diameter determine the initial vertical position. As time progresses and agglomerates are growing, thus both Kn_n and Kn_f are decreasing.

By comparing Fig. 4.2(a) and (b), it is observed that an acceptable variation of the monomer diameters (for soot particles) seems to have a stronger influence on both regimes than a large variation of the volume fraction. Except for the largest particle volume fraction, i.e. 10^4 ppm, the trends are generally related in a power-law with a constant exponent. In the particular case of $f_v = 10^4$ ppm, the system never reaches the diffusive regime since the nearest-neighbor distance is in competition with the fast increase of agglomerate size. This is interpreted as a trend towards the gelling process [293], being outside the scope of this thesis.
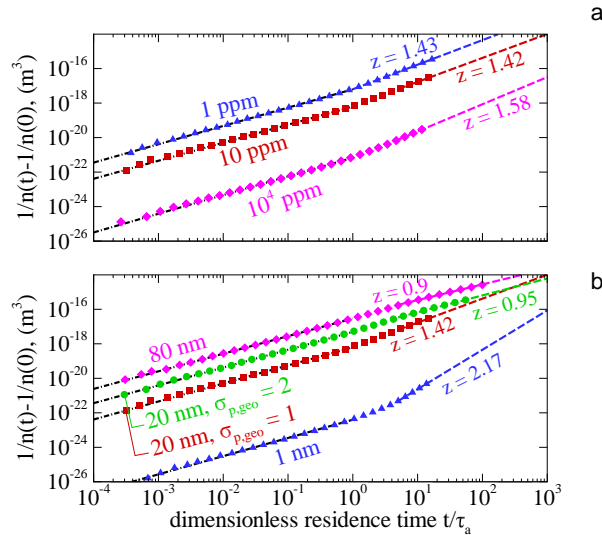
Figure 4.3: Inverse number concentration as a function of the normalized residence time. The τ_a stands for the characteristic time of agglomeration.

4.3.2 Kinetics of agglomeration

Figures 4.3(a) to 4.3(b) show the time evolution of the inverse particle number concentration $n(t)$, consisting of the number of particles divided by the volume of the containing box. Due to agglomeration, $1/n(t) - 1/n(0)$ is naturally increasing in time. At short times, when particles are small enough to be treated as spheres, the behavior is approximately linear as predicted by coalescing spheres theory [232] (represented by the black dash-dotted lines, i.e $1/n(t) - 1/n(0) = (t/\tau_a)^{\tilde{z}}$ with $\tilde{z} = 1$). This behavior is used to determine τ_a as the exponent of the intercept from the log-log plot of $1/n(t) - 1/n(0)$ as a function of time. The calculated values are reported in Table 4.1 and compared with the theoretical ones (τ_{cs}). The latter are determined as $\tau_{cs} = 2/(k_0 n_0)$, where $n_0 = n(0)$ is the initial particle number concentration and k_0 is the coagulation kernel of coalescing spheres taking into account the change in flow regime [302], calculated based on the monomer diameters. This parameter is now used to normalize the time on the horizontal axis, thus, enabling this axis to be standardized for the different curves presented. Indeed, the larger τ_a is, the longer the agglomeration process takes. This characteristic time is strongly affected by the variation of f_v and d_p. Nevertheless, both, τ_{cs} and τ_a are on the same order of magnitude except for the largest particle volume fraction (i.e. 10^4 ppm or 1%). Indeed, for this case, τ_{cs} is no longer accurate for predicting real coagulation efficiency [23, 178, 303]. The above-mentioned combination of $\tilde{z} \to 1$ and $\tau_a \approx \tau_{cs}$ ensures that there is a reliable simulation of the agglomeration kinetics by MCAC, at least for short times. For longer times corresponding to larger particles,

Table 4.1: Parameters for the analysis of agglomeration kinetics at short and long times.

Case	short times		long times		
	τ_a (µs)	τ_{cs} (µs)	$\tilde{z}$	$Kn_f{}^*$	$Kn_n{}^*$
f_v (ppm)					
1	1191	1262	1.43	9.2	0.02
10	107	126	1.42	8.9	0.05
10^4	0.06	0.13	1.58	9.7	3.5
d_p (nm)					
80	4550	4784	0.90	2.0	0.005
20 ($\sigma_{p,geo} = 2$)	505	–	0.95	3.5	0.01
20	107	126	1.42	8.9	0.05
1	0.03	0.07	2.17	201	6.1

*Taken at the end of the simulation, i.e. when $\overline{N_p} = 100$.

due to the agglomerate morphology, the behavior tends to a power law $1/n(t) - 1/n(0) = (t/\tau_a)^{\tilde{z}}$, where $\tilde{z}$ is the kinetic exponent that may be different from 1, and its value depends on the agglomeration and flow regimes [23, 235]. These values are shown in Fig. 4.3(a) and Fig. 4.3(b) and reported in Table 4.1. Kinetics of agglomeration is enhanced ($\tilde{z}$ increases) when increasing the volume fraction or decreasing the monomer diameters. The largest value is found for $d_p = 1$ nm, corresponding to ballistic agglomeration (the largest Kn_n in Fig. 4.3(b)). This is in very good agreement with Pierce et al. [235] who reported an asymptotic value of $\tilde{z} = 2.2$ in this regime compared to 2.17 found in the present study. When decreasing Kn_n in Fig. 4.3, it corresponds to a general decrease of $\tilde{z}$, which appears to be more sensitive to the change of agglomeration regime.

For the calculated kinetics exponents, the last two columns of Table 4.1 report a representative Kn_f and Kn_n. These results are in good agreement with the *ex-situ* analysis of soot coagulation (without surface growth and nucleation) reported in [304] for soot particles in the $0.5 < Kn_f < 10$ flow regimes where $\tilde{z} = 1.4 - 1.9$ was obtained when the agglomeration is in the near-free molecular regime to $\tilde{z} = 0.69, 0.72$ when agglomeration is in the near-continuum flow regime. Although it is not reported, according to the simulations of coagulation, where better agreement is found based on a transition coagulation kernel, it is concluded that agglomeration takes place in the BLCA-DLCA transition regime. The present results show $\tilde{z} = 1.42$ when $Kn_f \sim 8.9$ and $\tilde{z} = 0.9$ when $Kn_f \sim 2.0$. Additionally, the current results are in qualitatively good agreement with the sensitivity analysis of the population balance equation conducted in [78], where $\tilde{z} = 0.7$ was reported in the transition regime, $\tilde{z} = 1.0$ in the continuum and $\tilde{z} = 2.0$ in the free molecular flow regimes for agglomerates consisting of imposed $D_f = 1.0 - 3.0$. The kinetics of agglomeration is determined
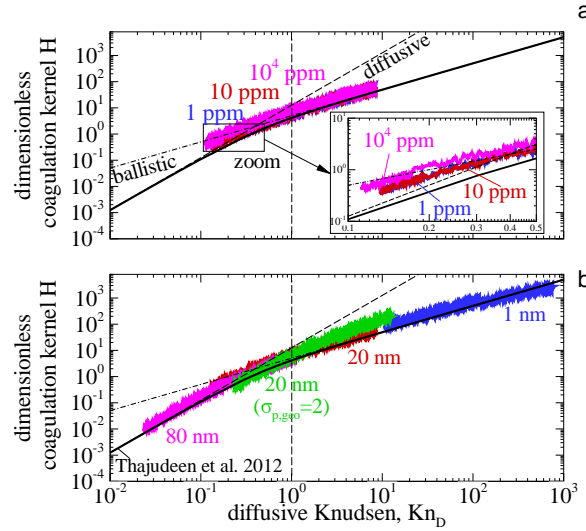
Figure 4.4: Dimensionless coagulation kernel H as a function of the diffusive Knudsen number Kn_D for (a) different particle volume fraction and (b) different monomer diameters.

by the number of collisions between agglomerates over time. This is quantified by the collision or coagulation kernels to be discussed in the following section.

4.3.3 Coagulation kernels

As explained in the introduction, an important input parameter for the Population Balance Equation for evaluating the evolution of the particle size distribution is the coagulation kernel ($k(i, j)$, i.e. the rate of collisions between particles consisting of i and j monomers). Fig. 4.4(a) to 4.4(b) show the dimensionless

coagulation kernel H for monodisperse particles as formulated by Thajudeen et al. [41],

$$H = \frac{k_{ii} m_i \pi^2 R_{s,ii}}{f_i PA_{ii}^2},$$
(4.3.1)

where k_{ii}, m_i, and f_i are the coagulation kernel, mass and friction coefficient respectively. The symbols in the figure correspond to the k_{ii} obtained from the present simulation based on the local slopes of Fig. 4.3(a-b) ($k_{ii} = 2dn^{-1}/dt$ as proposed by Heine et al. [178]). Mass and friction coefficients are evaluated from the MCAC simulations. Also, $R_{s,ii}$ and PA_{ii} are the Smoluchowski radius and projected area, respectively. Both are calculated based on the fractal dimensions reported later in this chapter (see Fig. 4.7) and the expressions proposed in [41]. All the above mentioned properties are evaluated based on population average values. In order to compare the current results (symbols) with the empirical relation proposed in [41] (continuous solid curves), the results are plotted as a function of the diffusive Knudsen number as introduced by the same authors and calculated as follows,

$$Kn_D = \frac{(2m_i k_B T)^{1/2} \pi R_{s,ii}}{f_i PA_{ii}},$$
(4.3.2)

where k_B is the Boltzmann constant. This Knudsen number has the same physical meaning as Kn_n used in the present study but it is limited to a diluted system. As can be seen in Fig. 4.4(a-b) for all the simulated cases, very good agreement is found between the present results and those by Thajudeen et al. [41] even if the considered range of primary particle diameters and volume fraction is within 4 orders of magnitude. Nevertheless, a departure is observed for the high volume fraction case (10^4 ppm, Fig. 4.4(a)) explained by the deviation from the diluted assumption made in [41]. This illustrates that MCAC is able to reproduce reliable kernels from ballistic to diffusive regimes since Thajudeen et al. [41] obtained their results based on Langevin Dynamics simulations. However, MCAC is able to explore larger volume fractions and also to take into account, the primary particle polydispersity with a reduced computational cost. Also, contrary to Thajudeen et al. [41], the agglomerate morphology is not imposed in MCAC simulations. It is interesting to note in Fig. 4.4(b), that monomer polydispersity tends to increase the dimensionless coagulation kernels, especially for larger Kn_D.

4.3.4 Self preserving size distributions

It has been suggested in the literature that agglomerates attain a Self-Preserving Size Distribution (SPSD) in both the free molecular and continuum flow regimes [67, 234]. In particular, concerning soot without nucleation and surface growth [304], or simply when coagulation is dominant, SPSD has been experimentally observed [305]. This means that, after a given time, the dimensionless representation of the density of particles having a certain number of primary particles, converges toward an asymptotic form [306]. In certain cases, especially for fractal agglomerates, the coagulation kernel $k(i, j)$ is a homogeneous function, i.e. $k(\alpha i, \alpha j) = \alpha^\lambda k(i, j)$ where λ is the agglomeration kernel homogeneity parameter. Thus, λ can be used to

monitor the SPSD. Therefore, it is very interesting to study how this parameter is sensitive to a change in agglomeration or flow regimes. Usually, λ is determined by fitting the SPSD [66, 235] or, as proposed by Dongen and Ernst [307], relying on the scaling hypothesis ($\lambda = 1 - 1/\tilde{z}$) based on the above mentioned kinetic exponent $\tilde{z}$. However, these approaches may not be accurate and robust. For these reasons, an original and more robust method for determining λ and thus the agglomerate size distribution is proposed here. Indeed, the SPSD is found to follow a generalized Gamma distribution function (the demonstration is given in Section S3.1 in the SM A),

$$f(x) = \frac{\left(p/a^d\right)}{\bar{x}\Gamma(d/p)} X^{d-1} \exp\left[-\left(\frac{X}{a}\right)^p\right], \tag{4.3.3}$$

where $f(x)$ is the probability density function of the particle size. Here, x corresponds to one of the four size parameters considered in the present study as indicated in Table 4.2. In this equation, $\Gamma(y) = \int_0^\infty t^{y-1} e^{-t} dt$ is the Gamma function, p is a dimension parameter, $a = (1 - \lambda)^{-1/p}$, $d = p(1 - \lambda)$, and $X = x/\widetilde{x}$ is a dimensionless size where $\widetilde{x} = (\overline{x^p})^{1/p}$. In addition to this generalized analytical expression for the SPSD, an

Table 4.2: Parameters for the generalized SPSD given by Eq. (4.3.3).

Size descriptor	x	p
number monomers	N_p	1
volume eq. diameter	d_v	3
gyration diameter*	d_g	D_f
mobility diameter**	d_m	D_{fm}

*Gyration diameter based or mass fractal dimension D_f.
**Mobility diameter based fractal dimension D_{fm} (scaling exponent).

analytical expression of the q-moment of the generalized SPSD is provided in Section S3.2 of the SM A. In Eq. (4.3.4), in particular, the q-moment based on the volume equivalent diameter $d_v = (6v/\pi)^{1/3}$ distribution is shown,

$$\overline{d_v^q} = \widetilde{d_v}^q \frac{\Gamma(1 - \lambda + q/3)}{(1 - \lambda)^{q/3}\Gamma(1 - \lambda)}, \tag{4.3.4}$$

In the present work, the evaluation of the homogeneity coefficient λ based on a new and robust method is proposed. It consists in solving Eq. (4.3.4) based on the volume equivalent diameters distribution by letting the homogeneity coefficient as the unknown searched variable. This operation is performed for the first ($q = 1$) and second ($q = 2$) moments of the distribution, thus providing two corresponding homogeneity coefficients denoted as λ_{M1} and λ_{M2}, respectively and reported in Fig. 4.5 with filled and empty symbols, respectively.

Let's begin the analysis by focusing on the monodisperse case. At short times (corresponding to small $\overline{N_p}$), both, λ_{M1} and λ_{M2} are different, indicating the initial size distributions (Dirac) are not self-preserving. That difference is not clear in Fig. 4.5 due to the amplitude of the overall variations of these parameters. Nevertheless, a study of the difference between λ_{M1} and λ_{M2} (see Section S3.3 of the SM A) enables determining the time (or equivalently the mean N_p) needed to reach a convergence, i.e. the time

needed to tend toward a self-preserving state. This time-lag for SPSD is found to be on average $\sim 5\tau_a$ (not shown here) and appears to be equivalent to $\overline{N_p} \approx 20$ as represented by the gray zone in this figure. Consequently, before this convergence, the corresponding value of the homogeneity coefficient ($-\infty$ in the present case) is difficult to interpret in physical terms even considering the initial value is clearly determined by the monodisperse agglomerate size distribution. However, for longer times (or larger $\overline{N_p}$), both parameters generally converge well toward a common value evolving in time suggesting that the particle size distributions are quasi self-preserving throughout the agglomeration process. The range of observed values of λ for larger agglomerates is between -0.5 and 0.5, in the acceptable physical range discussed by Pierce et al. [235], and in good agreement with experimentally measured ones. Indeed, Wang and Sorensen [278] reported λ between -0.28 and -0.46 in the range of $Kn_f \approx 1.8 - 2.2$ for silica and titania nanoparticles. From the results of Maricq [304], λ between -0.39 and -0.45 are deduced (based on the scaling approach) for soot particles in the same range of fluid Knudsen numbers.

The largest values of λ are observed for $d_p = 1$ nm and $f_v = 10^4$ ppm, where the agglomeration is ballistically limited (see Fig. 4.2). In this regime, the increase in particle sizes means an increase in the coagulation kernels since the projected particle area increases faster than the drag force [23] therefore, positive λ are expected. In the case of $d_p = 80$ nm, corresponding to agglomeration in the DLCA-near diffusive flow regime ($Kn_f \sim 2.0$), negative values of λ are observed, meaning that larger agglomerates have smaller coagulation kernels as a consequence of the increase in the drag force due to the larger number of monomers per agglomerate [56].

To evaluate the impact of the flow regime, the case of $d_p = 80$ nm and $f_v = 10$ ppm, for which $\lambda = -0.5$ (pink symbols), is again simulated by forcing the drag force to stay in the "classical" DLCA-Epstein regime throughout the agglomeration process to serve as a reference case (black symbols, labeled DLCA in the figure). Note that the reference DLCA case is much more stable in terms of λ compared to the initial simulations for which flow regime variation is taken into account. Also, an asymptotic and different value is quickly attained. This highlights the importance of considering the natural evolution of the flow regime. This is confirmed by the observed important role played by d_p as shown in Fig. 4.5(b), which is a key parameter for evaluating the friction coefficient and its dependence on the fluid regime. In comparison, f_v seems to have a less relative impact.

Let's now focus on the case of polydisperse monomers represented by green circles symbols in Fig. 4.5(b). For short times (corresponding to small $\overline{N_p}$), both, λ_{M1} and λ_{M2} do not differ considerably. This is explained by the fact that SPSD is not very different from a lognormal distribution [308, 309]. Also, a very different behaviour for λ_{M1} and λ_{M2} can be noted in this case compared to monodisperse monomers. This is a promising result suggesting that an experimental tracking of the evolution of the homogeneity coefficient at early stages of the agglomeration process, could be used to assess the primary particle polydispersity.

As can be noted, the convergence between λ_{M1} and λ_{M2} is reached for a larger agglomerate size ($\overline{N_p} \sim 70$) when primary particle polydispersity is relevant. But when comparing the polydisperse and monodisperse cases (with the same monomers geometric mean), a convergence toward the same asymptotic value is observed, suggesting that primary particle polydispersity does not influence the agglomeration process at long times. This is consistent with the results of Friedlander [232] and Goudeli et al. [310].
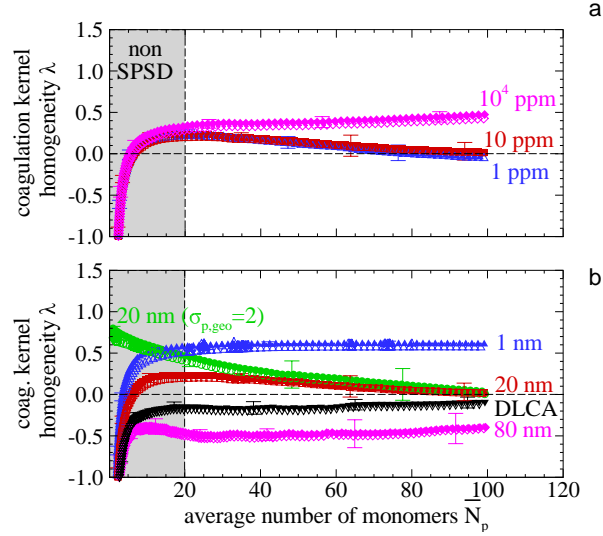
Figure 4.5: Coagulation kernel homogeneity coefficients for (a) different particle volume fraction and (b) different monomer diameters. Calculated from the first (λ_{M1}, filled symbols) and second (λ_{M2}, non-filled symbols) moments of the volume equivalent diameter distributions.

Since homogeneity coefficients are found to be more influenced by the monomer diameters than particle volume fraction, Fig. 4.6(a)-4.6(c) report the corresponding asymptotic SPSD obtained as a function of the dimensionless volume equivalent diameter, gyration and mobility diameters, respectively. To avoid overloading the figure, direct evaluation of the size distribution is reported in symbols only for the reference case (i.e. $d_p = 20$ nm), whereas continuous curves correspond to the theoretical self-preserving functions (Eq. 4.3.3) evaluated with the final λ_{M1} found in Fig. 4.5, i.e. when $\overline{N_p} = 100$. First of all, a good agreement with the theoretical expression for the reference case is observed. This confirms that the size distribution corresponds well to a SPSD. Secondly, the smaller the primary particle diameter, the wider the distribution becomes. This is also found with larger f_v (not presented here) indicating that ballistic and free molecular flow regimes are characterized by wider agglomerate size distributions. This result is in agreement with coalescing spheres for all regimes [234] and with agglomerates in the asymptotic regimes [67]. It is worth highlighting the ability of MCAC to simulate the quasi-SPSD in the transition regime in terms of the different agglomerate size parameters (volume equivalent, gyration, and mobility radius). However, the size distribution expressed in terms of mobility diameter, does not converge exactly towards a lognormal size distribution (dashed red line in Fig. 4.6(c)) as experimental measurements usually report. This discrepancy may be related to some physical phenomena, relevant for soot formation in flames, yet not considered in these simulations (for

example, interaction potentials, surface growth or thermophoretic forces). It should also be noted that the simulated agglomerates are simplified in terms of morphology (one point contact spheres) compared to real soot particles as experimentally seen in TEM images [6, 44].
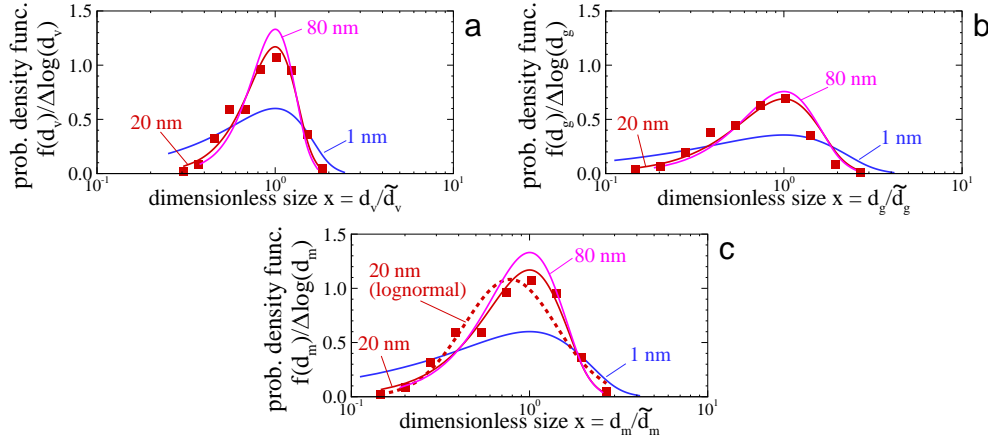
Figure 4.6: Asymptotic particle size distribution expressed in terms of (a) the volume equivalent diameter, (b) the diameter of gyration and (c) the mobility diameter.

The comparison of the particle size distribution, as expressed in terms of d_v, d_m or d_g show different degrees of apparent polydispersity. Indeed, for current simulations of $f_v = 10$ ppm and $d_p = 1 - 20$ nm, the following geometric standard deviations are obtained $\sigma_{geo,dv} = 1.50 - 1.85$, $\sigma_{geo,dm} = 1.58 - 1.98$ and $\sigma_{geo,dg} = 1.95 - 2.60$ (these results are reported in Section S3.3 in the SM A). It is interesting to observe the good agreement with the ranges of polydispersities observed experimentally. In fact, for soot particles in ethylene diffusion flames, it has been reported that $\sigma_{geo,dm} = 1.31 - 1.33$ as measured by Differential Mobility Spectrometer [311] and $\sigma_{geo,dg} = 2.1$ and $\approx 2.1 - 2.9$ based on TEM images analysis reported in [311] and [6], respectively.

4.3.5 Agglomerate morphology

The morphology of agglomerates is described by the population based fractal dimension D_f and prefactor k_f obtained based on the fractal law,

$$\frac{v_a}{\overline{v_p}} = k_f \left(\frac{d_g}{\overline{d_p}} \right)^{D_f} \tag{4.3.5}$$

where $v_a/\overline{v_p}$ is the ratio between the agglomerate volume and the average monomers volume (corresponding to the number of primary particles N_p), d_g is the diameter of gyration and $\overline{d_p}$ is defined here as the numerical average monomer diameter. It should be noted that there is no strict rule for using the fractal law when dealing with polydisperse primary particles [140, 312]. Defining the representative primary particle radius differently affects the thus determined fractal prefactor but not the fractal dimension. Also, the fractal law has been considered to be valid only for sufficiently large agglomerates, typically $N_p > 20$, however this number

may be even in the order of 100 monomers [53]. When plotting N_p in a log-log plot as a function of $d_g/\overline{d_p}$, a linear fit provides D_f and k_f. This procedure is repeated in the present study at each time iteration during the agglomeration process. The resulting fractal dimensions D_f are reported in Fig. 4.7(a-b) as a function of the mean number of primary particles per agglomerate. An exactly time-invariant fractal dimension is not achieved. However, its variation is very small for $\overline{N_p} > 20$ and depending on the application it may be neglected. This indicates a non-fractal domain for $\overline{N_p} < 20$, highlighted in gray in the figure. It should be noted that this limit is qualitative and values between 15 to 30 can be found in the literature [313, 314]. In Fig. 4.7(a), an increase in the asymptotic fractal dimension as a function of particle volume fraction is observed, thus being in agreement with previous studies [257, 270, 287, 298]. This is because agglomeration becomes more ballistic when increasing f_v. Nevertheless, for soot agglomeration processes, such high volume fractions may not be common. Furthermore, the observed variation of D_f is not large (between 1.80 and 1.88). Thus, it is unlikely that this parameter alone can explain the variability of the fractal dimensions found in the literature [6]. Fig. 4.7(b) shows the more influencing effect of the primary particle diameter (D_f between 1.62 to 1.86). First, it is very remarkable that this value decreases when increasing the monomer diameters. The present results seems to indicate that the primary particle diameter, that plays an important role in the evaluation of the drag force (see Eq. (2) in the preceding work [274]) and therefore, due to the change in flow regime, has a significant impact on soot morphology. Thus, a small fractal dimension (down to 1.62) can result in the agglomeration of large monodisperse primary particles or at least containing a few large primary particles as seen in Fig. 4.7(b) for the polydisperse case $\sigma_{p,geo} = 2$ reported in green. As indicated in Chapter 2, some authors [310, 315] also reported consistent dependencies of particle morphology on primary particle polydispersity, however the simultaneous change in agglomeration and flow regimes was not taken into account.

As discussed before, the change in flow regime is evaluated by comparing the results with the reference DLCA-Epstein case (black inverted triangle symbols in Fig. 4.7(b)). In this case, an asymptotic fractal dimension of 1.77 is found. Therefore, taking into account the change in the flow regime, may have a strong impact in the agglomerate morphology.

The evolution of k_f as a function of $\overline{N_p}$ can be interpreted as a morphological signature different from the fractal dimension [316], and which is linked to the packing factor (see Chapter 2). Nevertheless, as for the fractal dimension, the fractal prefactor is more influenced by the primary particle diameter and polydispersity than by the particle volume fraction (see the Section S3.3 in the SM A). An interesting variation is observed when analyzing the fractal prefactor as a function of the corresponding fractal dimension. This is shown in Fig. 4.7(c-d) for $\overline{N_p} > 20$. The results are compared with the literature [35, 313]. The overall trend is that both parameters are inversely related, which is in accordance with the cited references. It is interesting to note that for both $d_p = 80$ nm ($\sigma_{p,geo} = 1$) and $d_p = 20$ nm ($\sigma_{p,geo} = 2$), the relative variation observed during the agglomeration process shows a very different D_f compared with other cases simulated having different primary particle diameter and volume fraction.
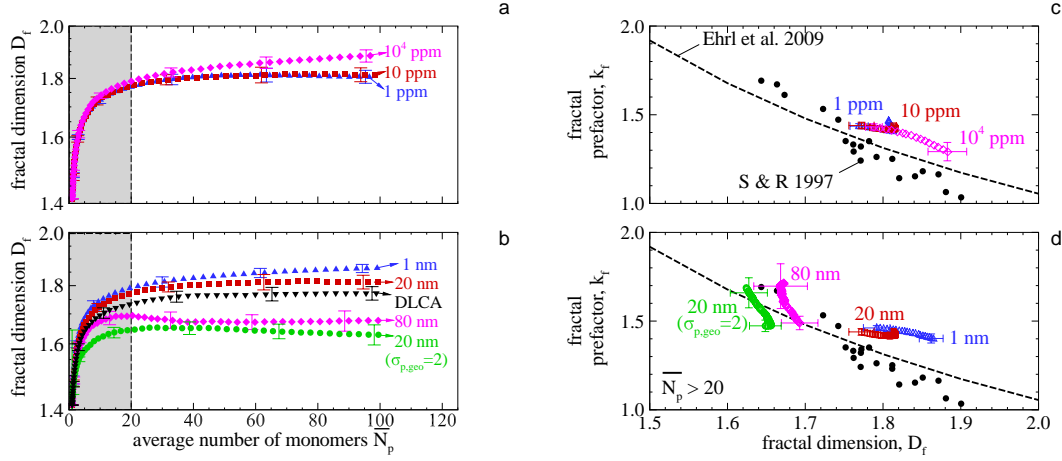
Figure 4.7: (a-b) Population based fractal dimension D_f as a function of the average number of monomers per agglomerate $\overline{N_p}$. (c-d) Fractal prefactor dependence on the fractal dimension for $\overline{N_p} > 20$ compared with Ehrl et al. [313] and Sorensen & Roberts [35].

Finally, when analyzing the fractal dimension in Fig. 4.7(b) at large $\overline{N_p}$, a significant sensitivity to the primary particle diameter is observed. Thus, the analysis is extended up to $d_p = 160$ nm to explore this dependency. The results are presented in Fig. 4.8 where, the fractal dimensions of agglomerates simulated by MCAC, are compared with the experimental measurements reported by [317] and the classical DLCA and BLCA limits under fixed flow regimes [286]. Here, the role played by primary particle size on agglomerate morphology becomes evident as smaller fractal dimensions are found for larger d_p, being in good agreement with the referenced experimental data [317]. It is very remarkable that fractal dimensions below the classical DLCA limit are observed when taking into account the simultaneous change of agglomeration and flow regimes.
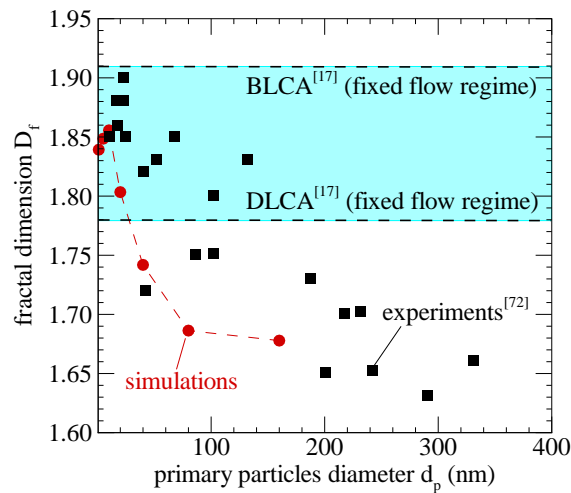
Figure 4.8: The variation of the fractal dimension as a function of the primary particle diameter compared with the BLCA ($D_f = 1.91$) and DLCA ($D_f = 1.78$) limits under fixed flow regimes [286] and experimental measurements [317].

4.3.6 Projected area scaling-laws

Projected area scaling-laws are widely used to analyze experimental TEM images (see Section 2.1.8.1) to infer 3d morphological properties of agglomerates from 2d projections [45, 77]. They are also used in numerical simulations to determine the molecule-particle collision frequencies that depends on their projected area [41, 78]. Table 4.3 reports the scaling exponent and prefactor obtained by a log-log fit of equation (2.1.13) as shown in Fig. 4.9. This figure, reports the fits for the cases having primary particle diameter $d_p = 10$ nm and $d_p = 80$ nm as examples. Both α and k_α are overall close to the DLCA agglomerates $k_\alpha = 1.10$ and
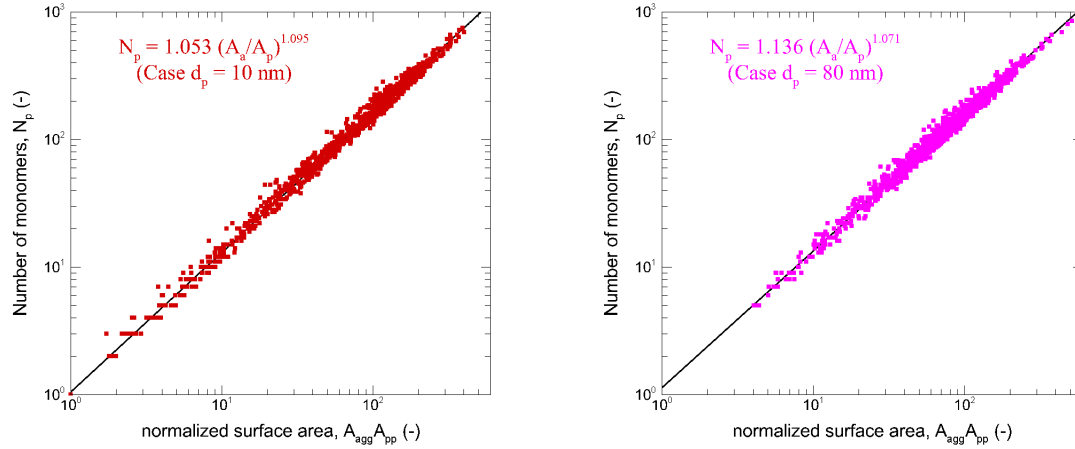
Figure 4.9: Number of primary particles vs projected area scaling fits.

$\alpha = 1.08$ values obtained by [30]. These parameters do not exhibit a systematic dependence on particle volume fraction. However, a more relevant variation is observed for different primary particle sizes and specially for $d_p > 10$ nm where the scaling exponent is overall decreasing while the prefactor is increasing when compared to $d_p \leq 10$ nm. Nevertheless, the variation in α is still less than 3% and less than 13% for k_α. Consequently, the scaling exponent and prefactor are robust with regard to changes in both agglomeration and flow regimes.

4.4 Conclusions

Numerical simulations of soot agglomeration are carried out based on the Monte Carlo Aggregation Code, MCAC proposed in this thesis, taking into account the variation through time of the nearest-neighbor and fluid Knudsen numbers, enables a continuous transition to occur from ballistic to diffusive agglomeration and, simultaneously, a continuous transition from free molecular to near-continuum flow regimes. Remarkably, considering that the change in both regimes is seldom found in the literature, excepting the notable work of Thajudeen et al. [289], focused on the determination of the agglomerates projected area and hydrodynamic

Table 4.3: Projected area scaling parameters.

Case	exponent α	prefactor k_α
f_v (ppm)		
0.1	1.0736	1.1532
1	1.0903	1.0748
100	1.0786	1.1286
10^4	1.0962	1.0464
d_p (nm)		
1	1.0964	1.0484
5	1.0994	1.0447
10	1.0955	1.0534
40	1.0646	1.1731
80	1.0716	1.1369
160	1.0586	1.1913
Brasil et al. [30]	1.0800	1.1000

radius, under diluted conditions (low particle volume fraction). This work is extended here to study the agglomeration kinetic, size distribution and morphology. The present work explores the role played by the particle volume fraction, the primary particle size and polydispersity.

Except in the case of $f_v = 10^4$ ppm, the dimensionless coagulation kernel is found to be in good agreement with Thajudeen et al. [41]. The latter also found good agreement with subsequent works [299, 318, 319], therefore it is recommended for conducting population balance simulations of nanoparticle coagulation under diluted systems [143, 287, 320]. This is especially important for nanoparticle coagulation in the transition regime where collision kernels are treated separately and a limit to the fractal dimension is usually considered for BLCA [78, 304].

The current investigation also enables some very interesting and original results to be highlighted. In particular, the role played by the primary particle size and polydispersity. Indeed, it is observed that increasing the primary particle diameter:

- Slows down the agglomeration kinetics. Increases the agglomerate size geometric standard deviation while keeping the quasi self-preserving size distribution.

- Induces an substantial decrease in the mass fractal dimension down to $D_f = 1.67$ for large monomers ($d_p = 80$ nm) at flame conditions. This is much lower than the typical 1.78 usually considered for agglomerates generated by pure DLCA. This was empirically observed by Wu et al. [287, 317] who highlighted the lack of explanation for this trend.

An inverse correlation between the fractal dimension and prefactor is observed during the agglomeration process. This has only been studied previously in an asymptotic fashion before [35, 313]. This finding is of great importance for improving the physical representation of agglomerates generated with tunable algorithms [140, 166]. The homogeneity coefficient is found to be (highly) dependent on the primary particle

polydispersity only at the beginning of the agglomeration process.

All these results highlight how the change of regimes experienced by the particles has a significant impact on the dynamics of agglomeration, particle size distribution and morphology. In addition, the present work proposes:

- A generalized expression for the Self Preserving Size Distribution taking the form of a generalized Gamma distribution irrespective of the considered agglomerate size parameter. This opens the way to an experimental determination of the homogeneity coefficient by measuring the distribution of gyration diameters by light-scattering [97, 278, 300, 311, 321], by TEM images analysis [6] or electrical mobility particle classification [56, 304]. It also enables the different ranges of agglomerate size polydispersity to be understood when determined as a function of the selected size parameter (the standard deviation is found to be larger for gyration diameters than for mobility or equivalent volume ones).

- A new and robust method for numerically determining the coagulation homogeneity coefficient λ, is introduced, being therefore, an alternative to the classical scaling approach [293, 294, 307]. It is based on the first and second moments of the introduced generalized self-preserving particle size distribution [66, 235, 236].

5 | Surface reactions and nucleation[3]

Soot particle surface growth may have a significant impact on aggregation kinetics, particle morphology, and both aggregate and monomer size distributions. Particularly, the morphological effects of surface growth are currently poorly understood. This is complex since surface growth also affects the kinetics of aggregation resulting in a time-dependent competition between both phenomena, producing very different morphological markers. This Chapter aims at improving our understanding of the morphological impact of surface growth by implementing this process in MCAC for the simulation of soot formation in an ethylene premixed flame. An asymptotic average primary particle overlapping $\sim$ 30% is observed for different flame conditions. The primary particle coordination number is highly sensitive to surface growth rate and particle volume fraction, and maximum values are on average within the 4 - 8 range. The particle local compacity, as quantified by the packing factor, is also considerably increased when aggregates experience surface growth, contrarily to the fractal structure of individual aggregates that seems more dependent on the aggregation regime rather than surface growth. Finally, surface growth narrows both the primary particle and aggregate size distributions.

5.1 Introduction

Up to now, as done in previous chapters, most of the numerical studies have considered the role played by pure aggregation, explaining the fractal-like nature of soot particles [23, 183, 185, 257, 322]. However, limiting the study to the agglomeration alone (without considering additional mechanisms of soot formation) results in point-touching primary particles which are commonly not representative of experimentally measured particles. Notably, for particles formed in flames (such as soot), surface reactions and particularly surface growth cannot be neglected. This is because they occur simultaneously with aggregation process producing overlapped primary particles [30, 31], as commonly observed in TEM images of aged soot particles in diffusion and premixed flames [6, 77, 323, 324]. This overlap is suspected to affect the particle surface area to volume ratio

---

[3]Part of this Chapter has been published in: Morán, J., Poux, A., & Yon, J. (2021). Impact of the competition between aggregation and surface growth on the morphology of soot particles formed in an ethylene laminar premixed flame. Journal of Aerosol Science, 152, 105690.

(specific surface area) which has been suggested as one of the most important dose metrics for nanoparticle toxicity by inflammatory response and oxidative stress of pulmonary cells [7–12]. Surface growth may provide nearly all the mass of the ultimately formed soot particles in flames [238, 325], in consequence, many authors attribute the primary particle overlapping to surface growth [110, 326, 327]. Nevertheless, some authors attribute monomer overlapping to partial sintering [73, 328], or both partial sintering and surface growth [329].

In addition to the impact of inter-penetrated primary particles on the specific surface area, it should be noted that primary particle overlapping plays an important role in soot particles radiative properties [47, 164, 330]. Thus, it can also affect climate models and particle sizing by optical techniques such as time-resolved laser-induced incandescence. Indeed, the latter technique requires an accurate determination of both aggregate's volume and surface area [91, 118, 331] but also the amount of overlapping between monomers which influences the heat transfer (notably, conduction) rates with the surrounding gas [332].

Surface growth is a complex chemical process involving the heterogeneous reaction between molecules and particles with time-evolving composition and consequently reactivity [218, 240, 333]. In this context, primary particle overlapping produced by surface growth has been shown by a few remarkable works [110, 112, 326, 327, 329]. However, it has not been quantified and systematically studied. Here, we support the idea that a temporal competition between aggregation and surface growth mechanisms can affect the resulting particle morphology, and thus the degree of primary particle overlapping. This can be easily illustrated by considering two asymptotic cases. Let us firstly consider surface growth acting on isolated monomers is achieved before any aggregation takes place. This will naturally produce agglomerates made of point-touching large spheres (without overlapping), corresponding to the agglomerates formed under no surface growth [23, 183, 185, 257, 322]. Let us secondly consider that highly mobile initially isolated monomers collide and aggregate very quickly before any surface growth takes place. For sufficiently long subsequent residence time under surface growth, this will certainly produce nearly spherical very compact aggregates [326, 334, 335]. In this context, the balance between aggregation and surface growth is suspected to play an important role in particle morphology. This balance is not trivial since both mechanisms are inter-dependent. Indeed, since surface growth increases the mass of individual clusters, it may also influence the kinetics of aggregation. The present work aims at studying this competition between aggregation and surface growth and its impact on particle morphology. To focus on these two mechanisms, we consider experimental data available for soot surface growth from a premixed laminar flame without considering the nucleation and particle fragmentation induced by oxidation.

However, primary particle overlapping is not the only consequence of the simultaneous aggregation and surface growth. A special attention is paid to the particle coordination number n_c (i.e. the number of intersections of monomers with neighbors [72, 336]). Unfortunately, this parameter is commonly overlooked in the literature. And yet, along with the overlapping coefficient, it plays an important role in the funda-

mental physicochemical properties of aggregates such as the heat/electrical conduction, catalytic/chemical performance, radiative properties, and mechanical resistance [194, 270, 337–339]. The combination of the time-evolving overlapping and coordination number of primary particles makes the determination of aggregate volume and surface area quite challenging. Some numerical methods exist, such as the highly accurate libraries ARVO [340] and SBL [341] as used in [79, 210], approximate ones by calculating the spherical caps [30, 45, 323] as done in [45, 187], by using Monte Carlo methods [334, 335], and based on aggregate discretization [31, 111, 342]. The aforementioned methods are commonly computationally expensive, especially the aggregate discretization and the accurate libraries ARVO or SBL. One exception is the approximate methods based on the spherical caps, however as further discussed later, they quickly fail when increasing primary particles overlapping and coordination number since multi-sphere intersections is neglected. In this context, we propose a new accurate semi-analytical and quite computationally affordable method to calculate both the aggregate's volume and surface area.

An additional fundamental question that arises when considering the complex morphological evolution of soot particles under surface growth is about the change in its fractal-like structure. Some authors have suggested that only the fractal prefactor should increase due to primary particle overlapping [30, 31, 73] at least for overlapping coefficients no larger than 30%. However, strong surface growth rates may lead to sphere-like particles that can hardly retain the same fractal structure [326, 334, 335]. Most of the cited works are based on the population fractal structure derived from the fractal-law. However, remarkably different results are obtained when analyzing the morphology of individual aggregates as experimentally done by the box-counting method in Refs. [15, 324], and recently numerically by analyzing the volume-based pair correlation function [53]. The latter enables accurate characterization of the aggregate morphology by determining the individual fractal dimension and packing factor [51]. These parameters represent the global structure and the local compacity of aggregates, respectively. For this reason, this method is adopted in the present work to investigate the effect of surface growth on soot aggregates morphology.

5.2 Methodology

5.2.1 Surface growth model

As schematically shown in Fig. 5.1 and without loss of generality, an individual monomer belonging to an aggregate is increasing in radius from $r_p(t)$ to $r_p(t + \Delta t)$ due to a local adsorption governed by a specific surface mass flux density φ in (kg/m^2/s) units during a time step Δt. In this context, the increase in the monomer mass and volume can be calculated as,

$$\Delta m_p = \Delta v_p \rho_p = \int_{s_p} \varphi ds_p \Delta t \tag{5.2.1}$$
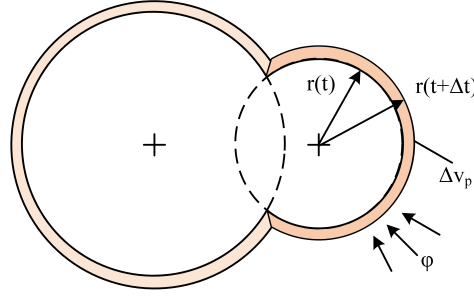
Figure 5.1: Surface growth modeling as exemplified by an aggregates of 2 primary spheres.

where Δm_p and Δv_p represent respectively the increase in mass and volume and s_p is the surface area of the monomer exposed to the molecular flux φ. The ratio $\varphi/\rho_p = u$ is homogeneous to a velocity and can be interpreted as the surface growth rate. In addition, for small Δt and φ uniform along the primary sphere exposed surface area, Δv_p can be approximated as $\Delta v_p = s_p \Delta r$. Finally, combining this expression with Eq. (5.2.1) the following expression is obtained,

$$r_p(t + \Delta t) = r_p(t) + u\Delta t \tag{5.2.2}$$

Thus, under the assumption of uniform mass flux, it appears that the absolute increase in primary particle radius is uniform for all monomers belonging to an aggregate. Note that a similar approach has been carried out by [334]. In this approach, the surface growth rate is a function of time because soot particles reactivity reduces when ageing through the flame [237, 240, 333, 343, 344].

5.2.2   Numerical simulation of the coupled aggregation and surface growth

The MCAC code introduced in Chapter 3 is adapted to particles surface growth. In order to accurately simulate the particle dynamics and collisions with other clusters, the mass and friction coefficient has to be calculated by MCAC. In the context of the present study, these two quantities have to be evaluated by considering the structure of aggregates under surface growth. Thus, the friction coefficient is calculated based on Eq. (3.2.3) where the aggregate's friction coefficient f is proportional to the individual monomer friction one f_p according to the following power-law: $f = f_p \left(N_{p,\text{eff}}\right)^{\Gamma_p/D_f}$, where Γ_p is given by Eq. (3.2.4). Additionally, $N_{p,\text{eff}}$ is the effective number of primary particles per aggregate defined as $N_{p,\text{eff}} = V_a/v_p$ where V_a and v_p are the aggregate and averaged primary particle volumes, respectively. Without overlapping between monomers we have: $N_{p,\text{eff}} = N_p$, with N_p the number of constituent primary particles in the aggregate. However, in the case of aggregates consisting of overlapped monomers, $N_{p,\text{eff}}$ is smaller than N_p. For example, if two primary particles are perfectly overlapped we have $N_p = 2$ but $N_{p,\text{eff}} = 1$.

Thus, in order to evaluate $N_{p,\text{eff}}$, the actual aggregate's volume must be determined. Without over-

lapping, we simply find $V_a = N_{\mathrm{p}} \times v_p$, which was used in Chapter 4. However, when primary particles are overlapped, we have to consider a correction factor $\alpha_v \in]0, 1]$ such that the total volume of the aggregate is $V_a = \alpha_v \times N_{\mathrm{p}} \times v_p$. Consequently the effective number of monomers is calculated as $N_{\mathrm{p,eff}} = \alpha_v N_{\mathrm{p}}$. For the aforementioned example of a totally overlapped dimer, $\alpha_v = N_{\mathrm{p,eff}}/N_{\mathrm{p}} = 1/2$. The same correction is naturally used for the evaluation of the particle mass $m = \rho_p \times \alpha_v \times N_{\mathrm{p}} \times v_p$. This correction is thoroughly explained in the following section.

5.2.3 Volume and surface area approximation

In this section we introduce two corrective factors $\alpha_v \in]0, 1]$ and $\alpha_s \in]0, 1]$ used to calculate the volume and surface area of aggregates experiencing surface growth and therefore a certain overlap between the constituting primary particles. These factors are defined as a correction to bring to the volume and surface area evaluated without considering any overlapping, i.e. $V_a = \left(\sum_{i=1}^{N_p} \frac{4\pi}{3} r_{p,i}^3 \right) \times \alpha_v$ and $S_a = \left(\sum_{i=1}^{N_p} 4\pi r_{p,i}^2 \right) \times \alpha_s$. When particles do not experience surface growth then $\alpha_v = \alpha_s = 1$ and therefore the volume and surface area of aggregates correspond to the sum of the total spherical primary particle ones, respectively. When more than 2 primary particles are overlapped there is no analytical solution for α_v and α_s and only approximate expressions can be obtained only when neglecting multi-sphere intersection [30, 45, 323, 345]. Indeed, neglecting this term is commonly done in the literature [30, 45, 187] however it can lead to a large underestimation of the real particle's volume and surface area. This simplification can also produce negative values in certain cases of high overlapping and multi-sphere intersection. Here a method to estimate the volume and surface area of fractal-like aggregates composed of N_p primary particles is introduced by proposing an analytical correction for the multi-sphere intersection. The derivation of the proposed volume and surface area factors is provided in S5.1 of the SM A, and the final expressions are given as follows,

$$\alpha_v = 1 - \frac{1}{4}\overline{n_c}\left(3c_{20}^2 - c_{30}^3\right) + \beta_v \tag{5.2.3a}$$

$$\alpha_s = 1 - \frac{1}{2}\overline{n_c}c_{10} + \beta_s \tag{5.2.3b}$$

where $\overline{n_c}$ is the average coordination number over the primary particles of a given aggregate [346], c_{q0} is the q-moment average overlapping coefficient. These parameters are calculated based on all the intersections between monomers belonging to an aggregate. Additionally, β_v and β_s are the proposed correction factors for multi-sphere intersection,

$$\beta_v = a_v c_{30}^3(\overline{n_c} - \overline{n_{c,\min}}) + b_v(\overline{n_c} - \overline{n_{c,\min}})^{1.5} \tag{5.2.4a}$$

$$\beta_s = a_s c_{10}^2(\overline{n_c} - \overline{n_{c,\min}}) + b_s(\overline{n_c} - \overline{n_{c,\min}})^2 \tag{5.2.4b}$$

where,

$$\overline{n_{c,\min}} = 2(N_p - 1)/N_p \tag{5.2.5}$$

is the minimum average coordination number. It ensures $\beta_v = \beta_s = 0$ when no multi-sphere intersection exists, i.e. when $\overline{n_c} = \overline{n_{c,\min}}$. For example, for a dimer $\overline{n_c} = \overline{n_{c,\min}} = 1$ can be easily verified. This is true for any agglomerate consisting of point-touching primary particles. In the limit $N_p \longrightarrow \infty$ this expression leads to $\overline{n_{c,\min}} \longrightarrow 2$, this is quite robust regarding particles morphology considering that both DLCA and RLCA agglomerates show $\overline{n_{c,\min}} \longrightarrow 2$ for very large agglomerates [52]. This parameter is also unaffected by the primary particle polydispersity for DLCA agglomerates [53]. The same conclusion has been obtained for monomer-cluster aggregation mechanisms where much compact structures are formed [72], and also for cluster-cluster tunable aggregates [347]. In these expressions a_v, b_v, a_s, and b_s are constant values obtained by post-processing fits (see Section S5.2 of the SM A). Considering primary particles as monodisperse is a good conceptual starting point however, soot primary particles are never monodisperse [6, 91] and therefore an equivalent expression is provided in this Appendix for polydisperse monomers.

5.3 Numerical simulations

MCAC introduced and validated in the previous chapters is adapted here to simulate soot particles aggregation and surface growth by considering the correction factor α_v in the evaluation of the particle mass and friction coefficient as discussed in the previous sections. The simulations are conducted by fixing $T = 1700$ K and $P = 1$ atm, corresponding to the ethylene laminar premixed flames studied by [238, 239]. More recent measurements have confirmed the temperature to be within the $1650 - 1770$ K range [348], and for a wider range of argon-ethylene premixed flames between 1600 and 1900 K by [349].

As shown in Fig. 5.2, two scenarios of time-decreasing surface growth rate u are considered in the present study. These rates are based on the referred experimental measurements considering a constant soot particle mass bulk density $\rho_p = 1800$ kg/m^3 for two flame conditions. This corresponds to soot particles with low organic content [296]. To ease the interpretation of results they are referred all along the manuscript based on their initial surface growth rate ($u_0 = 0, 0.4$, and 0.6 (see Fig. 5.2)) and particle volume fraction f_v. Cases with $u_0 = 0.4$ and $u_0 = 0.6$ correspond to C/O = 0.82, and 0.94 rich premixed flames, respectively. This was achieved by changing the fuel-oxidizer equivalence ratio [238, 239]. As a reference case, we also consider a simulation of pure aggregation ($u = 0$). Based on the available data of surface growth rates from [238], the current modeling covers the $8.3 - 30$ ms range in residence time, corresponding approximately to $5 - 25$ mm in height above the burner. According to the referred measurements, the initial geometric mean diameter is $d_p = 8$ nm. Simulating aggregation for shorter residence times is challenging without considering nucleation and nascent soot coalescence. Then, starting the simulation at $d_p = 8$ nm consists in considering mature soot without nucleation, sintering and coalescence [215, 350]. We hypothesize that aggregation is negligible at
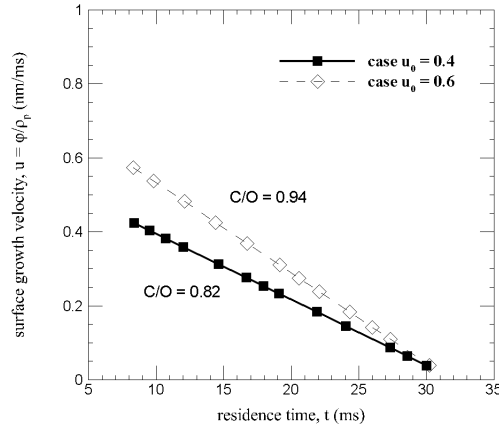
Figure 5.2: Surface growth rates [239].

residence times $t \leq 8.3$ ms due to particle coalescence. The primary particle geometric standard deviation is fixed to $\sigma_{p,geo} = 1.2$ at the beginning of the simulation in accordance with data from the literature of premixed flames [96, 324, 329].

Based on [238, 239], an initial particle volume fraction of $f_v = 0.118$ ppm is considered for cases with $u = 0$, $u_0 = 0.4$ and $u_0 = 0.6$. In addition to the change of surface growth rate, we also evaluate the impact of the initial volume fraction. To this end, we also simulate the case $u_0 = 0.6$ by considering a larger volume fraction, namely $f_v = 0.357$ ppm. In consequence, a total of four cases are simulated in the present work, corresponding to different levels of surface growth and initial volume fraction. In addition, for each simulation, a total of 1024 primary particles are randomly distributed in a cubic box avoiding overlap between each other [274]. This number is smaller than in our previous work [322] since surface growth considerably increases the CPU time cost of simulations. Indeed, one typical simulation of this work takes between 15 to 19 h in CPU time (Intel Xeon E5-2683 v4, with 20 Gb of RAM memory). A total of 10 simulations are carried out for each case and results presented later correspond to the average over these simulations. Finally, the current procedure is validated by comparison of the kinetics of aggregation and aggregate size distribution for the case $u = 0$ with macroscopic Population Balance simulations. In this context, the nodal method proposed by [351] for coalescing spheres is adapted to aggregation based on the method proposed by [41] and the results are reported in Section S4 of the SM A. Considering the uncertainties of Population Balance simulations (particularly in terms of aggregate's fractal dimension and prefactor), the comparison reports satisfactory consistent results.

5.4 Results and discussions

5.4.1 Aggregation and flow regimes

Smaller soot particles tend to agglomerate more ballistically while larger particles or aggregates come to contact in diffusive motion. At the same time, the interaction with the surrounding gas transits from free-molecular to near continuum. This simultaneous change in aggregation and flow regime can have a significant impact on aggregation kinetics, particle morphology, and the particle size distribution (see Chapter 4). Fig. 5.3a presents the evolution of the aggregation (nearest-neighbor Knudsen number Kn_n; ratio between the persistence distance and nearest-neighbor distance) and fluid flow regimes (gas Knudsen number Kn_g; ratio between the gas mean free path and particle mobility radius). Due to the flame temperature, particle size and volume fraction, a simultaneous transition in aggregation (from near-ballistic to diffusive) and flow regime (from free molecular to near continuum) is observed. While cases $u_0 = 0.4$ and $u_0 = 0.6$ (low f_v) show a similar evolution, case $u_0 = 0.6$ (high f_v) is much ballistic at the beginning and much diffusive at the end of the simulation. In all cases, near-BLCA under free molecular flow regime is only observed at the very beginning of the simulation when particles consist of isolated or a few aggregated monomers. For larger residence times, the aggregation reaches the DLCA regime under near continuum flow regime. This simultaneous evolution of aggregation/flow regimes has important consequences on the aggregation kinetics, particle size distribution, and particle morphology to be further discussed in the following sections.
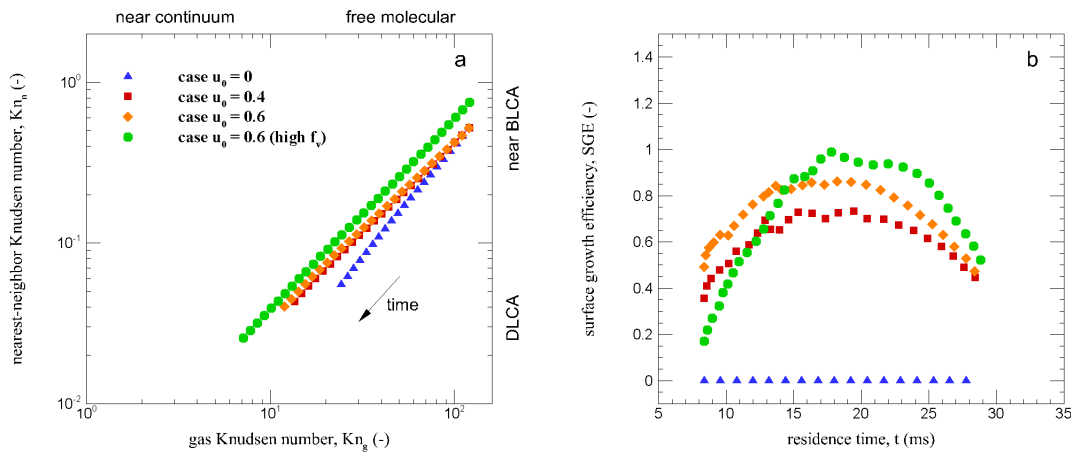
Figure 5.3: Simultaneous change in flow and aggregation regimes and surface growth efficiency.

5.4.2 Surface Growth Efficiency

A new dimensionless parameter called surface growth efficiency (SGE) is introduced in order to quantify the competition between aggregation and surface growth during the particle formation process,

$$SGE = \frac{\tau_a}{\tau_{sg}} \tag{5.4.6}$$

where $\tau_a = 2/(kN)$ and $\tau_{sg} = d_p/(6u)$ correspond to the time needed to duplicate the mass of particles by aggregation and surface growth, respectively. k is the monodisperse collision kernel, N the particle number concentration, and d_p is the average primary particle diameter (See Section S5.3 of the SM A). In this context, when $SGE \longrightarrow 0$ means that surface growth process is very slow compared to aggregation. On the other hand, $SGE \longrightarrow \infty$ means that surface growth is much faster and therefore more effective than aggregation in duplicating the mass of particles. Note that definitions with the same spirit have been introduced in previous works [111, 352, 353].

Fig. 5.3b presents the SGE as a function of time for all the simulated cases. For case $u_0 = 0$ the value is constant and equal to zero since no surface growth is considered. Cases with $u > 0$ show a similar time evolution by attaining a maximum value. This behavior is due to the fact that both τ_{sg} and τ_a are increasing in time in a competitive way. At the beginning of the simulation, SGE is proportional to the surface growth rate, excepting for the case with high f_v which promotes the aggregation efficiency. But surprisingly, when comparing both low and large volume fractions at the same growth rate ($u_0 = 0.6$), it appears that initially larger f_v will produce lower surface growth efficiency. However at a residence time ~ 20 ms the opposite behavior is observed. This indicates that surface growth is more efficient compared to aggregation when acting on already formed clusters. Considering that both cases have the same τ_{sg}, this behavior is explained by the faster increase in τ_a as a function of time for the case $u_0 = 0.6$ (high f_v). This phenomenon leads SGE for the case $u_0 = 0.6$ (high f_v) to cross the cases $u_0 = 0.4$ and $u_0 = 0.6$ (low f_v) at times around $10 - 15$ ms.

5.4.3 Particle volume fraction and aggregation kinetics

Fig. 5.4a shows the evolution of the particle volume fraction as a function of time. For the case $u_0 = 0$ it remains constant in time since there is no mass transfer between particles and gas species. Cases with $u > 0$ show different levels of increase corresponding to different surface growth rates in time. Although cases $u_0 = 0.6$ under low and high f_v seems very different, their percent increase in f_v relative to the beginning of the simulation is approximately the same (a factor of ~ 10) meanwhile the case with $u_0 = 0.4$ increase by a factor of ~ 7. This shows that the overall relative variation of the volume fraction is more sensitive to the surface growth rate evolution compared to the initial volume fraction. Fig. 5.4b shows the time evolution of
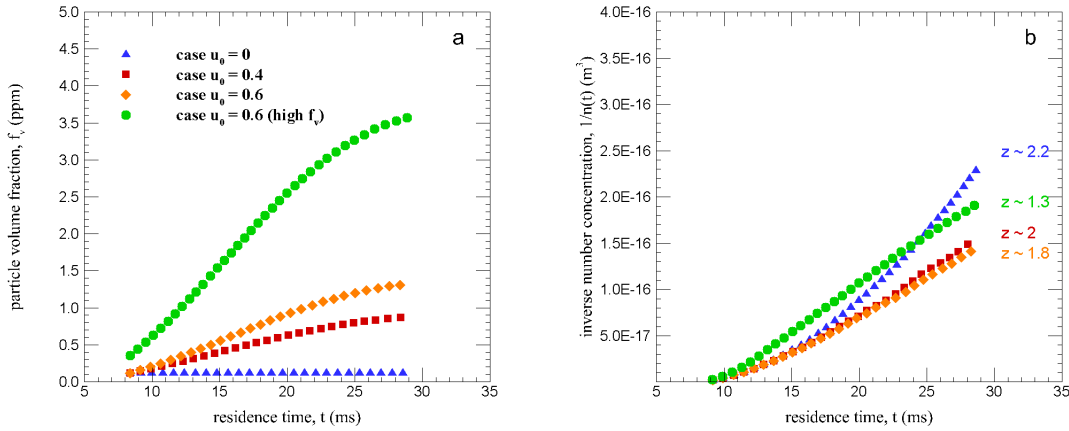
Figure 5.4: Time evolution of particle volume fraction and the inverse of the number concentration. Kinetic exponents are reported for $t \to 30$ ms.

the inverse of the particle number concentration. Its slope in log-log plot is the kinetic exponent (z) indicating the collision and thus aggregation efficiency. In consequence, it is larger at short times for the case having high volume fraction whereas other cases report similar trends up to approximately 15 ms. However, for larger times ($t \to 30$ ms, kinetic exponents are reported in the figure) a considerable impact on the aggregation kinetics is observed. It is observed when comparing cases with $u_0 = 0.4$ and $u_0 = 0.6$ (low f_v) with the case without surface growth ($u_0 = 0$). Case $u_0 = 0.6$ (high f_v) shows a different evolution from the very beginning, where the aggregation is much more ballistic than other cases. Conversely, for large residence times, it has a lower kinetic exponent than other cases because it becomes much diffusive at the end of the simulation (see Fig. 5.3a). Indeed, surface growth makes the particles increase in mass and thus less mobile, which seems more important in terms of collision frequency than the increase in particle collision radius. This would not be the case in pure free molecular flow regime where collision radius predominates over mobility. This shows the importance of considering the change in the flow regime (see Fig. 5.3a).

5.4.4 Primary particle coordination number

Fig. 5.5a shows in symbols the time evolution of the population average particle coordination number [72]. Even in the absence of surface growth this parameter is increasing in time due to aggregation and its evolution can be accurately predicted by: $\overline{n_{c,\min}} = 2(N_p - 1)/N_p$ as introduced in section 5.2.3 (this is represented by a continuous line for each case in this figure). We can note that $\overline{n_{c,\min}}$ increase is moderated compared to $\overline{n_c}$ and not very dependent on the simulated case, excepting case $u_0 = 0.6$ (high f_v) showing $\overline{n_{c,\min}}$ to increase faster. For large residence times $\overline{n_{c,\min}}$ asymptotically tends towards 2 for all cases. This value is explained by the nature of cluster-cluster aggregation regardless of the primary particle polydispersity [52, 53, 72].

Note that case $u_0 = 0.6$ (high f_v) is the most ballistic at the beginning of the simulation and thus, a

faster increase in $\overline{n_c}$ may be linked to larger fractal dimensions as observed by [336]. However, when plotting $\overline{n_c}$ as a function of $\overline{N_p}$ (see Fig. S5.10 of the SM A), it is not larger than other cases at equivalent $\overline{N_p}$. This suggests that aggregate compacity as revealed by fractal dimension is not the main cause of the observed faster increase in $\overline{n_c}$ as it will be confirmed in section 5.4.7. In turn, the more ballistic aggregation regime makes the aggregation faster at the beginning of the simulation, explaining the faster increase in $\overline{n_c}$ (and also in $\overline{n_{c,\min}}$).

On the other hand, $\overline{n_c}$ attains a maximum value between 1.9 to 8. Difference between $\overline{n_c}$ and $\overline{n_{c,\min}}$ is governed by the SGE (Fig. 5.3b), showing the importance of surface growth mechanism in the local compacity of particles. Local n_c (for individual monomers) can be as high as 16 as shown in Fig. 5.5(c1-c4). This can be observed in detail in Fig. S5.10 of the SM A, reporting the distribution of n_c at the end of the simulation. Due to the observed large magnitudes of coordination numbers, we strongly recommend not neglecting the multi-sphere intersections to calculate the volume and surface area of aggregates consisting of overlapped monomers (when $u > 0$). Indeed, the difference $\overline{n_c} - \overline{n_{c,\min}}$ plays an important role for the particle's volume and surface area evaluation.

5.4.5   Primary particle overlapping coefficient

Fig. 5.5b presents the time evolution of the average overlapping coefficient ($\overline{c_{ov}}$) between primary particles [30, 31]. This is calculated for each pair of intersecting primary particles of radii r_i and r_j, having a distance between centers d_{ij} as $c_{ov} = (r_i + r_j - d_{ij})/(r_i + r_j)$. When particles are point-touching then $d_{ij} = r_i + r_j$ and $c_{ov} = 0$, on the other hand when particles are completely fused then $d_{ij} = 0$ and $c_{ov} = 1$. In this context, when particles experience surface growth their radii is continuously increasing in time which leads to an increasing overlap with neighbors. The local degree of overlapping depends consequently on the residence time that particles have been in contact under surface growth meanwhile, the average value for an individual aggregate depends also on the frequency of collisions with other particles (aggregation). Indeed, the latter tends to decrease the average overlapping coefficient. Additionally, surface growth plays a twofold and less evident role on $\overline{c_{ov}}$ to be explained as follows. Within an aggregate, the increase of monomers radii increases the overlapping with touching neighbors but also induces new intersections with monomers belonging to the same aggregate. These new internal-intersections consequently decrease $\overline{c_{ov}}$. Finally, it is due to these 3 aforementioned factors that the average overlapping coefficient attains a quite robust value around 30% for cases with $u > 0$ even though they have different levels of surface growth and aggregation/flow regimes. However, as shown in Fig. 5.5(c5-c7) local values of c_{ov} (averaged over each individual primary particle) may be as high as 60% (see the case with $u_0 = 0.4$ under low f_v). This can be observed in detail in Fig. S5.11 of the SM A, reporting the distribution of c_{ov} at the end of the simulations.

Experimental measurements of c_{ov} from TEM image analysis can only access to a 2d projected value
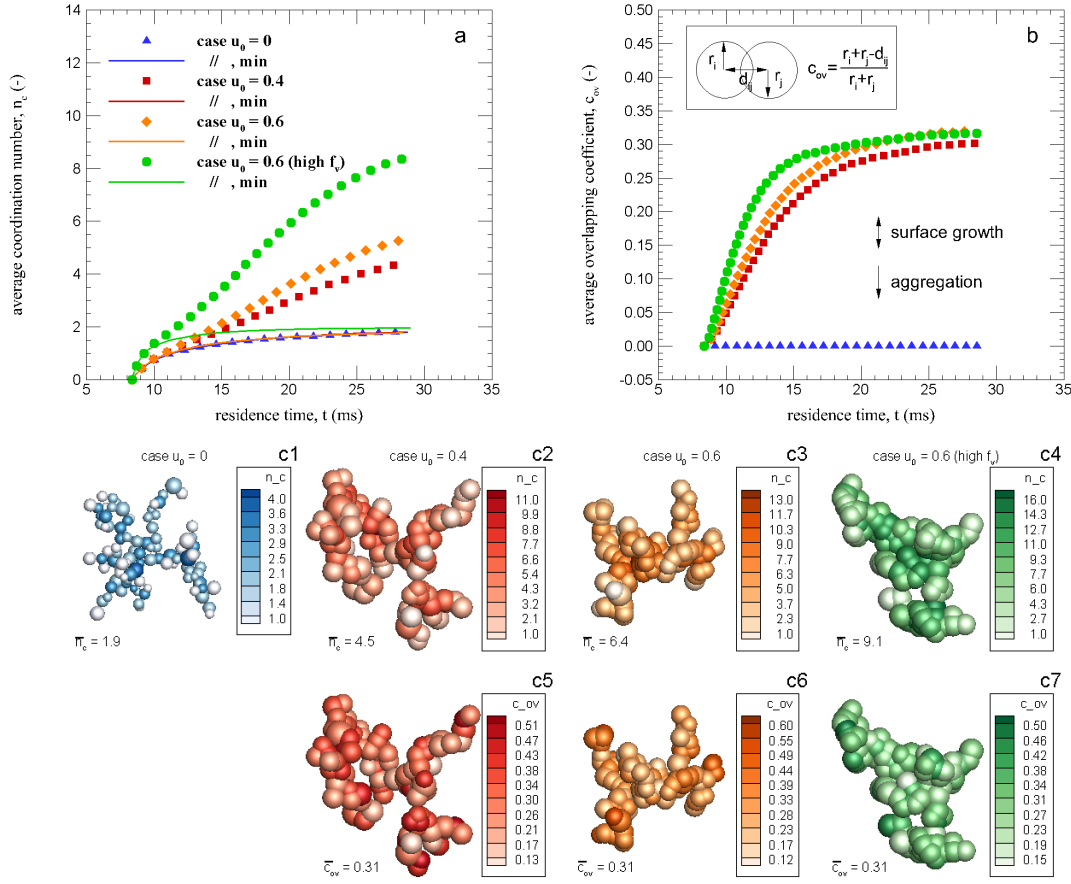
Figure 5.5: Time evolution of the average overlapping coefficient and coordination number. Continuous lines correspond to the minimum coordination number $\overline{n_{c,\min}}$ for each case. Examples of aggregates highlighting (by the color bar) the local coordination number (Figs. c1 - c4), and average overlapping coefficient per primary particle (Figs. c5 - c7).

$c_{ov,p}$. This is commonly measured on the periphery of the clusters where overlapping is visible and primary particle are clearly identifiable. It has been found to be within $c_{ov,p} = 0.11 - 0.29$ for Diesel soot [323], within $c_{ov,p} = 0.13 - 0.30$ for soot from diffusion flames [77]. Particularly for ethylene diffusion flames it has been found to vary within the $c_{ov,p} = 0.26 - 0.36$ range for aged soot at different oxygen indices [6] and more recently within the $c_{ov,p} = 0.20 - 0.22$ range for aged soot from an ethylene premixed flame [324]. Overall, these values are in good agreement with our numerical simulations.

5.4.6   Primary particle and aggregate size distributions

Considering Eq. (5.2.2), for cases with $u > 0$ the primary particle size distribution experiences an uniform shift towards larger values in time. The geometric mean primary particle diameter increases from the initial value of $d_p = 8$ nm up to 18 nm for the case $u_0 = 0.4$, and up to 21.5 nm for cases $u_0 = 0.6$ (see Fig. S5.12a of the SM A). However, this results in a decrease of the corresponding geometric standard deviation ($\sigma_{p,geo}$)

as reported in Fig. 5.6a whereas the standard deviation is time-invariant for all cases. Since, the only way to keep a geometric standard deviation constant is to shift the distribution in log scale, a shift in normal scale necessarily causes a decrease of the geometric standard deviation. This decrease of $\sigma_{p,geo}$ has not been found by [112]. We expect this discrepancy to be explained by the different ways to simulate the evolution of primary particle radii in the present study (Eq. 5.2.2). While in Ref. [112] considered a monomer size dependent surface growth rate, in the present work all the primary particles grow at the same rate (under the hypothesis of a uniform flux density). This decrease in $\sigma_{p,geo}$ is governed by the surface growth rates presented in Fig. 5.2. Obviously, in the case $u = 0$, it remains constant in time. The present study tends to conclude that surface growth reduces the geometric standard deviation of the primary particle diameter. Note that considering other mechanisms of soot formation, such as oxidation could lead to a different $\sigma_{p,geo}$ evolution [354].
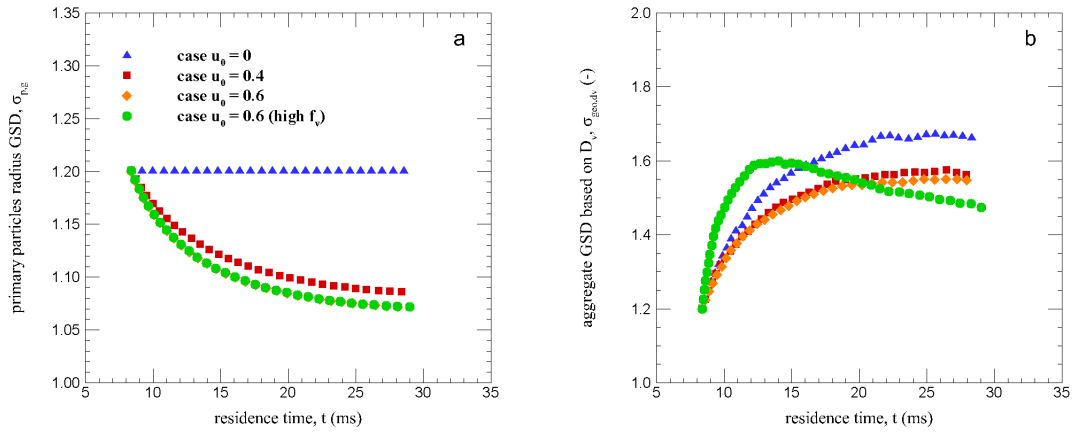
Figure 5.6: Time evolution of the geometric standard deviation (number-based) of primary particles and aggregate volume equivalent diameter.

On the other hand, the geometric mean volume-equivalent aggregate diameter increases from the initial value of 8 nm up to 26, 50, 57, and 90 nm for cases $u_0 = 0$, $u_0 = 0.4$, $u_0 = 0.6$, and $u_0 = 0.6$ (high f_v), respectively (see Fig. S5.12b of the SM A). Fig. 5.6b shows the time evolution of the corresponding aggregate geometric standard deviation $\sigma_{dv,geo}$. Aggregation mechanism increases $\sigma_{dv,geo}$ during time, with a maximum asymptotic value reached in the absence of surface growth ($u = 0$). This asymptotic value depends on the aggregation/flow regime [322]. Conversely, surface growth tends to limit the increase in $\sigma_{dv,geo}$, being consistent with previous works [23, 112, 355]. This is attributed to the fact that larger aggregates experience a larger increase in mass due to surface growth however, they are also characterized by larger levels of overlapping and larger n_c which tends to decrease the population of larger particles and thus the geometric standard deviation. This may be the reason why for case $u_0 = 0.6$ (high f_v) the attained $\sigma_{dv,geo}$ at $t = 30$ ms is the smallest among all simulated cases. This case is indeed the most diffusive at the end of the simulation (see Fig. 5.3a), consequently having a lower $\sigma_{dv,geo}$ is expected. This because $\sigma_{dv,geo}$ has been observed to

be smaller for diffusive/transition than ballistic aggregation regimes (see Chapter 4). In addition, Table 5.1

Table 5.1: Aggregate geometric standard deviation (number-based) at the end of the simulation ($t = 30$ ms).

Case	$\sigma_{dm,geo}$	$\sigma_{dg,geo}$	$\sigma_{dv,geo}$
$u_0 = 0$	1.77	2.23	1.63
$u_0 = 0.4$	1.70	2.00	1.57
$u_0 = 0.6$	1.61	1.85	1.49
$u_0 = 0.6$ (high f_v)	1.56	1.79	1.45

shows the values of $\sigma_{dm,geo}$ (based on the mobility diameter), $\sigma_{dg,geo}$ (based on the gyration diameter), and $\sigma_{dv,geo}$ calculated at $t = 30$ ms. For the case with $u = 0$, these values are in good agreement with [322]. Also, these results are in good agreement with experimental measurements. Indeed, for aged soot particles sampled in an ethylene premixed flame, [324] found $\sigma_{dg,geo}$ between 1.82 and 1.87 based on different methods to determine d_g from TEM image analysis. Additionally, for aged soot particles from rich premixed ethylene flames studied by [63] found $\sigma_{dm,geo} \sim 1.6$ from SMPS measurements. Also the SMPS measurements of [59] confirmed $\sigma_{dm,geo}$ for aged soot particles to be between 1.50 to 1.64.

5.4.7 Particle morphology

Finally, in order to evaluate the impact of the surface growth/aggregation competition on the individual particle's morphology, we report (in symbols) in Fig. 5.7 the volume-based normalized pair correlation function for a set of representative aggregates. It is numerically determined by calculating the exact volume of intersection between the aggregate and an identical copy which is shifted randomly in a 3-dimensional space [140]. $A(0)$ corresponds to the aggregate volume. The morphological information is contained in the radial dependence of $A(r)$ and thus, we report here the normalized expression of that function. This volume is calculated by using the SBL library [341]. A total of 300 orientations and 200 radial positions (logarithmically spaced) are considered for all the aggregates studied as done in [53, 140].

As recently suggested by [53], $A(r)$ consists of two components such that: $A(r) = A_{pp} + A_{agg}$, where A_{pp} is the contribution of primary particles to the aggregate morphology (self-intersection of primary particles), and A_{agg} is the contribution of the aggregate structure by considering the intersection between neighbor spheres. A_{pp} dominates at small scales, namely $r \rightarrow R_{pv}$ (where R_{pv} is the monomer average volume-equivalent radius) whereas A_{agg} becomes predominant for larger scales. Fig. 5.7 shows an increase in the region governed by A_{pp} when increasing u, and a less evident hump at the transition between A_{pp} and A_{agg} is observed. Thus, in both figures surface growth makes it very difficult to dissociate their contribution to the total pair correlation function, especially when $u_0 = 0.6$. This also evidences that larger structures are needed to observe a well-established fractal (self-similar) behavior in $A(r)$. This is remarkably similar to increasing the primary particle polydispersity where also larger monomers are in competition with the scale of the aggregate in terms of volume and subsequently, A_{pp} cannot be easily differentiated from A_{agg} [53, 140].

We attempt to fit the so determined pair correlation function based on the following model which is a modification of Eq. (5.4.7a) and Eq. (5.4.7b) originally proposed in Ref. [53],

$$A_{pp}(r) = \left(1 + \frac{r}{4\widetilde{R_{pv}}}\right)\left(1 - \frac{r}{2\widetilde{R_{pv}}}\right)^2, \qquad r \in [0, 2\widetilde{R_{pv}}] \qquad (5.4.7a)$$

$$A_{agg}(r) = \frac{\phi D_{f,i}}{3}\left(\frac{r}{R_{pv}}\right)^{D_{f,i}-3}\left[e^{-(r/\xi_{max})^\beta} - e^{-(r/\xi)^\beta}\right], \qquad r > 0 \qquad (5.4.7b)$$

In this context, the packing factor ϕ, the individual fractal dimension $D_{f,i}$, the maximum and minimum equivalent length scales ξ_{max} and ξ, respectively, the stretching exponent β and the volume-equivalent primary particle radius $\widetilde{R_{pv}}$ are the fitted parameters. Note that this model has not been rigorously adapted to over-lapped spheres. This could alter the expression of A_{pp} and A_{agg} at small scales. In the present study, we focus on ϕ and $D_{f,i}$ which are found at large scales and thus expected to be physically meaningful. A direct fit of all the aforementioned parameters is quite challenging and therefore a *fit-by-parts* procedure is proposed as thoroughly explained in Section S5.2 of the SM A.

A total of 2 aggregates per condition (sampled at the end of the simulations $t = 30$ ms) are fitted. They are selected according to N_p (within the $100 - 105$ range in Fig. 5.7a, and within the $430 - 450$ range in Fig. 5.7b). These aggregates are also selected for having representative anisotropy coefficients (A_{13}), where the most probable values are within the $1.7 - 4.0$ range (see Fig. S5.13 of the SM A). When analyzing the fitted parameters (reported in the figures), a significant increase in the packing factor ϕ is found when increasing u_0. The packing factor expresses the local compacity at the scale of primary particles [51, 53]. Note that the obtained ϕ values for the cases with $u_0 = 0$ are slightly different from those reported by [53] where DLCA aggregates under the Epstein flow regime were simulated, while in the present study the change in aggregation/flow regimes is taken into account. It appears that surface growth increases the local compacity. This is explained by the increase in overlapping coefficient and coordination number as previously discussed. The effect of volume fraction seems to be of second-order since the two cases with $u_0 = 0.6$ at low and high volume fractions exhibit similar $A(r)$ curves.

The individual fractal dimensions determined during the fitting procedure are also reported in the figures. For aggregates consisting of $N_p = 100 - 105$, as shown in Fig. 5.7a, a fractal dimension can only be confidently found for the case $u = 0$. On the other hand, as shown in Fig. 5.7b, because the aggregates are larger, the individual fractal dimension can be robustly determined for each case. Except for the case $u_0 = 0.6$ (high f_v), it seems that the fractal structure of aggregates, as described by $D_{f,i}$, is not considerably affected by surface growth. The fractal dimension for the case $u_0 = 0.6$ (high f_v) is larger. This particular case has been shown to experience a more ballistic aggregation at the beginning of the simulation, consequently explaining the observed larger fractal dimension. In consequence, the morphology of the particles is affected by surface

growth in the sense that the packing factor is increased (which may be related to the increase in the fractal prefactor [53] but the fractal dimension seems not really sensitive to the surface growth itself. It is however strongly dependent on the change of aggregation regime as previously reported in this manuscript.
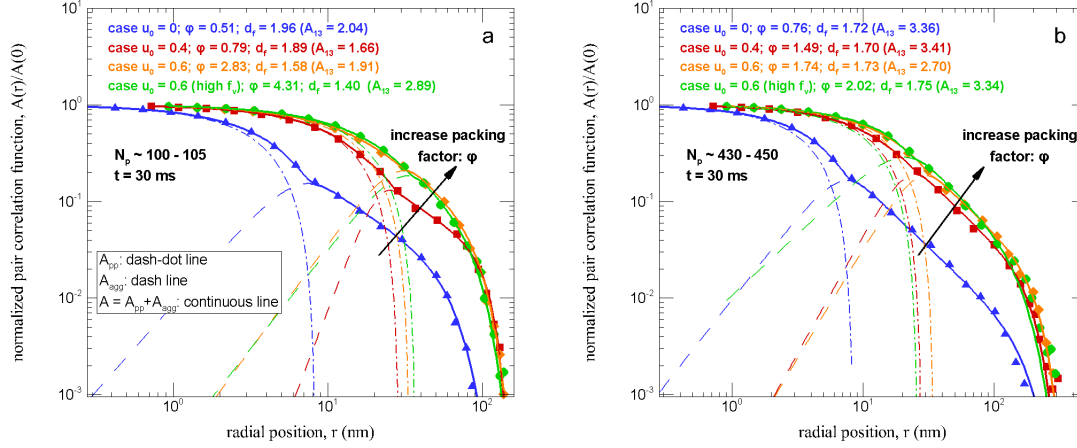
Figure 5.7: The symbols correspond to the normalized pair correlation function of aggregates with representative anisotropy and sampled at the end of the simulations (t = 30 ms). Aggregates made of $N_p \in [100, 105]$ and $N_p \in [430, 450]$ are reported on Fig. a and b, respectively. Continuous lines present the total fitted $A(r) = A_{pp} + A_{agg}$, while the two components A_{pp} and A_{agg} are the contribution of primary particles (dash-dot lines) and aggregate (dashed lines), respectively. Anisotropy coefficient A_{13}, and the fitted parameters (ϕ and $D_{f,i}$) are reported in the legends.

5.4.8   Projected area scaling-laws

Figure 5.8 shows the fits of the scaling-laws between the effective number of primary particles per aggregate and the normalized average projected area already given by Eq. (2.1.13) is adapted to primary particles overlapping as,

$$N_{\mathrm{p,eff}} = k_\alpha \left(\frac{A_a}{A_p} \right)^\alpha \tag{5.4.8}$$

where A_a and A_p are the orientationally averaged projected area of the aggregate and primary particle, respectively. Also, α and k_α are the power-law exponent and prefactor, respectively. First, for all the studied cases a power-law is observed showing that aggregates retain a fractal geometry even when there is surface growth. Secondly, both k_α and α seem to be affected by surface growth. The case without surface growth shows $k_\alpha = 1.074$ and $\alpha = 1.091$ which is quite close to the values found for DLCA aggregates $k_\alpha = 1.10$ and $\alpha = 1.08$ obtained by [30]. As observed in Fig. 5.8, for the different cases studied the scaling exponent α exhibit a maximum increase of 7% for the case $u_0 = 0.6$ (high f_v) compared with the case without surface growth, depending on the application, this variation may be considered negligible. However, the scaling prefactor k_α exhibit a remarkable increase with surface growth with a maximum increase of 23% for the case $u_0 = 0.6$ compared with the case without surface growth. This increase in k_α may be linked to the increase in local compactness as evidenced by the packing factor ϕ reported in the previous sections. This

variation should be considered in experimental TEM image analysis to obtain soot particles morphological properties [15]. This is also relevant for numerical studies where collision kernels in the free molecular flow regime are determined based on aggregate's projected surface area [177].
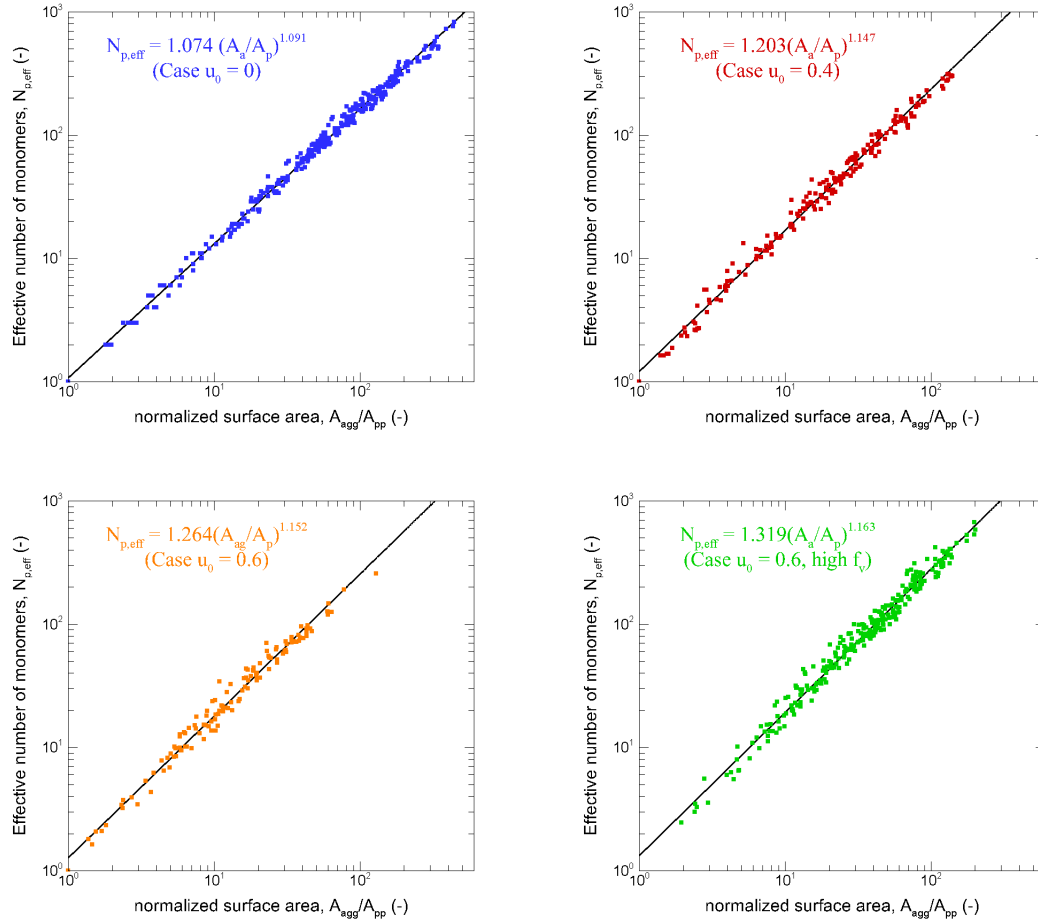
Figure 5.8: Projected area and effective number of primary particle scaling laws.

5.5 Soot aggregates total volume and surface area approximation

PBE simulations codes are highly used by engineers in particle technology, particularly in industrially relevant flame synthesis of nanoparticles [356]. These codes are also used to simulate the production of atmospheric pollutants. These simulations typically neglect the overlapping between primary particles to evaluate the volume and surface area of aggregates. This induces a high uncertainty especially related to particles dynamics and surface reactions modeling. This can considerably affect the ability of these simulations to predict nanoparticles yield. It is worth mentioning that the corrections proposed for MC DEM simulations as introduced in Section 5.2.3 cannot be easily applied for PBE simulations because the prediction of the
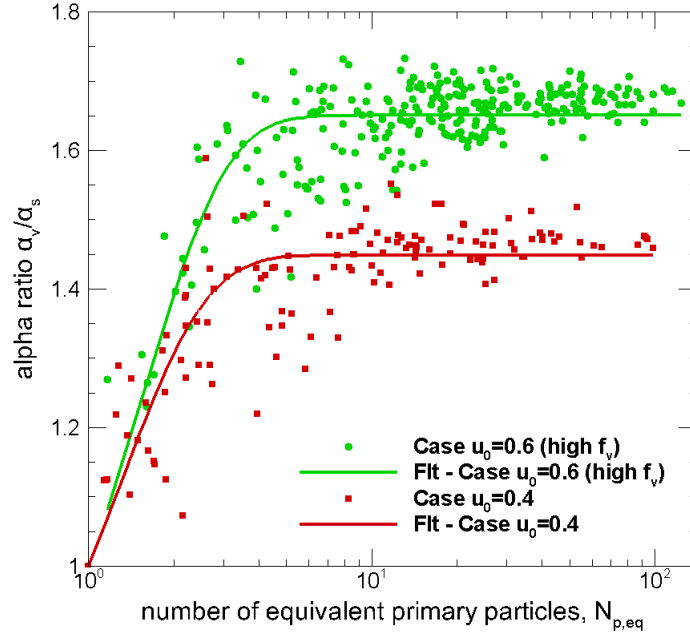
Figure 5.9: Ratio between volume (α_v) and surface area (α_s) correction factors as a function of the equivalent number of primary particles per aggregate. ($N_{p,eq}$). For particles sampled at the end of the simulations ($t = 30$ ms).

averaged primary particle overlapping, and coordination numbers is not trivial. Therefore, in this section we attempt to propose 2 different methods to determine total soot volume and surface area that can eventually be used for these applications.

5.5.1   Method 1: Volume/Surface area ratio correction

Since the work of Kruis et al. [357], different authors in the literature [42, 112, 358] have used an equivalent primary particle diameter when overlapping between primary particles exist,

$$d_{p,eq} = \frac{6V_a}{S_a} \tag{5.5.9}$$

This diameter depends on individual aggregate's volume (V_a) and surface area (S_a),

$$V_a = \alpha_v \frac{\pi}{6} \sum_{i=1}^{N_p} d_{p,i}^3 \tag{5.5.10a}$$

$$S_a = \alpha_s 4\pi \sum_{i=1}^{N_p} d_{p,i}^2 \tag{5.5.10b}$$

Table 5.2: Fitting parameters for Eq. 5.5.12.

Case	a	b	c
$u_0 = 0.4$	1.4151	0.9768	-0.4487
$u_0 = 0.6$	1.9933	1.3448	-0.4821
$u_0 = 0.6$ (high f_v)	1.2526	0.7590	-0.6503

Where α_v and α_s are the correction to volume and surface area, respectively as introduced in Section 5.2.3, due to primary particle overlapping. Based on this equivalent diameter, a corresponding equivalent number of primary particles is typically considered,

$$N_{p,eq} = \frac{V_a}{\pi d_{p,eq}^3 / 6} \tag{5.5.11}$$

Based on this approach, the ratio α_v / α_s is an input parameter needed for CFD simulations of soot formation in flames. Therefore, it is reported in Fig. 5.9 as a function of $N_{p,eq}$ for particles sampled at the end of the simulations ($t = 30$ ms). As can be observed, it is always an increasing function of $N_{p,eq}$ up to a certain critical $N_{p,eq}$ where a quasi-asymptotic curve is observed. This asymptotic value is found to be determined by primary particle overlapping and coordination numbers. The latter explains why case $u_0 = 0.6$ (high f_v) achieves a larger asymptotic value than other cases. In this context, the ratio $\alpha_v / \alpha_s = f(N_{p,eq})$ is modeled by equation (5.5.12),

$$f(N_{p,eq}) = \frac{a}{b + (a - b)\exp(-a(N_{p,eq} - 1))} + c, \tag{5.5.12}$$

where a, b, and c are fitting parameters reported in Table 5.2 for the different cases simulated here. Therefore, Eq. (5.5.12) based on the parameters reported in Table 5.2 may be used as an input for CFD simulations dealing with aerosol particles based on the PBE.

5.5.2 Method 2: Population average overlapping

Method 1 introducing a correction for the ratio volume to surface area is simple and may be enough for some applications however, it is simulation-dependent. Therefore, in this final section, a new method to approximate the time-evolving total soot volume and surface area is proposed. The objective is to provide a method that could eventually be used in Population Balance simulations of soot formation. In this context, the exact positions and sizes of primary particles are unavailable information consequently primary particle overlapping is generally neglected in the literature. The total volume V and surface area S concentration are approximated as,

$$V = N\bar{v} \approx N\overline{\alpha_v}\overline{N_p}\frac{\pi}{6}\overline{D_p^3}, \tag{5.5.13a}$$

$$S = N\bar{s} \approx N\overline{\alpha_s}\overline{N_p}\pi\overline{D_p^2}, \tag{5.5.13b}$$

Where the primary particle diameter D_p, number of primary particles per aggregate N_p, and aggregate number concentration N are commonly known parameters. However, the determination of the average volume (α_v) and surface area (α_s) correction coefficients are difficult to determine since as shown in previous sections, they depend on primary particle overlapping and coordination numbers. Therefore, we propose to approximate these parameters as follows,

$$\overline{\alpha_v} \approx 1 - \frac{1}{4}\overline{n_c c_{ov}}^2(3 - \overline{c_{ov}})\psi, \tag{5.5.14a}$$

$$\overline{\alpha_s} \approx 1 - \frac{1}{2}\overline{n_c c_{ov}}\psi, \tag{5.5.14b}$$

where the mean coordination number can be approximated as $\overline{n_c} = \overline{n_{c,min}} = 2(\overline{N_p} - 1)/\overline{N_p}$, which means that only a minimal number of contacts between monomers is considered. As noted, in equations (5.5.14) multi-sphere intersections is not considered and therefore a correction factor is introduced $\psi = \psi(N_p)$. By analyzing a population of aggregates generated based on FracVAL [140] and having different levels of overlapping, the following expression is obtained,

$$\psi(N_p) = \frac{a}{b + (a - b)\exp(-a(N_p - 2))} + c, \qquad N_p \geq 2 \tag{5.5.15}$$

where $a = 0.06421$, $b = 0.05658$, and $c = 0.006155$ are constant fitted parameters. Note that a similar approach has been proposed by Brasil et al. [30] for Eq. (5.5.14b) however, they ignored the dependence of $\psi = \psi(N_p)$. The final problem is how to approximate the mean overlapping coefficient. As shown in previous sections, the latter is determined by the competition between aggregation and surface growth (SGE). Indeed, for a given contact between primary particles arriving at time t_0 the overlapping at a later time t $c_{ov}(t) = (D_p(t) - D_p(t_0))/D_p(t)$. Considering the time derivative of this expression $dc_{ov}/dt = 2u_{sg}D_p(t_0)/(D_p(t))^2$. This means that knowing the surface growth rate u_{sg} the overlapping of this pair of primary particles can be predicted as,

$$c_{ov}(t_0, t) = 2D_p(t_0) \int_{t_0}^{t} \frac{u_{sg}}{(D_p(t))^2} \, dt', \tag{5.5.16}$$

Equation (5.5.16) means that the population average overlapping coefficient may be predicted based on the total number of collisions in time $B(t)$ as follows,

$$\overline{c_{ov}} = \frac{\int_{t_0}^{t} c_{ov}(t_0, t)B(t) \, dt'}{\int_{t_0}^{t} B(t) \, dt'} \tag{5.5.17}$$

where the total number of collisions per unit of time is simply $B(t) = dN/dt$ when there is no nucleation or particle disappearance due to oxidation. In the case of population balance simulations, $B(t)$ can be determined from the coagulation source term of the PBE.

Equations (5.5.13) to (5.5.17) have been implemented in post-processing in this thesis work to predict the time evolution of V and S and results are presented in Fig. 5.10. The so referred "calculated values" were determined based on the exact SBL library [341]. First, neglecting particle overlapping leads to a maximum overestimation of total particle volume and surface area of 91 and 218%, respectively. Second, the proposed method exhibits a maximum error of 0.6% for total volume and 5.75% for total surface area, respectively. This approach seems promising to improve the accuracy of CFD-PBE simulations.
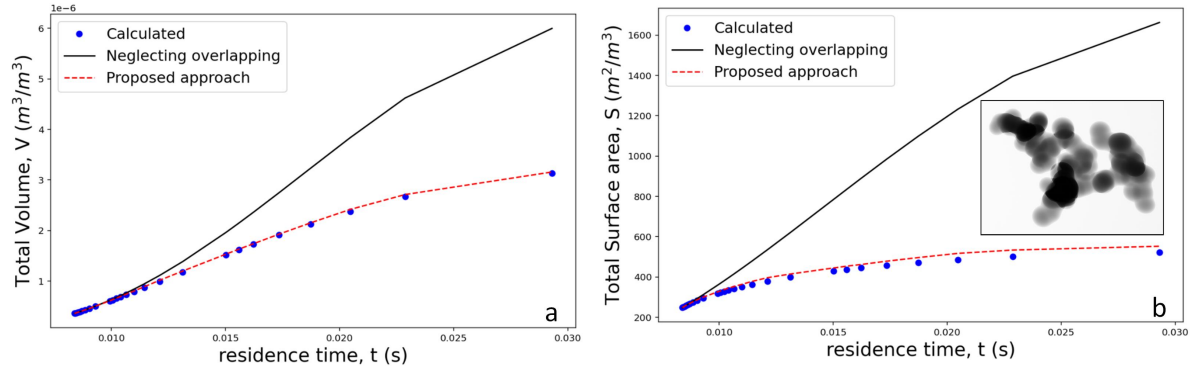
Figure 5.10: Total volume and surface area approximation based on Eqs.(5.5.13)-(5.5.17).

5.6 Oxidation and nucleation

In previous sections, the MCAC code was validated to study soot agglomeration. In this section, the adaption of this code to both oxidation and nucleation and their validations are described,

- Oxidation: In terms of the variation of primary particle size, oxidation is just considered as the reversible process of surface growth as described in previous sections. This means that surface growth is considered as a surface phenomenon leading to primary particles radii decrease in time. At each time iteration, all primary particles experiencing oxidation are inspected to check $D_p \geq D_c$, where D_c is the critical coalescence diameter (further discussed later in Chapter 6). Below this critical diameter, soot particles behave as molecular clusters and their dynamics are beyond the scope of this thesis. Potentially, at some time, the primary particles may no longer be in contact and therefore oxidation leads to the fragmentation of the corresponding aggregates. This is implemented based on the theory of graphs to efficiently check all the connections between monomers belonging to a given aggregate. When the distance between two primary particles is larger than the sum of their radii, the corresponding aggregate is split at this point. This means that one aggregate can fragment into one or more sub-aggregates.

- Nucleation in time: By considering a nucleation flux given in mass or particle number concentration such as $J_{\text{nucl}} = dN/dt$ with units $(1/m^3/s)$, the increase of the number of primary particles Δn

(dimensionless) in the domain during a time step Δt is given by $\Delta n = J_{\text{nucl}} \Delta t V_{box}$, where V_{box} is the volume of the simulation domain. At every time iteration, the quantity $n(t + \Delta t) = n(t) + \Delta n$ is determined. Subsequently, a total of $\lfloor n \rfloor \geq 1$ (where $\lfloor n \rfloor$ is the floor function of n) primary particles, are introduced in random locations in the simulation box (avoiding overlapping with existing particles), and $n(t) = n(t) - \lfloor n \rfloor$ is updated.

These modifications to MCAC need a validation in order to ensure the conservation of mass, the correct primary particle deletion from the system, the correct fragmentation of aggregates, and the correct insertion of new particles to the system (nucleation).

5.6.1   Validation of fragmentation and individual surface reactions

This section aims at validating MCAC regarding two main aspects namely (1) the fragmentation of aggregates due to oxidation, and (2) the individual surface reactions scheme. Indeed, we can distinguish two alternatives to simulate surface reactions as,

1. **Population-based:** In Step 6 of MCAC (see Chapter 3), all the particles in the system experience surface reactions during a physical MC time step.

2. **Individual-based surface reactions:** In Step 6 of MCAC (see Chapter 3), only the displaced particle experiences surface reactions during its individual time of displacement $\Delta t = 3\tau$ (or less if a collision with a neighbor is detected).

The latter alternative has the advantage of being more computationally efficient since less calculations are done, however it is to be probed if this procedure induces an error on the simulation process. To test this error and to test the correct fragmentation of particles due to oxidation, a validation case is simulated. In this test case, surface growth takes place at a constant mass flux until a specific residence time (0.1 ms) then, soot oxidation is simulated by considering exactly the same magnitude of surface growth flux but now with a negative sign until the end of the simulation (time 0.21 ms). For these simulations, 1024 monomers of 10 nm diameter (GSD=1.2) and mass bulk-density of 1.8 g/cm^3 are initially randomly placed in a cubic box. These particles are allowed to experience Brownian motion with periodic boundary conditions and they irreversibly agglomerate when colliding with neighbors. The thermodynamics conditions are $P = 101.3$ kPa, $T = 1700$ K. The initial volume fraction is 10 ppm. A constant surface growth flux of magnitude $\varphi_0 = 2 \cdot 10^{-2}$ kg/m^2/s and a constant oxidation flux $(-\varphi_0)$ are considered. At a residence time 0.1 ms the transition from surface growth to oxidation takes place.

Results

Figure 5.11 shows the evolution of different macroscopic physical properties, including the particle number concentration, volume fraction, average monomers per aggregate, and average monomers overlapping as a function of time. Fig. 5.11a shows a decrease in the particle number concentration up to a residence time 0.1 ms due to agglomeration. From this time on, the particle number concentration is increasing in time due to particles' fragmentation induced by oxidation. This fragmentation process stops at a residence time of 0.2 ms where it remains constant until the end of the simulation. At this point, all particles are in the form of spherical monomers that continue oxidizing in time, however particle number concentration is unchanged since particles are not completely consumed by oxidation. Particle volume fraction shown in Fig. 5.11b exhibits an inverted quite linear variation determined by the surface reaction rates. Once all the particles have became spherical at 0.2 ms they continue decreasing in time due to primary particles mass loss by oxidation. The average number of primary particles per aggregate shown in Fig. 5.11c shows a symmetric increase/decrease driven by agglomeration and fragmentation, and remains constant and equal to unity after 0.2 ms. A similar behavior is observed for the local compactness of aggregates as characterized by the PP overlapping coefficient (Fig. 5.11d). These results suggest that population and individual based surface reactions lead to consistent results. Also, the almost symmetric behavior of results suggests that MCAC is correctly simulating soot particles surface growth and oxidation, and the corresponding consequences in the kinetics of agglomeration, agglomerate size, and particles connectivity are correctly simulated. Other important properties to be analyzed are the primary particle and aggregate size distributions. Fig.5.12a and Fig.5.12b show the geometric mean and standard deviations of the aggregates volume equivalent radius, respectively. While agglomeration leads to an increase in both $R_{v,geo}$ and $\sigma_{rv,geo}$, fragmentation leads to a decrease in both parameters (understood as the reversible process). Note that after 0.2 ms, all particles have became spherical, consequently $R_{v,geo}$ decreases at a different rate, and the $\sigma_{rv,geo}$ starts to increase due to primary particle oxidation. The differences in $\sigma_{rv,geo}$ at around 0.1 ms are normal since the number of particles in the box is reducing in time and also because it is larger at this time, making more difficult to accurately retrieve this parameter. Fig.5.12c and Fig.5.12d show the geometric mean and standard deviation of the primary particle radii, respectively. As expected, $r_{p,geo}$ is linearly evolving in time due to the constant surface reaction rates. Please observe the small vertical shift in $\sigma_{p,geo}$ is expected since only in both cases a total of 1024 random primary particles radii are sampled from a lognormal distribution which induced a small uncertainty in this values. This uncertainty normally disappear when averaging over different simulations. These simulations show an increase in primary particle polydispersity due to oxidation. In this test case, based on individual surface reactions, CPU time is reduced by a factor of 10 compared to the population ones. Individual surface reactions lead to a small effect on particle's dynamics and therefore on aggregation kinetics. This because at the scale of time of individual particle displacements ($3\tau = 3m/f$) the current mass and collision cross section of particles is not considerably affected by surface reactions. It may be critical

(a) Particle number concentration

(b) Volume fraction

(c) Monomers per aggregate

(d) Overlapping
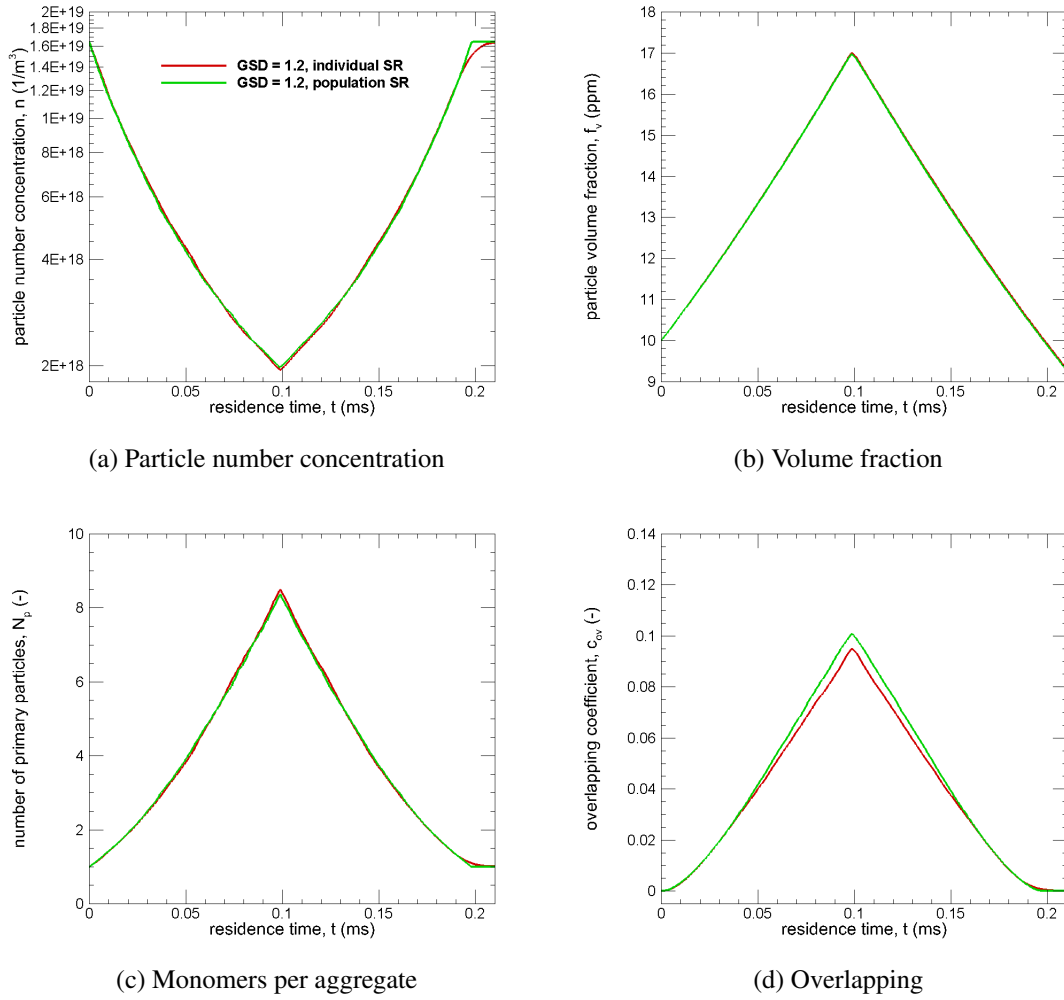
Figure 5.11: Comparison of physical properties between the individual and population based surface reactions.

when studying extremely high volume fractions, where the characteristic time of aggregation is too small and eventually comparable to 3τ, or when the characteristic time of surface growth is very small. This is not expected to be the case for soot particles formation in flames, which is very diluted and characteristic times of surface growth are always comparable with the aggregation one, i.e., SGE$\approx$ 1 (see earlier discussions in this Chapter). Individual surface reactions lead to unavoidable differences with population one such as the smoother variation in the particle number concentration observed at the end of simulations (see Fig. 5.11a). Despite these sources of uncertainties, and small differences between both approaches, individual surface reactions leads to overall consistent and accurate results compared to the population ones. The symmetric behavior of results suggests that oxidation and subsequent aggregate fragmentation lead to consistent/coherent results with surface growth, consequently validating this numerical implementation in MCAC.

(a) Geometric mean R_v

(b) GSD R_v

(c) Geometric mean r_p

(d) GSD r_p
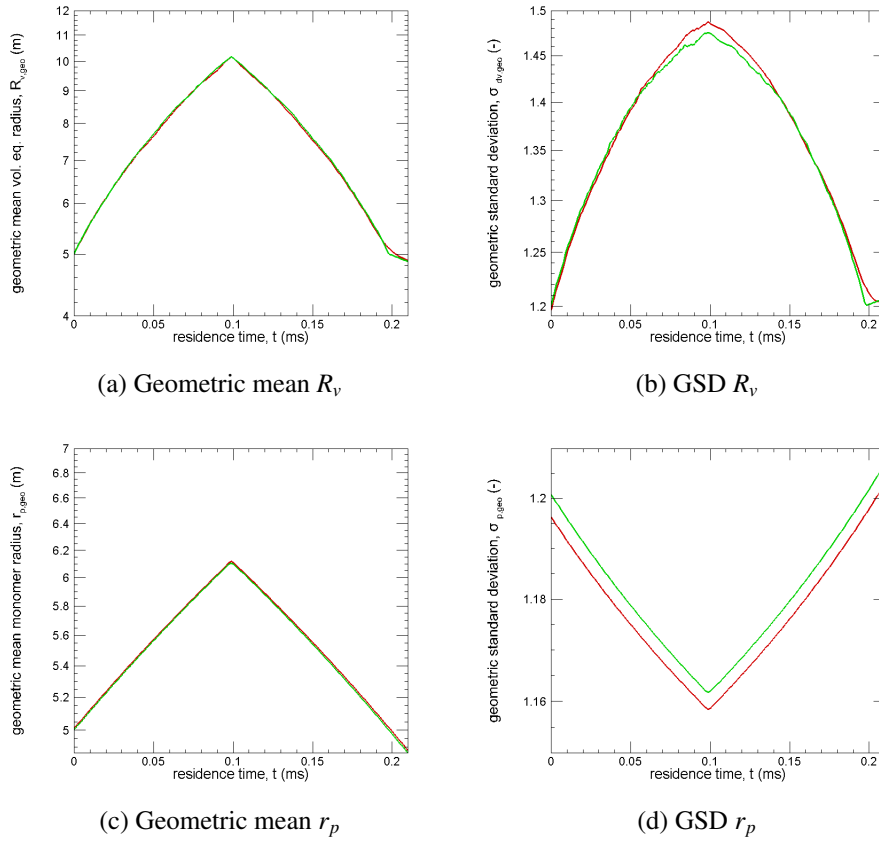
Figure 5.12: Comparison of aggregate and monomer size distribution, between the individual and population based surface reactions.

5.6.2   Validation of nucleation

Following the same logic than the previous section, a validation test is proposed for primary particle nucleation in time. For these simulations, 1024 monomers of diameter 10 nm (polydisperse: GSD=1.2 and monodisperse: GSD=1) and mass bulk-density of 1.8 g/cm^3 are randomly placed in a cubic box avoiding overlapping. Particles are allowed to experience Brownian motion with periodic boundary conditions. When two particles collide, agglomeration is forbidden and therefore the movement is repeated until the particles move in a direction avoiding collisions with neighbors. In this way only spherical particles are simulated as a function of time without considering agglomeration. The thermodynamic conditions are the same as in previous validations (P=101.3 kPa, T=1700 K). The initial volume fraction is 1 ppm. A constant oxidation rate is imposed $\varphi_0 = -1.11 \cdot 10^{-4}$ kg/m^2/s. Particles disappear from the box when they achieve a lower bound diameter of 2 nm (arbitrarily selected). In addition, a constant nucleation rate of $J_{nucl} = 7.19 \cdot 10^{21}$ (1/m^3/s) is considered. For these simulations, an individual oxidation scheme is used (see previous section), this means that individual particles being displaced experience oxidation.

Results

Fig. 5.13a shows the time evolution of the particle number concentration $N(t)$. In both monodisperse and polydisperse cases this number is initially increasing in time due to nucleation. As observed in Fig. 5.13c when the particle radius approaches $r_c = 1$ nm, i.e. the size at which particles disappear from the system $N(t)$ drastically reduces in time and this reduction is faster for monodisperse particles because all the particles will reach the radius r_c at the same time while in the case of polydisperse monomers smaller particles will be deleted in first place. After this time, an asymptotic plateau is achieved corresponding to the balance between nucleation and disappearance of particles due to oxidation.

It is very interesting to note that the number concentration N_{eq} in this asymptotic regime can be predicted analytically. We have found the analytical solution for this problem for sufficiently long residence times.

- First, we need to introduce the idea of "lifetime" of particles in the box i.e., how long particles will survive until they are consumed by oxidation. This time depends on the initial mean particle's radii (r_0) and the minimum one (r_c) at which they disappear from the box. Consequently this characteristic time can be defined as,

$$\tau_{life} = \frac{r_c - r_0}{u_{ox}}$$

  where $u_{ox} < 0$ is the constant oxidation rate in (m/s).

- Second, the amount of particles in equilibrium for large residence times will also depend on the nucleation rate J_{nucl} in (1/m^3/s). Therefore at equilibrium of creation/deletion, the particle number concentration in the box is,

$$N_{eq} = \tau_{life} \cdot J_{nucl}$$

Finally, for the current simulations considering $r_0 = 5$ nm, $r_c = 1$ nm we obtain $N_{eq} = 2.59 \cdot 10^{17}$ (1/m^3) being in excellent agreement with simulations as observed in Fig. 5.13a. In addition, as shown in Fig. 5.13b, particle volume fraction f_v is initially decreasing in time due to the predominance of oxidation over nucleation in terms of net mass transfer to the system. For longer residence times, an asymptotic constant limit is reached corresponding to the equilibrium between mass addition by nucleation and mass loss by oxidation. Fig. 5.13d shows the time evolving $\sigma_{v,geo}$. This is increasing very fast from the initial imposed value (1 for monodisperse and 1.2 for polydisperse monomers) until a residence time of 0.05 ms where a plateau is reached, this increase in polydispersity is explained by the predominance of nucleation over oxidation at the beginning of the simulation. Also, additional tests showed that the asymptotic value depends on the magnitudes of nucleation mass flux and oxidation rate.

(a) Particle number concentration

(b) Volume fraction

(c) Geometric mean R_v

(d) GSD R_v
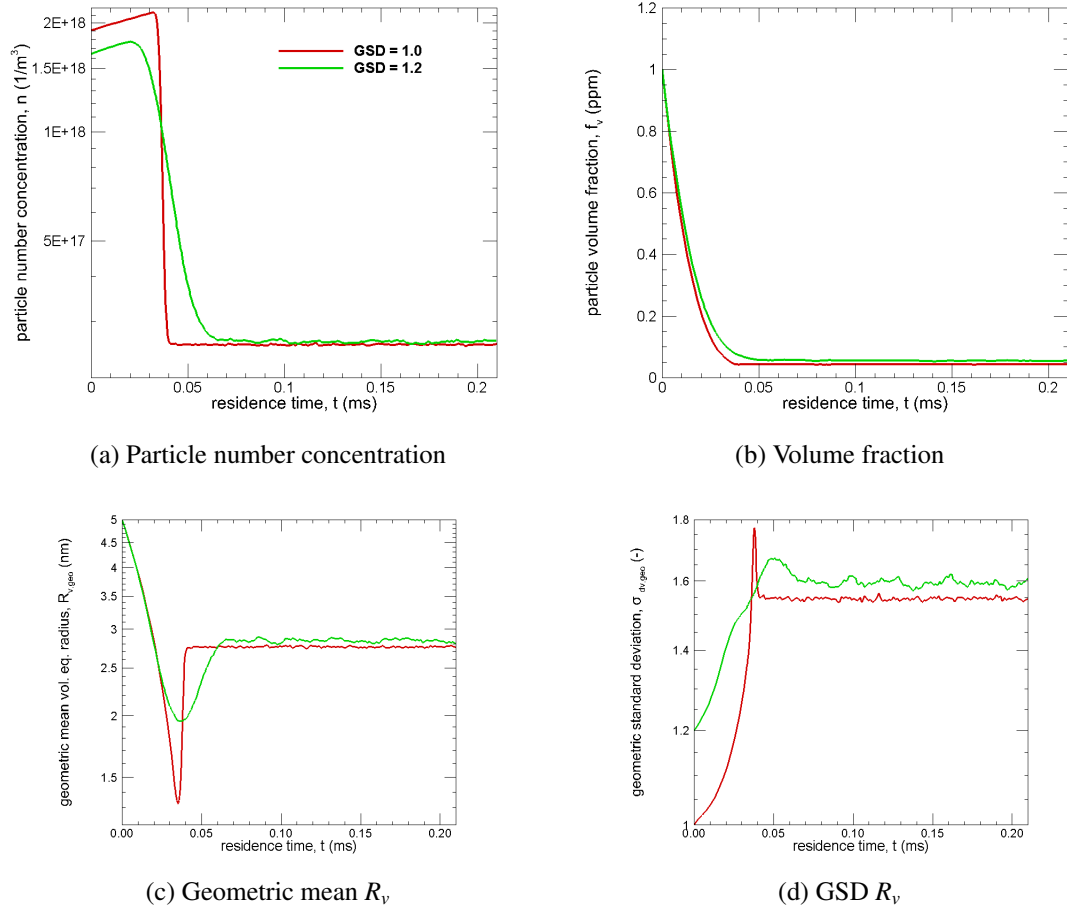
Figure 5.13: Comparison of physical properties and particle size distribution for 2 cases of different particle polydispersity, namely $\sigma_{p,geo} = 1$ (monodisperse) and $\sigma_{p,geo} = 1.2$.

5.7 Conclusions

The simultaneous aggregation and surface growth of soot particles formed in an ethylene premixed flame is numerically simulated. Surface growth plays an important role in both particle aggregation and flow regime. Indeed, the added mass tends to reduce the particle mobility and subsequently slows down aggregation at large residence times. Also, it is found to decrease both the aggregate and primary particle geometric standard deviations.

In the present study, the competition between surface growth and aggregation mechanisms during time is quantified by introducing a new dimensionless parameter called the Surface Growth Efficiency. This parameter seems well correlated with the average primary particle coordination number (accounting for the number of intersections for monomer with nearest-neighbors). This parameter, commonly overlooked in the literature, is found to increase in time. For individual monomers, it can increase up to 16 while the global average attains a non-asymptotic maximum value between 4 to 8. This evidences that multi-sphere

intersections should not be neglected when studying the physical properties of these types of aggregates, notably their volume and surface area.

According to the increase of the number of primary particle in contact, the local overlapping coefficient can be as high as 60% (depending on the surface growth rates and particles residence time), even though the global average values attain an asymptotic value around 30% irrespective of the Surface Growth Efficiency, in good accordance with experimental observations.

The morphological effect of surface growth is also studied by calculating the pair correlation function of individual aggregates representative of each case studied. The local compacity of aggregates, as quantified by the packing factor, considerably increases with Surface Growth Efficiency. This is linked to the increase in primary particles overlapping and coordination number. In addition, the analysis of large aggregates (consisting of ~ 440 monomers) reveals that individual fractal dimension is not strongly affected by surface growth and thus may be more sensitive to the change in aggregation regime [322].

The effect of surface growth on the projected area of soot aggregates is explored and correlations power-laws with the effective number of monomer per aggregate are proposed based on current simulations. The parameters of these correlation are in good agreement with DLCA agglomerates studied in the literature [30] and their dependence to surface growth rate under different flame conditions is explored. Both the scaling exponent and prefactor are increasing with surface growth. Scaling prefactor is found more sensible to surface growth than the fractal scaling exponent. Indeed, it may increase up to 23% while the scaling exponent increases up to a maximum of 7% compared with the case without considering surface growth.

In order to accurately simulate the competition between aggregation and surface growth, it is necessary to evaluate the volume and surface area of highly overlapped primary particles. This is particularly challenging when the coordination number is larger than the introduced minimum bound as shown in this work. Exact methods exist, such as ARVO [340] or SBL [341] but they are too much expensive in terms of CPU time for being systematically integrated in a code aiming at simulating soot formation in flames, such as MCAC used here. For this reason, a semi-analytical method is proposed taking into account the multi-spheres intersection. The latter is commonly neglected in the literature [30, 45, 187]. The proposed determination of aggregate volume and surface area is shown to be very dependent on the coordination number $\overline{n_c}$ and more precisely to its difference with the minimum bound $\overline{n_{c,\min}}$. The proposed method can be potentially integrated in population balance [148], Monte Carlo [345] simulations, and may also improve experimental measurements of particle volume and surface area based on TEM image analysis [77, 323, 359, 360]. Indeed, in this work we have proposed a simplified version of this method allowing to predict the evolution of total particle volume and surface based on the population average overlapping coefficient. Despite the simplifications considered, this method showed remarkable accuracy and may be implemented in codes based on the population balance equation that currently ignore the primary particle overlapping.

Finally, a new scheme of surface reactions have been introduced, it is referred to as individual surface

reactions since only the individual particles under displacement experience surface reactions during their time of displacement. This method leads to a reduction in CPU time in a factor of 10! A validation test showed consistent results when comparing both individual and population surface reactions. The validation test also showed the ability of MCAC to simulate the fragmentation of aggregates as induced by oxidation. An additional validation test has shown the correct inclusion of nucleation and deletion of particles by oxidation. This rigorous validation procedure validates MCAC to simulate the aggregation of soot particles under the action of time-evolving nucleation, surface growth, and oxidation. Also, the simulation strategy of surface reactions carried out in this work has never been discussed in the literature and corresponds to a new approach.

6 | Soot maturity[4]

Mature soot aggregates exhibit a morphology which is up to now mimicked by DLCA codes, i.e. with a sticking probability = 1 when two aggregates collide. Nevertheless, nascent soot particles (a few nanometers in size and having low C/H ratio) may grow in the RLCA regime, i.e. with a sticking probability << 1. Yet, it remains to be seen how fast the transition from RLCA to DLCA is for soot particles. Also, what is the impact on aggregation kinetics, particle size distribution and morphology. This chapter intends to fill this gap by exploring the aggregation of soot particles formed in a laminar premixed flame. Results show that the transition from RLCA to DLCA is very fast and produces a moderate impact on soot formation dynamics and morphology. However, soot particles mass bulk density is found to play an important role and should be considered in future simulations of soot formation in flames.

6.1 Introduction

This chapter focuses on the role played by soot maturity (here the change in chemical composition and particles bulk density) on the aggregation kinetics and morphology. The formation of these complex aggregates can be modeled by classical DLCA or RLCA codes when detailed information on aggregate's morphology is intended [361]. In this type of simulations, the motion of each individual particle is explicitly solved and agglomeration can occur when two particles collide. More precisely, DLCA and RLCA simulations assume that particles undergo purely diffusive motion (i.e. convective transport by an underlying flow is neglected). This means that these methods are restricted to small particles, typically within the colloidal range (i.e. lower than a few micrometers, for which gravity forces are negligible compared to Brownian motion). DLCA and RLCA simulations are able to produce morphologies similar to soot aggregates.

The main difference between DLCA and RLCA simulations lies in the treatment of collisions between two particles: DLCA assumes that agglomeration is driven by particle diffusion while agglomeration is driven by the physico-chemical interactions between particles in RLCA codes. To put it differently, in DLCA codes, every collision between a pair of particles leads to their adhesion and, hence, to the formation of aggregates

---

[4]Part of this Chapter has been published in: Morán, J., Henry, C., Poux, A., & Yon, J. (2021). Impact of the maturation process on soot particle aggregation kinetics and morphology. Carbon, 182, 837-846.

(i.e. the sticking probability is 1). In RLCA codes, the sticking probability is close to 0, meaning that only a few collisions are successful to form an aggregate. In reality, nascent soot particles may have a very low sticking probability, i.e. they may rebound after collisions due to their higher mobility and lower potential well depths compared to mature soot [246]. On the contrary, mature soot have a higher tendency to form aggregates due to a sticking probability ≈ 1. Therefore, a second critical diameter d_s has to be considered as the transition between both regimes, as illustrated in Fig. 2.7. Little attention has been paid to this second critical diameter. Therefore, in the present work, we focus on identifying d_s. The question we intent to answer in the current investigation is the d_s to simulate the transition from RLCA to DLCA and what would be the consequences on soot aggregation kinetics, morphology and size distribution?

This transition is expected to be related to the evolution of particle mobility and their composition. In fact, nascent particles are small (a few nanometers diameter) and have a mass bulk density ~ 1.2 g/cm^3 at typical flame temperatures [362] whereas, mature soot primary particles have a larger diameter, are solid, with a graphitic structure and a bulk mass density of ~ 1.8 g/cm^3 [296, 362]. Similarly, the chemical composition, parametrized by the C/H ratio, increases with maturity due to soot dehydrogenation [215, 344]. Indeed, soot maturity evolution has many physico-chemical consequences as further discussed in Refs. [101, 242]. These progressive modifications of the physico-chemical properties of soot particles may consequently induce a change of particle mobility but also affect their sticking probability [246, 363].

Another factor, commonly overlooked in the literature, is the role played by the particle electric charges. Different works have found soot particles to acquire a natural electric charge in flames due to chemi-ionization reactions and ion attachment to PAH clusters or primary particles [258–260, 364, 365]. The interaction between charged colloidal particles leads to the presence of repulsive electrostatic forces that can hamper agglomeration. Indeed, when the kinetic energy of the approaching particles is not strong enough to overcome the repulsive electrostatic forces, particles repel each other and prevent agglomeration [254]. Therefore, accurate predictions of the outcome of soot particle interactions require simulations that include both the sticking and the collision probabilities. To the authors' knowledge, such modifications of electrical properties have never been taken into account to study the morphological properties and kinetics of soot aggregation. The present work intends to fill this gap by considering the bulk density, sticking probability and electrostatic forces evolving in time. As shown in Fig. 2.7, it is important to note that the dynamics of PAH molecular cluster formation is out of the scope of the present work. Here, we investigate the kinetics of non-coalescing soot primary particle aggregation and surface growth in a laminar premixed flame together with detailed calculations of inter-particle interactions.

6.2   Methodology

To answer the main question raised by the current investigation, a physical evaluation of the collision and sticking probabilities of soot aggregates (described in Section 6.2.1) is carried out and then implemented in a Monte Carlo discrete element code as explained in section 6.2.3. The principle of the collision and sticking probabilities determination relies on fine-scale evaluations of the interaction energy between two soot aggregates (more details are provided in Section 6.2.2).

6.2.1   Interaction energy between particles

6.2.1.1   Interaction between primary spheres

Drawing on the previous study by Hou et al. [246], the interaction energy E between two spherical soot particles separated by a distance h is obtained by integrating the Lennard-Jones interactions between atoms over the volume of each body. This integration results in the sum of an attractive force and a repulsive force (more details can be found in Section S6.1 of the SM A).

$$E_{\text{L-J}} = E_{\text{att}}(h) + E_{\text{rep}}(h) \tag{6.2.1}$$

The attractive term due to the van der Waals contribution can be written as

$$E_{\text{att}}(h) = -\frac{A_{ham}}{6} f_a\left(R_{p,1}, R_{p,2}, h\right) \tag{6.2.2}$$

where h is the separation distance between the two spheres, A_{ham} the Hamaker constant and f_a a function containing geometrical factors. The repulsive term is due to the overlap of electron orbitals occurring at very short separation distances. It is given by [246],

$$E_{\text{rep}}(h) = \frac{1}{37800} A_{ham} \left(\frac{\sigma_{ab}}{2\,R_{p,1}}\right)^6 \left(U_{rep,1} + U_{rep,2} + U_{rep,3} + U_{rep,4}\right) \tag{6.2.3}$$

with σ_{ab} the distance of zero potential between atoms. Each of the four components $U_{rep,i}$ are detailed in Section S6.1 of the SM A.

In addition to these short-ranged inter-molecular forces, we also account for electrostatic interaction between charged soot particles. The formula for the potential energy of two charged spherical particles (each one having a given number of elementary charge z_p) is given by,

$$E_{\text{electro}}(h) = \frac{\kappa_0\, z_{p,1}\, z_{p,2} e^2}{h} \tag{6.2.4}$$

where $\kappa_0 = 8.9875517923 \times 10^9$ is the Coulomb constant (in $kg\,m^3\,s^{-2}\,C^{-2}$) and e is the elementary charge. As a result, the total interaction energy E_{tot} between two primary soot particles is given by,

$$E_{\text{total}}(h) = E_{\text{att}}(h) + E_{\text{rep}}(h) + E_{\text{electro}}(h) \tag{6.2.5}$$

6.2.1.2 Parametrization

To solve Eq. (6.2.5), further information is required on particle properties. The Hamaker constant A_{ham} is estimated using the number density of carbon atoms and hydrogen atoms within each soot particle as well as the particle mass bulk density (similarly to the procedure in [246]). This means that, by changing the chemical composition of one particle and/or its density to account for maturity effects, the Hamaker constant is automatically updated to fit this new composition. Further details on the parametrization used here are provided in Section S6.1 of the SM A. Soot particles charging may be determined by different mechanisms including the attachment of ions and electrons to soot molecular clusters, primary particles, and soot aggregates. Positive and negative ions are naturally produced in the flame as it has been experimentally observed [364, 366, 367]. These ions and electrons are believed to be produced mainly by chemi-ionization reactions [260]. However, thermo-emission may be an important mechanism to be considered. Indeed, Balthasar and Mauss [368] suggested that this mechanism might explain the appearance of charged molecular clusters. More recently, Starik et al. [260] found no relevant role played by thermoemission. The relation between soot charging and maturity seems *a priori* not strong since flames with different fuels and different flame conditions show similar charge distributions [258, 259, 369, 370]. The detailed modeling of soot charging dynamics is beyond the scope of the present work (interested readers can refer to [260, 368, 371]). In this chapter, the electric charge of soot particles is estimated using available measurements on the charge distribution of soot particles in premixed flames [259]. Aggregates electric charges are obtained by randomly sampling a number of elementary charges (z_p) from the Boltzmann distribution [259],

$$f(z_p) = \left(\frac{K_E e^2}{\pi d_m k_B T}\right)^{1/2} \exp\left(\frac{-K_E z_p^2 e^2}{d_m k_B T}\right) \tag{6.2.6}$$

where $K_E = 9.0 \cdot 10^9$ Nm^2/C^2, k_B is the Boltzmann constant, e is the elementary charge, and d_m is the mobility diameter of the aggregate obtained from the friction coefficient of the aggregate (see Chapter 3).

6.2.1.3 Interaction between aggregates

We further extend the previous work of Hou et al. [246] to compute the interaction energy between aggregates composed of a number of primary soot particles. As displayed in Figure 6.1, the difficulty that arises when computing the interaction between two aggregates is that it should take into account the aggregate morphology and its orientation with respect to the other aggregate/particle. In fact, depending on the aggregate morphology

and orientation, one or several primary particles within a first aggregate can be in close proximity to other particles in the second aggregate. Recent evaluations of van der Waals interactions between fractal DLCA aggregates have shown that the van der Waals interaction between aggregates is actually governed by the interaction between the closest pair(s) of primary particles [372]. This result is mainly due to the short-range nature of van der Waals forces, which usually act within the nanoscopic scale. As a result, we have simplified the present calculations of aggregate-aggregate interactions by accounting only for the interaction between the closest pair of primary particles.

Concerning electrostatic forces between aggregates, a similar issue arises since the exact repartition of charges within an aggregate is unknown. Several simplifications can be considered, including: (a) placing all charges on the closest pair of primary particles, (b) considering aggregates as full spheres with an equivalent radius where charges are homogeneously distributed and (c) placing all charges on the furthest pair of primary particles within aggregates. Since one of the objectives of this study is to assess the impact of electrostatic interaction on soot aggregation, we report here only the results obtained with case (a), which tends to overestimate the electrostatic contribution and thus corresponds to the worst case scenario.

6.2.2 Collision efficiency

As mentioned in the introduction, simulations of particle agglomeration require to couple a model for the aggregate transport (collision step) and a model for aggregate interactions (adhesion step). However, these two phenomena occur at various spatial and temporal scales: soot particles can indeed be transported near the flame over several centimeters while inter-aggregate forces are composed of short-ranged Lennard-Jones forces (within the nanoscopic scale) and long-range electrostatic forces. Since precise calculations of the combined motion of interacting aggregates at the nanoscopic scale are out of scope of the present chapter (it will require much smaller time steps for the transport model), the coupling of the two phenomena is obtained using energetic considerations that are similar to boundary conditions used in standard CFD simulations (see also [373]). This means here that only reduced information on the interaction energy is extracted from the whole energy-versus-distance curve (see also Fig. 6.1): the potential well $E_{well} \leq 0$ (i.e. the minimum of the interaction energy) and the energy barrier $E_{barr} \geq 0$ (i.e. the maximum of the interaction energy). As displayed in Fig. 6.1, three possible outcomes of an interaction are considered depending on the following energetic criteria:

1. no collision occurs when the repulsive energy barrier E_{barr} overpowers the relative kinetic energy along the direction of collision E_{kin}, i.e. $E_{kin} < E_{barr}$;

2. a collision occurs when the relative kinetic energy along the direction of collision E_{kin} is high enough to overcome the repulsive energy barrier E_{barr}, i.e. $E_{kin} > E_{barr}$. Once a collision occurs, two subsequent results are possible:
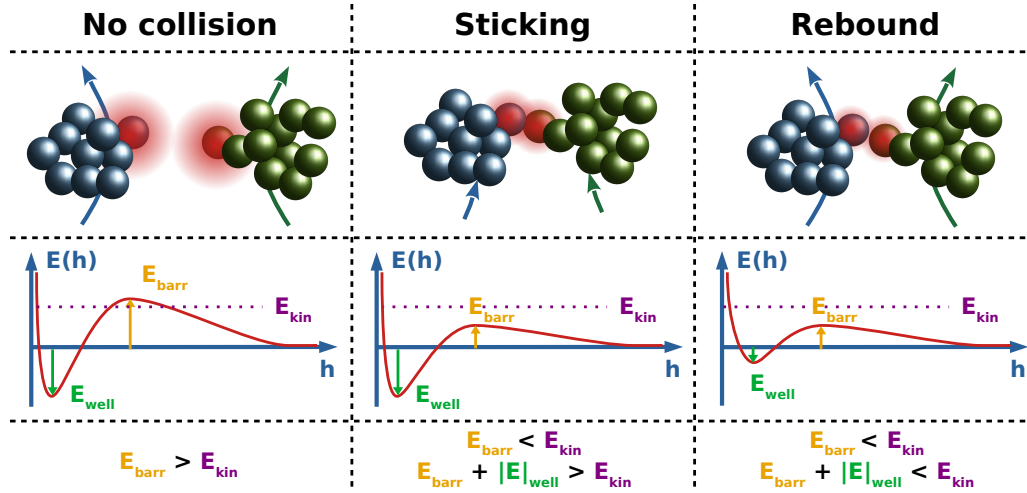
Figure 6.1: Sketch showing the three possible outcomes of a collision between two aggregates and the corresponding criteria (based on the potential well E_{well}, the energy barrier E_{barr} and the relative kinetic energy E_{kin}).

2.a. The two particles/aggregates stick to each other when the particle cannot escape the potential well, i.e. $E_{kin} < |E|_{well} + E_{barr}$;

2.b. The two particles/aggregates rebound when their kinetic energy (again taken equal to the incoming one) prevails over the potential well, i.e. $E_{kin} > |E|_{well} + E_{barr}$;

Drawing on this scenario for the outcome of an interaction between soot particles/aggregates, a collision probability and a sticking probability are evaluated. The formula for these probabilities are obtained by analogy with a Brownian diffusion of particles in a force field (more details are provided in Section S6.2 of the SM A):

$$P_{coll} \quad = 1 - \mathrm{erf}\left(\sqrt{\widetilde{E_{barr}}} \right) + \sqrt{\widetilde{E_{barr}}} \times \exp\left(-\widetilde{E_{barr}} \right) \tag{6.2.7}$$

$$P_{stick} \quad = \mathrm{erf}\left(\sqrt{\widetilde{E_{stick}}} \right) - \sqrt{\widetilde{E_{stick}}} \times \exp\left(-\widetilde{E_{stick}} \right) \tag{6.2.8}$$

with the dimensionless potential energies $\widetilde{E_{barr}} = E_{barr}/(k_B T)$ and $\widetilde{E_{stick}} = (|E|_{well} + E_{barr})/(k_B T)$ (k_B being the Boltzmann constant and T the flame temperature).

6.2.3 Integration in MCAC

MCAC code, thoroughly explained in Chapter 3, considering the transition in both flow and aggregation regimes is adapted. In the context of the current chapter, MCAC has been adapted to non-unitary collision and sticking probabilities. In this context, a collision-check step is done each time two aggregates come to close contact. The outcome of this check depends on a uniformly distributed random number $\delta_1 \in [0, 1]$ such that, particles collide when $\delta_1 \leq P_{coll}$, or repel each other when $\delta_1 > P_{coll}$. If collision is found, a second random

number is generated $\delta_2 \in [0, 1]$ such that, particles stick together after collision when $\delta_2 \leq P_{stick}$, or rebound when $\delta_2 > P_{stick}$. This procedure is inspired by the classical RLCA codes found in the literature [374, 375]. As explained in previous sections, P_{coll} and P_{stick} depend on both the electrostatic barrier, and Lennard-Jones potential well depth, respectively. These properties depend on the flame temperature, aggregate's mobility diameter, primary particle size and soot maturity. To simulate a time-evolving soot maturity, the properties of individual aggregates are introduced as new parameters in MCAC (including the C/H ratio, the density ρ_p, and electric charge). The C/H ratio is correlated to the average primary particle size (within an aggregate) and used to determine ρ_p (see section Section S6.3 of the SM A). The potential well depth is determined based on the chemical composition and diameter of the colliding primary particles. The electrostatic barrier is determined based on the electric charge of the interacting aggregates. Indeed, the mobility diameters of the approaching aggregates is obtained based on the friction coefficient of aggregates [45, 376]. Thus, equation (6.2.6) is used to sample a given charge for each aggregate that respects the Boltzmann distribution. This new version of MCAC allows to investigate the kinetics of aggregation, the particle size distribution, and aggregates morphology.

Kinetics of aggregation is studied by quantifying the time evolution of the aggregate number concentration $N(t)$ in (1/m^3) and the monodisperse equivalent coagulation kernel k_{ii} in m^3/s. The latter is determined from the local slopes of $1/N(t)$ as a function of t, as done in Section 4.3.2.

Particle size distribution is studied in terms of the volume-equivalent radius. The morphology of particles is studied in terms of the population-based fractal dimension, and fractal prefactor obtained by a log-log fit of the fractal-law expressed as,

$$\frac{V_{agg}}{\overline{V_p}} = k_f \left(\frac{R_g}{R_{pv}} \right)^{D_f} \tag{6.2.9}$$

where, V_{agg} is the aggregate volume corrected by overlapping monomers and obtained based on the SBL library [341], $\overline{V_p} = 1/N_p \sum_{i=1}^{N_p} (\pi/6) d_{p,i}^3 = (4\pi/3) R_{pv}^3$ is the average primary particle volume, and R_g is the aggregate's radius of gyration obtained by discretizing the aggregate [45] (see Section S6.4 of the SM A). In addition, the pair correlation function for representative aggregates is calculated and fitted to search the packing factor ϕ which is an indicator of the local compacity in the cluster. The details on its determination are given elsewhere [140, 377] and the fitting procedure is the same than in Ref. [376]. Further details can also be found in Section S6.5 of the SM A.

6.3 Results

6.3.1 Case studied and parametrization

A premixed ethylene flame (C/O = 0.82) is selected as a test case. This flame has been already simulated by considering the simultaneous aggregation and surface growth in Chapter 5 but change of maturity was not considered and thus, the collision and sicking probabilities were fixed to 1. In order to start the current simulation with smaller primary particle size than in the aforementioned chapter, surface growth rates (u in nm/ms) from Chapter 5 have been linearly extrapolated to shorter residence times. Current simulations start at t = 3.5 ms, with 1024 spherical primary particles [378] corresponding to a lognormal size distribution with a geometric diameter of d_p = 2.4 nm and geometric standard deviation of 1.2. The domain size is set to respect the initial volume fraction to f_v = 0.002 ppm. Constant temperature T = 1700 K and 1 atm of pressure are considered. The simulation ends at t = 30 ms.

In this chapter, based on a literature survey, nascent soot are considered to have C/H = 1.1 and a corresponding bulk density of ρ_p = 1.2 g/cm^3. In contrast, mature soot are characterized by C/H = 10 and ρ_p = 1.8 g/cm^3. Mass bulk density of nascent and mature soot particles are obtained from [296], being in good agreement with [362].

Table 6.1: Selected cases for numerical simulations.

Case	Description
Mature (no potentials)	P_{coll} = 1 and P_{stick} = 1, ρ_p = 1.8 g/cm^3
Nascent (no potentials)	P_{coll} = 1 and P_{stick} = 1, ρ_p = 1.2 g/cm^3
Mature (only LJ)	P_{coll} = 1, and P_{stick} is evaluated, ρ_p = 1.8 g/cm^3, C/H = 10.0
Nascent (only LJ)	P_{coll} = 1, and P_{stick} is evaluated, ρ_p = 1.2 g/cm^3 C/H = 1.1
Variable maturity (LJ + electrostatic)	P_{coll} and P_{stick} are evaluated, ρ_p and C/H evolve in time electrostatic forces considered

Different cases are considered in order to evaluate the role played by maturity and electrostatic forces (see Table 6.1). The first one called "mature (no potentials)" consists in keeping the properties of mature soot during all the simulation and considering systematic collision and sticking when two aggregates approach each other (i.e. whatever the size of the colliding primary spheres). This corresponds to the usual DLCA approach. The second one called "nascent (no potentials)" is identical to the previous one but now considering the physical properties of nascent soot. The comparison with the previous case is then used to study the role played by the bulk density.

Cases 3 and 4 called respectively "mature (only LJ)" and nascent "(only LJ)" will also conserve the physical properties of respectively mature and nascent soot, but for these cases the sticking probabilities are evaluated based on the colliding primary particle radii according to the their composition.

Case 5 "variable maturity (LJ+electrostatic)" considers a transition of soot maturity induced by a variation of C/H and consequently in ρ_p according to the primary sphere radius based on Refs. [215, 379] (see the Section S6.3 of the SM A for further details). This case also considers the electrostatic forces as described in Section 6.2.1.

For each case studied, a total of 10 simulations are conducted and results presented later are averaged over these ten simulations as done in previous chapters.

### 6.3.2 Collision and sticking probabilities of soot particles

6.3.2.1 Effect of maturity

We first assess the role of soot maturity (expressed though particle size, mass bulk density and composition) on the collision and sticking probabilities. To this end, we evaluate the behavior for mature soot, nascent soot and soot with variable maturity but zero electric charges. In that case, since no repulsive forces act on a range longer than van der Waals forces, no energy barrier occurs (not shown here). Hence, the collision probability is always equal to unity. However, the balance between van der Waals forces and Born repulsion leads to an existing potential well whose value depends on the particle size, bulk density and chemical composition.

Figure 6.2 displays the evolution of the potential well and sticking probability as a function of the reduced particle radius $R_{red} = R_{p,1}R_{p,2}/(R_{p,1} + R_{p,2})$, where $R_{p,i}$ expresses the radius of the i'th colliding primary particle. Several conclusions can be drawn from this figure:

- when the particle properties are fixed ("mature" or "nascent" cases), the depth of the potential well increases with increasing reduced particle diameter. This is consistent with previous studies of neutrally charged particles (e.g. [246]). As a result, the sticking probability quickly increases from 0.1 at $R_{red} = 0.5$ nm to values close to 1 around $R_{red} = 3$ nm. Based on the definition of the reduced particle radius, we can evaluate the critical primary diameter at which the sticking probability is roughly equal to 1, which happens to be around $d_s \sim 8$ nm for nascent particles (resp. $d_s \sim 12$ nm for mature soot). This means that, except for very small particles, a collision does induce agglomeration of the two particles involved. This result is comparable to the one obtained by Hou et al. [246], who obtained $d_s \sim 14$ nm for soot particles at $T = 1500$ K. The slight difference is due to the different formula used to evaluate the sticking probability (see Section S6.2.3 of the SM A) as well as to differences in the density and C/H ratio considered for nascent or mature soot.

- the depth of the potential well for mature particles (and consequently the sticking probability) is higher than the one for nascent particles. This is related to the fact that mature particles have a higher Hamaker constant due to their higher density and C/H ratio, leading to stronger short-ranged attractive forces.

- the results obtained with the variable maturity case are bounded by the two limit cases of "nascent" and "mature" particles. When one of the particle diameter is fixed, the depth of the potential well (and consequently the sticking probability) increases with the reduced particle diameter. Moreover, it clearly appears that the results obtained for the variable maturity case are very close to the "nascent" case when the reduced size is below 0.7 nm while they become very close to the "mature" case when the reduced size is above 4 nm (in which case, the sticking probability reaches a plateau value $P_{stick} \simeq 1$).
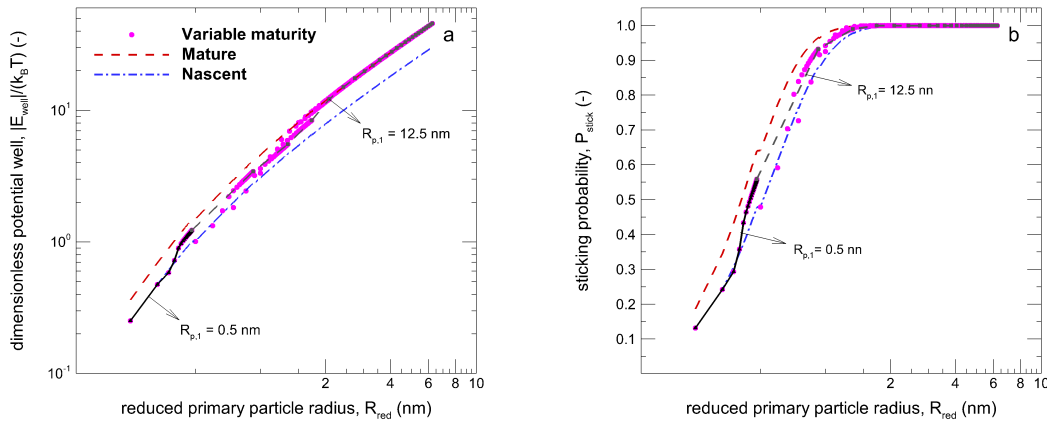
Figure 6.2: Evolution of the potential well (left) in absolute value, and sticking probability (right) as a function of the reduced particle radius $R_{red} = R_{p,1}R_{p,2}/(R_{p,1} + R_{p,2})$. Results obtained for spherical soot particles with zero electric charge and a size ranging between 1 and 25 nm. The particle density and C/H ratio are obtained either in the case of nascent soot, mature soot or variable maturity.

6.3.2.2   Effect of electrostatic forces

The role of electric charges on the interaction between soot particles has been assessed by changing the value of each particle charge between $-6e$ and $+6e$ while keeping all other properties fixed. Experimental determination of soot charge distribution in ethylene premixed flames [369] have reported to be narrow and symmetric within the $-2e$ to $+2e$ range for soot particles with mobility diameter $d_m \approx 13$ nm. As time evolves, this distribution considerably broadens but remains symmetric within the $-4e$ to $+4e$ for $d_m \approx 62$ nm. Indeed, Eq. (6.2.6) shows that the distribution of charges (z_p) is Gaussian distribution whose variance is $\sigma^2 = (d_m k_B T)/(2K_E e^2)$, thus increasing with mobility diameter of the aggregate (see Section S6.4 of the SM A). Based on these measurements, we have opted to consider a range of charges between $-6e$ to $+6e$ to ensure that all possible situations are covered.

In the following, we consider the case of "variable maturity" particles with a fixed particle radius

of 5 nm. Figure. 6.3 displays 2D contours of the energy and probability values (E_{barr}, E_{well}, $\mathcal{P}_{coll}$, $\mathcal{P}_{stick}$) as a function of the elementary charge present in each particle. It can be seen that a range of values can be
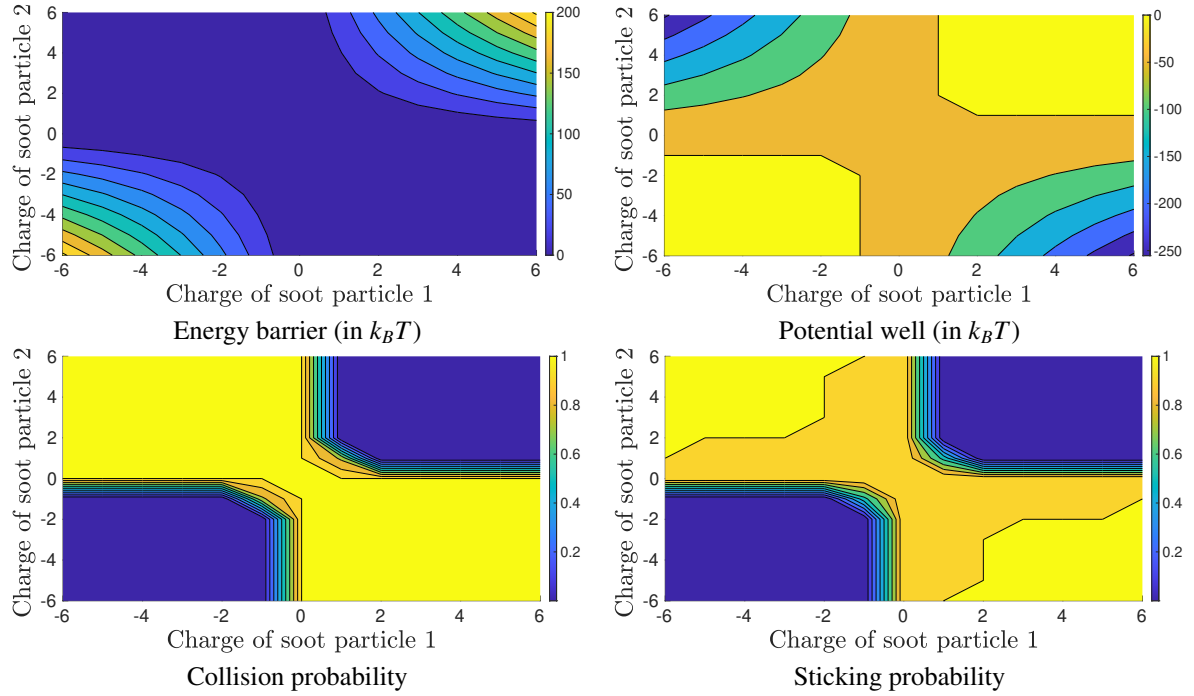
Figure 6.3: 2D plot showing the evolution of ($\widetilde{E_{barr}}$, $\widetilde{E_{well}}$, $\mathcal{P}_{coll}$, $\mathcal{P}_{stick}$) as a function of the electric charge of each particle. Results obtained for spherical soot particles with $R_{p,1} = R_{p,2} = 5$ nm and variable maturity (density and C/H ratio).

obtained depending on the elementary charge present in each particle. In particular, the collision and sticking probabilities are close to 1 only when particles have high but opposite charges. On the contrary, when both particles have a high and similar charges, the collision and sticking probabilities quickly drop to values close to 0.

Due to the symmetry in the effect of particle charges (see also Eq. (6.2.4)), we further analyze the effect of electrostatic charges by plotting the same results as a function of the product of the particle elementary charges $z_{12} = z_{p,1} z_{p,2}$. This is displayed in Figure 6.4. This allows to confirm and quantify the two aspects mentioned before. First, for similarly charged particles, the potential well is close to zero (except for $z_{12} \ll 1$) while the energy barrier increases linearly with z_{12}. As a result, the collision probability (and hence the sticking probability) quickly drops to very small values when the particle charge increases. Second, for oppositely charged particles, no energy barrier occurs (except for $z_{12} \ll 1$) while the depth of the potential well is increased due to the attractive electrostatic force. In that case, both collision and sticking probabilities have values close to 1. Although these results indicate a clear effect of soot maturity and electrostatic forces on the collision probability and sticking probability, it remains to be seen how this affects the actual agglomeration of soot particles. This is done in the next sections where these collision & sticking probabilities are coupled to the MCAC code to simulate the formation and growth of soot aggregates.
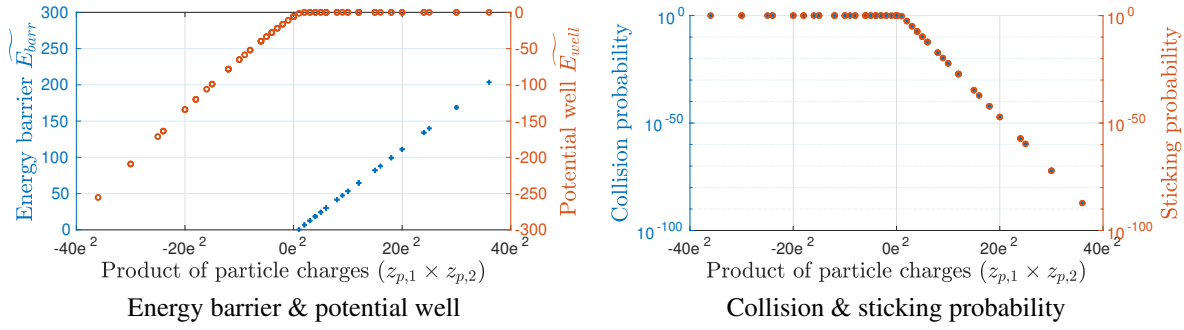
Figure 6.4: Evolution of $(\widetilde{E_{well}}, \widetilde{E_{barr}}, \mathcal{P}_{coll}, \mathcal{P}_{stick})$ as a function of the product of the particle electric charges. Results obtained for spherical soot particles with a size of 5 nm. The particle density and C/H ratio are obtained with variable maturity.

6.3.3   Agglomeration of soot particles

Figure 6.5a presents the time evolution of the inverse particle number concentration $1/N(t)$. The local slope of this curve in log-log correspond to the kinetic exponent z, which indicates how fast aggregation is. The $1/N(t)$ is naturally increasing in time due to irreversible aggregation in the absence of continuous nucleation and fragmentation. All cases show a similar evolution except in the cases of nascent soot particles. Indeed, nascent soot particles have a lower mass bulk density, consequently they move faster and more ballistically. This leads to an enhanced kinetics of aggregation that becomes more evident over time. When comparing the two cases involving nascent soot (no potentials and only LJ), a clearer difference is observed at early residence times. Agglomeration is initially faster for the case without potential which is explained by the larger sticking probability (unity). However, the role played by bulk density seems relatively more important than taking into account of a time evolving sticking probability. This conclusion is reinforced by the comparison with the three remaining cases (mature with and without potentials and variable maturity). This means that considering the change of collision and sticking probability induced by the maturation process have a reduced impact on the aggregation kinetics. This is explained by the fact that d_s is very small, and also by the large surface growth efficiency (SGE) as shown in Section S6.6 of the SM A. This parameter has been introduced in Chapter 5 and quantifies the predominance of surface growth over aggregation to explain soot mass growth. We recall that SGE $\rightarrow \infty$ means that surface growth dominates soot mass growth over aggregation, while SGE $\rightarrow 0$ means the opposite. In this chapter, non-unitary sticking or collision probabilities lead to larger values of SGEs, which is especially evident for early residence times. However at these residence times, the SGE is still high even without considering LJ or electrostatic potentials. The latter is explained by the low nascent soot volume fractions making difficult to observe a big impact on the soot formation process.

However, when analyzing the kinetic exponents z obtained by a power-law fitting $1/N(t) \propto t^z$ for $t \in [23, 35]$ ms, other conclusions can be drawn. First, all the values correspond to aggregation in the transition regime since z is smaller than purely ballistic value ($z \approx 2.2$) and larger than purely diffusive ($z \approx 1$) regimes (see Chapter 4). Second, comparison between different simulations suggest that inclusion of the

van der Waals sticking and electrostatic collision probabilities tends to accelerate agglomeration for large residence times (larger z). Third, comparing both cases involving purely LJ sticking probability reveals that nascent soot tends to agglomerate faster, with a kinetic exponent closer to the one for a purely ballistic regime. Nascent soot without potentials shows the lowest kinetic exponent explained by it faster aggregation at earlier residence times approaching faster to transition regime where kinetic exponent could be as small as $z \approx 0.8$.
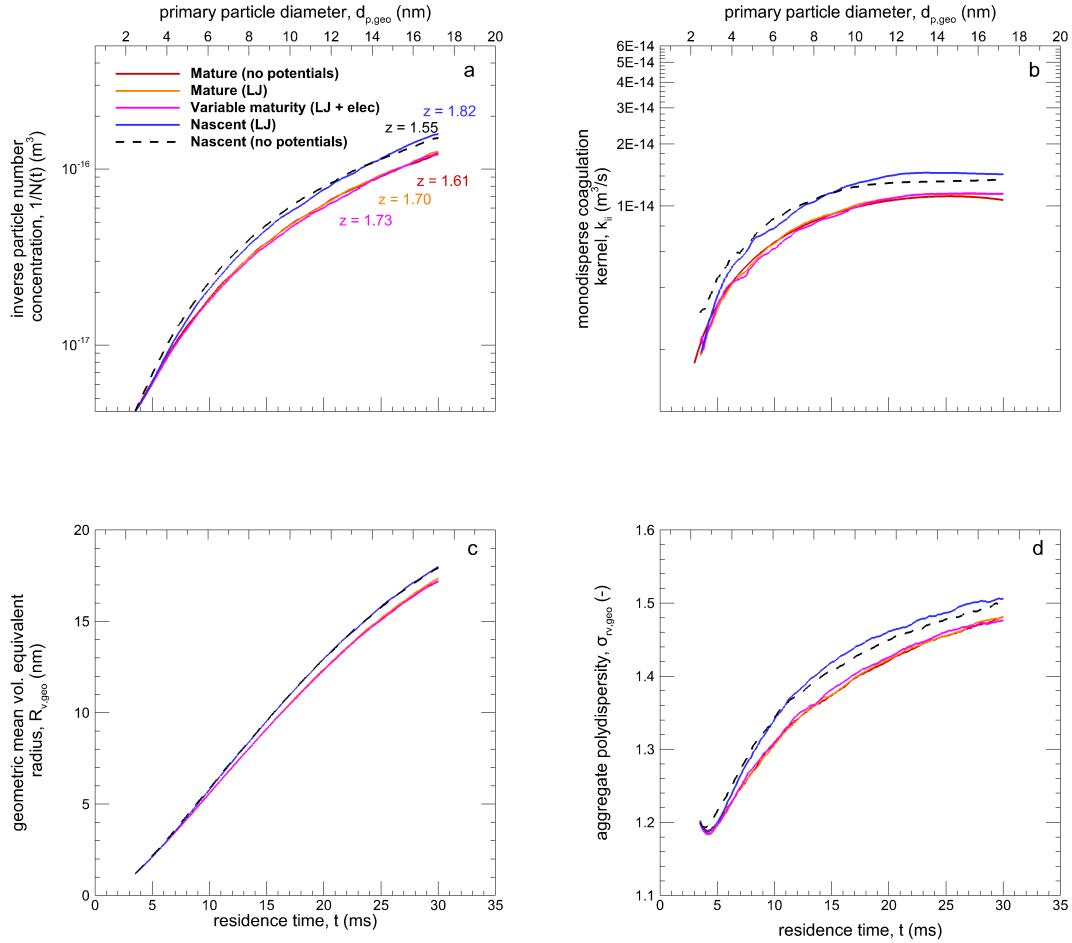
Figure 6.5: Time evolution of the inverse particle number concentration $1/N(t)$, monodisperse equivalent coagulation kernels, geometric mean volume-equivalent radius, and the corresponding geometric standard deviation.

Fig. 6.5b reports the monodisperse equivalent coagulation kernel. This also expresses the agglomeration kinetics but is of great interest for soot modeling in CFD codes since kernels are essential to simulate aggregation by population balance methods. This representation is also complementary since it provides a larger sensitivity to the agglomeration processes at early residence times. Indeed, this highlights the rapid transition from low to high kernels at early residence times $t < 8$ ms (corresponding to $d_{p,geo} < 5$ nm) of the nascent soot composition depending on considering the collision and sticking probabilities or not. For larger residence times, the differences are mainly explained by the particles mass bulk density. Nascent soot

particles coagulate faster due to their more ballistic motion, their larger collision surface and larger particle size polydispersity (see Fig. 6.5d).

The evolution of the geometric mean $R_{v,geo}$ (Fig. 6.5c) and geometric standard deviation $\sigma_{Rv,geo}$ (Fig. 6.5d) of the volume-equivalent radius of aggregates are also evaluated. The $R_{v,geo}$ parameter increases monotonically in time due to aggregation. Nascent soot leads to larger aggregate sizes due to the more efficient aggregation process driven by lower bulk density as discussed above. In turn, the impact of maturation process, sticking probability or electrostatic repulsion is clearly negligible (no significant differences are observed when comparing all the cases related to mature soot). The $\sigma_{Rv,geo}$ reported in (Fig. 6.5d) expresses a more complex trend, in particular at early residence times. At these early residence times the decrease in polydispersity is linked to the dominance of surface growth in the competition with agglomeration (see section Section S6.6 of the SM A), to produce larger soot aggregates [376]. Both cases considering nascent soot all along the simulation are characterized by more ballistic aggregation, consequently leading to larger $\sigma_{Rv,geo}$ for larger residence times, in agreement with the observations reported in Chapter 5.

Table 6.2: Morphological parameters characterizing aggregates sampled at the end of the simulation ($t = 30$ ms). Population fractal dimension (D_{fp}), and prefactor (k_{fp}) as well as average individual packing factor ($\overline{\phi}$) are reported. Error values lead to the 95% confidence intervals.

Case	Population		Individual
	D_{fp}	k_{fp}	$\overline{\phi}$
Mature (no potentials)	1.85 ± 0.01	2.15 ± 0.01	-
Mature (LJ)	1.83 ± 0.01	2.18 ± 0.01	1.57 ± 0.08
Variable maturity (LJ+elec.)	1.82 ± 0.01	2.19 ± 0.01	-
Nascent (LJ)	1.86 ± 0.02	2.19 ± 0.02	1.49 ± 0.10
Nascent (no potentials)	1.83 ± 0.02	2.24 ± 0.02	-

Table 6.2 summarizes the main morphological properties of aggregates sampled at the end of the simulation ($t = 30$ ms). The population-based fractal dimension (D_{fp}) and the corresponding fractal prefactor (k_{fp}) are reported, and further details on their determination are provided in Section S6.7 of the SM A. Overall, both D_{fp} and k_{fp} are very close for all the cases. Notably, the fractal dimension is larger than the one observed for DLCA aggregates $D_f = 1.78$, but smaller than BLCA $D_f = 1.91$ limits. Particularly, k_{fp} are considerably larger than those observed for aggregates formed by pure agglomeration in the absence of surface growth, whose values attain a maximum quite asymptotic limit ~ 1.4 (see Chapter 4). The larger fractal prefactors observed in this chapter are explained by the increase in local compacity due to the overlapping of primary particles and the increase in the coordination number due to surface growth (see Chapter 5). These values seem quite close to those determined experimentally [324, 379, 380]. The population averaged packing factors $\overline{\phi}$ are also reported for the "Mature (LJ)" and "Nascent (LJ)" cases. As explained in Section 6.2.3, they are determined by fitting the pair correlation function for individual aggregates sampled at the end of the simulation ($t = 30$ ms). This parameter is related to the local compacity of primary particles, and has been found to increase with the number of monomers per aggregate. It attains a maximum value between

1 to 1.4 for DLCA aggregates consisting of 10^3 point-touching monodisperse and polydisperse monomers, respectively [377]. Current aggregates contain ~ 100 monomers per aggregate and their packing factor ($\overline{\phi} \approx 1.5$) is larger than those found in the referred work. This is explained by primary particle overlapping (see Chapter 5). These packing factors are in good agreement with the previous chapter where we obtained $\overline{\phi} \approx 1.49$ for large aggregates ($N_p \in [430, 450]$) generated under the same flame conditions. However, no relevant difference is observed in local compacity for the different cases studied.

6.4 Conclusion

A numerical simulation of soot particles aggregation and surface growth is performed by a Monte Carlo Discrete Element Method in a laminar premixed flame. The role played by soot maturity evolution during time is explored by modeling the collision and sticking probabilities as well as the evolution of the primary particle bulk density. The possible impact of the electrostatic repulsion of soot particles has also been investigated. Numerical results showed that both the particle maturity and the electrostatic forces affect the value of the collision and sticking probabilities. One raised questions was the evaluation of a critical primary diameter from which the sticking probability achieves its asymptotic value (unity). We evaluated this critical diameter around $d_s = 10$ nm for mature and nascent soot. However, when coupling these probabilities within the Monte Carlo Aggregation Code, it appears that inter-particle interactions do not considerably influence soot aggregation kinetics, particle size distribution, and morphology. This because the sticking probability of soot particles tends toward 1 in a very short period of time (a few milliseconds) that corresponds to a low collision frequency due to the very low soot volume fraction ($\sim 10^{-3}$ ppm) at this time. Therefore, under the studied conditions, we conclude that the assumption of a sticking probability = 1 is valid all along the soot formation process for soot particles even if the simulation begins with particles as small as $d_p = 2.4$ nm, which is lower than d_s. This tends to neglect the role played by electrostatic forces at short ranges as well as the effect of maturation on the collision and sticking probabilities in the simulation of aggregates formation for example by solving the population balance equation as in Ref. [148]. This also explains why most classical DLCA codes, where a sticking probability = 1 is assumed, succeed to produce fractal-like aggregates quite in good agreement with those measured experimentally under different flames conditions and fuel types [6, 233, 316, 381]. Also, classical RLCA simulations show that a relevant variation in aggregates morphology (at least in terms of the fractal dimension) is found for extremely low sticking probability in the order of 10^{-3} [52, 130, 382] which is far to be representative of soot formation even when soot particles are still nascent.

However, the variation of soot particles bulk density due to maturity evolution in time has been shown to significantly influence the kinetics of agglomeration and thus the related coagulation kernels. Therefore, we recommend to consider the variation of the bulk density from nascent to mature soot in numerical simulations

of nanoparticles formation in flames. This is explained by an increased mobility of the particles having a lower bulk density. Nevertheless, this seems not to have a significant impact on the resulting particles morphology.

7 | CFD → MCAC coupling

7.1 Introduction

It is worth recalling that one of the main objectives of this thesis is to simulate a realistic soot particle morphology evolution under flame conditions. To this end, and based on the developments introduced in previous chapters, MCAC is used. This approach is coupled with CFD simulations solving the flame transport equations and chemical reactions leading to soot formation, growth, and oxidation. One of the main questions we intend to answer here is: can the history of flame temperature and gas-particle mass transfer have a significant impact on soot morphology? is there a morphological signature of soot particles produced along different streamlines of the flame? To answer these questions, ideally, the coupling CFD-MCAC approach needs a CFD simulation based on Lagrangian tracking of soot particles in the flame as proposed by Gallen et al. [383]. Instead, here we propose a post-processing Lagrangian approach based on CoFlame [148] simulations. Section 7.2 describes the target flame. Section 7.3 specifies the details of the numerical simulations, including the coupling strategy, and Lagrangian trajectory data extraction from CoFlame simulations. Section 7.4 presents the results of simulations for 4 selected trajectories. Section 7.5 presents a sensitivity analysis of the key parameters influencing the accuracy of current simulations. Finally, section 7.6 concludes this chapter and suggests some perspectives.

7.2 Target flame

The target flame is an ethylene/air laminar diffusion flame generated in a Gülder burner. This flame is more representative of most industrial combustion systems compared to the premixed flame studied in the previous chapters. This is a convenient flame whose chemical kinetics is validated and has shown good agreement with experiments [218, 297, 384–386]. It is an academic flame with different experimental measurements available in the literature [213]. For instance, it has been experimentally studied recently to accurately determine its temperature, volume fraction, and soot particle maturity based on emission/extinction measurements [242]. It has also been studied to determine soot aggregates gyration diameter, particle number concentration, and

primary particle diameter based on angular light scattering measurements [89].

In Fig. 7.1a and Fig. 7.1b the experimentally measured soot volume fraction (f_v) and flame temperature (T) from Ref. [242] are presented. They were determined by combining line of sight attenuation (LOSA) and emission measurements at different wavelengths. In these figures, a maximum soot volume fraction in the order of 13 ppm is observed in the wings of the flame at a radial position between 2 to 3.5 mm for axial positions $z > 20$ mm. Also, maximum flame temperatures are observed in the wings with values not larger than 1900 K. Please note that this temperature is inferred from soot particles thermal emission and therefore they are not measured in zones where no (or too small concentration) of soot particles exist. In addition, Fig. 7.1c shows experimental laser velocimeter measurements in a similar ethylene/air Santoro diffusion flame [387]. Despite this flame is not exactly the same studied in this chapter in terms of burner dimensions and fluid/oxidizer flow rates, a similar and comparable behavior is expected in current simulations. In this figure the streamlines of the gas flow show a clear trend to bend towards the centerline which is more pronounced for lower z positions. The laminar flow is also verified.
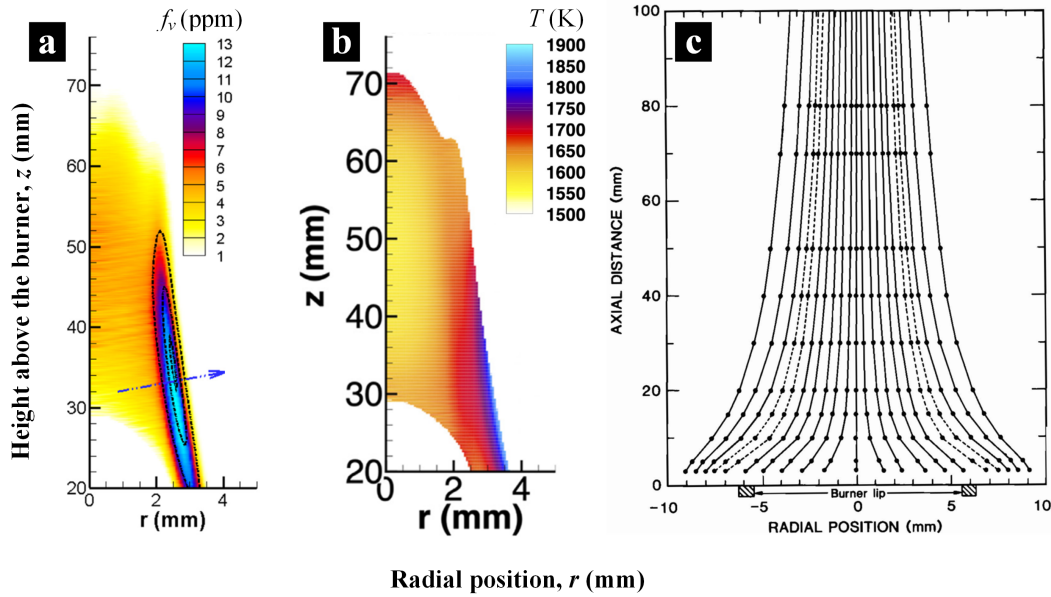
Figure 7.1: Overview of experimental data from similar laminar diffusion flames, (a) soot volume fraction [242], (b) flame temperature [242], and (c) gas flow streamlines [387].

7.3 Numerical simulations

The numerical simulation strategy involves the combination of two different approaches namely, a CFD (continuum/macroscopic) approach where the flame chemistry, fluid dynamics, and simplified particle dynamics are solved, and a DEM (mesoscale) MCAC simulation. Coupling these two approaches allows the

detailed soot particle morphology, agglomeration kinetics, and size distribution to be explored by considering the time evolving flame temperature and gas-particle interactions. The coupling procedure is *one way*, which means that the CFD code will feed the MCAC code without taking feedback from the latter. As discussed later, this is justified by the small size and inertia of soot nanoparticles that are carried by the flow field without disturbing it. This is typically considered in many applications in colloid and aerosol particle dynamics, whose sizes are comparable to soot, as can be seen in the literature [187, 388]. A *two way* coupling may be envisaged for the future in terms of soot contribution to flame radiation, particles morphology, and agglomeration dynamics.

7.3.1 CFD flame simulation

The target laminar diffusion flame (see Fig.7.1) is generated by a Gülder burner, the same studied experimentally in Ref. [89]. The fuel (ethylene) is injected in the central tube (10.9 mm and 12.7 mm inner and external diameters, respectively) at a flow rate 0.194 ln/min, and the oxidizer (21% oxygen and 79% nitrogen mixture) of 90 mm inner diameter coflow tube at a flow rate of 150 ln/min. This flame is simulated by using CoFlame [148] thanks to a collaboration with EC^{2}G group from Chile. This code has been widely used in the literature and validated to study soot formation in premixed [245, 389], and diffusion flames [217, 292] under different fuel and gas compositions. In addition, this code has been recently used to simulate soot formation in an inverse diffusion flame [390]. In this code, the elliptic conservation equations of mass, momentum, energy, and species mass fractions are solved. These equations are solved in a 2-dimensional (radial r and axial z) cylindrical coordinates taking advantage of the flame axisymmetric configuration. The flame chemistry is modeled by using the chemical mechanism developed at the German Aerospace Center (DLR) [391] with the modifications proposed by Dworkin et al. [392]. A 5-ring (A5) PAH model is used to predict soot particles nucleation and condensation. The computational domain extends up to 14.342 cm in the axial, and up to 2.741 cm in the radial direction. This is divided into 202 and 92 non-regularly spaced volume elements in the axial and radial directions, respectively. This mesh is finer near the centerline and near burner exit ($z \rightarrow 0$), symmetric condition is considered at $r = 0$, and free-slip condition and zero gradient condition at the maximum radial and axial positions, respectively [384]. Soot particles modeling is achieved by solving the General Dynamics or Population Balance equation for the aggregate and primary particle number concentration. These equations are solved by a fixed sectional method similar to the one described in Section S4 of the SM A. The primary particle and aggregate size distributions are logarithmically divided into 35 discrete sections each. This equation involves convective, diffusive, and thermophoretic transport as well as soot particle nucleation, coagulation, PAH condensation and HACA surface growth, oxidation, and oxidation-induced fragmentation.

Fig. 7.2a, Fig. 7.2b and Fig. 7.2c present the CoFlame simulated soot volume fraction, flame tempera-

ture, and flow velocity magnitude (and streamlines), respectively. By comparing with the previously shown experimental results we can highlight CoFlame's ability to predict the overall soot particle concentration and temperature gradients within the flame. Also, streamlines ($r < 7$ mm) show a very similar trend to deviate towards the centerline as previously highlighted for experimental measurements (see Fig. 7.1c). However, soot volume fraction is still under-predicted. This is linked to CoFlame's difficulties in simulating surface reactions and nucleation. Flame temperature may be slightly over-predicted and overall shows a good agreement with experiments. These parameters are compared in more details in Section 7.4.1.
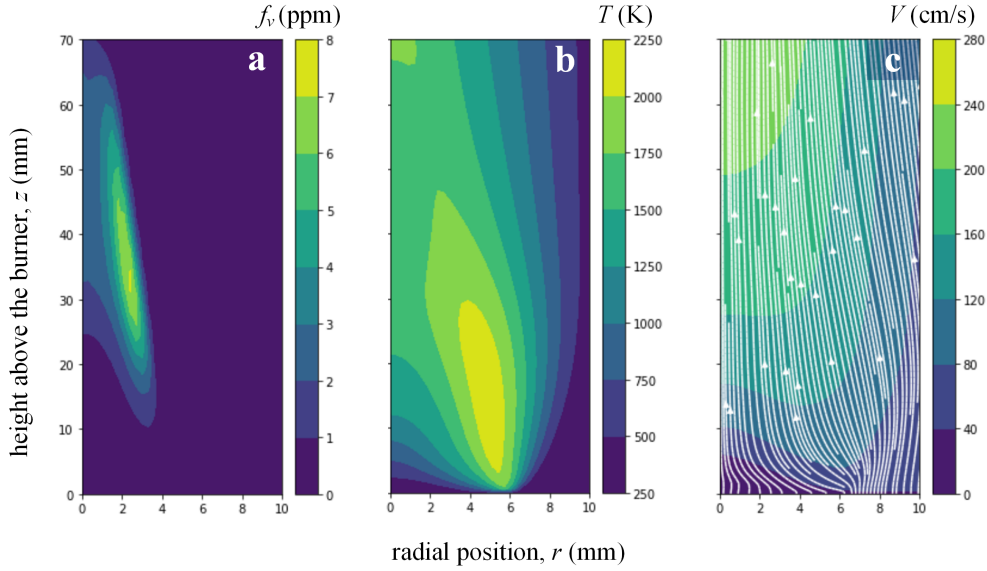
Figure 7.2: Overview of the CoFlame CFD simulated diffusion flame, (a) soot volume fraction, and (b) flame temperature, (c) gas flow velocity field.

7.3.2   Coupling strategy and hypotheses

As explained in Chapter 3, current Monte Carlo DEM simulations rely on CFD simulations. As shown in Fig. 7.3, MCAC input properties are the initial condition and time-dependent properties extracted from the CFD simulation along the selected Lagrangian trajectory of particles. In these simulations, the advective flux of particles through the domain boundaries are neglected because the simulation box is carried by the flow. Thus, soot particle mass evolve due to surface reactions, and nucleation. In this context, the total soot aggregates number concentration N evolution in the simulation box following the Lagrangian trajectory (see Fig. 3.1) can be modeled based on the General Dynamics Equation,

$$\frac{dN}{dt} + \vec{V}_g \nabla \cdot N - D\Delta N = \left.\frac{dN}{dt}\right|_{agg} + \left.\frac{dN}{dt}\right|_{ox} + \left.\frac{dN}{dt}\right|_{nuc} \tag{7.3.1}$$
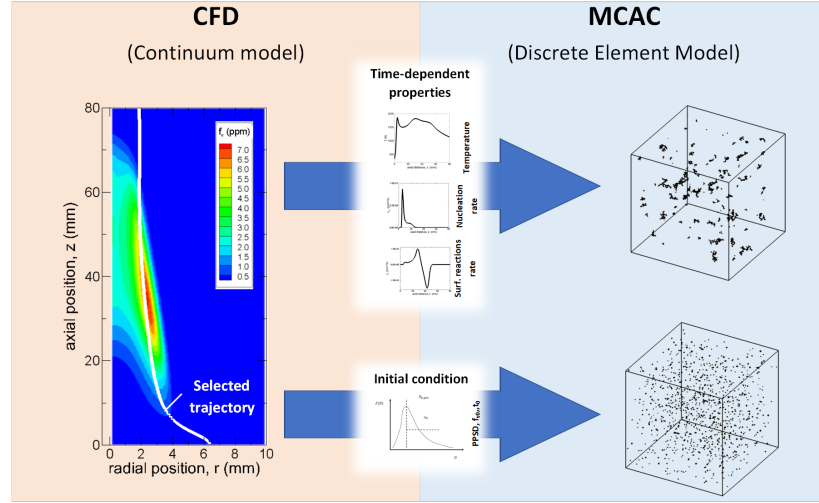
Figure 7.3: CFD→MCAC one-way coupling strategy.

The advective term on the left hand side is neglected since the simulation system is carried by the flow (with equivalent velocity to the gas $\vec{V}_g$) and therefore there is no relative advection. On the right hand side, the mechanisms leading to soot number concentration variation are included i.e., agglomeration (*agg*), oxidation (*ox*), and nucleation (*nuc*), respectively. Please note that surface growth is not included since it only leads to an increase in particles' mass but does not modify the total number of particles in the system. In the same sense, oxidation is included just because we simulate particles with diameters $D_p > D_c$ where D_c is a critical diameter below which the particle behaves as a liquid-like cluster of molecules. So, oxidation leads to delete particles from the system and consequently can reduce N. Under these considerations, Eq. (7.3.1) becomes,

$$\frac{dN}{dt} = D\Delta N + \frac{dN}{dt}\bigg|_{agg} + \frac{dN}{dt}\bigg|_{ox} + \frac{dN}{dt}\bigg|_{nuc} \tag{7.3.2}$$

By focusing only on the contribution of the 2 first terms on the right hand side (i.e., diffusion and agglomeration) and considering the dimensionless parameters $\tilde{N} = N/N_0$, $\tilde{t} = t/t_0$, and $\tilde{x} = x/x_0$. Considering also that agglomeration follows a power-law $1/N(t) \propto t^{\tilde{z}}$ in time, where $\tilde{z}$ is the kinetic exponent. Replacing in Eq. (7.3.2) becomes,

$$\frac{1}{\tilde{z}}\frac{d\tilde{N}}{d\tilde{t}} = D\frac{t_0}{\tilde{z}x_0^2}\Delta\tilde{N} + \frac{\tilde{N}}{\tilde{t}}(1 - \tilde{N}) \tag{7.3.3}$$

Therefore, the predominance of agglomeration over diffusion happens when $Dt_0/(\tilde{z}x_0^2) \ll 1$. As has been discussed in previous chapters $\tilde{z}$ is within the 0.8 to 2.2 range. Indeed, for soot particles generated in flames ($x_0 \sim 60$ mm, and $t_0 \sim 50$ ms) whose size is in the nanometer range and mobility depends on the flame temperature we can verify $Dt_0/x_0^2 \ll 1$. In particular, for the simulations conducted in this chapter, the contribution of diffusion to all mechanisms in Eq. (7.3.2) is lower than 0.05%. Based on this analysis, not only advective net flux of particles through the box boundaries can be neglected but also diffusive. Therefore, each simulations has only to deal with nucleation, agglomeration, surface growth, and oxidation

mechanisms.

7.3.3   Lagrangian trajectory

Based on the CFD macroscopic simulation of the flame, a post-processing data extraction procedure along a Lagrangian trajectory is proposed. The idea is to find the path within the flame that soot particles follow. To this end, the 2nd Newton law of linear momentum conservation for individual tracers particles is solved numerically,

$$m_p \frac{d\vec{V}_p}{dt} = \vec{F}_b + \vec{F}_d + \vec{F}_t + \vec{F}_g + \vec{F}_l \tag{7.3.4}$$

where m_p and $\vec{V}_p$ are the particle's mass and velocity vector, respectively. Also, $\vec{F}_b$, $\vec{F}_d$, $\vec{F}_t$, $\vec{F}_g$, and $\vec{F}_l$ are the Brownian, drag, thermophoretic, gravitational, and lift or buoyancy forces. Since we are interested in an average macroscopic trajectory of soot particles within the flame, the Brownian force can be neglected (average is 0 at a macroscopic scale), this because the particle persistent distance is much smaller than the characteristic size of the simulation box (see Chapter 4). The gravitational and buoyancy can be neglected due to soot nanoparticles negligible mass. The latter becomes relevant for particle's size in the micrometer scale which is far larger than typical soot particles found in flames. Under these considerations, Eq. (7.3.4) reduces to,

$$m_p \frac{d\vec{V}_p}{dt} = \vec{F}_d + \vec{F}_t \tag{7.3.5}$$

In addition, drag and thermophoretic forces are calculated as follows [393],

$$\vec{F}_d = f(\vec{V}_g - \vec{V}_p) = \frac{3\pi\eta d_m}{C_c(d_m)}(\vec{V}_g - \vec{V}_p) \tag{7.3.6a}$$

$$\vec{F}_t = -0.5\pi \frac{\eta^2 d_m^2}{\rho_g \lambda_g} \frac{\vec{\nabla}T}{T} \tag{7.3.6b}$$

where λ_g and ρ_g are the mean free path and bulk density of the surrounding gas. This is a simplified calculation considering tracers soot particles to be spherical, with a mobility diameter d_m and thermophoretic force assumed in the free molecular flow regime ($d_m << 2\lambda_g$). Thermophoretic force has not been properly adapted to aggregates in the literature [394, 395] and therefore Eq. (7.3.6b) should be interpreted as an approximation.

Fig. 7.4a reports the four trajectories studied here, being representative soot particles along the centerline (red line), two intermediate paths (orange and pink), and the wings (black line) of the flame. As observed in this figure, the wings trajectory is selected for traversing the zone where the maximum local soot volume fraction is found in CoFlame simulations. Since the flame is axisymmetric, there is negligible uncertainty related to thermophoretic force along the centerline, however for the intermediates and wing trajectories a sensible horizontal displacement was observed in the trajectory (this is only reported in
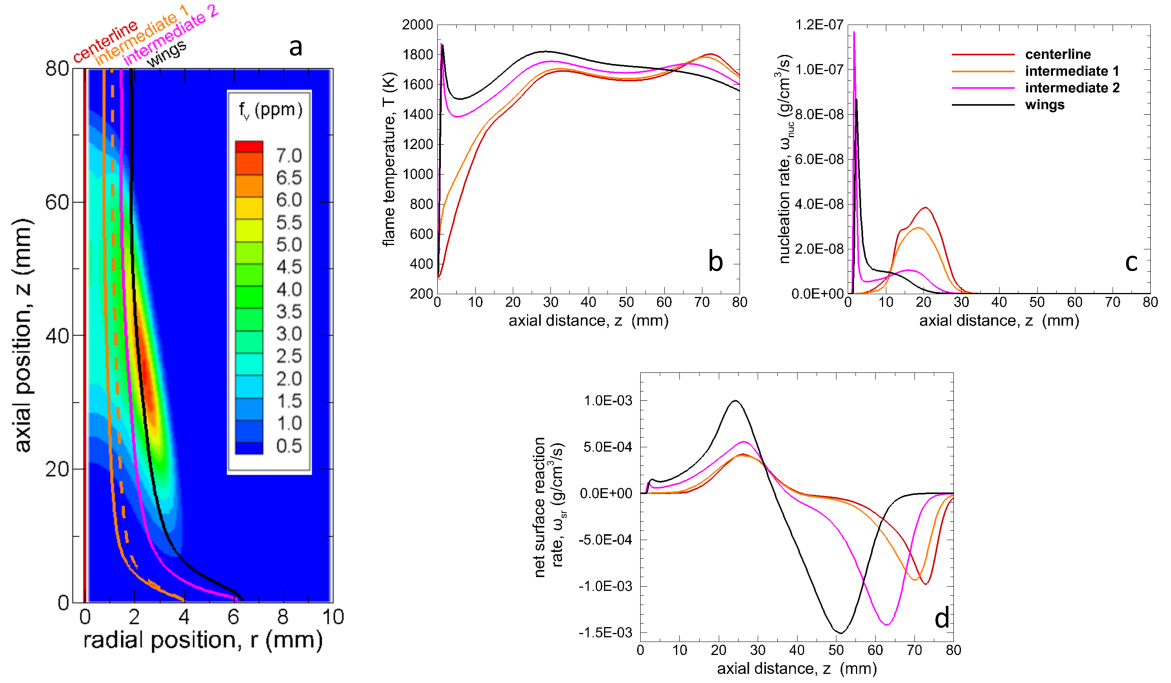
Figure 7.4: Lagrangian trajectories and the corresponding relevant input parameters for MCAC simulations. Continuous lines correspond to values determined considering thermophoretic force and dashed lines without considering it (only shown for trajectory intermediate 1).

dashed line for the case intermediate 1 in this figure). This deviation is specially relevant for the trajectory intermediate 1 reaching a maximum of $\Delta r = -0.3$ mm from the one neglecting thermophoresis, while wings trajectory deviates in maximum of $\Delta r = -0.1$ mm in the zones where a relevant soot volume fraction exist ($f_v > 0.2$ ppm). Despite the deviation in the trajectory due to thermophoresis may seem "small", it may become very important in this flame where strong temperature and particle concentration gradients are observed. Fig. 7.4b to Fig. 7.4d report the time-dependent input parameters for MCAC simulations for the four selected trajectories. These parameters correspond to the flame temperature, nucleation, and surface reactions mass rates (PAH condensation, HACA surface growth, and oxidation), respectively. In the following section the MCAC initial condition and processing of these time-dependent input parameters is explained.

7.3.4 MCAC input parameters and processing

7.3.4.1 Initial conditions

Setting up MCAC simulations involves determining the size of the simulation box according to an initial volume fraction ($f_{v,0}$), primary particle size distribution ($D_{p,0}$ and $\sigma_{Dp0,geo}$), and total number of monomers (1024 for all simulations). Once the size of the box is determined, the initial number of spherical primary

particles are randomly placed in the simulation domain (see chapter 3). This means that an initial time of coupling between MCAC and CoFlame simulations has to be selected. This initial coupling time (t_0), the corresponding axial position (z_0), and all the aforementioned parameters are reported in Table 7.1 for the 4 selected trajectories. These initial conditions are selected based on two criteria, namely (1) the minimum f_v that CoFlame can accurately simulate, (2) primary particle diameter is approximately equal or larger than the critical coalescence one $D_c \sim 5$ nm. The polydispersity of primary particles ($\sigma_{Dp0,geo}$) is assumed to be representative of values found in experiments [96].

Table 7.1: Initial condition for CoFlame→MCAC coupling simulations.

Case	z_0 (mm)	t_0 (ms)	$f_{v,0}$ (ppm)	$D_{p,0}$ (nm)	$\sigma_{Dp0,geo}$ (-)
centerline	2.75	86.1	0.0020	5.8	1.2
intermediate 1	0.77	6.4	0.0077	5.5	1.2
intermediate 2	1.64	7.4	0.0174	5.1	1.2
wings	1.92	5.4	0.0134	4.8	1.2

7.3.4.2   Time-dependent properties

MCAC simulates the dynamics of non-coalescing soot primary particles whose diameter is $D_p > D_c$ where D_c is the coalescence critical diameter as introduced in Chapter 6. Below this diameter, soot particles behave as molecular clusters and their dynamics are beyond the scope of this thesis. The interested reader on primary particle formation may refer to [222, 230, 334]. The total surface reactions $\dot{\omega}_{sr}$ and nucleation mass flux $\dot{\omega}_{nuc}$ in kg-soot/m^3-flame/s, determined by the macroscopic CFD simulations are used as input for MCAC simulations. The surface reactions mass flux, for particles with $D_p > D_c$ reads as,

$$\dot{\omega}_{sr} = \dot{\omega}_{HACA} + \dot{\omega}_{Condensation} + \dot{\omega}_{Oxidation} \qquad (7.3.7)$$

where $\dot{\omega}_{HACA} > 0$, $\dot{\omega}_{Condensation} > 0$, and $\dot{\omega}_{Oxidation} < 0$ are the HACA surface growth, condensation, and oxidation (by both OH and O$_2$) mass flux. In addition, considering the surface reaction rate as $u_{sr} = dR_p/dt$ where R_p is the primary particle radius. Therefore, the surface reaction rate can be determined as,

$$u_{sr} = \frac{1}{\rho_p S}(\dot{\omega}_{HACA} + \dot{\omega}_{Condensation} + \dot{\omega}_{Oxidation}) \qquad (7.3.8)$$

where S is the total exposed surface area concentration (m^2−soot/m^3−flame) of soot particles. This surface area is determined by considering the overlapping between primary particles at each time step in MCAC simulations according to the approach described in section 5.2.3. Therefore, the increase (by HACA or condensation) or decrease (by oxidation) in primary particle radius during a simulation time step Δt is determined as $R_p(t + \Delta t) = R_p(t) + u_{sr}\Delta t$. Oxidation is simulated as explained in Chapter 5.

On the other hand, knowing the average mass of nucleated particles m_{nuc} with diameter D_c, and the

nucleation mass flux $\dot{\omega}_{nuc}$, the increase in the total primary particle number concentration is determined as,

$$\frac{dN}{dt} = \frac{1}{m_{nuc}}\dot{\omega}_{nuc} \tag{7.3.9}$$

### 7.3.4.3   MCAC simulations and sampling

Finally, for each selected trajectory, a total of 10 MCAC simulations are carried out and results presented in the following sections correspond to the average over these 10 simulations for each case. All the simulations start with a total of 1024 primary particles under the conditions described in section 7.3.4.1. Nucleated particles are monodisperse with a diameter $D_p = D_c = 5$ nm, and mass $m_{nuc} = 1.243 \cdot 10^{-22}$ kg. This critical diameter D_c is not clearly established in the literature and values between 5 to 10 nm have been previously considered [215]. Individual surface reactions scheme is considered (see Chapter 5) and particle volume and surface area are updated at each Monte Carlo iteration according to the corrections to volume and surface are introduced in section 5.2.3. At each time iteration, the flame temperature (and thus the particle's mobility), nucleation, and surface reaction rates are updated according to the parameters given by CoFlame simulations as described in in section 7.3.4.2. As concluded in Chapter 6, the time-evolving maturity of soot may influence the particle's formation dynamics mainly through the evolution of ρ_p. However, at this moment CoFlame simulations are not adapted to soot maturity evolution. Therefore, they are considered mature with a bulk density $\rho_p = 1.9$ g/cm^3 all along their trajectory in the flame. Also, soot electric charges are not taken into account. Both collision and sticking probabilities are assumed unitary (see Chapter 6). Simulations end when all the particles have disappeared from the simulation domain due to oxidation. Simulations are sampled from a minimum axial position (also called height above the burner) ranging from $z = 10$ up to $z = 70$ mm with 10 mm spacing between consecutive sampling locations. This allows a direct comparison with available experimental measurements to be carried out.

7.4   Results

7.4.1   Flame temperature and soot volume fraction

Fig. 7.5a and Fig. 7.5b show the flame temperature and soot volume fraction for the different simulated trajectories (dashed lines+symbol) as compared with the available experimental measurements (continuous lines) [242]. Flame temperatures are quite in good agreement with experiments for the different streamlines regarding trends and absolute values. The agreement seems better close to the centerline (uncertainty < 5%). On the other hand, as observed before, soot volume fractions are underpredicted by CoFlame simulations and therefore by current MCAC simulations. As surface reactions in MCAC are simulated based on the surface area of aggregates considering the overlapping of primary particles, which is lower than considering

primary particles to be point-touching as done in CoFlame, even lower volume fractions are observed in MCAC simulations (please see the Section S7.1 of the SM A for further details).

(a) Temperature   (b) Volume fraction
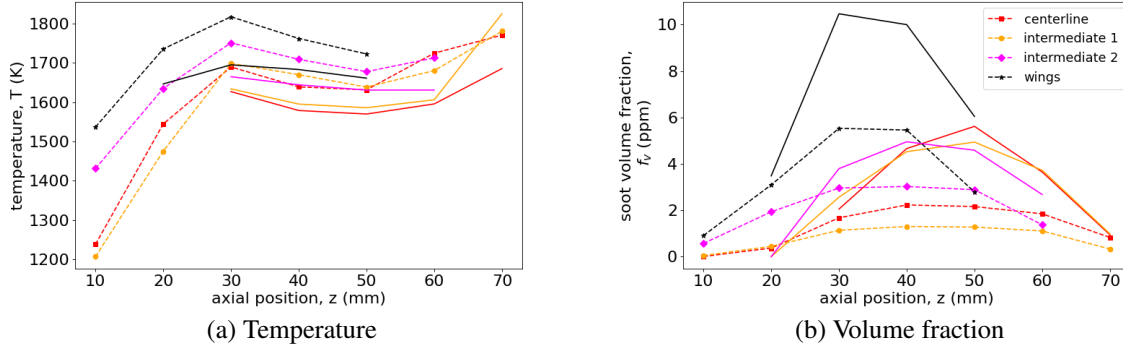
Figure 7.5: Comparison of flame temperature and soot volume fraction between simulations (dashed lines with symbols) and experimental data (continuous lines) from Ref. [242].

7.4.2 Soot particle number concentration

Soot aggregates number concentration as a function of z is shown in Fig. 7.6. For lower axial positions it is decreasing as a function of z due to the predominance of aggregation over primary particle nucleation until attaining a minimum value at z between 30 to 40 mm. The steepest decreases are observed in the wings and intermediate 2 trajectories where aggregation is more effective than nucleation due to the larger volume fractions (see Fig. 7.5b) compared to other trajectories. For larger axial positions it is increasing due to the aggregates fragmentation induced by oxidation. The steepest increases are also observed for the trajectories close to the wings due to the stronger oxidation rates as observed in Fig. 7.4d. Soot aggregate number concentrations are in the same order of magnitude as those experimentally measured [89]. In addition, Puri et al. [275] experimentally observed a continuous decrease in particle number concentration (measured by light scattering/extinction) in a similar ethylene flame, spanning residence times from 25 to 66 ms (corresponding to 10 to 70 mm in z) along the path of maximum f_v. According to their measurements, oxidation started at 50 ms and did not observed an increase in $N(t)$ i.e., did not observed oxidation-induced fragmentation. However, soot fragmentation has been observed in premixed flames under lean conditions and not observed under flame rich conditions [396]. In addition, real-time Environmental TEM observations reveal that oxidation can effectively lead to soot fragmentation [397, 398]. Therefore, we think that the increase of $N(t)$ due to oxidation has a physical meaning in current simulations.
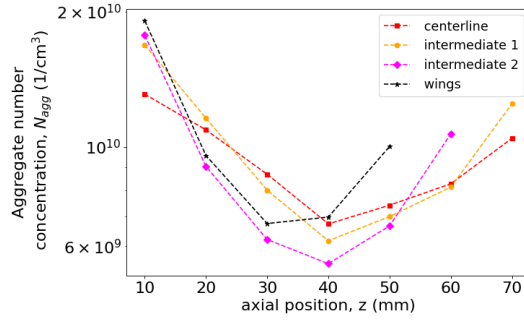
Figure 7.6: The evolution of the aggregate number concentration.

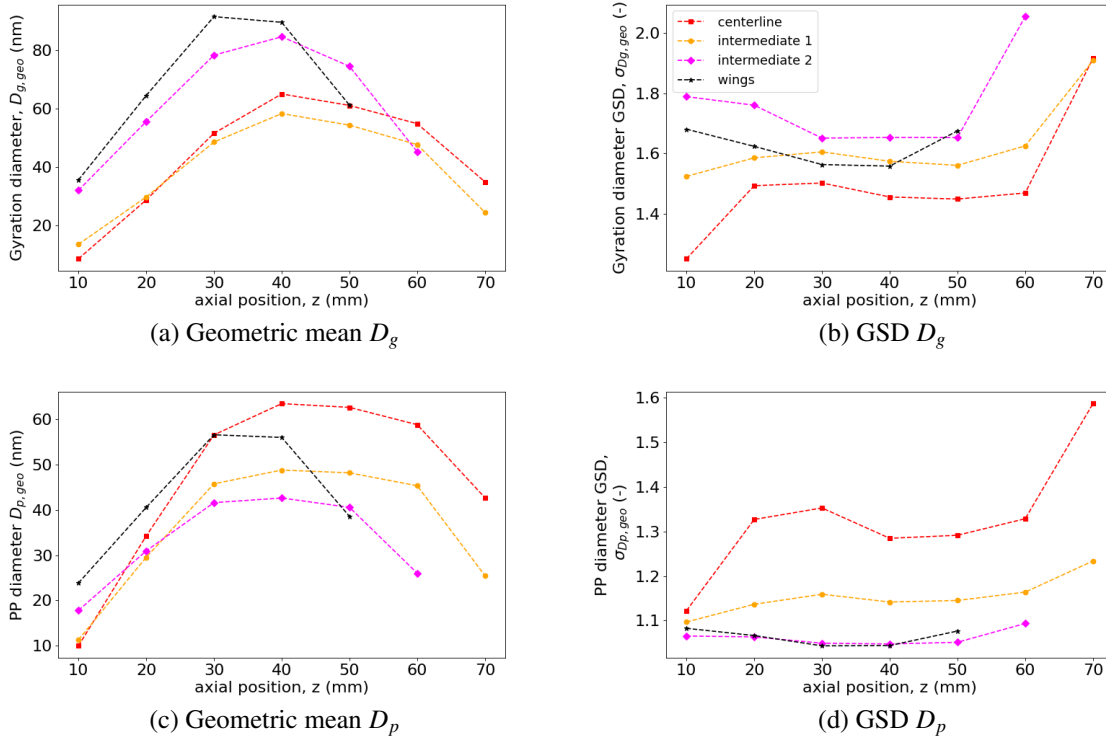### 7.4.3 Soot aggregates and primary particles size distribution

The moment D_f average gyration diameter $\widetilde{D_g} = \left(\overline{D_g^{D_f}}\right)^{1/D_f}$ as introduced in section 4.3.4 is reported in Fig. 7.7 and compared to available experimental data [89]. For a consistent comparison with Yon et al. [89] experiments, a constant fractal dimension of 1.77 is used to determine $\widetilde{D_g}$ from current simulations. The D_g of individual aggregates are determined based on Eq. (2.1.12). Subsequently $\widetilde{D_g}$ is determined based on the population of aggregates simulated. This figure shows much larger soot aggregates in the trajectories closer to the wings with values above 100 nm which is in good agreement with the available experimental values, specially for lower axial positions. However, for $z = 50$ mm, the experimental values are much larger (by a factor between 1.5 to 2) than those numerically simulated here. This is expected to be related to CoFlame underestimation of soot volume fraction as previously observed in Fig. 7.5b. Figure 7.8a and
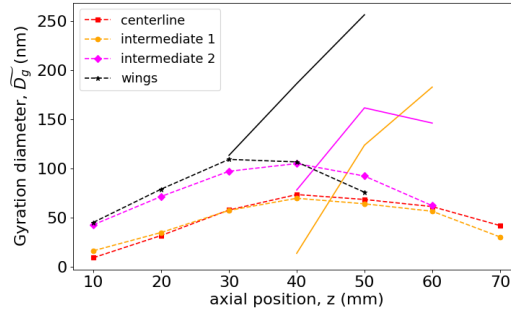
Figure 7.7: Moment D_f average gyration diameter comparison between simulations (dashed lines with symbols) and experiments (continuous lines).

Fig. 7.8b report the geometric mean and geometric standard deviation gyration diameter. Firstly, the lower magnitude of $D_{g,geo}$ compared to $\widetilde{D_g}$ is observed. This is normal, and is related to the definition of each parameter. Secondly, this figure suggests the presence of slightly larger aggregates in the centerline compared to intermediate 1 trajectory for $z > 20$ mm. This may be surprising, however Fig. 7.4b, c and d suggest larger temperature, and nucleation peak for the centerline compared to the intermediate 1 trajectory. Also, similar

maximum surface growth rates are observed for both trajectories. The polydispersity level characterized by $\sigma_{Dg,geo}$ remained between 1.4 and 1.8 during most part of the simulations, excepting when approaching to the oxidation zones where these values may be even larger than 1.8 for most cases excepting the wings trajectory. The largest values were observed along the intermediate 2 trajectory. All these $\sigma_{Dg,geo}$ values are smaller than those experimentally measured by TEM image analysis by Cortés et al. [6] who obtained $\sigma_{Dg,geo} = 2.9$ at $z = 27$ mm (centerline) under similar flame conditions. Also, Caumont-Prim et al. [311] obtained $\sigma_{Dg,geo}$ between 2.0 to 2.2 for soot particles from an ethylene diffusion flame whose $D_{g,geo}$ is within 149 and 93 nm, respectively based on TEM image analysis. This discrepancy may be explained by the overestimation of $D_{g,geo}$ deduced from TEM image analysis that is typically based on the maximum projected diameter which has larger polydispersity than gyration diameter.

(a) Geometric mean D_g

(b) GSD D_g

(c) Geometric mean D_p

(d) GSD D_p

Figure 7.8: Soot aggregates size distribution in terms of the geometric mean and geometric standard deviation (GSD) gyration diameter (Figs. a-b) and primary particle (PP) diameter (Figs. c-d).

Figure 7.8c and Fig. 7.8d report the geometric mean $D_{p,geo}$ and geometric standard deviation $\sigma_{Dp,geo}$ of the primary particle diameter. The $D_{p,geo}$ exhibits values between 10 and 60 nm and these values are increasing in the surface growth zone and decreasing in the oxidation zones of each trajectory (cf. Fig. 7.4d). Primary particle diameters evolution along the centerline seem in good qualitative agreement with Chu et al. [399] who observed values between 20 to 40 nm, reaching a maximum at $z = 30$ mm under a similar flame conditions. Excepting the centerline, all the $\sigma_{Dp,geo}$ remained below 1.3. As observed in Chapter 5, this value decreases with surface growth, but increases with both nucleation and oxidation. The largest values were

observed along the centerline of the flame and are due to more important nucleation (integrated in time), and also because nucleation arrives much later along this trajectory as compared to other cases. A complementary simulation (not reported here) of this case without considering nucleation in time revealed that this increase in polydispersity along the centerline is indeed mainly due to nucleation. In addition, primary particle polydispersity increases with oxidation, which is consistent with the experimental observations [354].

7.4.4 The evolution of soot morphology

7.4.4.1 Numerical TEM images

Fig. 7.9a shows the 7 selected sampling points in the flame along the 4 different trajectories simulated here. Soot volume fractions as simulated by CoFlame are shown in color as a reference. On the right hand side of this figure, some numerical Transmission Electron Microscopy images (nTEM) are shown. These nTEM images are obtained based on a sample population of aggregates (randomly selected) at each axial position. All the images have a size of 1024×1024 pix^2 and the same scale (pix/nm) as indicated in the figure. The surface coverage of each image is selected proportional to the local volume fraction and variates between 0.05 to 0.20, these are typical experimental target values [88]. The positions of aggregates in the image are randomly selected avoiding apparent 2d overlapping between aggregates. This means that the distance between aggregates in these images are not representative of the simulation and the size of the image is not related to the size of the simulation box. This figure intends to qualitatively illustrate the morphological aspect of particles formed under different trajectories in the flame when compared at equivalent axial positions as usually done when analyzing experimental TEM images [399–402]. Despite the figure of soot volume fraction field on the left hand side shows values below 1 ppm at $z = 10$ mm for the different trajectories, it is remarkable to observe the particles that are already present as observed on the nTEM images and indeed, specially for intermediate 2 and wing trajectories, some relatively large aggregates can already be observed. This is due to the earlier nucleation peak found for these trajectories as already observed in Fig. 7.4c. When observing the evolution of nTEM along the same trajectory, the different steps of soot formation can be verified including soot production for lower z, agglomeration is observed when increasing in z axis and finally, in the last images of each trajectory, a considerable reduction in both primary particle and aggregate size are observed. This is due to oxidation and consequent fragmentation. Smaller and more spherical particles are observed along the centerline and intermediate 1 trajectories. On the opposite, much larger and irregularly shaped aggregates can be observed in intermediate 2 and wings trajectories. Finally, as has been previously observed in experiments, large primary particles are observed in the presence of very small ones (even within the same aggregate) which in current simulations is attributed to the monomer nucleation profile for each case. Close observation to aggregates also reveals their complex morphology, the degree of monomers overlapping, and how challenging would be their identification for automated algorithms [77].
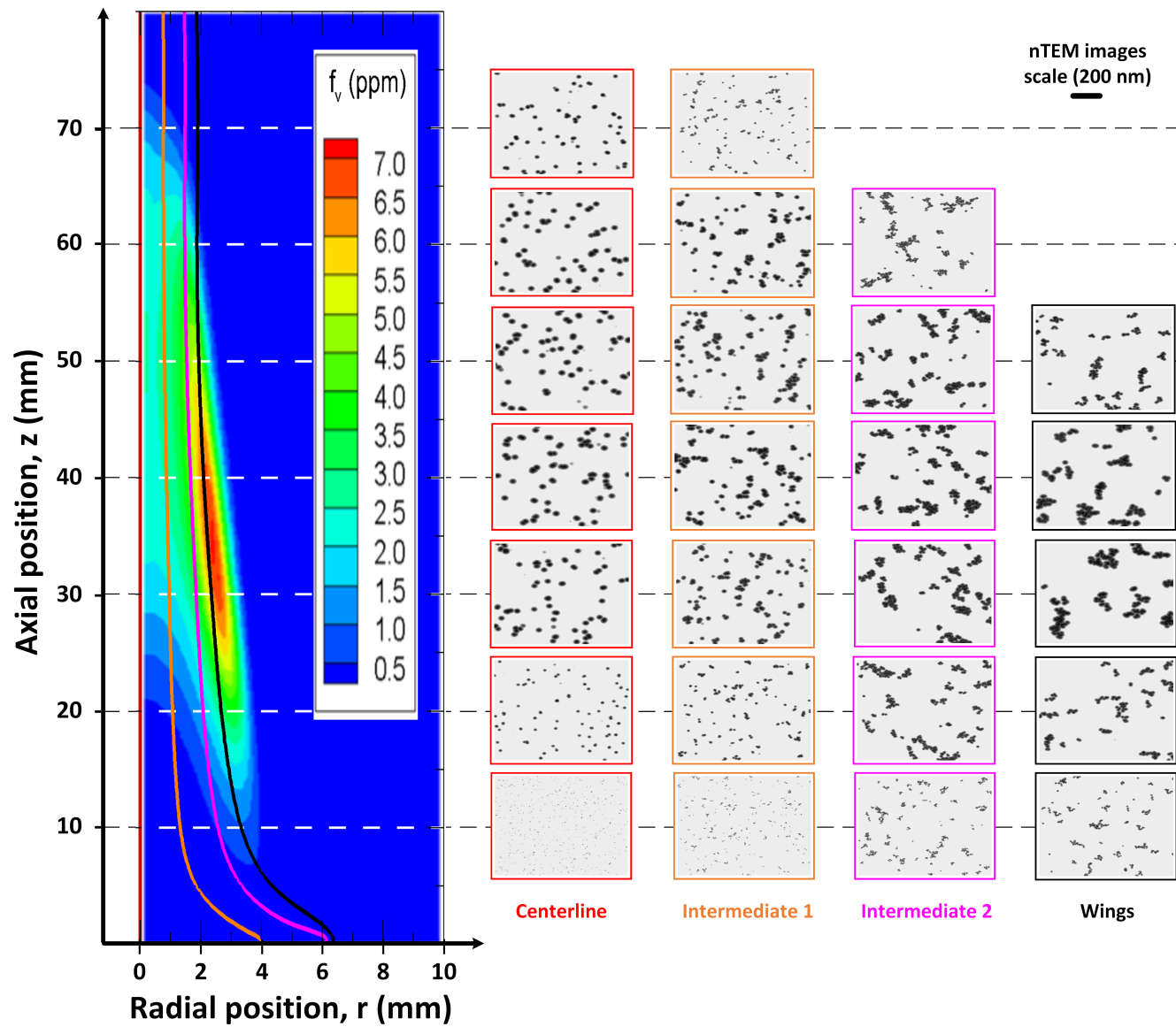
Figure 7.9: nTEM images for the selected trajectories.

7.4.4.2 Population morphological parameters

Fig. 7.10a, b, and c show the evolution of the population mean coordination number, overlapping coefficient, and anisotropy coefficient, respectively. The evolution of both primary particle coordination number and overlapping coefficient seem to be correlated to surface growth and oxidation zones. As previously observed in chapter 5, the mean coordination number is increasing due to both aggregation and surface growth and values larger than 2 are purely explained by surface growth. The latter is an essential parameter to which $\overline{n_c}$ is highly sensitive. The largest $\overline{N_p}$ are observed along the intermediate 2 trajectory explaining why this case attains the largest $\overline{n_c}$ observed in these simulations. The $\overline{n_c}$ seems to be increasing in the surface growth zones and decreasing in the oxidation (fragmentation) zones of each trajectory. Population average primary particle

(a) Coordination number

(b) Overlapping coefficient
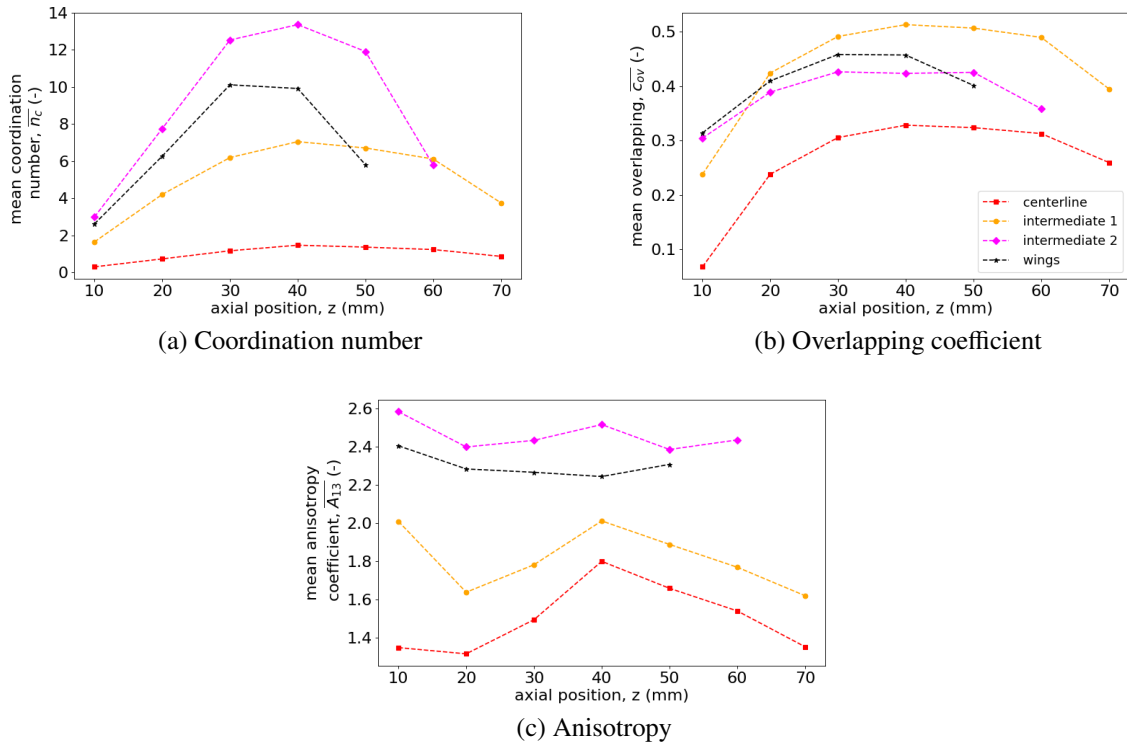
(c) Anisotropy

Figure 7.10: Soot aggregates morphological parameters including the mean coordination number, overlapping, and anisotropy coefficient.

overlapping $\overline{c_{ov}}$ is increasing due to surface growth but attains a maximum value due to the competition with aggregation. Then it decreases due to oxidation. In the centerline of the flame it does not exceed 30% however, close to the wings it attains values as high as 50%. Mean anisotropy coefficient, determined as the ratio of the largest and smaller squared eigenvalues of the aggregate's inertia matrix, shows a clear difference in morphology between those aggregates formed closer to the centerline or closer to the wings. This may be related to aggregate's size, indeed $A_{13} = 1$ for isolated spheres is verified, while A_{13} as large as 16 or even 19 may be observed for very elongated aggregates (see chapter 5). This explains why the wings and intermediate

2 trajectories exhibit larger $\overline{A_{13}}$ compared to other trajectories. It also explains why for $z \geq 20$ it is increasing in the surface growth/aggregation part and decreasing in the oxidation zone. However, in the same range of axial positions, the intermediate 2 and wings trajectories $\overline{A_{13}}$ remains approximately constant.

(a) Fractal dimension   (b) Fractal prefactor
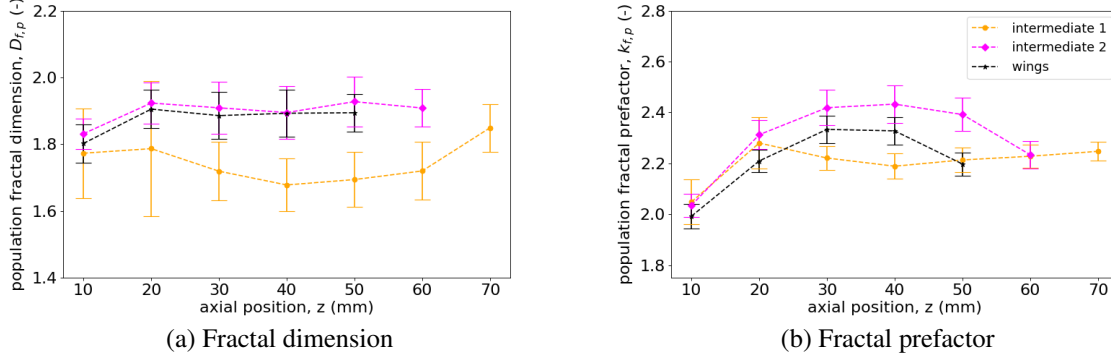
Figure 7.11: Population fractal dimension ($D_{f,p}$) and fractal prefactor ($k_{f,p}$) evolution ($N_{p,\text{eff}} > 3$). Error bars represent the 95% confidence intervals.

Fig. 7.11a and Fig. 7.11b report the population fractal dimension and prefactor, respectively. They are determined by fitting the fractal-law based on the effective number of primary particles per aggregate $N_{p,\text{eff}} = \alpha_v \cdot N_p$ as a function of the normalized radius of gyration by the volume-equivalent primary particle radius R_g/R_{pv}, where R_g is accurately determined by discretizing the 3d structure of the aggregates (see chapter 6). Here, it is very important to consider that $V_p = (4\pi/3)R_{pv}^3$ is obtained considering $V_p = (1/N_p)\sum_{j=1}^{N_p}(4\pi/3)R_{p,j}^3$, where $R_{p,j}$ is the radius of the j'th primary sphere. These fractal parameters are obtained by setting $N_{p,\text{eff}} > 3$. Indeed, when omitting this limit, larger fractal dimensions and lower prefactors are obtained. Fractal dimension shows different morphologies for the trajectories close to the centerline compared to those close to the wings of the flame. Less compact aggregates seem to exist near the centerline with a fractal dimension closer to 1.4 which is the limit for aggregates whose $N_{p,\text{eff}} \to 3$, showing a high degree of uncertainty due to the small aggregates observed along this trajectory. On the other hand, for intermediate 2 and wings trajectories show fractal dimensions remaining almost constant (for $z > 10$ mm) around 1.9. Fractal prefactors are between 2 and 2.6 for almost all trajectories. These values seem to be associated to the comparable size between aggregates as compared to primary spheres that are naturally more compact. The larger $k_{f,p}$ values observed for intermediate 2 trajectory compared to other trajectories suggests that these aggregates may have a larger local compacity which is consistent with results shown in Fig. 7.10. Both fractal dimension and fractal prefactor are in good agreement with experimental measurements based on TEM image analysis where $k_{f,p} \approx 2.2$ and $D_f \approx 1.75$ have been measured in ethylene diffusion flames [6, 77]. Finally, it is worth mentioning that population-based morphological parameters tend to lose information about the variety of particles studied and may be biased by different mechanisms, for example population fractal dimension can be deviated by soot nucleation. Consequently, in order to have a closer look to the actual morphology of the particles studied in this chapter, individual morphological analysis is reported in the

following section.

7.4.4.3 Individual fractal dimension, and packing factor

As discussed in previous chapters, individual fractal dimension and packing factor can be obtained by fitting a model for the pair correlation function of individual aggregates. However, this procedure is challenging due to the large number of parameters searched (6 in total). For this reason, for example in chapters 5 and 6 a fit-by-part procedure was proposed. This procedure is tedious, and showed difficulty to find aggregate's fractal dimension due to the difficulty of small aggregates to show an established fractal domain in $A(r)$. For instance, we may try to overcome this problem by fitting aggregates with a large number of monomers however, due to the high degree of primary particle overlapping due to surface growth, their size is in competition with aggregate's size itself (see Section 5.4.7) which makes difficult to observe a clear fractal regime of aggregates. Consequently, in this chapter a new method to determine the fractal dimension of aggregates is introduced. This method is thoroughly described and validated in Section S7.4 of the SM A and briefly explained here. It consists in fitting Eq. 2.1.7 in log-log based on the radial evolution of the normalized aggregate's volume ($N_{p,eff}(r) = V(r)/V_p$) averaged over all the monomers belonging to the aggregate and considering a total of 50 radial positions ranging from $2R_{pv}$ to r_{cr}. The latter corresponds to the radial position where $V(r_{cr}) = 0.7V_a$, with V_a being the total volume of the aggregate (corrected by monomers overlapping). Fig. 7.12a shows an example of fit for an aggregate sampled in the wings at $z = 50$ mm. As shown in this figure, a fractal dimension $D_{f,i} = 1.84 \pm 0.03$ and a packing factor $\phi_i = 1.15 \pm 0.05$ were found by a robust fit. These parameters are then used to fit the numerically determined volume-based pair correlation function as shown in Fig. 7.12b. The latter is determined based on the aggregate volume density function self-convolution, considering a total of 300 orientations and 200 radial positions (logarithmically spaced) [53, 140]. This calculation takes primary particle overlapping into account (see 5.4.7). Subsequently, the pair correlation function is modeled as $A(r) = A_{pp} + A_{agg}$, where A_{pp} and A_{agg} are the primary particle and aggregate contributions to the total pair correlation function.

$$A_{pp}(r) = \left(1 + \frac{r}{4\widetilde{R_{pv}}}\right)\left(1 - \frac{r}{2\widetilde{R_{pv}}}\right)^2, \qquad r \in [0, 2\widetilde{R_{pv}}] \tag{7.4.10a}$$

$$A_{agg}(r) = \frac{\phi D_{f,i}}{3}\left(\frac{r}{R_{pv}}\right)^{D_{f,i}-3}\left[e^{-(r/\xi_{max})^\beta} - e^{-(r/\xi)^\beta}\right], \qquad r > 0 \tag{7.4.10b}$$

The model used is the same introduced in section 5.4.7, and the expressions for A_{pp} and A_{agg} are given by Eq. (7.4.10a) and Eq. (7.4.10b), respectively. Therefore, based on the determined fractal dimension and packing factor, this model is fitted to search the remaining unknown parameters: the maximum and minimum equivalent length scales ξ_{max} and ξ, respectively, the stretching exponent β, and the monodisperse volume-equivalent primary particle radius $\widetilde{R_{pv}}$ (modeling A_{pp}). Some of these parameters are reported in

Fig. 7.12b including the stretching exponent and $2\widetilde{R_{pv}}$ as indicated in red at the bottom of the figure. The


(a) $D_{f,i}$ and ϕ_i (b) Fit pair correlation
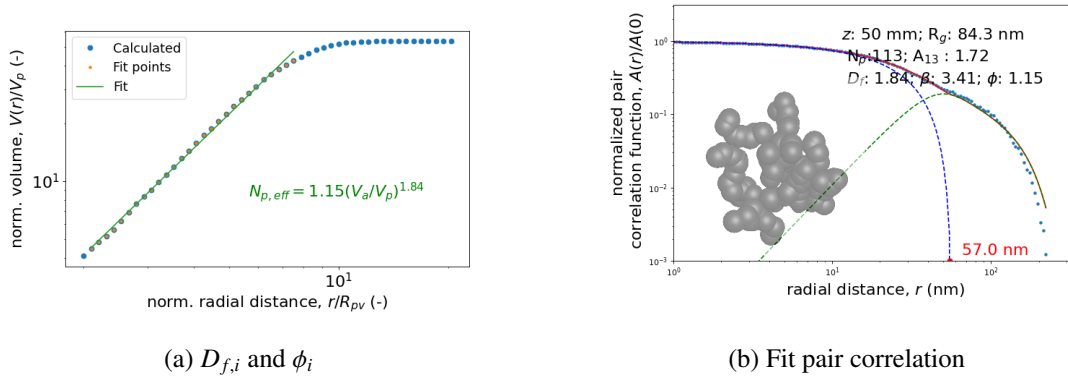
Figure 7.12: Individual fractal dimension ($D_{f,i}$) and packing factor (ϕ_i) determination, and pair correlation fit. Calculated values are presented in symbols, total fit in continuous red line, A_{pp} in dashed blue line, and A_{agg} in dash-dotted green line

same procedure has been applied for representative aggregates sampled at the selected axial positions for all the studied trajectories, and the results are shown in Table 7.2. Exception is intermediate 2 trajectory which is reported in Table S7.5 of the SM A. Inserts on each figure allow the morphology of the analyzed particles to be observed, however aggregates from different figures do not have the same scale. Different conclusions can be obtained from analyzing Table 7.2. For instance, when observing the evolution of $2\widetilde{R_{pv}}$ along the same trajectory, the effect of surface reactions characterized by an initial surface growth and subsequent oxidation stages are observed. Secondly, the proximity between $2\widetilde{R_{pv}}$ and the aggregate's cutoff length (specially evident at the centerline and intermediate 1 trajectories) makes the competition between primary particle and aggregate size more evident. This means that obtaining a fractal dimension for aggregates formed along these trajectories is particularly challenging and the values reported in this table are subject to considerable variability, specially along the centerline. These $2\widetilde{R_{pv}}$ values are larger than $D_{p,geo}$ as previously reported in Fig. 7.8c. This means that, in terms of the fractal structure as studied from the pair correlation function, an effective primary particle size has to be considered. As discussed in more details in the following section, when primary particles are highly overlapped they may be easily interpreted as larger spheres. This effective primary particle size is larger than the one deduced by analyzing individual overlapped primary spheres (as done in Fig. 7.8c and Fig. 7.8d). Excepting certain very high values, the packing factor of aggregates formed in the intermediate 2 and wings seem to be larger than those associated to other trajectories. The latter seem to show values much larger than those previously found for point touching primary particles [53]. The question here is: can we conclude statistically about these parameters? To answer this question, $D_{f,i}$ and ϕ_i were determined for the population of particles simulated along each trajectory. These parameters were obtained for aggregates with $N_p > 20$ and they are presented in Fig. 7.13a, and Fig. 7.13b, respectively. This figure shows that individual fractal dimensions are not considerably impacted by the history of particles formation in the flame. These individual fractal dimensions are much lower than the population ones as previously reported in Fig 7.11a. This discrepancy between individual and population average values is

consistent with Ref. [53] who studied DLCA agglomerates. In addition, experimental TEM image analysis of soot formed in premixed [324], and diffusion flames [15] have also revealed lower individual than population fractal dimensions. Packing factor is clearly larger for aggregates formed in the intermediate 2 and wings trajectories compared to intermediate 1. It may be surprising the large packing factors obtained (compared to the values of DLCA agglomerates [53]). This is attributed to the increase in local compactness produced by surface growth.
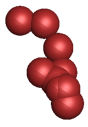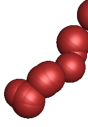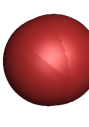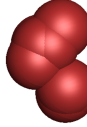

(a) Fractal dimension
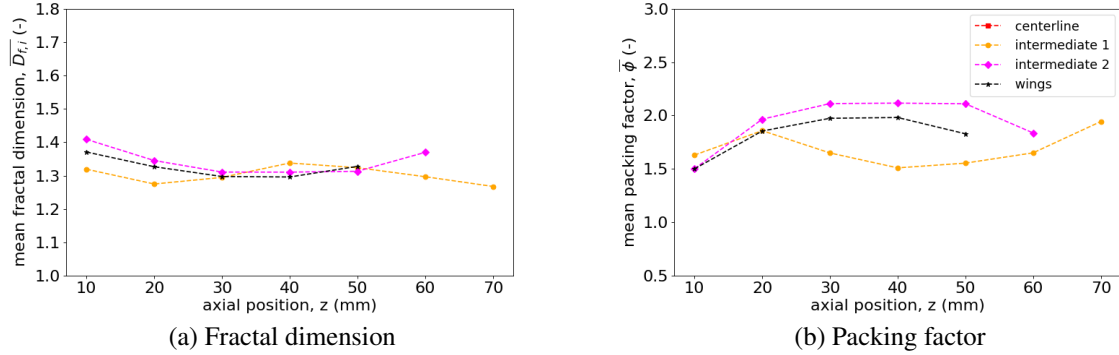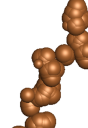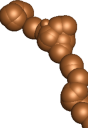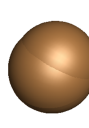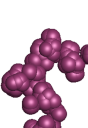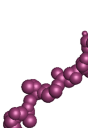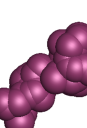
(b) Packing factor

Figure 7.13: Average individual fractal dimension ($\overline{D_{f,i}}$) and packing factor ($\overline{\phi}$) evolution for aggregates with $N_p > 20$.

7.4.4.4   Other individual morphological parameters

Fig. 7.14 reports the 3-dimensional images showing the aspect of the aggregates having the largest effective number of monomers, the largest anisotropy coefficient, the largest mean overlapping coefficient, and the largest mean coordination number for the 4 trajectories studied here. On the right hand side of each particle's image, the sampling height above the burner is reported between parenthesis. Also, a number of morphological parameters are reported including, the effective number of primary particles per aggregate, the anisotropy coefficient, overlapping, coordination number, primary particle polydispersity, specific surface area S_s with units (m^2/kg), and gyration radius. Maximum effective number of primary particles per aggregate ranges from 7.4 (centerline) to 59.5 (intermediate 2). In addition, maximum overlapping coefficient up to $A_{13} = 15.8$ have been observed. These particles are chain-like showing a tortuosity characteristic of their stochastic formation process. These maximum values do not considerably differ from those observed for soot formation in a premixed flame with pure agglomeration or agglomeration and surface growth (see Figures S7.13 in the SM A). Overla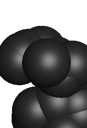pping coefficients as high as 93% were observed which confirms the needs of redefining primary particle size as suggested in the previous paragraph concerning the pair correlation function analysis. This high primary particle overlapping has been observed but not quantified in previous numerical works from the literature focused on soot formation in premixed flames [327, 334]. The largest overlapping coefficients were observed for aggregates consisting of $N_{p,eff} \to 1$. Note that these aggregates have the largest mean overlapping coefficient as determined considering all the pairs of intersecting monomers per each aggregate.

Consequently, this does not necessarily correspond to the largest level of overlapping between pairs of monomers in the system. In addition, maximum coordination numbers up to 34.4 have been observed. Both primary particle overlapping and coordination number are much larger than those observed in premixed flames 5 suggesting that local compactness is larger for soot aggregates formed in diffusion flames (under the conditions studied in this thesis).

Figure 7.14: Examples of aggregates with extreme morphological parameters including, maximum effective number of monomers, maximum anisotropy, maximum aggregate's overlapping, and maximum aggregate's coordination number found for each trajectory.

Fig. 7.14 clearly shows how the different morphological parameters (anisotropy, overlapping and coordination number) allow to observe different but complementary information about particles. Other morphological parameters reported in this figure include soot specific surface area S_s. This is an important parameter and maybe one of the most important determining the toxicity of nanoparticles [7–12]. According to the sample positions in the flame, the largest S_s where observed in the oxidation zone of the flame which is very worrying considering that these particles are the most prone escape the flame and be released to the atmosphere in real combustion systems! The values reported in this figure go from 32 to 125 m²/g. These values are comparable to those measured by BET technique. Indeed, as reviewed by Ouf et al. [360], for soot particles from different sources, BET determined S_s goes from 10 to 807 m²/g. Another parameter shown in this figure is the primary particle polydispersity. All the values shown in this figure are ≤ 1.15. An independent analysis showed values to be at maximum around 2.5 found in the centerline and wings trajectory, however these values were generally observed for small aggregates consisting of a few monomers. These values are explained by the late nucleation peaks observed for these trajectories as compared to other

streamlines (see Fig. 7.4).

7.4.5 Projected area scaling-law

Projected area scaling-law exponent (α) and prefactor (k_α) are derived in the same way as done in chapter 5 i.e., based on the equivalent number of primary particles per aggregate and the ratio of the orientationally averaged projected area of the aggregate and primary particles. The projected scaling-law exponent and prefactor are respectively larger and smaller than those obtained by Brasil et al. [30]. This is normal since Brasil et al. [30] did not considered an effective number of monomers per aggregates which explain why their k_α values are larger than the ones found in this chapter. Also, as observed in chapter 5, one possible explanation for these values is the non-uniform and larger overlapping of primary particles induced by surface growth in current simulations. Also, as already seen in Fig. 7.11, the morphology of current aggregates is not exactly equivalent to those DLCA ones studied by Brasil et al. [30] (see section 7.4.4 for further details). We also note a moderate dependence of α and k_α parameters on the particles trajectory in the flame.

(a) Scaling exponent   (b) Scaling prefactor
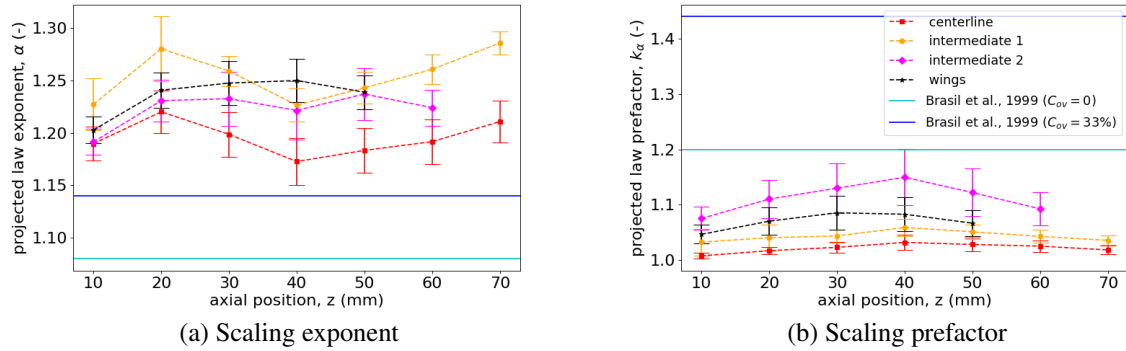
Figure 7.15: Prefactor (k_α) and exponent (α) of projected area power-law. Error bars represent the 95% confidence intervals.

7.4.6 CPU time and computational details

Computer simulations for individual runs of a given trajectory range between 9.15 to 13.18 hours in a single processor at CRIANN[5] computing center. This means that for obtaining the final results for each individual trajectory these times should be multiplied by a factor of 10, however they can be run in parallel in different processors. Simulation time is found to be highly sensible to the number of primary particles in the simulation box. Current simulations involved a total of primary particles ranging from 1024 (initial condition) up to a limit of 8450 (intermediate 1 case) determined by domain duplication and nucleation rate. Finally, the error in aggregate's volume and surface area approximation based on the introduced correlations (α_v and

---

[5]CRIANN: *Centre Régional Informatique et d'Applications Numériques de Normandie.*

α_s, described in Section 5.2.3) has been observed being below 10% for volume, which is very encouraging considering the high degree of primary particle overlapping observed in these simulations (see Fig. 7.14). However, the error in surface area may be as high as 60%, this means that the fit for α_s proposed in chapter 5 should be adapted to these higher levels of soot monomers overlapping.

7.5 Sensitivity Analysis

As thoroughly explained in Section S7.3 of the SM A, a sensibility analysis for the proposed CoFlame→MCAC coupling approach is presented. The sensibility to the following key properties or parameters is tested: the Lagrangian trajectory, primary particle diameter for nucleation, and the total number of primary particles in the simulation box. Case intermediate 1 is selected to this end for representing an intermediate case between the centerline and the wings. The sensitivity analysis is focused on the soot volume fraction (mass conservation), aggregate number concentration (aggregation kinetics), geometric mean aggregate's gyration diameter (particle size distribution), and population fractal dimension (aggregate's morphology) allowing a quick and global description of simulations. Firstly, this analysis shows an important sensitivity to the determination of the soot particle's Lagrangian trajectory when determined by considering or neglecting thermophoretic effects (see trajectory intermediate 1 in Fig. 7.4). This is relevant in this diffusion flame where strong temperature gradients exist. Secondly, the sensitivity analysis shows the initial number of particles in the box (1024) to be effectively a good compromise between accuracy and computational time. Thirdly, the dependence on the nucleation particle diameter is found important in the oxidation zones of the flame when nucleation happens at a diameter larger than 5 nm as considered in this chapter. Also, for a nucleation diameter $D_p = 0.9$ nm very different results are observed, for instance, nucleation predominates over aggregation for low axial positions ($z < 30$ mm). This uncertainty arises from the fact that CoFlame nucleation takes place at a lower primary particle diameter than D_c considered for MCAC simulations. Therefore, future simulations should determine an equivalent nucleation at D_c.

7.6 Conclusions

CoFlame→MCAC coupling is successfully done in an ethylene diffusion flame. A total of 4 trajectories covering from the centerline up to the wings of the flame (where the peak soot volume fraction exists) are carried out. The determination of soot particle Lagrangian trajectories presents an important source of uncertainty in the current approach. Particularly, the inclusion of thermophoretic force for the determination of soot trajectories may play an important role as suggested by the free molecular flow regime thermophoretic force for spherical tracer particles adopted in this chapter. This determination of trajectories becomes specially important close to the wings of the flame. This is due to the strong gradients of temperature, and mainly

due to a nucleation peak found close to the burner exit at the interface between the fuel and oxidizer tubes exit. This suggests that more accurate Lagrangian tracking methods such as the one proposed by Gallen et al. [383] should be implemented to improve the accuracy of these simulations. Thermophoretic force is poorly understood in the literature and its role on soot Lagrangian trajectory by considering the morphology of particles should be systematically studied in the future. A model of thermophoretic force for aggregates is currently needed.

Soot aggregates formed in the wings have significantly different morphology and sizes compared to those formed in the centerline of the flame. This is consistent with previous experimental TEM images observations in diffusion flames [399–402]. The aggregates formed in the wings are much larger and showed the largest local compactness as expressed by the primary particle overlapping coefficient and coordination number. Also, less evidently, those aggregates formed in the wings exhibit larger anisotropy coefficients which is expected to be explained by the larger size of aggregates compared to the centerline.

The low variability in fractal dimension when comparing different trajectories in the flame is an important result for Population Balance simulations were typically a constant fractal dimension is assumed. This is also important for experimental measurements were fractal parameters are commonly assumed constant all along the flame [64, 89, 311].

Primary particle polydispersity, in the sense of spherical nuclei simulated in this work, is found to be much larger for particles formed closer to the centerline of the flame. This is explained by the more important role of time-integrated nucleation in this trajectory than others in the flame. In terms of residence time, nucleation becomes relevant much later in the centerline than the wings of the flame.

Projected area power-law prefactor and exponent were found o be moderately dependent on the trajectory followed in the flame and overall values are $\alpha = 1.20$ and $k_{alpha} = 1.05$. This suggests that higher overlapping between primary particles and morphology evolution due to different agglomeration/flow regimes as revealed by MCAC simulations, are relevant. These parameters are especially important for numerical simulations relying on orientationally averaged projected area for example to determine collision frequencies [41] or mobility diameters [78]. They are also very important to analyze experimental TEM images. These parameters have never been derived before for soot particles in flames as simulated without *a priori* assumptions in morphology.

Finally, the evolution of soot maturity along their trajectories in the flame may be important, specially regarding the evolution of soot bulk density and therefore may be explored in the future.

Table 7.2: Fit of the pair correlation function of representative aggregates. Calculated values are presented in symbols, total fit in continuous red line, A_{pp} in dashed blue line, and A_{agg} in dash-dotted green line (for selected aggregates whose $A_{13} < 3.5$).

z (mm)	Centerline	Intermediate 1	Wings
70			-
60			-
50			
40			
30			
20			
10			
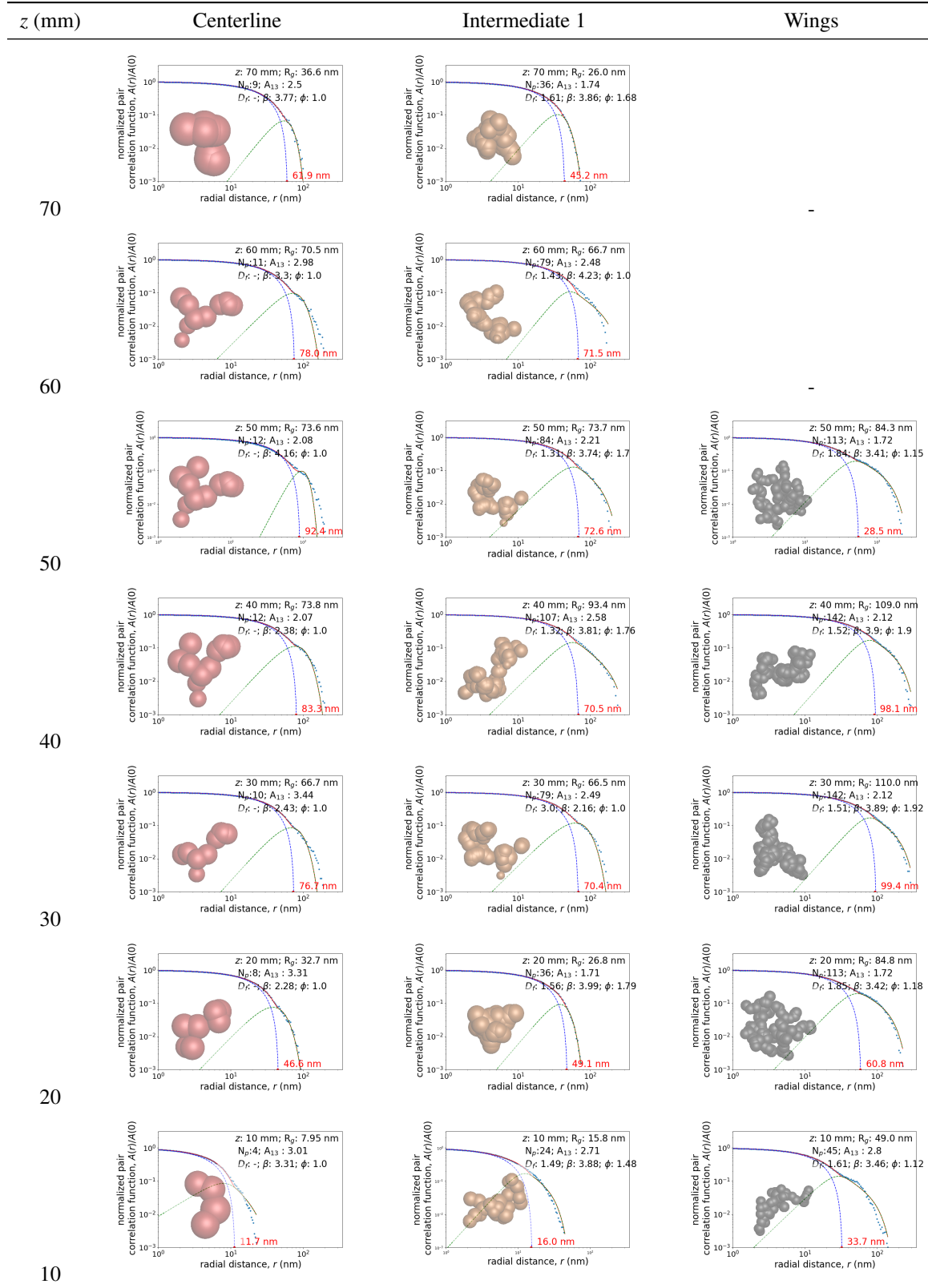
Table 7.3: Summary of CoFlame→MCAC coupling simulation results (only Temperature is a result directly from Coflame, the rest correspond to MCAC results).

z (mm)	r (mm)	t (ms)	T (K)	f_v (ppm)	$\overline{N_{p,eff}}$	$\widetilde{D_g}$ (nm)	$D_{g,geo}$ (nm)	$\sigma_{Dg,geo}$	N_{agg} (1/cm^3)	$D_{p,geo}$ (nm)	$\sigma_{Dp,geo}$	$\overline{n_c}$	$\overline{c_{ov}}$	$\overline{A_{13}}$	$D_{f,p}$	$k_{f,p}$	α	k_α
								centerline										
10		100	1238	0.01	1.3	9.0	8.5	1.25	1.3e+10	10.0	1.12	0.3	0.07	1.35	-	-	1.19	1.01
20		109	1544	0.37	1.4	31.6	28.7	1.49	1.1e+10	34.2	1.33	0.7	0.24	1.31	-	-	1.22	1.02
30		116	1690	1.67	1.6	57.5	51.5	1.50	8.7e+09	56.5	1.35	1.2	0.31	1.49	-	-	1.20	1.02
40	0	122	1639	2.23	2.0	73.3	64.9	1.46	6.7e+09	63.4	1.28	1.5	0.33	1.80	-	-	1.17	1.03
50		127	1631	2.16	1.9	68.2	61.0	1.45	7.4e+09	62.6	1.29	1.4	0.32	1.66	-	-	1.18	1.03
60		132	1725	1.85	1.7	61.0	54.8	1.47	8.3e+09	58.8	1.33	1.2	0.31	1.54	-	-	1.19	1.03
70		136	1771	0.83	1.4	41.7	34.9	1.91	1.0e+10	42.7	1.59	0.9	0.26	1.35	-	-	1.21	1.02
								intermediate 1										
10	1.32	31	1207	0.05	3.6	16.1	13.5	1.52	1.7e+10	11.3	1.10	1.6	0.24	2.01	1.77	2.05	1.23	1.03
20	1.06	40	1475	0.44	2.8	34.6	29.7	1.59	1.2e+10	29.5	1.14	4.2	0.42	1.64	1.79	2.28	1.28	1.04
30	0.96	47	1699	1.14	3.0	57.1	48.5	1.61	8.0e+09	45.7	1.16	6.2	0.49	1.78	1.72	2.22	1.26	1.04
40	0.87	53	1670	1.30	3.7	69.5	58.2	1.57	6.2e+09	48.8	1.14	7.0	0.51	2.01	1.68	2.19	1.23	1.06
50	0.80	58	1638	1.28	3.3	63.8	54.3	1.56	7.0e+09	48.2	1.15	6.7	0.51	1.89	1.69	2.21	1.24	1.05
60	0.77	63	1680	1.11	3.0	56.2	47.6	1.63	8.1e+09	45.3	1.16	6.1	0.49	1.77	1.72	2.23	1.26	1.04
70	0.76	67	1781	0.33	2.8	30.1	24.4	1.91	1.2e+10	25.5	1.23	3.7	0.39	1.62	1.85	2.25	1.29	1.04
								intermediate 2										
10	2.56	20	1431	0.57	10.1	42.5	32.0	1.79	1.8e+10	17.8	1.07	3.0	0.30	2.58	1.83	2.03	1.19	1.08
20	2.07	29	1635	1.93	11.8	71.3	55.5	1.76	9.0e+09	30.9	1.06	7.8	0.39	2.40	1.92	2.31	1.23	1.11
30	1.84	35	1751	2.96	12.4	96.9	78.2	1.65	6.2e+09	41.6	1.05	12.5	0.43	2.43	1.91	2.42	1.23	1.13
40	1.66	41	1709	3.02	13.6	104.8	84.5	1.65	5.5e+09	42.6	1.05	13.4	0.42	2.52	1.89	2.43	1.22	1.15
50	1.53	46	1678	2.89	11.9	92.1	74.4	1.65	6.7e+09	40.5	1.05	11.9	0.43	2.39	1.93	2.39	1.24	1.12
60	1.47	51	1713	1.37	12.0	61.9	45.1	2.05	1.1e+10	26.0	1.09	5.8	0.36	2.44	1.91	2.23	1.22	1.09
								wings										
10	3.03	17	1537	0.91	6.2	44.9	35.5	1.68	1.9e+10	23.8	1.08	2.6	0.31	2.40	1.80	1.99	1.20	1.05
20	2.60	25	1735	3.09	8.0	78.8	64.4	1.62	9.6e+09	40.5	1.07	6.3	0.41	2.28	1.91	2.21	1.24	1.07
30	2.39	32	1817	5.53	8.1	109.0	91.4	1.56	6.7e+09	56.6	1.04	10.1	0.46	2.27	1.89	2.33	1.25	1.09
40	2.19	37	1762	5.46	7.9	106.5	89.4	1.56	7.0e+09	56.0	1.04	9.9	0.46	2.24	1.89	2.33	1.25	1.08
50	2.07	43	1723	2.79	8.0	75.6	61.1	1.68	1.0e+10	38.6	1.08	5.8	0.40	2.31	1.89	2.20	1.24	1.07

8 | Conclusions and perspectives

Conclusions

MCAC is a new and powerful code enabling the formation of complex soot aggregates in flames to be simulated. The kinetics of aggregation, particle size distribution, and morphology can be studied. In these simulations, the morphology of aggregates of nanoparticles is simulated almost entirely based on first principles without big assumptions on particles morphology. This has never been achieved before, excepting a few recent remarkable works [112, 117, 183, 185]. However, these works neglected soot particles continuous nucleation in time, soot collision/sticking probabilities, and the detailed morphology of aggregates were not investigated. On the other hand, MCAC is able to simulate all the mechanisms relevant for soot formation in flames i.e., nucleation in time, surface growth, oxidation (and fragmentation), and agglomeration. At the same time, the soot maturity evolution and its effects on collision efficiency can be taken into account by MCAC. This code has been validated by comparison with Langevin Dynamics to accurately predict the dynamics of individual particles, and precisely consider their residence time for both individual and populations of polydisperse particles. The latter has been historically considered a limitation of Monte Carlo DEM methods [102]. The code has shown good agreement with macroscopic Population Balance simulations of agglomerating soot particles in terms of coagulation kinetics, and particle size distribution. MCAC is much computationally efficient alternative compared to the aforementioned codes. Also, the individual surface reactions scheme introduced in this thesis may reduce the CPU time by a factor of 10 compared to typical population-based surface reactions. Current MCAC approach may open the door to a new type of soot formation modeling which is both accurate and computationally efficient. MCAC is an open-source code and different versions are available in Gitlab (see Appendix B). Based on this new approach, the following conclusions are obtained:

A new energetic approach predicts soot particles collision efficiency: In this thesis, soot maturity is considered as the increase in C/H ratio and soot particles bulk density due to surface growth. Soot particles interactions are complex, and three outcomes are possible; (1) collision may be inhibited when their kinetic energy is lower than the electrostatic barrier, (2) rebound may happen when colliding with too

much kinetic energy compared to the electrostatic barrier and potential well depth, and (3) sticking only takes place when particle collide with just enough kinetic energy. In this context, we have introduced probabilities of sticking and collision of soot particles depending on their kinetic energy, electrostatic barrier and Lennard-Jones potential well depth. These probabilities are commonly ignored in current Population Balance simulations of soot formation in flames excepting a few remarkable and very recent works where only Lennard-Jones have been incorporated [246, 247]. These expressions may be used in future numerical simulations. Collision probability does not play a critical role in soot formation based on their bipolar charges naturally produced in the flame. As explained in Chapter 6, soot particles can be modeled as condensed matter i.e., their atomic composition (C/H) determines their Lennard-Jones interactions and particularly their rebound probability upon collisions.

A new critical diameter for soot monomers systematic sticking is proposed: A critical sticking diameter for soot formation in flames around 10 nm has been found. This means that sticking probability becomes relevant for soot primary particles which diameter is smaller than this critical value. This diameter is not strongly dependent on soot chemical composition (maturity). This critical sticking diameter should be considered for future DEM or Population Balance simulations of soot formation in flames. The idea of introducing a critical diameter for sticking was just previously hypothesized to explain low coagulation rates of 1 to 10 nm soot particles [363]. It was suggested as the explanation of the counterintuitive degradation of small soot particles coagulation frequency when increasing temperature [62]. More recently, numerical simulations suggested low coagulation frequency of nascent soot particles [246]. However such diameter was never clearly identified as done in this work.

Agglomeration and flow regimes evolution are important: The role played by the change in agglomeration regimes (particle-particle) ranging from ballistic to diffusive has been explored. The simultaneous change in flow regime (particle-gas) ranging from free molecular to continuum has also been studied. Both regimes are commonly confused and poorly understood in the literature. For example, free molecular flow regime is commonly confused or assumed to represent ballistic agglomeration. This is a misconception that should be eradicated. These regimes were clearly identified and quantified in this thesis by monitoring the evolution of the fluid (flow regime) Knudsen, and the nearest-neighbor (agglomeration regime) Knudsen numbers. Soot particles agglomeration in flames takes place in the transition flow and agglomeration regimes, contrarily to the typically assumed free molecular flow regime [61, 112, 383]. These assumptions only hold for small isolated primary particles ($\ll 30$ nm) and becomes inaccurate for agglomerates as they are growing and experience more diffusive movement and their size becomes relevant compared to the fluid mean free path. Primary particle size and polydispersity greatly influence both agglomeration and flow regimes and subsequently the coagulation kinetics, particle size distribution, and agglomerate's morphology. Indeed, the population fractal dimension is dependent on primary particle size and values below the classical DLCA limit were found in this thesis. This observation is coherent with experiments of colloids agglomeration [124] and has never

been shown numerically before.

Soot aggregation kinetics is affected by maturity: Under the flame conditions studied in Chapter 6, soot maturity evolution does not influence relevantly particle's morphology. However, it plays a role on aggregation kinetics and particle size distribution. The latter is more important in terms of soot bulk density evolution rather than collision or sticking probabilities. The impact of the sticking probability (linked to particle's potential well and kinetic energy) is not so strong due to higher efficiency of surface growth as compared to agglomeration to increase the size of particles. Indeed, primary particles overcome the critical sticking diameter after a few milliseconds passing the zone where these probabilities are relevant. These probabilities are relevant in the zone in the flame where soot particle volume fraction is very low ($\sim 10^{-3}$ ppm) to considerably influence agglomeration kinetics. This explains the low impact of sticking probability on soot agglomeration kinetics, and aggregate size distribution. The low relative importance of collision probability (mainly linked to soot electrostatic charges and kinetic energy) is explained by soot bipolar charges with narrow distribution dependent on their mobility diameters (< 80 nm).

Self-preserving size distributions are unified: Coagulation naturally increases the geometric standard deviation (polydispersity) of the population of agglomerates until reaching a self-preserving asymptotic curve depending on both agglomeration and flow regimes. This geometric standard deviation is different for volume-equivalent, mobility, and gyration radius. Similar observations were done in Ref. [67] however, unlike this work, they did not consider the simultaneous change in agglomeration and flow regimes. The self-preserving size distribution is found to follow a generalized Gamma distribution that can be expressed in terms of the number of primary particles, volume, volume-equivalent diameter, mobility diameter, and gyration diameter. Before this work, the self-preserving particle size distribution were only observed for specific agglomeration regimes such as ballistic [67, 236] or diffusive [403, 404] alone, and transition regimes for spherical coalescing particles [232]. This is a useful finding to compare the experimentally measured distribution based on different techniques such as SMPS (mobility radius) and light-scattering (gyration radius) as done in Ref. [89].

Aggregate's local compactness is highly sensible to surface growth: Agglomeration is a key mechanism of nanoparticles formation in flames, leading to particle morphologies in some resemblance with those observed experimentally. Compared with simulations involving pure agglomeration, including surface growth considerably influences the agglomeration kinetics, particle size distribution, and aggregate's morphology. Indeed, the latter is found to be more impacted at the scale of primary particles rather than aggregate's fractal structure (under the hypothesis of isotropic surface growth), specially in terms of their packing and overlapping which is referred as local compactness. This local compactness is characterized by primary particle overlapping, coordination number, and packing factor. Surface growth is proposed as the main explanation of soot primary particle overlapping as experimentally

observed in TEM images. In this context, other physical mechanisms such as sintering/coalescence may also be important [328, 329, 405] however, this may be relevant only for incipient soot particles [230] which is beyond the scope of this thesis. Primary particle overlapping is maybe the most relevant and complex morphological properties of soot particles. This overlapping considerably influences the physical properties of soot aggregates such as their volume, surface area, and mechanical resistance which plays an important role on their numerical simulations of surface reactions and soot formation dynamics. This property also plays a fundamental role on soot-light interaction which is important to understand their role in climate change [47, 164, 330, 406]. Physically-driven soot overlapping has never been systematically studied numerically before. The overlapping coefficient is quantified in an ethylene premixed and diffusion flames. It is found to evolve in time according to the competition between agglomeration and surface reactions and attains a quite-asymptotic value between 30% to 50% in the zones of soot formation, and decreases in the oxidation zone. These values are in good agreement with experiments [77]. However, local overlapping coefficients (averaged at each individual primary particle) may be as high as twice the population average ones depending on aggregates residence time under surface growth. Mean primary particle coordination number is a simple but very important parameter typically overlooked in the literature. This parameter directly determines the mechanical resistance [337] of aggregates and may influence their radiative properties. When agglomeration takes place in the absence of surface reactions, this parameter is accurately predicted by Eq. (5.2.5) which is robust for different agglomerate's morphology ranging from chain-like agglomerates up to more compact RLCA agglomerates [52]. In these cases, it tends asymptotically towards 2, and larger values are only possible when other mechanisms affecting primary particle size are present such as surface reactions. Systematic determination of the coordination number is proposed in order to take multi-sphere intersections into account to more accurately evaluate their volume and surface area based on the introduced semi-empirical equations. When considering surface reactions, it evolves in a complex way in time and may be much larger (up to 400%) than the asymptotic value found for agglomerates formed without surface growth. Another parameter that also increases with surface growth is the packing factor. It is an important parameter relating primary particles and aggregate's volume. It is determined by primary particles compactness but also to the aggregate's fractal dimension. It is analogous and directly linked to the fractal prefactor which is a commonly overlooked and poorly understood morphological parameter.

Soot aggregates volume and surface area can be predicted by new expressions: Both primary particle overlapping coefficient and coordination number are key parameters used to predict the volume and surface area evolution of soot aggregates. Many works in the literature neglect the effect of overlapping on aggregates volume and surface area without justification [148, 327, 383, 407]. Other studies have tried to include it, but they simplified the problem neglecting multi-sphere intersection [187] or considered a constant overlapping [408]. As shown in Chapter 5, this may lead to large errors in

both volume and surface area (up to a factor of 3 for individual aggregates). The proposed equations are combined to accurately predict the total soot volume (< 0.6% error) and surface area (< 5.75% error) in a premixed ethylene flame. The proposed method can be (hopefully) easily implemented in current Population Balance (macroscopic) or Discrete Element(mesoscale) simulations to improve the accuracy and/or the computational time. Both overlapping coefficient and primary particle coordination number may be used to predict the aggregate physicochemical properties such as chemical reactions, heat and mass transfer.

Individual aggregate's morphology is characterized by new methods: The inclusion of primary particles contribution to the total pair correlation function is relevant to soot formation in flames where aggregates present a complex morphology determined by the competition between aggregation and surface reactions. In this context, determining the individual fractal properties of particles is not evident and therefore different approaches have been proposed to this purpose including: modeling and fitting procedures of the pair correlation function (see Chapters 5, and 6), individual fractal dimension from radial volume evolution (see Chapter 7). This represents a progress considering previous works trying to model aggregate's pair correlation function neglecting the role played by primary particle polydispersity and focused on the limit of infinitely large aggregates [51]. These new methods allow a more precise evaluation of aggregate's local compacity as quantified by the packing factor.

Different streamlines produce remarkably different soot particles: in an ethylene diffusion flame. Primary particle polydispersity is larger for particles formed close to the centerline and this is attributed to higher nucleation mass rate as compared to other streamlines. Aggregates formed in the wings of the flame are much larger than those formed in the centerline and the former exhibit a considerably larger local compactness.

How to define primary particles belonging to aggregates? Under some flame conditions, a high degree of overlapping between primary particles has been observed by numerical simulations. This means that according to the different method used to analyze these aggregates, they may be able to identify this high level of overlapping or not. For example, two monomers with high degree of overlapping (see Fig. 7.14) may be interpreted as one equivalent sphere when conducting TEM image analysis. This may have a big impact on all the morphological parameters subsequently derived such as the number of primary particles per aggregate, the measured overlapping coefficient, the coordination number, and also on the fractal parameters derived from the fractal-law. On the other hand, from an autocorrelation function point of view, an aggregate is characterized by two important size scales namely the aggregate's size and the primary particle size. The latter has been clearly identified thanks to the generalized pair correlation function model developed in parallel of this work, and intensively used here. This leads to define an effective primary particle size that may be closer to the one measured by different techniques such as TEM image analysis or light-particle interaction.

Perspectives

Future MCAC developments may include modeling the **coalescence** of incipient soot particles leading to the formation of primary particles may be incorporated. In addition, surface reactions and nucleation may be directly based on the concentrations of gaseous species instead of mass flux rates. Also, the chemical composition of soot particles (C/H ratio) may be tracked based on the surface reactions modeling in order to accurately take soot maturity into account. As discussed in chapter 6 this may not be critical for soot formation dynamics but may be important for subsequent studies of soot radiative properties. Indeed, the radiative properties of particles simulated in this thesis will be studied in terms of optical cross sections in the context of the ASTORIA ANR project.

MCAC computational time is currently very sensitive to the initial number of primary particles. This is expected to be determined by the nature of the Monte Carlo approach. This means that simulating incipient soot particles ($D_p < D_c$) is a challenge because the number of particles increases very fast and some computational strategies, such as domain division, should be implemented to overcome this limitation. This is similar (but not directly equivalent) to what has been implemented in PBE Monte Carlo simulations [409].

Improving the accuracy of CFD→MCAC coupling based on CFD simulations including **Lagrangian tracking** [383] may be envisaged. This is expected to reduce the uncertainties related to the trajectory determination as expressed by the difference between soot volume fraction from CFD simulations and the one obtained by integrating soot formation mechanisms along the trajectory. Also, comparison of this more accurate Lagrangian methods with the current post-processing methodology may may be done. An approach to the thermophoretic force adapted to aggregates is currently needed.

Future works may involve modeling more complex flames such as **turbulent** with special interest in aeronautical applications. On the other hand, the formation of soot super-aggregates and transition towards gelation may be simulated in the future. Studying these type of particles may be especially relevant in the context of fires and atmospheric pollutants formation. However, the high concentration limit has to be carefully treated because most of the approaches considered in this thesis consider the characteristic time of agglomeration and surface reactions to be much larger than particle's momentum relaxation time which holds in the diluted regime (volume fraction lower than 1%).

MCAC is a versatile code that can be adapted to simulate different problems in Aerosol Science involving the formation, transport, deposition, resuspension, and filtration of particles in flows. The study of the physical properties such as mobility, heat transfer, and particle-light interaction of these particles considering their complex morphology. In this context, this type of codes may encounter great applications in the context of synthesis of nanomaterials in/out flames.

Bibliography

[1] Christopher R Shaddix and Timothy C Williams. Soot: Giver and taker of light: The complex structure of soot greatly influences the optical effects seen in fires. *American scientist*, 95(3):232–239, 2007. 1

[2] C Kleinstreuer and Z Zhang. Airflow and particle transport in the human respiratory system. *Annual review of fluid mechanics*, 42:301–334, 2010.

[3] Saeed Khodabakhshi, Pasquale F Fulvio, and Enrico Andreoli. Carbon black reborn: Structure and chemistry for renewable energy harnessing. *Carbon*, 162:604–649, 2020. 1, 1, E.1

[4] Ulrike Lohmann, Franz Friebel, Zamin A Kanji, Fabian Mahrt, Amewu A Mensah, and David Neubauer. Future warming exacerbated by aged-soot effect on cloud formation. *Nature Geoscience*, 13(10):674–680, 2020. 1, 1.1, E.1

[5] Tami C Bond, Sarah J Doherty, David W Fahey, Piers M Forster, Terje Berntsen, Benjamin J DeAngelo, Mark G Flanner, Steven Ghan, Bernd Kärcher, Dorothy Koch, et al. Bounding the role of black carbon in the climate system: A scientific assessment. *Journal of geophysical research: Atmospheres*, 118(11):5380–5552, 2013. 1

[6] D Cortés, José Morán, F Liu, F Escudero, J-L Consalvi, and Andrés Fuentes. Effect of fuels and oxygen indices on the morphology of soot generated in laminar coflow diffusion flames. *Energy & fuels*, 32(11):11802–11813, 2018. 1.1, 2.1.3, **??**, 2.1.8.1, 4.2, 4.3.4, 4.3.4, 4.3.5, 4.4, 5.1, 5.2.3, 5.4.5, 6.4, 7.4.3, 7.4.4.2, E.3.2.3, E.3.2.3, E.3.4.3, E.4

[7] Tobias Stoeger, Otmar Schmid, Shinji Takenaka, and Holger Schulz. Inflammatory response to tio2 and carbonaceous particles scales best with bet surface area. *Environmental health perspectives*, 115(6):A290–A291, 2007. 1, 5.1, 7.4.4.4

[8] Salik Hussain, Sonja Boland, Armelle Baeza-Squiban, Rodolphe Hamel, Leen CJ Thomassen, Johan A Martens, Marie Annick Billon-Galland, Jocelyne Fleury-Feith, Frédéric Moisan, Jean-Claude Pairon, et al. Oxidative stress and proinflammatory effects of carbon black and titanium dioxide nanoparticles: role of particle surface area and internalized amount. *Toxicology*, 260(1-3):142–149, 2009.

[9] Tina M Sager and Vincent Castranova. Surface area of particle administered versus mass in determining the pulmonary toxicity of ultrafine and fine carbon black: comparison to ultrafine titanium dioxide. *Particle and fibre toxicology*, 6(1):15, 2009. E.1

[10] Manzoor Ahmad Gatoo, Sufia Naseem, Mir Yasir Arfat, Ayaz Mahmood Dar, Khusro Qasim, and Swaleha Zubair. Physico-chemical properties of nanomaterials: implication in associated toxic manifestations. *BioMed research international*, 2014, 2014.

[11] Otmar Schmid and Tobias Stoeger. Surface area is the biologically most effective dose metric for acute nanoparticle toxicity in the lung. *Journal of Aerosol Science*, 99:133–143, 2016.

[12] Hyouk-Soo Kwon, Min Hyung Ryu, and Christopher Carlsten. Ultrafine particles: unique physicochemical properties relevant to health and disease. *Experimental & Molecular Medicine*, pages 1–11, 2020. 1, 5.1, 7.4.4.4

[13] Sotiris E Pratsinis. Aerosol-based technologies in nanoscale manufacturing: from functional materials to devices through core chemical engineering. *AIChE journal*, 56(12):3028–3035, 2010. 1

[14] HA Michelsen. Probing soot formation, chemical and physical evolution, and oxidation: A review of in situ diagnostic techniques and needs. *Proceedings of the Combustion Institute*, 36(1):717–735, 2017. 1, 2.1.8.3, 2.3, E.1

[15] M Wozniak, FRA Onofri, S Barbosa, J Yon, and J Mroczka. Comparison of methods to derive morphological parameters of multi-fractal samples of particle aggregates from tem images. *Journal of Aerosol Science*, 47:12–26, 2012. 1, 2.1.8.1, 5.1, 5.4.8, 7.4.4.3, E.1

[16] Avrom I Medalia. Morphology of aggregates: I. calculation of shape and bulkiness factors; application to computer-simulated random flocs. *Journal of Colloid and Interface Science*, 24(3):393–404, 1967. 2.1.1, 2.1.7

[17] AI Medalia and FA Heckman. Morphology of aggregates—ii. size and shape factors of carbon black aggregates from electron microscopy. *Carbon*, 7(5):567–582, 1969. 2.1.1, 2.1.7

[18] Avrom I Medalia. Morphology of aggregates: Vi. effective volume of aggregates of carbon black from electron microscopy; application to vehicle absorption and to die swell of filled rubber. *Journal of Colloid and Interface Science*, 32(1):115–131, 1970.

[19] AI Medalia and FA Heckman. Morphology of aggregates: Vii. comparison chart method for electron microscopic determination of carbon black aggregate morphology. *Journal of Colloid and Interface Science*, 36(2):173–190, 1971. 2.1.1, 2.1.7

[20] SR Forrest and TA Witten Jr. Long-range correlations in smoke-particle aggregates. *Journal of Physics A: Mathematical and General*, 12(5):L109, 1979. 2.1.1

[21] Benoit B Mandelbrot. Fractals. *Form, chance and dimension*, 1977. 2.1.1

[22] Thomas A Witten Jr and Leonard M Sander. Diffusion-limited aggregation, a kinetic critical phenomenon. *Physical review letters*, 47(19):1400, 1981. 2.1.1

[23] Raymond D Mountain, George W Mulholland, and Howard Baum. Simulation of aerosol agglomeration in the free molecular and continuum flow regimes. *Journal of Colloid and Interface Science*, 114(1):67–81, 1986. 2.5, 4.1, 4.3.2, 4.3.2, 4.3.4, 5.1, 5.4.6

[24] Remi Jullien and Robert Botet. Aggregation and fractal aggregates. *Ann. Telecomm.*, 41:343–short, 1987. 2.1.1, 2.1.4, 2.2.3

[25] Paul Meakin. A historical introduction to computer models for fractal aggregates. *Journal of Sol-Gel Science and Technology*, 15(2):97–117, Aug 1999. 2.1.1, 2.1.9, 2.1.9.1, 2.1.9.2, 2.1.9.5, 2.2, 2.2.3

[26] RA Dobbins and CM Megaridis. Morphology of flame-generated soot as determined by thermophoretic sampling. *Langmuir*, 3(2):254–259, 1987. 2.1.1, 2.1.8.1

[27] RJ Samson, George W Mulholland, and JW Gentry. Structural analysis of soot agglomerates. *Langmuir*, 3(2):272–281, 1987. 2.1.1

[28] Richard A Dobbins and Constantine M Megaridis. Absorption and scattering of light by polydisperse aggregates. *Applied optics*, 30(33):4747–4754, 1991. 2.1.1

[29] Ümit Özgür Köylü, GM Faeth, Tiago L Farias, and Maria da Gracia Carvalho. Fractal and projected structure properties of soot aggregates. *Combustion and Flame*, 100(4):621–633, 1995. 2.1.1, 2.5

[30] AM Brasil, Tiago L Farias, and MG Carvalho. A recipe for image characterization of fractal-like aggregates. *Journal of Aerosol Science*, 30(10):1379–1389, 1999. 2.1.1, 2.1.5, 2.1.5, 2.1.7, 2.5, 4.1, 4.3.6, 4.3, 5.1, 5.2.3, 5.4.5, 5.4.8, 5.5.2, 5.7, 7.4.5

[31] C Oh and CM Sorensen. The effect of overlap between monomers on the determination of fractal cluster morphology. *Journal of Colloid and Interface Science*, 193(1):17–25, 1997. 2.1.1, 2.1.5, 2.1.5, 2.1.7, 5.1, 5.4.5

[32] Taco Nicolai, Dominique Durand, and Jean-Christophe Gimel. Static structure factor of dilute solutions of polydisperse fractal aggregates. *Physical Review B*, 50(22):16357, 1994. 2.1.1, 2.1.4, 2.1.5

[33] Jian Cai, Ninglong Lu, and Christopher M Sorensen. Analysis of fractal cluster morphology parameters: structural coefficient and density autocorrelation function cutoff. *Journal of Colloid and Interface Science*, 171(2):470–473, 1995. 2.1.1, 2.1.4

[34] Murray K Wu and Sheldon K Friedlander. Note on the power law equation for fractal-like aerosol agglomerates. *Journal of colloid and interface science*, 159(1):246–248, 1993. 2.1.1

[35] Christopher M Sorensen and Gregory C Roberts. The prefactor of fractal aggregates. *Journal of colloid and interface science*, 186(2):447–452, 1997. 2.1.1, 2.1.5, 4.3.5, 4.7, 4.4

[36] CM Sorensen. The mobility of fractal aggregates: a review. *Aerosol Science and Technology*, 45(7):765–779, 2011. 2.1.1

[37] Chonglin Zhang, Thaseem Thajudeen, Carlos Larriba, Thomas E Schwartzentruber, and Christopher J Hogan Jr. Determination of the scalar friction factor for nonspherical particles and aggregates across the entire knudsen number range by direct simulation monte carlo (dsmc). *Aerosol Science and Technology*, 46(10):1065–1078, 2012. 3.2.2.4

[38] James Corson, George W. Mulholland, and Michael R. Zachariah. Analytical expression for the friction coefficient of DLCA aggregates based on extended Kirkwood–Riseman theory. *Aerosol Science and Technology*, 2017. 2.1.1, 2.1.2, 3.2.2.4

[39] C. M. Sorensen. Light Scattering by Fractal Aggregates: A Review. *Aerosol Science and Technology*, 35(2):648–687, jan 2001. 2.1.1, 2.1.4, 2.1.4, 2.1.9, 2.2.3

[40] Christopher M Sorensen. Q-space analysis of scattering by particles: A review. *Journal of Quantitative Spectroscopy and Radiative Transfer*, 131:3–12, 2013. 2.1.1

[41] Thaseem Thajudeen, Ranganathan Gopalakrishnan, and Christopher J Hogan Jr. The collision rate of nonspherical particles and aggregates for all diffusive knudsen numbers. *Aerosol Science and Technology*, 46(11):1174–1186, 2012. 2.1.1, 2.1.7, 2.2, 2.4.2, 4.3.3, 4.3.3, 4.3.3, 4.3.6, 4.4, 5.3, 7.6

[42] Maximilian L. Eggersdorfer and Sotiris E. Pratsinis. Agglomerates and aggregates of nanoparticles made in the gas phase. *Advanced Powder Technology*, 25(1):71–90, jan 2014. 2.1.1, 2.1.9.2, 2.1.9.4, 2.2, 2.2.1, 2.2.3, 5.5.1

[43] Stefan Christian Endres, Lucio Colombi Ciacchi, and Lutz Mädler. A review of contact force models between nanoparticles in agglomerates, aggregates, and films. *Journal of Aerosol Science*, page 105719, 2020. 2.1.1, 2.1.9.1

[44] Magín Lapuerta, Rosario Ballesteros, and Francisco J Martos. A method to determine the fractal dimension of diesel soot agglomerates. *Journal of Colloid and Interface Science*, 303(1):149–158, 2006. 2.1.1, 4.3.4

[45] J Morán, J Cuevas, F Liu, J Yon, and A Fuentes. Influence of primary particle polydispersity and overlapping on soot morphological parameters derived from numerical tem images. *Powder technology*, 330:67–79, 2018. 2.1.1, 2.1.7, 2.2.2, 4.3.6, 5.1, 5.2.3, 5.7, 6.2.3, 6.2.3

[46] Ranganathan Gopalakrishnan, Peter H McMurry, and Christopher J Hogan Jr. The bipolar diffusion charging of nanoparticles: A review and development of approaches for non-spherical particles. *Aerosol Science and Technology*, 49(12):1181–1194, 2015. 2.1.1

[47] J Yon, A Bescond, and F Liu. On the radiative properties of soot aggregates part 1: Necking and overlapping. *Journal of Quantitative Spectroscopy and Radiative Transfer*, 162:197–206, 2015. 2.1.1, 2.1.9.3, 5.1, 8, E.1

[48] Fengshan Liu, Jérôme Yon, and Alexandre Bescond. On the radiative properties of soot aggregates–part 2: Effects of coating. *Journal of Quantitative Spectroscopy and Radiative Transfer*, 172:134–145, 2016. 2.1.1

[49] Rajan K Chakrabarty, Nicholas D Beres, Hans Moosmüller, Swarup China, Claudio Mazzoleni, Manvendra K Dubey, Li Liu, and Michael I Mishchenko. Soot superaggregates from flaming wildfires and their direct radiative forcing. *Scientific reports*, 4:5508, 2014. 2.1.1, 2.1.3

[50] WR Heinson, CM Sorensen, and A Chakrabarti. Does shape anisotropy control the fractal dimension in diffusion-limited cluster-cluster aggregation? *Aerosol Science and Technology*, 44(12):i–iv, 2010. 2.1.1

[51] WR Heinson, CM Sorensen, and A Chakrabarti. A three parameter description of the structure of diffusion limited cluster fractal aggregates. *Journal of colloid and interface science*, 375(1):65–69, 2012. 2.1.1, 2.1.4, 2.1.5, 2.1.5, 2.1.6, 2.1.6, 5.1, 5.4.7, 8

[52] Marco Lattuada, Hua Wu, and Massimo Morbidelli. A simple model for the structure of fractal aggregates. *Journal of colloid and interface science*, 268(1):106–120, 2003. 2.1.1, 5.2.3, 5.4.4, 6.4, 8

[53] J Yon, J Morán, F-X Ouf, M Mazur, and J.B. Mitchell. From monomers to agglomerates: A generalized model for characterizing the morphology of fractal-like clusters. *Journal of Aerosol Science*, 151:105628, 2020. 2.1.1, 2.1.4, 2.1.4, 2.1.4, 2.1.5, 4.3.5, 5.1, 5.2.3, 5.4.4, 5.4.7, 5.4.7, 7.4.4.3, 7.4.4.3, E.3.2.3, E.3.2.3

[54] Peter F DeCarlo, Jay G Slowik, Douglas R Worsnop, Paul Davidovits, and Jose L Jimenez. Particle morphology and density characterization by combined mobility and aerodynamic diameter measurements. part 1: Theory. *Aerosol Science and Technology*, 38(12):1185–1205, 2004. 2.1.2

[55] C. M. Sorensen. The Mobility of Fractal Aggregates: A Review. *Aerosol Science and Technology*, 45(7):765–779, jul 2011. 2.1.9.3, 2.2.3, 3.2.2.4

[56] J Yon, A Bescond, and F-X Ouf. A simple semi-empirical model for effective density measurements of fractal aggregates. *Journal of Aerosol Science*, 87:28–37, 2015. 2.1.2, 3.2.2.4, 3.2.2.4, 4.2, 4.3.4, 4.4, E.2.1

[57] Pratim Biswas, Yang Wang, and Michel Attoui. Sub-2 nm particle measurement in high-temperature aerosol reactors: a review. *Current Opinion in Chemical Engineering*, 21:60–66, 2018. 2.1.3

[58] J Lahaye and G Prado. Morphology and internal structure of soot and carbon blacks. In *Particulate carbon*, pages 33–55. Springer, 1981. 2.1.3

[59] Bin Zhao, Zhiwei Yang, Murray V Johnston, Hai Wang, Anthony S Wexler, Michael Balthasar, and Markus Kraft. Measurement and numerical simulation of soot particle size distribution functions in a laminar premixed ethylene-oxygen-argon flame. *Combustion and Flame*, 133(1-2):173–188, 2003. 2.1.3, 2.1.8.3, 5.4.6

[60] Bin Zhao, Zhiwei Yang, Zhigang Li, Murray V Johnston, and Hai Wang. Particle size distribution function of incipient soot in laminar premixed ethylene flames: effect of flame temperature. *Proceedings of the Combustion Institute*, 30(1):1441–1448, 2005. 2.1.3

[61] Jasdeep Singh, Robert IA Patterson, Markus Kraft, and Hai Wang. Numerical simulation and sensitivity analysis of detailed soot particle size distribution in laminar premixed ethylene flames. *Combustion and Flame*, 145(1-2):117–127, 2006. 2.1.3, 8

[62] Mariano Sirignano and Andrea D'Anna. Coagulation of combustion generated nanoparticles in low and intermediate temperature regimes: An experimental study. *Proceedings of the Combustion Institute*, 34(1):1877–1884, 2013. 2.1.3, 8

[63] M Matti Maricq, Stephen J Harris, and Joseph J Szente. Soot size distributions in rich premixed ethylene flames. *Combustion and Flame*, 132(3):328–342, 2003. 2.1.3, 5.4.6

[64] Nathan J Kempema and Marshall B Long. Combined optical and tem investigations for a detailed characterization of soot aggregate properties in a laminar coflow diffusion flame. *Combustion and Flame*, 164:373–385, 2016. 2.1.3, 7.6

[65] SK Friedlander and CS Wang. The self-preserving particle size distribution for coagulation by brownian motion. *Journal of Colloid and interface Science*, 22(2):126–132, 1966. 2.1.3.1, 4.1

[66] C Oh and CM Sorensen. Light scattering study of fractal cluster aggregation near the free molecular regime. *Journal of Aerosol Science*, 28(6):937–957, 1997. 2.1.3.1, 4.1, 4.3.4, 4.4

[67] Eirini Goudeli, Maximilian L Eggersdorfer, and Sotiris E Pratsinis. Coagulation–agglomeration of fractal-like particles: Structure and self-preserving size distribution. *Langmuir*, 31(4):1320–1327, 2015. 2.1.3.1, 2.2.3.2, 2.4.2, 2.5, 4.1, 4.3.4, 4.3.4, 8

[68] R Jullien. Aggregation phenomena and fractal aggregates. *Contemporary Physics*, 28(5):477–493, 1987. 2.1.4

[69] Manuel Rottereau, Jean Christophe Gimel, Taco Nicolai, and Dominique Durand. Monte carlo simulation of particle aggregation and gelation: Ii. pair correlation function and structure factor. *The European Physical Journal E*, 15(2):141–148, 2004. 2.1.4

[70] CM Sorensen, J Cai, and N Lu. Test of static structure factors for describing light scattering from fractal soot aggregates. *Langmuir*, 8(8):2064–2069, 1992. 2.1.4

[71] Karl-Heinz Naumann. COSIMA—a computer program simulating the dynamics of fractal aerosols. *Journal of Aerosol Science*, 34(10):1371–1397, 2003. 2.1.5

[72] AM Brasil, Tiago L Farias, Maria da Gracia Carvalho, and Ü Ö Köylü. Numerical characterization of the morphology of aggregated particles. *Journal of Aerosol Science*, 32(4):489–508, 2001. 2.1.5, 2.1.5, 5.1, 5.2.3, 5.4.4

[73] Magín Lapuerta, Juan José Expósito, and Francisco J Martos. Effect of sintering on the fractal prefactor of agglomerates. *Powder Technology*, 271:141–154, 2015. 2.1.5, 5.1

[74] M. L. Eggersdorfer and S. E. Pratsinis. The Structure of Agglomerates Consisting of Polydisperse Particles. *Aerosol Science and Technology*, 46(3):347–353, mar 2012. 2.1.5, 2.1.7, 2.1.9.4

[75] Zbigniew H Stachurski. *Fundamentals of amorphous solids: structure and properties*. John Wiley & Sons, 2015. 2.1.5

[76] Alfred P Weber and Sheldon K Friedlander. In situ determination of the activation energy for restructuring of nanometer aerosol agglomerates. *Journal of aerosol science*, 28(2):179–192, 1997. 2.1.5, 2.1.8

[77] Soleiman Bourrous, Quentin Ribeyre, Laura Lintis, Jérôme Yon, Sébastien Bau, Dominique Thomas, Cécile Vallières, and François-Xavier Ouf. A semi-automatic analysis tool for the determination of primary particle size, overlap coefficient and specific surface area of nanoparticles aggregates. *Journal of Aerosol Science*, 126:122–132, 2018. 2.1.7, 4.3.6, 5.1, 5.4.5, 5.7, 7.4.4.1, 7.4.4.2, 8, E.3.2.3, E.3.2.3, E.3.2.4, E.3.4.3

[78] Steven N Rogak and Richard C Flagan. Coagulation of aerosol agglomerates in the transition regime. *Journal of Colloid and Interface Science*, 151(1):203–224, 1992. 2.1.7, 4.3.2, 4.3.6, 4.4, 7.6

[79] Max L Eggersdorfer, Dirk Kadau, Hans J Herrmann, and Sotiris E Pratsinis. Aggregate morphology evolution by sintering: Number and diameter of primary particles. *Journal of aerosol science*, 46:7–19, 2012. 2.1.7, 5.1

[80] M Dadkhah, M Peglow, and E Tsotsas. Characterization of the internal morphology of agglomerates produced in a spray fluidized bed by x-ray tomography. *Powder technology*, 228:349–358, 2012. 2.1.8

[81] Laura H Van Poppel, Heiner Friedrich, Jacob Spinsby, Serena H Chung, John H Seinfeld, and Peter R Buseck. Electron tomography of nanoparticle clusters: Implications for atmospheric lifetimes and radiative forcing of soot. *Geophysical research letters*, 32(24), 2005. 2.1.8

[82] Kouji Adachi, Serena H Chung, Heiner Friedrich, and Peter R Buseck. Fractal parameters of individual soot particles determined using electron tomography: Implications for optical properties. *Journal of Geophysical Research: Atmospheres*, 112(D14), 2007.

[83] Gizem Okyay, E Héripré, T Reiss, P Haghi-Ashtiani, T Auger, and Franck Enguehard. Soot aggregate complex morphology: 3d geometry reconstruction by sem tomography applied on soot issued from propane combustion. *Journal of Aerosol Science*, 93:63–79, 2016.

[84] Alberto Baldelli, Una Trivanovic, and Steven N Rogak. Electron tomography of soot for validation of 2d image processing and observation of new structural features. *Aerosol Science and Technology*, 53(5):575–582, 2019. 2.1.8

[85] G Beaucage. Determination of branch fraction and minimum dimension of mass-fractal aggregates. *Physical Review E*, 70(3):031401, 2004. 2.1.8

[86] Andrew Mulderig, Gregory Beaucage, Karsten Vogtt, Hanqiu Jiang, and Vikram Kuppa. Quantification of branching in fumed silica. *Journal of Aerosol Science*, 109:28–37, 2017. 2.1.8

[87] Maria L Botero, Jethro Akroyd, Dongping Chen, Markus Kraft, and John R Agudelo. On the thermophoretic sampling and tem-based characterisation of soot particles in flames. *Carbon*, 171:711–722, 2021. 2.1.8

[88] José Morán, J Yon, F Liu, and A Fuentes. Thermophoretic sampling of soot in a laminar coflow diffusion flame. `https://doi.org/10.13140/RG.2.2.10340.94087`, 2019. 2.1.8, 2.1.8.1, 7.4.4.1

[89] Jérôme Yon, José Morán, Florian Lespinasse, Felipe Escudero, Gilles Godard, Marek Mazur, Fengshan Liu, and Andrés Fuentes. Horizontal planar angular light scattering (hpals) characterization of soot produced in a laminar axisymmetric coflow ethylene diffusion flame. *Combustion and Flame*, 232:111539, 2021. 2.1.8, **??**, 2.1.8.2, 7.2, 7.3.1, 7.4.2, 7.4.3, 7.6, 8, E.3.4.1, E.4

[90] Maxime Bouvier, Gilles Cabot, Jérôme Yon, and Frédéric Grisch. On the use of piv, lii, pah-plif and oh-plif for the study of soot formation and flame structure in a swirl stratified premixed ethylene/air flame. *Proceedings of the Combustion Institute*, 2020. 2.1.8

[91] F Patiño, JJ Cruz, I Verdugo, J Morán, JL Consalvi, F Liu, X Du, and A Fuentes. Soot primary particle sizing in a n-heptane doped methane/air laminar coflow diffusion flame by planar two-color tire-lii and tem image analysis. *Fuel*, 266:117030, 2020. 2.1.8.1, 2.1.8.3, 4.1, 4.2, 5.1, 5.2.3

[92] Christof Schulz, Boris F Kock, Max Hofmann, Hope Michelsen, Stefan Will, Bas Bougie, Rainer Suntz, and Greg Smallwood. Laser-induced incandescence: recent trends and current questions. *Applied Physics B*, 83(3):333–354, 2006. 2.1.8.3

[93] H.A. Michelsen, C. Schulz, G.J. Smallwood, and S. Will. Laser-induced incandescence: Particulate diagnostics for combustion, atmospheric, and industrial applications. *Progress in Energy and Combustion Science*, 51:2–48, dec 2015. 2.1.8.3, 2.1.9.3

[94] Hope A Michelsen, Fengshan Liu, Boris F Kock, Henrik Bladh, Andreï Boïarciuc, Marcus Charwath, Thomas Dreier, Redjem Hadef, Max Hofmann, Joerg Reimann, et al. Modeling laser-induced incandescence of soot: a summary and comparison of lii models. *Applied physics B*, 87(3):503–521, 2007. 2.1.8.3

[95] F Liu, DR Snelling, KA Thomson, and GJ Smallwood. Sensitivity and relative error analyses of soot temperature and volume fraction determined by two-color lii. *Applied Physics B*, 96(4):623–636, 2009. 2.1.8.3

[96] Christopher Betrancourt, Fengshan Liu, Pascale Desgroux, Xavier Mercier, Alessandro Faccinetto, Maurin Salamanca, Lena Ruwe, Katharina Kohse-Höinghaus, Daniel Emmrich, André Beyer, et al. Investigation of the size of the incandescent incipient soot particles in premixed sooting and nucleation flames of n-butane using lii, him, and 1 nm-smps. *Aerosol Science and Technology*, 51(8):916–935, 2017. 2.1.8.3, 4.1, 4.2, 5.3, 7.3.4.1

[97] Maxime Bouvier, J Yon, Guillaume Lefevre, and Frederic Grisch. A novel approach for in-situ soot size distribution measurement based on spectrally resolved light scattering. *Journal of Quantitative Spectroscopy and Radiative Transfer*, 225:58–68, 2019. 2.1.8.3, 4.4

[98] T Dreier and P Ewart. Applied combustion diagnostics, k. kohse-höinghaus and j. b. jeffries, 2002. 2.1.8.3

[99] Florian Meierhofer and Udo Fritsching. Synthesis of metal oxide nanoparticles in flame sprays: Review on process technology, modeling, and diagnostics. *Energy & Fuels*, 35(7):5495–5537, 2021. 2.2.1

[100] C Schulz, T Dreier, M Fikri, and H Wiggers. Gas-phase synthesis of functional nanomaterials: challenges to kinetics, diagnostics, and process development. *Proceedings of the Combustion Institute*, 37(1):83–108, 2019.

[101] Alberto Baldelli, Una Trivanovic, Timothy A Sipkens, and Steven N Rogak. On determining soot maturity: A review of the role of microscopy-and spectroscopy-based techniques. *Chemosphere*, 252:126532, 2020. 2.1.8.3, 6.1

[102] S. Lazzari, L. Nicoud, B. Jaquet, M. Lattuada, and M. Morbidelli. Fractal-like structures in colloid science. *Advances in Colloid and Interface Science*, 235:1–13, sep 2016. 2.1.9, 2.2, 2.2.3, 2.2.3.3, 2.5, 8

[103] Mihaela Osaci and Matteo Cacciola. Study about the nanoparticle agglomeration in a magnetic nanofluid by the Langevin dynamics simulation model using an effective Verlet-type algorithm. *Microfluidics and Nanofluidics*, 21(2):19, feb 2017. 2.1.9.1, 2.2.3.2

[104] D. Markauskas, R. Kačianauskas, and A. Maknickas. Numerical particle-based analysis of the effects responsible for acoustic particle agglomeration. *Advanced Powder Technology*, 26(3):698–704, may 2015. 2.1.9.1, 2.2.3.2

[105] G. Bertoni, B. Torre, A. Falqui, D. Fragouli, A. Athanassiou, and R. Cingolani. Nanochains Formation of Superparamagnetic Nanoparticles. *The Journal of Physical Chemistry C*, 115(15):7249–7254, apr 2011. 2.1.9.1

[106] Prithwish Biswas, Pankaj Ghildiyal, George W Mulholland, and Michael R Zachariah. Modelling and simulation of field directed linear assembly of aerosol particles. *Journal of Colloid and Interface Science*, 592:195–204, 2021. 2.1.9.1

[107] M. Y. Lin, H. M. Lindsay, D. A. Weitz, R. C. Ball, R. Klein, and P. Meakin. Universality in colloid aggregation. *Nature*, 339(6223):360–362, jun 1989. 2.1.9.1

[108] Swetlana Jungblut, Jan-Ole Joswig, and Alexander Eychmüller. Diffusion-and reaction-limited cluster aggregation revisited. *Physical Chemistry Chemical Physics*, 21(10):5723–5729, 2019. 2.1.9.1, 2.1.9.5, 2.2.3.1

[109] Pankaj Ghildiyal, Prithwish Biswas, Steven Herrera, George W Mulholland, Yong Yang, Reza Abbaschian, and Michael R Zachariah. Magnetic-field directed vapor-phase assembly of low fractal dimension metal nanostructures: Experiment and theory. *The Journal of Physical Chemistry Letters*, 12(16):4085–4091, 2021. 2.1.9.1

[110] Michael Balthasar and Michael Frenklach. Detailed kinetic modeling of soot aggregate formation in laminar premixed flames. *Combustion and Flame*, 140(1-2):130–145, 2005. 2.1.9.2, 5.1

[111] Belal Al Zaitone, Hans-Joachim Schmid, and Wolfgang Peukert. Simulation of structure and mobility of aggregates formed by simultaneous coagulation, sintering and surface growth. *Journal of aerosol science*, 40(11):950–964, 2009. 5.1, 5.4.2

[112] Georgios A Kelesidis, Eirini Goudeli, and Sotiris E Pratsinis. Flame synthesis of functional nanostructured materials and devices: Surface growth and aggregation. *Proceedings of the Combustion Institute*, 36(1):29–50, 2017. 2.1.9.2, 2.2, 2.2.3, 2.4.2, 3.2.2.5, 5.1, 5.4.6, 5.4.6, 5.5.1, 8

[113] Tamás Vicsek. *Fractal growth phenomena*. World scientific, 1992. 2.1.9.2

[114] ML Eggersdorfer, D Kadau, Hans Jürgen Herrmann, and Sotiris E Pratsinis. Fragmentation and restructuring of soft-agglomerates under shear. *Journal of colloid and interface science*, 342(2):261–268, 2010. 2.1.9.2

[115] Andrea Gastaldi and Marco Vanni. The distribution of stresses in rigid fractal-like aggregates in a uniform flow field. *Journal of colloid and interface science*, 357(1):18–30, 2011. 2.1.9.2

[116] Andrea D'Anna and Mariano Sirignano. Detailed kinetic mechanisms of pah and soot formation. In *Computer Aided Chemical Engineering*, volume 45, pages 647–672. Elsevier, 2019. 2.1.9.2, 2.4.1, 2.4.2, 2.4.5

[117] Georgios A Kelesidis and Sotiris E Pratsinis. Estimating the internal and surface oxidation of soot agglomerates. *Combustion and Flame*, 209:493–499, 2019. 2.1.9.2, 8

[118] Ray P Bambha and Hope A Michelsen. Effects of aggregate morphology and size on laser-induced incandescence and scattering from black carbon (mature soot). *Journal of Aerosol Science*, 88:159–181, 2015. 2.1.9.2, 5.1

[119] Fengshan Liu, Jérôme Yon, and Alexandre Bescond. On the radiative properties of soot aggregates – Part 2: Effects of coating. *Journal of Quantitative Spectroscopy and Radiative Transfer*, 172:134–145, mar 2016. 2.1.9.3

[120] J. Yon, F. Liu, J. Morán, and A. Fuentes. Impact of the primary particle polydispersity on the radiative properties of soot aggregates. *Proceedings of the Combustion Institute*, 37(1):1151–1159, jan 2019. 2.1.9.3

[121] Laigui Hu, Shaomin Wang, Binzhi Zhang, and Yuewu Zeng. Structural changes in soot particles induced by diode laser irradiation. *Carbon*, 44(9):1725–1729, 2006. 2.1.9.3

[122] Donggeun Lee and Mansoo Choi. Coalescence enhanced synthesis of nanoparticles to control size, morphology and crystalline phase at high concentrations. *Journal of Aerosol Science*, 33(1):1–16, jan 2002.

[123] Cheng Wang, Qing N Chan, Sanghoon Kook, Evatt R Hawkes, Jeonghoon Lee, and Paul R Medwell. External irradiation effect on the growth and evolution of in-flame soot species. *Carbon*, 102:161–171, 2016. 2.1.9.3

[124] Hua Wu, Marco Lattuada, and Massimo Morbidelli. Dependence of fractal dimension of DLCA clusters on size of primary particles. *Advances in Colloid and Interface Science*, 195-196:41–49, jul 2013. 2.1.9.4, 8

[125] M. Tence, J.P. Chevalier, and R. Jullien. On the measurement of the fractal dimension of aggregated particles by electron microscopy : experimental method, corrections and comparison with numerical models. *Journal de Physique*, 47(11):1989–1998, nov 1986. 2.1.9.4

[126] Graeme Bushell and Rose Amal. Fractal Aggregates of Polydisperse Particles. *Journal of Colloid and Interface Science*, 205(2):459–469, sep 1998. 2.1.9.4

[127] E. Goudeli, M. L. Eggersdorfer, and S. E. Pratsinis. Coagulation of Agglomerates Consisting of Polydisperse Primary Particles. *Langmuir*, 32(36):9276–9285, sep 2016. 2.1.9.4

[128] C Xiong and SK Friedlander. Morphological properties of atmospheric aerosol aggregates. *Proceedings of the National Academy of Sciences*, 98(21):11851–11856, 2001. 2.1.9.4

[129] P. Meakin and Z.R. Wasserman. Some universality properties associated with the cluster-cluster aggregation model. *Physics Letters A*, 103(6-7):337–341, jul 1984. 2.1.9.5

[130] Paul Meakin and Fereydoon Family. Structure and kinetics of reaction-limited aggregation. *Physical Review A*, 38(4):2110, 1988. 2.1.9.5, 6.4

[131] Swetlana Jungblut, Jan-Ole Joswig, and Alexander Eychmuüller. Diffusion-limited cluster aggregation: Impact of rotational diffusion. *The Journal of Physical Chemistry C*, 123(1):950–954, 2018. 2.1.9.5

[132] Hailing Xiong, Hang Li, Weiping Chen, Jian Xu, and Laosheng Wu. Application of the Cluster–Cluster Aggregation model to an open system. *Journal of Colloid and Interface Science*, 344(1):37–43, apr 2010. 2.1.9.6

[133] Ben Gigone, Ahmet E Karataş, and Ömer L Gülder. Soot aggregate morphology in coflow laminar ethylene diffusion flames at elevated pressures. *Proceedings of the Combustion Institute*, 37(1):841–848, 2019. 2.1.9.6

[134] Hafiz MF Amin, Anthony Bennett, and William L Roberts. Determining fractal properties of soot aggregates and primary particle size distribution in counterflow flames up to 10 atm. *Proceedings of the Combustion Institute*, 37(1):1161–1168, 2019.

[135] Mario Commodo, Ahmet E Karataş, Gianluigi De Falco, Patrizia Minutolo, Andrea D'Anna, and Ömer L Gülder. On the effect of pressure on soot nanostructure: A raman spectroscopy investigation. *Combustion and Flame*, 219:13–19, 2020.

[136] Hafiz MF Amin, Anthony Bennett, and William L Roberts. Morphology of soot sampled from n2-diluted methane/air counterflow flames at elevated pressures via tem imaging. *Combustion and Flame*, 216:92–99, 2020. 2.1.9.6

[137] Eric Dickinson. Structure and rheology of colloidal particle gels: Insight from computer simulation. *Advances in Colloid and Interface Science*, 199-200:114–127, nov 2013. 2.2, 2.2.3

[138] Paul Meakin. Progress in dla research. *Physica D: Nonlinear Phenomena*, 86(1):104 – 112, 1995. 2.2

[139] Francisco J Martos, Magín Lapuerta, Juan José Expósito, and Enrique Sanmiguel-Rojas. Overestimation of the fractal dimension from projections of soot agglomerates. *Powder Technology*, 311:528–536, 2017. 2.2

[140] José Morán, A Fuentes, F Liu, and J Yon. Fracval: An improved tunable algorithm of cluster–cluster aggregation for generation of fractal structures formed by polydisperse primary particles. *Computer Physics Communications*, 239:225–237, 2019. 2.2, 2.2.2, 3.2.2.3, 3.4, 4.3.5, 4.4, 5.4.7, 5.5.2, 6.2.3, 7.4.4.3

[141] AV Filippov, My Zurita, and DE Rosner. Fractal-like aggregates: relation between morphology and physical properties. *Journal of colloid and interface science*, 229(1):261–273, 2000. 2.2

[142] S Rigopoulos. Population balance modelling of polydispersed particles in reactive flows. *Progress in Energy and Combustion Science*, 36(4):412–443, 2010. 2.2, 2.2.1

[143] Ricardo I. Jeldres, Phillip D. Fawell, and Brendan J. Florio. Population balance modelling to describe the particle aggregation process: A review. *Powder Technology*, 326:190–207, feb 2018. 2.2, 2.2.1, 4.4

[144] M von Smoluchowski. Drei vortrage uber diffusion, brownsche bewegung und koagulation von kolloidteilchen. *Zeitschrift fur Physik*, 17:557–585, 1916. 2.2.1

[145] C.J. Meyer and D.A. Deglon. Particle collision modeling – A review. *Minerals Engineering*, 24(8):719–730, jul 2011. 2.2.1

[146] Tue Johannessen, Sotiris E. Pratsinis, and Hans Livbjerg. Computational fluid-particle dynamics for the flame synthesis of alumina particles. *Chemical Engineering Science*, 55(1):177–191, jan 2000. 2.2.1

[147] Chiara Saggese, Sara Ferrario, Joaquin Camacho, Alberto Cuoci, Alessio Frassoldati, Eliseo Ranzi, Hai Wang, and Tiziano Faravelli. Kinetic modeling of particle size distribution of soot in a premixed burner-stabilized stagnation ethylene flame. *Combustion and Flame*, 162(9):3356–3369, sep 2015. 2.2.1

[148] Nick A Eaves, Qingan Zhang, Fengshan Liu, Hongsheng Guo, Seth B Dworkin, and Murray J Thomson. Coflame: A refined and validated numerical algorithm for modeling sooting laminar coflow diffusion flames. *Computer Physics Communications*, 207:464–477, 2016. 2.2.1, 4.1, 5.7, 6.4, 7.1, 7.3.1, 8, E.3.2.4, E.3.4, E.3.4.1

[149] R Thouy and R Jullien. A cluster-cluster aggregation model with tunable fractal dimension. *Journal of Physics A: Mathematical and General*, 27(9):2953–2963, may 1994. 2.2.2

[150] Daniel W. Mackowski. Electrostatics analysis of radiative absorption by sphere clusters in the Rayleigh limit: application to soot particles. *Applied Optics*, 34(18):3535, jun 1995. 2.2.2

[151] Romain Thouy and Rémi Jullien. Structure Factors for Fractal Aggregates Built Off-Lattice with Tunable Fractal Dimension. *Journal de Physique I*, 6(10):1365–1376, oct 1996.

[152] Romain Thouy and Rémi Jullien. Geometrical properties of aggregates with tunable fractal dimension. *Journal of Physics A: Mathematical and General*, 30(19):6725–6735, oct 1997.

[153] Romain Thouy and Rémi Jullien. Structure and dynamics of fractal aggregates with tunable fractal dimension. *Philosophical Magazine B*, 77(2):321–331, feb 1998.

[154] A.V. Filippov, M. Zurita, and D.E. Rosner. Fractal-like Aggregates: Relation between Morphology and Physical Properties. *Journal of Colloid and Interface Science*, 229(1):261–273, sep 2000. 2.2.2

[155] Uwe Kätzel, Rainer Bedrich, Michael Stintz, Roland Ketzmerick, Torsten Gottschalk-Gaudig, and Herbert Barthel. Dynamic Light Scattering for the Characterization of Polydisperse Fractal Systems: I. Simulation of the Diffusional Behavior. *Particle & Particle Systems Characterization*, 25(1):9–18, apr 2008.

[156] Rajan K. Chakrabarty, Mark A. Garro, Shammah Chancellor, Christopher Herald, and Hans Moosmüller. FracMAP: A user-interactive package for performing simulation and orientation-specific morphology analysis of fractal-like solid nano-agglomerates. *Computer Physics Communications*, 180(8):1376–1381, aug 2009.

[157] Lyonel Ehrl, Miroslav Soos, and Marco Lattuada. Generation and Geometrical Analysis of Dense Clusters with Variable Fractal Dimension. *The Journal of Physical Chemistry B*, 113(31):10587–10599, aug 2009.

[158] Benjamin Gilbert, Reyn K. Ono, Kristen A. Ching, and Christopher S. Kim. The effects of nanoparticle aggregation processes on aggregate structure and metal uptake. *Journal of Colloid and Interface Science*, 339(2):285–295, nov 2009.

[159] Christian Ringl and Herbert M. Urbassek. A simple algorithm for constructing fractal aggregates with pre-determined fractal dimension. *Computer Physics Communications*, 184(7):1683–1685, jul 2013.

[160] E. Guesnet, R. Dendievel, D. Jauffrès, C.L. Martin, and B. Yrieix. A growth model for the generation of particle aggregates with tunable fractal dimension. *Physica A: Statistical Mechanics and its Applications*, 513:63–73, jan 2019. 2.2.2

[161] Krzysztof Skorupski, Janusz Mroczka, Thomas Wriedt, and Norbert Riefler. A fast and accurate implementation of tunable algorithms used for generation of fractal-like aggregate models. *Physica A: Statistical Mechanics and its Applications*, 404:106–117, jun 2014. 2.2.2

[162] J Yon, Fengshan Liu, J Morán, and Andres Fuentes. Impact of the primary particle polydispersity on the radiative properties of soot aggregates. *Proceedings of the Combustion Institute*, 37(1):1151–1159, 2019. 2.2.2

[163] Lucas Paulien, Romain Ceolato, Frédéric Fossard, Patrick Rairoux, and Alain Miffre. (uv, vis) laboratory evaluation of the lidar depolarization ratio of freshly emitted soot aggregates from pool fire in ambient air at exact backscattering angle. *Journal of Quantitative Spectroscopy and Radiative Transfer*, 260:107451, 2021.

[164] Ezgi Sutcu, Nimeti Doner, Fengshan Liu, Umran Ercetin, Fatih Sen, Jérôme Yon, Jose Morán, and Andrés Fuentes. Morphological and radiative characteristics of soot aggregates: Experimental and numerical research. *Scientific Reports*, 10(1):1–12, 2020. 5.1, 8

[165] Padryk Merkl, Shuzhi Zhou, Apostolos Zaganiaris, Mariam Shahata, Athina Eleftheraki, Thomas Thersleff, and Georgios A Sotiriou. Plasmonic coupling in silver nanoparticle aggregates and their polymer composite films for near-infrared photothermal biofilm eradication. *ACS applied nano materials*, 4(5):5330–5339, 2021. 2.2.2

[166] Abhinandan Kumar Singh and Evangelos Tsotsas. A tunable aggregation model incorporated in monte carlo simulations of spray fluidized bed agglomeration. *Powder Technology*, 364:417–428, 2020. 2.2.2, 4.4

[167] Reto Strobel and Sotiris E. Pratsinis. Flame aerosol synthesis of smart nanostructured materials. *Journal of Materials Chemistry*, 17(45):4743, nov 2007. 2.2.3

[168] Dieter Vollath. Plasma synthesis of nanopowders. *Journal of Nanoparticle Research*, 10(S1):39–57, dec 2008.

[169] Jan van Erven, David Munao, Zhao Fu, Tomek Trzeciak, Reyer Janssen, Erik Kelder, and Jan C. M. Marijnissen. The Improvement and Upscaling of a Laser Chemical Vapor Pyrolysis Reactor. *KONA Powder and Particle Journal*, 27(0):157–173, 2009. 2.2.3

[170] Paul Meakin. Formation of Fractal Clusters and Networks by Irreversible Diffusion-Limited Aggregation. *Physical Review Letters*, 51(13):1119–1122, sep 1983. 2.2.3.1, 2.2.3.3

[171] M. Kolb, R. Botet, and R. Jullien. Scaling of Kinetically Growing Clusters. *Physical Review Letters*, 51(13):1123–1126, sep 1983. 2.2.3.1, 2.2.3.3, 3.3

[172] R.C. Ball and R. Jullien. Finite size effects in cluster-cluster aggregation. *Journal de Physique Lettres*, 45(21):1031–1035, nov 1984. 2.2.3.1

[173] Paul Meakin and Fereydoon Family. Structure and dynamics of reaction-limited aggregation. *Physical Review A*, 36(11):5498, 1987. 2.2.3.1

[174] Raymond D Mountain, George W Mulholland, and Howard Baum. Simulation of aerosol agglomeration in the free molecular and continuum flow regimes. *Journal of Colloid and Interface Science*, 114(1):67–81, nov 1986. 2.2.3.2

[175] R. J. Samson, George W. Mulholland, and J. W. Gentry. Structural analysis of soot agglomerates. *Langmuir*, 3(2):272–281, mar 1987. 2.2.3.2

[176] Andreas Gutsch, Sotiris E. Pratsinis, and Friedrich Löfer. Agglomerate structure and growth rate by trajectory calculations of monomer-cluster collisions. *Journal of Aerosol Science*, 26(2):187–199, mar 1995. 2.2.3.2

[177] Ranganathan Gopalakrishnan, Thaseem Thajudeen, and Christopher J. Hogan. Collision limited reaction rates for arbitrarily shaped particles across the entire diffusive Knudsen number range. *The Journal of Chemical Physics*, 135(5):054302, aug 2011. 2.2.3.2, 5.4.8

[178] MC Heine and Sotiris E Pratsinis. Brownian coagulation at high concentration. *Langmuir*, 23(19):9882–9890, 2007. 2.2.3.2, 4.2, 4.3.2, 4.3.3

[179] B. Buesser, M.C. Heine, and S.E. Pratsinis. Coagulation of highly concentrated aerosols. *Journal of Aerosol Science*, 40(2):89–100, feb 2009.

[180] Tomasz M. Trzeciak, Albert Podgórski, and Jan C.M. Marijnissen. Brownian coagulation in dense systems: Thermal non-equilibrium effects. *Journal of Aerosol Science*, 69:1–12, mar 2014. 2.2.3.2

[181] P.V. Polovnikov, I.B. Azarov, and M.S. Veshchunov. Advancement of the kinetic approach to Brownian coagulation on the base of the Langevin theory. *Journal of Aerosol Science*, 96:14–23, jun 2016. 2.2.3.2

[182] Vikram Suresh and Ranganathan Gopalakrishnan. Tutorial: Langevin dynamics methods for aerosol particle trajectory simulations and collision rate constant modeling. *Journal of Aerosol Science*, 155:105746, 2021. 2.2.3.2

[183] G Inci, A Kronenburg, R Weeber, and D Pflüger. Langevin dynamics simulation of transport and aggregation of soot nano-particles in turbulent flows. *Flow, Turbulence and Combustion*, 98(4):1065–1085, 2017. 2.2.3.2, 5.1, 8

[184] Francis Sullivan and Raymond D. Mountain. An efficient algorithm for the brownian dynamics simulation of aggregation. *Computer Physics Communications*, 42(1):43–49, sep 1986. 2.2.3.2

[185] Lorenzo Isella and Yannis Drossinos. Langevin agglomeration of nanoparticles interacting via a central potential. *Physical Review E*, 82(1):011404, 2010. 2.2.3.2, 5.1, 8

[186] Alexandre Bouaniche, Jerome Yon, Pascale Domingo, and Luc Vervisch. Analysis of the soot particle size distribution in a laminar premixed flame: A hybrid stochastic/fixed-sectional approach. *Flow, Turbulence and Combustion*, 104(2):753–775, 2020. 2.2.3.3

[187] Casper S Lindberg, Manoel Y Manuputty, Jethro Akroyd, and Markus Kraft. A two-step simulation methodology for modelling stagnation flame synthesised aggregate nanoparticles. *Combustion and Flame*, 202:143–153, 2019. 2.2.3.3, 5.1, 5.2.3, 5.7, 7.3, 8

[188] Nicholas Metropolis, Arianna W. Rosenbluth, Marshall N. Rosenbluth, Augusta H. Teller, and Edward Teller. Equation of State Calculations by Fast Computing Machines. *The Journal of Chemical Physics*, 21(6):1087–1092, jun 1953. 2.2.3.3

[189] Michael P Allen and Dominic J Tildesley. *Computer simulation of liquids*. Oxford university press, 2017. 2.2.3.3

[190] Eric Dickinson and Stephen R. Euston. Monte Carlo simulation of colloidal systems. *Advances in Colloid and Interface Science*, 42:89–148, oct 1992. 2.2.3.3

[191] A. Satoh. *Introduction to molecular-microsimulation of colloidal dispersions*. Elsevier, 2003. 2.2.3.3

[192] Akira. Satoh. *Introduction to practice of molecular simulation : molecular dynamics, Monte Carlo, Brownian dynamics, Lattice Boltzmann, dissipative particle dynamics*. Elsevier, 2011. 2.2.3.3

[193] Akira Satoh. A new technique for metropolis Monte Carlo simulation to capture aggregate structures of fine particles: Cluster-moving Monte Carlo algorithm. *Journal of Colloid and Interface Science*, 150(2):461 – 472, 1992. 2.2.3.3

[194] Xiaoliang Deng, Zhonghui Huang, Wenqiang Wang, and Rajesh N Davé. Investigation of nanoparticle agglomerates properties using Monte Carlo simulations. *Advanced Powder Technology*, 27(5):1971–1979, sep 2016. 2.2.3.3, 5.1

[195] M. Kamal Akhtar, G. Glenn Lipscomb, and Sotiris E. Pratsinis. Monte Carlo Simulation of Particle Coagulation and Sintering. *Aerosol Science and Technology*, 21(1):83–93, jan 1994. 2.2.3.3

[196] K. Kikuchi, M. Yoshida, T. Maekawa, and H. Watanabe. Metropolis Monte Carlo method as a numerical technique to solve the Fokker—Planck equation. *Chemical Physics Letters*, 185(3-4):335–338, oct 1991. 2.2.3.3

[197] E. Sanz and D. Marenduzzo. Dynamic Monte Carlo versus Brownian dynamics: A comparison for self-diffusion and crystallization in colloidal fluids. *The Journal of Chemical Physics*, 132(19):194102, may 2010. 2.2.3.3

[198] Flavio Romano, Cristiano De Michele, Davide Marenduzzo, and Eduardo Sanz. Monte Carlo and event-driven dynamics of Brownian particles with orientational degrees of freedom. *The Journal of Chemical Physics*, 135(12):124106, sep 2011.

[199] Alessandro Patti and Alejandro Cuetos. Brownian dynamics and dynamic Monte Carlo simulations of isotropic and liquid crystal phases of anisotropic colloidal particles: A comparative study. *Physical Review E*, 86(1):011403, jul 2012.

[200] Alejandro Cuetos and Alessandro Patti. Equivalence of Brownian dynamics and dynamic Monte Carlo simulations in multicomponent colloidal suspensions. *Physical Review E*, 92(2):022302, aug 2015.

[201] Daniel Corbett, Alejandro Cuetos, Matthew Dennison, and Alessandro Patti. Dynamic Monte Carlo algorithm for out-of-equilibrium processes in colloidal dispersions. *Physical Chemistry Chemical Physics*, 20(22):15118–15127, jun 2018. 2.2.3.3

[202] B. Cichocki and K. Hinsen. Dynamic computer simulation of concentrated hard sphere suspensions: I. Simulation technique and mean square displacement data. *Physica A: Statistical Mechanics and its Applications*, 166(3):473–491, jul 1990. 2.2.3.3

[203] Anwar Hasmy, Marie Foret, Eric Anglaret, Jacques Pelous, René Vacher, and Rémi Jullien. Small-angle neutron scattering of aerogels: simulations and experiments. *Journal of Non-Crystalline Solids*, 186:118–130, jun 1995. 2.2.3.3

[204] Anwar Hasmy and Rémi Jullien. Sol-gel process simulation by cluster-cluster aggregation. *Journal of Non-Crystalline Solids*, 186:342–348, jun 1995.

[205] Anwar Hasmy. Aerogelation Process Simulation by a Cluster-Cluster Aggregation Algorithm. *Journal of Sol-Gel Science and Technology*, 15(2):137–146, 1999.

[206] Marco Lattuada, Hua Wu, Anwar Hasmy, and Massimo Morbidelli. Estimation of fractal dimension in colloidal gels. *Langmuir*, 19(15):6312–6316, 2003. 2.2.3.3

[207] Marco Lattuada and Lyonel Ehrl. Scattering Properties of Dense Clusters of Colloidal Nanoparticles. *The Journal of Physical Chemistry B*, 113(17):5938–5950, apr 2009. 2.2.3.3

[208] Songkil Kim, Kwang-Sung Lee, Michael R. Zachariah, and Donggeun Lee. Three-dimensional off-lattice Monte Carlo simulations on a direct relation between experimental process parameters and fractal dimension of colloidal aggregates. *Journal of Colloid and Interface Science*, 344(2):353–361, apr 2010. 2.5, 3.3

[209] S. Díez Orrite, S. Stoll, and P. Schurtenberger. Off-lattice Monte Carlo simulations of irreversible and reversible aggregation processes. *Soft Matter*, 1(5):364, oct 2005. 3.3

[210] Stefano Lazzari and Marco Lattuada. Growth and Aggregation Regulate Clusters Structural Properties and Gel Time. *The Journal of Physical Chemistry B*, 121(11):2511–2524, mar 2017. 2.2.3.3, 2.5, 3.3, 4.1, 5.1

[211] Jurgen Warnatz, Ulrich Maas, Robert W Dibble, and J Warnatz. *Combustion*. Springer, 2006. 2.3

[212] Andrea D'Anna. Combustion-formed nanoparticles. *Proceedings of the Combustion Institute*, 32(1):593–613, 2009. 2.3

[213] International Sooting Flame (ISF) Workshop. https://www.adelaide.edu.au/cet/isfworkshop/. Accessed: 2021-09-01. 2.3, 7.2

[214] Fokion N Egolfopoulos, Nils Hansen, Yiguang Ju, Katharina Kohse-Höinghaus, Chung King Law, and Fei Qi. Advances and challenges in laminar flame experiments and implications for combustion chemistry. *Progress in Energy and Combustion Science*, 43:36–67, 2014. 2.3

[215] Andrea D'Anna, Mariano Sirignano, and John Kent. A model of particle nucleation in premixed ethylene flames. *Combustion and flame*, 157(11):2106–2115, 2010. 2.3, 2.4.1, 5.3, 6.1, 6.3.1, 7.3.4.3, E.3.2.1

[216] Hai Wang. Formation of nascent soot and other condensed-phase materials in flames. *Proceedings of the Combustion institute*, 33(1):41–67, 2011. 2.3, 2.4.1

[217] Francisco Cepeda, Alejandro Jerez, Rodrigo Demarco, Fengshan Liu, and Andrés Fuentes. Influence of water-vapor in oxidizer stream on the sooting behavior for laminar coflow ethylene diffusion flames. *Combustion and Flame*, 210:114–125, 2019. 2.4, 7.3.1, E.3.4.1

[218] Jörg Appel, Henning Bockhorn, and Michael Frenklach. Kinetic modeling of soot formation with detailed chemistry and physics: laminar premixed flames of c2 hydrocarbons. *Combustion and flame*, 121(1-2):122–136, 2000. 2.4, 5.1, 7.2

[219] Hope A Michelsen, Meredith B Colket, Per-Erik Bengtsson, Andrea D'anna, Pascale Desgroux, Brian S Haynes, J Houston Miller, Graham J Nathan, Heinz Pitsch, and Hai Wang. A review of terminology used to describe soot formation and evolution under combustion and pyrolytic conditions. *ACS nano*, 14(10):12470–12490, 2020. 2.6, 2.4.4

[220] Michael Frenklach and Alexander M Mebel. On the mechanism of soot nucleation. *Physical Chemistry Chemical Physics*, 22(9):5314–5331, 2020. 2.4.1

[221] Charles A Schuetz and Michael Frenklach. Nucleation of soot: molecular dynamics simulations of pyrene dimerization. *Proceedings of the Combustion Institute*, 29(2):2307–2314, 2002. 2.4.1

[222] Angela Violi and Sergei Izvekov. Soot primary particle formation from multiscale coarse-grained molecular dynamics simulation. *Proceedings of the Combustion Institute*, 31(1):529–537, 2007. 2.4.1, 2.4.4, 7.3.4.2

[223] Steven L Fiedler, Sergei Izvekov, and Angela Violi. The effect of temperature on nanoparticle clustering. *Carbon*, 45(9):1786–1794, 2007.

[224] Qian Mao, Adri CT Van Duin, and KH Luo. Formation of incipient soot particles from polycyclic aromatic hydrocarbons: a reaxff molecular dynamics study. *Carbon*, 121:380–388, 2017. 2.4.1

[225] Angela Violi, Adel F Sarofim, and Gregory A Voth. Kinetic monte carlo–molecular dynamics approach to model soot inception. *Combust. Sci. Technol.*, 176(5-6):991–1005, 2004. 2.4.1

[226] Dongping Chen and Kai Hong Luo. Reactive sites on the surface of polycyclic aromatic hydrocarbon clusters: A numerical study. *Combustion and Flame*, 211:362–373, 2020.

[227] Kimberly Bowal, Laura Pascazio, Hongyu Wang, Dongping Chen, and Markus Kraft. Surface properties of heterogeneous polycyclic aromatic hydrocarbon clusters. *Proceedings of the Combustion Institute*, 38(1):1115–1123, 2021. 2.4.1

[228] Dongping Chen, Tim S Totton, Jethro WJ Akroyd, Sebastian Mosbach, and Markus Kraft. Size-dependent melting of polycyclic aromatic hydrocarbon nano-clusters: A molecular dynamics study. *Carbon*, 67:79–91, 2014. 2.4.1

[229] Laura Pascazio, Jacob W Martin, Kimberly Bowal, Jethro Akroyd, and Markus Kraft. Exploring the internal structure of soot particles using nanoindentation: A reactive molecular dynamics study. *Combustion and Flame*, 219:45–56, 2020. 2.4.1

[230] Akaash Sharma, Khaled Mosharraf Mukut, Somesh P Roy, and Eirini Goudeli. The coalescence of incipient soot clusters. *Carbon*, 180:215–225, 2021. 2.4.1, 7.3.4.2, 8

[231] Tim S Totton, Alston J Misquitta, and Markus Kraft. A quantitative study of the clustering of polycyclic aromatic hydrocarbons at high temperatures. *Physical Chemistry Chemical Physics*, 14(12):4081–4094, 2012. 2.4.1

[232] Sheldon K Friedlander et al. *Smoke, dust, and haze*, volume 198. Oxford university press New York, 2000. 2.4.2, 4.1, 4.3.2, 4.3.4, 8

[233] CM Sorensen and GD Feke. The morphology of macroscopic soot. *Aerosol Science and Technology*, 25(3):328–337, 1996. 2.4.2, 6.4

[234] Maximilian L Eggersdorfer and Sotiris E Pratsinis. Agglomerates and aggregates of nanoparticles made in the gas phase. *Advanced Powder Technology*, 25(1):71–90, 2014. 2.4.2, 4.3.4, 4.3.4

[235] F. Pierce, C. M. Sorensen, and A. Chakrabarti. Computer simulation of diffusion-limited cluster-cluster aggregation with an Epstein drag force. *Physical Review E*, 74(2):021411, aug 2006. 2.4.2, 3.3, 4.1, 4.1, 4.3.2, 4.3.4, 4.3.4, 4.4

[236] W. R. Heinson, F. Pierce, C. M. Sorensen, and A. Chakrabarti. Crossover from Ballistic to Epstein Diffusion in the Free-Molecular Regime. *Aerosol Science and Technology*, 48(7):738–746, jul 2014. 2.4.2, 2.5, 3.3, 4.1, 4.4, 8

[237] Michael Frenklach and Hai Wang. Detailed modeling of soot particle nucleation and growth. In *Symposium (International) on Combustion*, volume 23, pages 1559–1566. Citeseer, 1991. 2.4.3, 5.2.1

[238] Stephen J Harris. *Quantitative Chemical Mechanism for Heterogeneous Growth of Soot Particles in Premixed Flames*, chapter 2, pages 23–31. 2.4.3, 5.1, 5.3, 5.3, E.3.2.1

[239] Stephen J Harris. Surface growth and soot particle reactivity. *Combustion science and technology*, 72(1-3):67–77, 1990. 2.4.3, 5.3, 5.2, 5.3

[240] Dongping Chen, Jethro Akroyd, Sebastian Mosbach, and Markus Kraft. Surface reactivity of polycyclic aromatic hydrocarbon clusters. *Proceedings of the Combustion Institute*, 35(2):1811–1818, 2015. 2.4.3, 5.1, 5.2.1

[241] Xerxes López-Yglesias, Paul E Schrader, and Hope A Michelsen. Soot maturity and absorption cross sections. *Journal of Aerosol Science*, 75:43–64, 2014. 2.4.4

[242] Jérôme Yon, Juan José Cruz, Felipe Escudero, José Morán, Fengshan Liu, and Andrés Fuentes. Revealing soot maturity based on multi-wavelength absorption/emission measurements in laminar axisymmetric coflow ethylene diffusion flames. *Combustion and Flame*, 227:147–161, 2021. 2.4.4, 6.1, 7.2, 7.1, 7.4.1, 7.5, E.3.3, E.4

[243] Hope A Michelsen. Effects of maturity and temperature on soot density and specific heat. *Proceedings of the Combustion Institute*, 38(1):1197–1205, 2021. 2.4.4

[244] Jie Zhao, Yuyu Lin, Kai Huang, Mingyan Gu, Kun Lu, Ping Chen, Yang Wang, and Bencheng Zhu. Study on soot evolution under different hydrogen addition conditions at high temperature by reaxff molecular dynamics. *Fuel*, 262:116677, 2020. 2.4.4

[245] Mohammad Reza Kholghy, Armin Veshkini, and Murray John Thomson. The core–shell internal nanostructure of soot–a criterion to model soot maturity. *Carbon*, 100:508–536, 2016. 2.4.4, 7.3.1, E.3.4.1

[246] Dingyu Hou, Diyuan Zong, Casper S Lindberg, Markus Kraft, and Xiaoqing You. On the coagulation efficiency of carbonaceous nanoparticles. *Journal of Aerosol Science*, 140:105478, 2020. 2.4.4, 6.1, 6.2.1.1, 6.2.1.1, 6.2.1.2, 6.2.1.3, 6.3.2.1, 8, E.3.3

[247] Zhijie Huo, Matthew J Cleary, Mariano Sirignano, and Assaad R Masri. A sectional soot formation kinetics scheme with a new model for coagulation efficiency. *Combustion and Flame*, 230:111444, 2021. 2.4.4, 8

[248] Michael Frenklach, Zhenyuan Liu, Ravi I Singh, Galiya R Galimova, Valeriy N Azyazov, and Alexander M Mebel. Detailed, sterically-resolved modeling of soot oxidation: Role of o atoms, interplay with particle nanostructure, and emergence of inner particle burning. *Combustion and Flame*, 188:284–306, 2018. 2.4.5

[249] Mariano Sirignano, John Kent, and Andrea D'Anna. Modeling formation and oxidation of soot in nonpremixed flames. *Energy & fuels*, 27(4):2303–2315, 2013. 2.4.5

[250] Kurt Liffman. A direct simulation Monte-Carlo method for cluster coagulation. *Journal of Computational Physics*, 100(1):116–127, may 1992. 2.5, 3

[251] Matthew Smith and Themis Matsoukas. Constant-number Monte Carlo simulation of population balances. *Chemical Engineering Science*, 53(9):1777–1786, may 1998. 3, 3.3

[252] Michael Goodson and Markus Kraft. An efficient stochastic algorithm for simulating nano-particle dynamics. *Journal of Computational Physics*, 183(1):210–232, 2002. 2.5

[253] F Einar Kruis, Arkadi Maisels, and Heinz Fissan. Direct simulation monte carlo method for particle coagulation and aggregation. *AIChE Journal*, 46(9):1735–1742, 2000. 2.5

[254] Christophe Henry, Jean-Pierre Minier, Jacek Pozorski, and Gréegory Lefeévre. A new stochastic approach for the simulation of agglomeration between colloidal particles. *Langmuir*, 29(45):13694–13707, 2013. 2.5, 6.1

[255] Anwar Hasmy and Rémi Jullien. Sol-gel process simulation by cluster-cluster aggregation. *Journal of Non-Crystalline Solids*, 186:342–348, jun 1995. 2.5, 3.3

[256] Shinji Hayashi, Yutaka Hisaeda, Yuusuke Asakuma, Hideyuki Aoki, Takatoshi Miura, Hiroyuki Yano, and Yasuhisa Sawa. Simulation of soot aggregates formed by benzene pyrolysis. *Combustion and Flame*, 117(4):851–860, jun 1999. 2.5, 3.2.2.1, 3.2, 3.3

[257] M. D. Camejo, D. R. Espeso, and L. L. Bonilla. Influence of primary-particle density in the morphology of agglomerates. *Physical Review E*, 90(1):012306, jul 2014. 2.5, 3.3, 4.3.5, 5.1

[258] MM Maricq. Size and charge of soot particles in rich premixed ethylene flames. *Combustion and Flame*, 137(3):340–350, 2004. 2.5, 6.1, 6.2.1.2

[259] M Matti Maricq. Thermal equilibrium of soot charge distributions by coagulation. *Journal of Aerosol Science*, 39(2):141–149, 2008. 6.2.1.2

[260] AM Starik, AM Savel'ev, and NS Titova. Formation of charged nanoparticles in hydrocarbon flames: principal mechanisms. *Plasma Sources Science and Technology*, 17(4):045012, 2008. 2.5, 6.1, 6.2.1.2

[261] Nikolaj A Fuchs. *The mechanics of aerosols*. Dover Publications, 1989. 3.2.2.1, 3.3

[262] B Dahneke. Simple kinetic theory of brownian diffusion in vapors and aerosols. In *Theory of dispersed multiphase flow*, pages 97–133. Elsevier, 1983. 3.2.2.1, 3.3

[263] Albert Einstein. *Investigations on the Theory of the Brownian Movement*. Courier Corporation, 1956. 3.2.2.1, 3.2

[264] Subrahmanyan Chandrasekhar. Stochastic problems in physics and astronomy. *Reviews of modern physics*, 15(1):1, 1943. 3.2.2.2, 3.2.2.3, 3.3

[265] Tongcang Li, Simon Kheifets, David Medellin, and Mark G Raizen. Measurement of the instantaneous velocity of a brownian particle. *Science*, 328(5986):1673–1675, 2010. 3.2.2.2, 3.3

[266] Rongxin Huang, Isaac Chavez, Katja M Taute, Branimir Lukić, Sylvia Jeney, Mark G Raizen, and Ernst-Ludwig Florin. Direct observation of the full transition from ballistic to diffusive brownian motion in a liquid. *Nature Physics*, 7(7):576, 2011. 3.2.2.2, 3.3

[267] Michael D Allen and Otto G Raabe. Slip correction measurements of spherical solid aerosol particles in an improved millikan apparatus. *Aerosol Science and Technology*, 4(3):269–286, 1985. 3.2.2.3

[268] Computing Angle Between Vectors by james w. walker. https://www.jwwalker.com/pages/angle-between-vectors.html. Accessed: 2020-02-05. 3.2.2.3

[269] Xin Bian, Changho Kim, and George Em Karniadakis. 111 years of brownian motion. *Soft Matter*, 12(30):6331–6346, 2016. 3.3

[270] Riyan Zahaf, Song-Kil Kim, Juhwan Shin, Kihong Park, Tae-Youl Choi, and Donggeun Lee. Effect of Volume Fraction on Transient Structural Behavior of Aerosol Particles Using Off-Lattice Kinetic Monte Carlo Simulation. *Aerosol Science and Technology*, 49(12):1242–1255, dec 2015. 3.3, 4.1, 4.3.5, 5.1

[271] Lech Gmachowski. Fractal model of the transition from ballistic to diffusive motion of a brownian particle. *Journal of Aerosol Science*, 57:194–198, 2013. 3.3

[272] Anwar Hasmy. Aerogelation Process Simulation by a Cluster-Cluster Aggregation Algorithm. *Journal of Sol-Gel Science and Technology*, 15(2):137–146, 1999. 3.3

[273] Anwar Hasmy, Marie Foret, Eric Anglaret, Jacques Pelous, René Vacher, and Rémi Jullien. Small-angle neutron scattering of aerogels: simulations and experiments. *Journal of Non-Crystalline Solids*, 186:118–130, jun 1995. 3.3

[274] J Morán, J Yon, and A. Poux. Monte carlo aggregation code (mcac) part 1: Fundamentals. *Journal of Colloid and Interface Science*, 569:184 – 194, 2020. 4.1, 4.2, 4.3.5, 5.3

[275] RTFRJRA Puri, TF Richardson, RJ Santoro, and RA Dobbins. Aerosol dynamic processes of soot aggregates in a laminar ethene diffusion flame. *Combustion and flame*, 92(3):320–333, 1993. 4.1, 7.4.2

[276] Chr Feldermann, H Jander, and H Gg Wagner. Soot particle coagulation in premixed ethylene/air flames at 10 bar. *Zeitschrift für Physikalische Chemie*, 186(2):127–140, 1994. 4.1

[277] Andrei Kazakov and Michael Frenklach. Dynamic modeling of soot particle coagulation and aggregation: Implementation with the method of moments and application to high-pressure laminar premixed flames. *Combustion and flame*, 114(3-4):484–501, 1998. 4.1

[278] GM Wang and CM Sorensen. Aggregation kernel homogeneity for fractal aggregate aerosols in the slip regime. *Aerosol Science & Technology*, 34(3):297–306, 2001. 4.1, 4.3.4, 4.4

[279] DS Kim, SH Park, YM Song, DH Kim, and KW Lee. Brownian coagulation of polydisperse aerosols in the transition regime. *Journal of Aerosol Science*, 34(7):859–868, 2003. 4.1

[280] DS Kim, SB Hong, YJ Kim, and KW Lee. Deposition and coagulation of polydisperse nanoparticles by brownian motion and turbulence. *Journal of aerosol science*, 37(12):1781–1787, 2006. 4.1

[281] Paul E Wagner and Milton Kerker. Brownian coagulation of aerosols in rarefied gases. *The Journal of Chemical Physics*, 66(2):638–646, 1977. 4.1

[282] CN Davies. Coagulation of aerosols by brownian motion. *Journal of Aerosol Science*, 10(2):151–161, 1979. 4.1

[283] KW Lee and H Chen. Coagulation rate of polydisperse particles. *Aerosol Science and Technology*, 3(3):327–334, 1984.

[284] Ganesan Narsimhan and Eli Ruckenstein. The brownian coagulation of aerosols over the entire range of knudsen numbers: Connection between the sticking probability and the interaction forces. *Journal of colloid and interface science*, 104(2):344–369, 1985.

[285] David D Huang, John H Seinfeld, and William H Marlow. Bgk equation solution of coagulation for large knudsen number aerosols with a singular attractive contact potential. *Journal of colloid and interface science*, 140(1):258–276, 1990. 4.1

[286] Paul Meakin. A historical introduction to computer models for fractal aggregates. *Journal of Sol-Gel Science and Technology*, 15(2):97–117, 1999. 4.1, 4.3.5, 4.8, E.3.1.4, E.6

[287] Stefano Lazzari, Lucrèce Nicoud, Baptiste Jaquet, Marco Lattuada, and Massimo Morbidelli. Fractal-like structures in colloid science. *Advances in colloid and interface science*, 235:1–13, 2016. 4.3.5, 4.4

[288] Anthony Y Kim and John C Berg. Fractal aggregation: Scaling of fractal dimension with stability ratio. *Langmuir*, 16(5):2101–2104, 2000. 4.1

[289] Thaseem Thajudeen, Suhrid Deshmukh, and Christopher J Hogan Jr. Langevin simulation of aggregate formation in the transition regime. *Aerosol Science and Technology*, 49(2):115–125, 2015. 4.1, 4.4

[290] Fabian Schulz, Mario Commodo, Katharina Kaiser, Gianluigi De Falco, Patrizia Minutolo, Gerhard Meyer, DAnna Andrea, and Leo Gross. Insights into incipient soot formation by atomic force microscopy. *Proceedings of the Combustion Institute*, 37(1):885–892, 2019. 4.1

[291] Maria L Botero, Nick Eaves, Jochen AH Dreyer, Yuan Sheng, Jethro Akroyd, Wenming Yang, and Markus Kraft. Experimental and numerical study of the evolution of soot primary particles in a diffusion flame. *Proceedings of the Combustion Institute*, 37(2):2047–2055, 2019. 4.1

[292] Alejandro Jerez, Jean-Louis Consalvi, Andrés Fuentes, Fengshan Liu, and Rodrigo Demarco. Soot production modeling in a laminar coflow ethylene diffusion flame at different oxygen indices using a pah-based sectional model. *Fuel*, 231:404–416, 2018. 4.1, 7.3.1, E.3.4.1

[293] Pai Liu, William R Heinson, Christopher M Sorensen, and Rajan K Chakrabarty. Kinetics of sol-to-gel transition in irreversible particulate systems. *Journal of colloid and interface science*, 550:57–63, 2019. 4.1, 4.3.1, 4.4

[294] Raiya Husein Ebini and Christopher Michael Sorensen. Light scattering studies of the sol-to-gel transition in particulate systems. *Journal of colloid and interface science*, 556:577–583, 2019. 4.1, 4.4

[295] François Leyvraz. Scaling theory and exactly solved models in the kinetics of irreversible aggregation. *Physics Reports*, 383(2-3):95–212, 2003. 4.1

[296] F-X Ouf, S Bourrous, S Fauvel, A Kort, L Lintis, J Nuvoli, and J Yon. True density of combustion emitted particles: A comparison of results highlighting the influence of the organic contents. *Journal of Aerosol Science*, 134:1–13, 2019. 4.2, 5.3, 6.1, 6.3.1

[297] Yu Wang and Suk Ho Chung. Soot formation in laminar counterflow flames. *Progress in Energy and Combustion Science*, 74:152–238, 2019. 4.2, 7.2

[298] Agustin E Gonzalez, Mohammed Lach-Hab, and Estela Blaisten-Barojas. On the concentration dependence of the cluster fractal dimension in colloidal aggregation. *Journal of sol-gel science and technology*, 15(2):119–127, 1999. 4.2, 4.3.5

[299] Mingzhou Yu, Jianzhong Lin, Martin Seipenbusch, and Junji Cao. Verification of size-resolved population balance modeling for engineered nanoparticles under high concentration. *Chemical Engineering Journal*, 323:592–604, 2017. 4.4

[300] Peter Sandkühler, Jan Sefcik, and Massimo Morbidelli. Kinetics of aggregation and gel formation in concentrated polystyrene colloids. *The Journal of Physical Chemistry B*, 108(52):20105–20121, 2004. 4.2, 4.4

[301] Chen Gu, He Lin, Joaquin Camacho, Baiyang Lin, Can Shao, Ruoxin Li, Hao Gu, Bin Guan, Zhen Huang, and Hai Wang. Particle size distribution of nascent soot in lightly and heavily sooting premixed ethylene flames. *Combustion and Flame*, 165:177–187, 2016. 4.2

[302] E Otto, H Fissan, SH Park, and KW Lee. The log-normal size distribution theory of brownian aerosol coagulation for the entire particle size range: part ii—analytical solution using dahneke's coagulation kernel. *Journal of Aerosol Science*, 30(1):17–34, 1999. 4.3.2

[303] MS Veshchunov and VI Tarasov. Extension of the smoluchowski theory to transitions from dilute to dense regime of brownian coagulation: triple collisions. *Aerosol Science and Technology*, 48(8):813–821, 2014. 4.3.2

[304] M Matti Maricq. Coagulation dynamics of fractal-like soot aggregates. *Journal of aerosol science*, 38(2):141–156, 2007. 4.3.2, 4.3.4, 4.3.4, 4.4

[305] M Matti Maricq. Physical and chemical comparison of soot in hydrocarbon and biodiesel fuel diffusion flames: A study of model and commercial fuels. *Combustion and Flame*, 158(1):105–116, 2011. 4.3.4

[306] Srinivas Vemury and Sotiris E Pratsinis. Self-preserving size distributions of agglomerates. *Journal of Aerosol Science*, 26(2):175–185, 1995. 4.3.4

[307] PGJ Van Dongen and MH Ernst. Dynamic scaling in the kinetics of clustering. *Physical review letters*, 54(13):1396, 1985. 4.3.4, 4.4

[308] Kari EJ Lehtinen and Michael R Zachariah. Self-preserving theory for the volume distribution of particles undergoing brownian coagulation. *Journal of Colloid and Interface Science*, 242(2):314–318, 2001. 4.3.4

[309] Eckhard Otto, Frank Stratmann, Heinz Fissan, Srinivas Vemury, and Sotiris E Pratsinis. Quasi-self-preserving log-normal size distributions in the transition regime. *Particle & Particle Systems Characterization*, 11(5):359–366, 1994. 4.3.4

[310] Eirini Goudeli, Maximilian L Eggersdorfer, and Sotiris E Pratsinis. Coagulation of agglomerates consisting of polydisperse primary particles. *Langmuir*, 32(36):9276–9285, 2016. 4.3.4, 4.3.5

[311] Chloé Caumont-Prim, Jérôme Yon, Alexis Coppalle, François-Xavier Ouf, and Kuan Fang Ren. Measurement of aggregates' size distribution by angular light scattering. *Journal of Quantitative Spectroscopy and Radiative Transfer*, 126:140–149, 2013. 4.3.4, 4.4, 7.4.3, 7.6

[312] Graeme Bushell and Rose Amal. Fractal aggregates of polydisperse particles. *Journal of colloid and interface science*, 205(2):459–469, 1998. 4.3.5

[313] Lyonel Ehrl, Miroslav Soos, and Marco Lattuada. Generation and geometrical analysis of dense clusters with variable fractal dimension. *The Journal of Physical Chemistry B*, 113(31):10587–10599, 2009. 4.3.5, 4.3.5, 4.7, 4.4

[314] Lorenzo Isella and Yannis Drossinos. Langevin agglomeration of nanoparticles interacting via a central potential. *Physical Review E*, 82(1):011404, 2010. 4.3.5

[315] Max L Eggersdorfer and Sotiris E Pratsinis. The structure of agglomerates consisting of polydisperse particles. *Aerosol science and technology*, 46(3):347–353, 2012. 4.3.5

[316] Magín Lapuerta, Francisco J Martos, and Gema Martín-González. Geometrical determination of the lacunarity of agglomerates with integer fractal dimension. *Journal of colloid and interface science*, 346(1):23–31, 2010. 4.3.5, 6.4

[317] Hua Wu, Marco Lattuada, and Massimo Morbidelli. Dependence of fractal dimension of dlca clusters on size of primary particles. *Advances in colloid and interface science*, 195:41–49, 2013. 4.3.5, 4.8, 4.4, E.3.1.4, E.6

[318] Lech Gmachowski. The aerosol particle collision kernel considering the fractal model of particle motion. *Journal of Aerosol Science*, 59:47–56, 2013. 4.4

[319] PV Polovnikov, IB Azarov, and MS Veshchunov. Advancement of the kinetic approach to brownian coagulation on the base of the langevin theory. *Journal of Aerosol Science*, 96:14–23, 2016. 4.4

[320] John Gregory. Monitoring particle aggregation processes. *Advances in colloid and interface science*, 147:109–123, 2009. 4.4

[321] Hafiz MF Amin and William L Roberts. Investigating soot parameters in an ethane/air counterflow diffusion flame at elevated pressures. *Combustion Science and Technology*, 0(0):1–16, 2020. 4.4

[322] J Morán, J Yon, A Poux, F Corbin, F-X Ouf, and A Siméon. Monte carlo aggregation code (MCAC) part 2: Application to soot agglomeration, highlighting the importance of primary particles. *Journal of Colloid and Interface Science*, 575:274–285, 2020. 5.1, 5.3, 5.4.6, 5.4.6, 5.7

[323] M Wentzel, H Gorzawski, K-H Naumann, H Saathoff, and S Weinbruch. Transmission electron microscopical and aerosol dynamical characterization of soot aerosols. *Journal of aerosol science*, 34(10):1347–1370, 2003. 5.1, 5.2.3, 5.4.5, 5.7, E.3.2.4

[324] Michael Altenhoff, Simon Aßmann, Christian Teige, Franz JT Huber, and Stefan Will. An optimized evaluation strategy for a comprehensive morphological soot nanoparticle aggregate characterization by electron microscopy. *Journal of Aerosol Science*, 139:105470, 2020. 5.1, 5.3, 5.4.5, 5.4.6, 6.3.3, 7.4.4.3

[325] Stephen J Harris and Anita M Weiner. Chemical kinetics of soot particle growth. *Annual Review of Physical Chemistry*, 36(1):31–52, 1985. 5.1

[326] Pablo Mitchell and Michael Frenklach. Particle aggregation with simultaneous surface growth. *Physical Review E*, 67(6):061407, 2003. 5.1

[327] Neal Morgan, Markus Kraft, Michael Balthasar, David Wong, Michael Frenklach, and Pablo Mitchell. Numerical simulations of soot aggregation in premixed laminar flames. *Proceedings of the Combustion Institute*, 31(1):693–700, 2007. 5.1, 7.4.4.4, 8

[328] Kiminori Ono, Kazuki Dewa, Yoshiya Matsukawa, Yasuhiro Saito, Yohsuke Matsushita, Hideyuki Aoki, Koki Era, Takayuki Aoki, and Togo Yamaguchi. Experimental evidence for the sintering of primary soot particles. *Journal of Aerosol Science*, 105:1–9, 2017. 5.1, 8

[329] Dingyu Hou, Casper S Lindberg, Mengda Wang, Manoel Y Manuputty, Xiaoqing You, and Markus Kraft. Simulation of primary particle size distributions in a premixed ethylene stagnation flame. *Combustion and Flame*, 216:126–135, 2020. 5.1, 5.3, 8

[330] Nimeti Doner, Fengshan Liu, and Jérôme Yon. Impact of necking and overlapping on radiative properties of coated soot aggregates. *Aerosol Science and Technology*, 51(4):532–542, 2017. 5.1, 8

[331] Fengshan Liu, Barry J Stagg, David R Snelling, and Gregory J Smallwood. Effects of primary soot particle size distribution on the temperature of soot particles heated by a nanosecond pulsed laser in an atmospheric laminar diffusion flame. *International Journal of Heat and Mass Transfer*, 49(3-4):777–788, 2006. 5.1

[332] Jonathan Johnsson, Henrik Bladh, N-E Olofsson, and P-E Bengtsson. Influence of soot aggregate structure on particle sizing using laser-induced incandescence: importance of bridging between primary particles. *Applied Physics B*, 112(3):321–332, 2013. 5.1

[333] Armin Veshkini, Seth B Dworkin, and Murray J Thomson. A soot particle surface reactivity model applied to a wide range of laminar ethylene/air flames. *Combustion and flame*, 161(12):3191–3200, 2014. 5.1, 5.2.1

[334] Pablo Mitchell and Michael Frenklach. Monte carlo simulation of soot aggregation with simultaneous surface growth-why primary particles appear spherical. In *Symposium (International) on Combustion*, volume 27, pages 1507–1514. Elsevier, 1998. 5.1, 5.2.1, 7.3.4.2, 7.4.4.4

[335] Michael Balthasar and Michael Frenklach. Monte-carlo simulation of soot particle coagulation and aggregation: the effect of a realistic size distribution. *Proceedings of the Combustion Institute*, 30(1):1467–1475, 2005. 5.1

[336] Alfred P Weber and Sheldon K Friedlander. Relation between coordination number and fractal dimension of aerosol agglomerates. *Journal of Aerosol Science*, 1001(28):S765–S766, 1997. 5.1, 5.4.4

[337] H. Rumpf. Grundlagen und methoden des granulierens. *Chemie Ingenieur Technik*, 30(3):144–158, 1958. 5.1, 8

[338] M Gensch and AP Weber. Rebound behavior of nanoparticle-agglomerates. *Advanced Powder Technology*, 28(8):1930–1942, 2017.

[339] Patrick Post, M Bierwirth, and AP Weber. Mechanical stability measurements of surface modified nanoparticle agglomerates. *Journal of Aerosol Science*, 126:33–46, 2018. 5.1

[340] Ján Buša, Jozef Džurina, Edik Hayryan, Shura Hayryan, Chin-Kun Hu, Ján Plavka, Imrich Pokorný, Jaroslav Skřivánek, and Ming-Chya Wu. ARVO: A fortran package for computing the solvent accessible surface area and the excluded volume of overlapping spheres via analytic equations. *Computer physics communications*, 165(1):59–96, 2005. 5.1, 5.7

[341] Frederic Cazals, Harshad Kanhere, and Sébastien Loriot. Computing the volume of a union of balls: a certified algorithm. *ACM Transactions on Mathematical Software (TOMS)*, 38(1):1–20, 2011. 5.1, 5.4.7, 5.5.2, 5.7, 6.2.3, E.3.2.4

[342] Hans-Joachim Schmid, Belal Al-Zaitone, Christian Artelt, and Wolfgang Peukert. Evolution of the fractal dimension for simultaneous coagulation and sintering. *Chemical engineering science*, 61(1):293–305, 2006. 5.1

[343] Michael Frenklach. On surface growth mechanism of soot particles. In *Symposium (International) on Combustion*, volume 26, pages 2285–2293. Elsevier, 1996. 5.2.1

[344] C Russo, A Tregrossi, and A Ciajolo. Dehydrogenation and growth of soot in premixed flames. *Proceedings of the Combustion Institute*, 35(2):1803–1809, 2015. 5.2.1, 6.1

[345] Casper S Lindberg, Manoel Y Manuputty, Edward KY Yapp, Jethro Akroyd, Rong Xu, and Markus Kraft. A detailed particle model for polydisperse aggregate particles. *Journal of Computational Physics*, 397:108799, 2019. 5.2.3, 5.7, E.3.2.4

[346] George B Kauffman. *Alfred Werner: Founder of Coordination Chemistry*. Springer Science & Business Media, 2013. 5.2.3

[347] Anastasios D Melas, Lorenzo Isella, Athanasios G Konstandopoulos, and Yannis Drossinos. Morphology and mobility of synthetic colloidal aggregates. *Journal of colloid and interface science*, 417:27–36, 2014. 5.2.3

[348] Mariano Sirignano, Daniel Bartos, Marielena Conturso, Matthew Dunn, Andrea D'Anna, and Assaad R Masri. Detection of nanostructures and soot in laminar premixed flames. *Combustion and Flame*, 176:299–308, 2017. 5.3

[349] Aamir D Abid, Nicholas Heinz, Erik D Tolmachoff, Denis J Phares, Charles S Campbell, and Hai Wang. On evolution of particle size distribution functions of incipient soot in premixed ethylene–oxygen–argon flames. *Combustion and Flame*, 154(4):775–788, 2008. 5.3

[350] Steffen Salenbauch, Mariano Sirignano, Martin Pollack, Andrea D'Anna, and Christian Hasse. Detailed modeling of soot particle formation and comparison to optical diagnostics and size distribution measurements in premixed flames using a method of moments. *Fuel*, 222:287–293, 2018. 5.3

[351] A Prakash, AP Bapat, and MR Zachariah. A simple numerical algorithm and software for solution of nucleation, surface growth, and coagulation problems. *Aerosol Science & Technology*, 37(11):892–898, 2003. 5.3

[352] SH Park and SN Rogak. A novel fixed-sectional model for the formation and growth of aerosol agglomerates. *Journal of Aerosol Science*, 35(11):1385–1404, 2004. 5.4.2

[353] Christian Binder, Christian Feichtinger, Hans-Joachim Schmid, Nils Thürey, Wolfgang Peukert, and Ulrich Rüde. Simulation of the hydrodynamic drag of aggregated particles. *Journal of colloid and interface science*, 301(1):155–167, 2006. 5.4.2

[354] Jérôme Yon, F-X Ouf, Damien Hebert, James Brian Mitchell, Nadine Teuscher, Jean-Luc Le Garrec, Alexandre Bescond, Werner Baumann, Djoudi Ourdani, Thomas Bizien, and Javier Perez. Investigation of soot oxidation by coupling lii, saxs and scattering measurements. *Combustion and Flame*, 190:441 – 453, 2018. 5.4.6, 7.4.3

[355] Stavros Tsantilis and Sotiris E Pratsinis. Narrowing the size distribution of aerosol-made titania by surface growth and coagulation. *Journal of aerosol science*, 35(3):405–420, 2004. 5.4.6

[356] Jim Litster. *Design and processing of particulate products*. Cambridge University Press, 2016. 5.5

[357] F Einar Kruis, Karl A Kusters, Sotiris E Pratsinis, and Brian Scarlett. A simple model for the evolution of the characteristics of aggregate particles undergoing coagulation and sintering. *Aerosol science and technology*, 19(4):514–526, 1993. 5.5.1

[358] Michael Edward Mueller, Guillaume Blanquart, and Heinz Pitsch. A joint volume-surface model of soot aggregation with the method of moments. *Proceedings of the Combustion Institute*, 32(1):785–792, 2009. 5.5.1

[359] S Bau, O Witschger, F Gensdarmes, O Rastoix, and D Thomas. A tem-based method as an alternative to the bet method for measuring off-line the specific surface area of nanoaerosols. *Powder Technology*, 200(3):190–201, 2010. 5.7, E.3.2.4

[360] F-X Ouf, Soleiman Bourrous, Cécile Vallières, J Yon, and Laura Lintis. Specific surface area of combustion emitted particles: Impact of primary particle diameter and organic content. *Journal of Aerosol Science*, 137:105436, 2019. 5.7, 7.4.4.4, E.3.2.4

[361] S Tang, JM Preece, CM McFarlane, and Z Zhang. Fractal morphology and breakage of dlca and rlca aggregates. *Journal of Colloid Interface Science*, 221(1):114–123, 2000. 6.1

[362] Hope A Michelsen. Effects of maturity and temperature on soot density and specific heat. *Proceedings of the Combustion Institute*, 38(1):1197–1205, 2021. 6.1, 6.3.1

[363] A D'Alessio, AC Barone, R Cau, A D'Anna, and P Minutolo. Surface deposition and coagulation efficiency of combustion generated nanoparticles in the size range from 1 to 10 nm. *Proceedings of the Combustion Institute*, 30(2):2595–2603, 2005. 6.1, 8

[364] Alexander B Fialkov. Investigations on ions in flames. *Progress in Energy and Combustion Science*, 23(5-6):399–528, 1997. 6.1, 6.2.1.2

[365] Hartmut Mätzing, Werner Baumann, Henning Bockhorn, Hanns-Rudolf Paur, and Helmut Seifert. Detection of electrically charged soot particles in laminar premixed flames. *Combustion and Flame*, 159(3):1082–1089, 2012. 6.1

[366] Alexander M Starik, Alexander M Savel'ev, Natalia S Titova, and Ulrich Schumann. Modeling of sulfur gases and chemiions in aircraft engines. *Aerospace Science and Technology*, 6(1):63–81, 2002. 6.2.1.2

[367] AA Onischuk, S Di Stasio, VV Karasev, AM Baklanov, GA Makhov, AL Vlasenko, and et al. Evolution of structure and charge of soot aggregates during and after formation in a propane/air diffusion flame. *Journal of Aerosol Science*, 34(4):383–403, 2003. 6.2.1.2

[368] Michael Balthasar, Fabian Mauß, and H Wang. A computational study of the thermal ionization of soot particles and its effect on their growth in laminar premixed flames. *Combustion and Flame*, 129(1-2):204–216, 2002. 6.2.1.2

[369] M Matti Maricq. The dynamics of electrically charged soot particles in a premixed ethylene flame. *Combustion and Flame*, 141(4):406–416, 2005. 6.2.1.2, 6.3.2.2

[370] M Matti Maricq. A comparison of soot size and charge distributions from ethane, ethylene, acetylene, and benzene/ethylene premixed flames. *Combustion and Flame*, 144(4):730–743, 2006. 6.2.1.2

[371] J Prager, U Riedel, and J Warnatz. Modeling ion chemistry and charged species diffusion in lean methane–oxygen flames. *Proceedings of the Combustion Institute*, 31(1):1129–1137, 2007. 6.2.1.2

[372] Frank Babick, Karin Schießl, and Michael Stintz. van-der-waals interaction between two fractal aggregates. *Advanced Powder Technology*, 22(2):220–225, 2011. 6.2.1.3

[373] Christophe Henry, Jean-Pierre Minier, and Grégory Lefèvre. Towards a description of particulate fouling: From single particle deposition to clogging. *Advanced Colloid and Interface Science*, 185:34–76, 2012. 6.2.2

[374] Paul Meakin. Reaction-limited cluster-cluster aggregation in dimensionalities 2–10. *Physical Review A*, 38(9):4799, 1988. 6.2.3

[375] Stefano Lazzari and Marco Lattuada. Growth and aggregation regulate clusters structural properties and gel time. *Journal of Physical Chemistry B*, 121(11):2511–2524, 2017. 6.2.3

[376] José Morán, Alexandre Poux, and Jérôme Yon. Impact of the competition between aggregation and surface growth on the morphology of soot particles formed in an ethylene laminar premixed flame. *Journal of Aerosol Science*, 152:105690, 2021. 6.2.3, 6.2.3, 6.3.3

[377] J Yon, J Morán, F-X Ouf, M Mazur, and JB Mitchell. From monomers to agglomerates: A generalized model for characterizing the morphology of fractal-like clusters. *Journal of Aerosol Science*, 151:105628, 2021. 6.2.3, 6.3.3

[378] AD Abid, ED Tolmachoff, DJ Phares, H Wang, Y Liu, and A Laskin. Size distribution and morphology of nascent soot in premixed ethylene flames with and without benzene doping. *Proceedings of the Combustion Institute*, 32(1):681–688, 2009. 6.3.1

[379] S De Iuliis, S Maffi, F Migliorini, F Cignoli, and G Zizak. Effect of hydrogen addition on soot formation in an ethylene/air premixed flame. *Applied Physics B*, 106(3):707–715, 2012. 6.3.1, 6.3.3

[380] S De Iuliis, S Maffi, F Cignoli, and G Zizak. Three-angle scattering/extinction versus tem measurements on soot in premixed ethylene/air flame. *Applied Physics B*, 102(4):891–903, 2011. 6.3.3

[381] Constantine M Megaridis and Richard A Dobbins. Morphological description of flame-generated materials. *Combustion Science and Technology*, 71(1-3):95–109, 1990. 6.4

[382] DA Weitz, JS Huang, MY Lin, and J Sung. Limits of the fractal dimension for irreversible kinetic aggregation of gold colloids. *Physical Review Letters*, 54(13):1416, 1985. 6.4

[383] Lucien Gallen, Anne Felden, Eleonore Riber, and Bénédicte Cuenot. Lagrangian tracking of soot particles in les of gas turbines. *Proceedings of the Combustion Institute*, 37(4):5429–5436, 2019. 7.1, 7.6, 8, E.3.4, E.3.4.4, E.4

[384] Qingan Zhang. *Detailed modeling of soot formation/oxidation in laminar coflow diffusion flames*. University of Toronto Toronto, Canada, 2009. 7.2, 7.3.1

[385] Michael Frenklach and Hai Wang. Detailed mechanism and modeling of soot particle formation. In *Soot formation in combustion*, pages 165–192. Springer, 1994.

[386] A Jerez, JJ Cruz Villanueva, LF Figueira da Silva, R Demarco, and A Fuentes. Measurements and modeling of pah soot precursors in coflow ethylene/air laminar diffusion flames. *Fuel*, 236:452–460, 2019. 7.2

[387] RJ Santoro, TT Yeh, JJ Horvath, and HG Semerjian. The transport and growth of soot particles in laminar diffusion flames. *Combustion Science and Technology*, 53(2-3):89–115, 1987. 7.2, 7.1, E.3.4.1

[388] Christophe Henry, Jean-Pierre Minier, Mikaël Mohaupt, Christophe Profeta, Jacek Pozorski, and Anne Tanière. A stochastic approach for the simulation of collisions between colloidal particles at large time steps. *International journal of multiphase flow*, 61:94–107, 2014. 7.3

[389] Ali Naseri, Armin Veshkini, and Murray J Thomson. Detailed modeling of co2 addition effects on the evolution of soot particle size distribution functions in premixed laminar ethylene flames. *Combustion and Flame*, 183:75–87, 2017. 7.3.1, E.3.4.1

[390] Rodrigo Demarco, Alejandro Jerez, Fengshan Liu, Longfei Chen, and Andrés Fuentes. Modeling soot formation in laminar coflow ethylene inverse diffusion flames. *Combustion and Flame*, 232:111513, 2021. 7.3.1

[391] Nadezhda A Slavinskaya and Peter Frank. A modelling study of aromatic soot precursors formation in laminar methane and ethene flames. *Combustion and Flame*, 156(9):1705–1722, 2009. 7.3.1, E.3.4.1

[392] Seth B Dworkin, Qingan Zhang, Murray J Thomson, Nadezhda A Slavinskaya, and Uwe Riedel. Application of an enhanced pah growth model to soot formation in a laminar coflow ethylene/air diffusion flame. *Combustion and Flame*, 158(9):1682–1695, 2011. 7.3.1, E.3.4.1

[393] L Waldmann. Über die kraft eines inhomogenen gases auf kleine suspendierte kugeln. *Zeitschrift für Naturforschung A*, 14(7):589–599, 1959. 7.3.3

[394] Edouard Brugière, François Gensdarmes, François-Xavier Ouf, Jérôme Yon, Alexis Coppalle, and Denis Boulaud. Design and performance of a new device for the study of thermophoresis: The radial flow thermophoretic analyser. *Journal of aerosol science*, 61:1–12, 2013. 7.3.3

[395] E Brugière, F Gensdarmes, FX Ouf, J Yon, and A Coppalle. Increase in thermophoretic velocity of carbon aggregates as a function of particle size. *Journal of aerosol science*, 76:87–97, 2014. 7.3.3

[396] KG Neoh, JB Howard, and AF Sarofim. Soot oxidation in flames. In *Particulate Carbon*, pages 261–282. Springer, 1981. 7.4.2

[397] Anton D Sediako, Charles Soong, Jane Y Howe, Mohammad Reza Kholghy, and Murray J Thomson. Real-time observation of soot aggregate oxidation in an environmental transmission electron microscope. *Proceedings of the Combustion Institute*, 36(1):841–851, 2017. 7.4.2

[398] Pal Toth, Daniel Jacobsson, Martin Ek, and Henrik Wiinikka. Real-time, in situ, atomic scale observation of soot oxidation. *Carbon*, 145:149–160, 2019. 7.4.2

[399] Huaqiang Chu, Weiwei Han, Wenjian Cao, Changfa Tao, Mohsin Raza, and Longfei Chen. Experimental investigation of soot morphology and primary particle size along axial and radial direction of an ethylene diffusion flame via electron microscopy. *Journal of the Energy Institute*, 92(5):1294–1302, 2019. 7.4.3, 7.4.4.1, 7.6, E.3.4.3, E.3.4.4

[400] Mohammad Reza Kholghy, Meghdad Saffaripour, Christopher Yip, and Murray John Thomson. The evolution of soot morphology in a laminar coflow diffusion flame of a surrogate for jet a-1. *Combustion and Flame*, 160(10):2119–2130, 2013. E.4

[401] Mohammad Reza Kholghy, Jason Weingarten, Anton D Sediako, Javier Barba, Magín Lapuerta, and Murray J Thomson. Structural effects of biodiesel on soot formation in a laminar coflow diffusion flame. *Proceedings of the Combustion Institute*, 36(1):1321–1328, 2017.

[402] Maria L Botero, Yuan Sheng, Jethro Akroyd, Jacob Martin, Jochen AH Dreyer, Wenming Yang, and Markus Kraft. Internal structure of soot particles in a diffusion flame. *Carbon*, 141:635–642, 2019. 7.4.4.1, 7.6, E.3.4.3, E.3.4.4

[403] F Pierce, CM Sorensen, and A Chakrabarti. Computer simulation of diffusion-limited cluster-cluster aggregation with an epstein drag force. *Physical Review E*, 74(2):021411, 2006. 8

[404] Zongsheng Zhao, John C Crittenden, Hongchai Zhao, and Yongsheng Chen. The self-preserving size distribution of fractal aggregates coagulating by brownian motion and simultaneous fluid shear at low peclet numbers: numerical solutions. *Journal of Aerosol Science*, 87:1–16, 2015. 8

[405] Armin Veshkini, Seth B Dworkin, and Murray J Thomson. Understanding soot particle size evolution in laminar ethylene/air diffusion flames using novel soot coalescence models. *Combustion Theory and Modelling*, 20(4):707–734, 2016. 8

[406] Clément Argentin, Matthew J Berg, Marek Mazur, Romain Ceolato, and Jérôme Yon. Assessing the limits of rayleigh–debye–gans theory: Phasor analysis of a bisphere. *Journal of Quantitative Spectroscopy and Radiative Transfer*, 264:107550, 2021. 8

[407] Nicolas Dellinger, Nicolas Bertier, Francis Dupoirieux, and Guillaume Legros. Hybrid eulerian-lagrangian method for soot modelling applied to ethylene-air premixed flames. *Energy*, 194:116858, 2020. 8

[408] Binxuan Sun, Stelios Rigopoulos, and Anxiong Liu. Modelling of soot coalescence and aggregation with a two-population balance equation model and a conservative finite volume method. *Combustion and Flame*, 229:111382, 2021. 8

[409] Shraddha Shekar, William J Menz, Alastair J Smith, Markus Kraft, and Wolfgang Wagner. On a multivariate population balance model to describe the structure and composition of silica nanoparticles. *Computers & chemical engineering*, 43:130–147, 2012. 8

A | Supporting Material

In order to reduce the size of the present manuscript, Supporting Material has been included. In this companion document the different validations of numerical codes developed in this thesis are provided along with additional information about different subjects treated in this thesis.

Supporting Material contains the following sections,

S1 Langevin Dynamics simulations

S2 MCAC Fundamentals

S3 Agglomeration of nanoparticles

S4 Population Balance and MCAC comparison

S5 Surface growth modeling

S6 Soot maturity and collision efficiency

S7 Coupling MCAC-CFD

This document is accessible by scanning the following QR code (also clickable for the PDF version),

B | Numerical codes

B.1   Monte Carlo Aggregation Code

The updated version of MCAC is publicly available under the following website `https://gitlab.coria-cfd.fr/MCAC/MCAC`. In this website, the different versions of the code, associated with different stages of this thesis, are provided.

B.2   Population balance code

Population balance simulations have been conducted by using a developed C++ code, which is available under the following website `https://gitlab.com/jmoranc1/ngde_cpp.git`. This is a Git repository where contributions from anyone are welcome, and future developments of this code will hopefully be done.

C | Publications and Presentations

C.1 Referred publications

1. **Morán, J.**, Yon, J., & Poux, A. (2020). Monte Carlo aggregation code (MCAC) part 1: Fundamentals. *Journal of Colloid and Interface Science*, 569, 184-194.

2. **Morán, J.**, Yon, J., Poux, A., Corbin, F., Ouf, F. X., & Siméon, A. (2020). Monte Carlo Aggregation Code (MCAC) Part 2: Application to soot agglomeration, highlighting the importance of primary particles. *Journal of Colloid and Interface Science*, 575, 274-285.

3. **Morán, J.**, Poux, A., & Yon, J. (2021). Impact of the competition between aggregation and surface growth on the morphology of soot particles formed in an ethylene laminar premixed flame. *Journal of Aerosol Science*, 152, 105690.

4. **Morán, J.**, Henry, C., Poux, A., & Yon, J. (2021). Impact of the maturation process on soot particle aggregation kinetics and morphology. *Carbon*, 182, 837-846.

5. Yon, J., **Morán, J.**, Ouf, F. X., Mazur, M., & Mitchell, J. B. (2021). From monomers to agglomerates: A generalized model for characterizing the morphology of fractal-like clusters. *Journal of Aerosol Science*, 151, 105628.

6. Yon, J., Cruz, J. J., Escudero, F., **Morán, J.**, Liu, F., & Fuentes, A. (2021). Revealing soot maturity based on multi-wavelength absorption/emission measurements in laminar axisymmetric coflow ethylene diffusion flames. *Combustion and Flame*, 227, 147-161.

7. Yon, J., **Morán, J.**, Lespinasse, F., Escudero, F., Godard, G., Mazur, M., Liu, F., Fuentes, A. (2021). Horizontal Planar Angular Light Scattering (HPALS) characterization of soot produced in a Laminar Axisymmetric Coflow Ethylene Diffusion Flame. *Combustion and Flame*, 232, 111539.

C.2 Presentations

1. **J. Morán**, A. Poux, and J. Yon. "Soot particle formation under the competition between aggregation and surface growth". European Aerosol Conference - EAC 2021. 30 August - 3 September 2021, Birmingham, United Kingdom (on line).

2. **J. Morán**, C. Henry, A. Poux, and J. Yon. "Impact of the maturation process on soot particle aggregation kinetics and morphology". Cambridge Particle Meeting. June 2021. Cambridge, UK (on line).

3. **J. Morán**. "Soot aggregates: formation dynamics and morphology". Seminar (invited) for the Energy and Particle Technology Laboratory. June 2021. Ottawa, Canada (on line).

4. J. Yon, and **J. Morán**. *"Simulation de la formation des particules de suie : pour une meilleure caractérisation de ces particules"* at the 6th seminar (invited) of the Calisto group from INRIA, Sophia Antipolis, France.

5. **J. Morán**, J. Yon, and A. Poux. "The simultaneous aggregation and surface growth of soot particles formed in an ethylene laminar premixed flame". Congrès Francais sur les Aérosols - CFA. January 2021. Paris, France (On-line).

6. **J. Morán**, J. Yon, and A. Poux. "Numerical simulations of soot particles aggregation and surface growth in a premixed flame". First JDD du GDR Suie. December 2020. Paris, France (On-line).

7. **J. Morán**, J. Yon, and A. Poux. "The properties of the self-preserving size distribution of soot aggregates". Congrès Francais sur les Aérosols - CFA. January 2020. Paris, France. DOI: 10.25576/ASFERA-CFA2020-19711

8. **J. Morán**, J. Yon, and A. Poux. "Improving Monte Carlo simulations for an accurate modeling of soot aggregation". Reunion Plénière du GDR Suie. October 2019. Marseille, France. DOI: 10.13140/RG.2.2.16585.90723.

9. **J. Morán**, J. Yon, F. Liu and A. Fuentes. "Thermophoretic sampling of soot in a laminar coflow diffusion flame". GDR Suie sur la "Métrologie de suies". July 2019. Paris, France. DOI: 10.13140/RG.2.2.10340.94087.

10. **J. Morán**, A. Fuentes, F. Liu, and J. Yon, "FracVAL: An algorithm for the simulation of fractal-like aggregates of nanoparticles and subsequent numerical TEM images". 1st Franco-AMSUD Energy and Environment Meeting. March 18-21, 2019. Marseille, France. DOI: 10.13140/RG.2.2.34701.59368.

C.3   Posters

1. **J. Morán**, C. Henry, A. Poux, and J. Yon. "Impact of the maturation process on soot particle aggregation kinetics and morphology". European Aerosol Conference - EAC 2021. 30 August - 3 September 2021, Birmingham, United Kingdom (on line).

2. **J. Morán**, A. Poux, F. Liu, F. Escudero, A. Fuentes, and J. Yon. "Effects of overlapping in the evaluation of volume and surface area of complex soot aggregates in flames". 24th ETH-Conference on Combustion Generated Nanoparticles. June 2021. Zurich, Switzerland (on line). 10.13140/RG.2.2.33638.55364.

3. **J. Morán**, J. Yon, A. Poux, F. Liu, and A. Fuentes. "Improving Monte Carlo simulations for an accurate modeling of nanoparticles coagulation". European Aerosol Conference - EAC 2019. August 2019, Gothenburg, Sweden.

D | Curriculum Vitae

Education

PhD   Physics, at *Institut National des Sciences Appliquées INSA of Rouen*, Rouen, France.

Msc   Industrial Engineering (Thesis on Combustion), at *Universidad Técnica Federico Santa María*, Valparaíso, Chile. August 2017.

Bsc   Industrial Engineering, at *Universidad Técnica Federico Santa María*, Valparaíso, Chile. December 2014.

Experience

2019 - 2021   **Research assistant (2.5 years)** (as a PhD student) in the joint France-Chile project financed by ECOS-Sud and Conicyt (ECOS C19E01).

2019 - 2021   **Teaching assistant (96 h)** at INSA of Rouen, France.

2018   **Lecturer (70 h)** at *Universidad Adolfo Ibañes*, Chile.

2017 - 2018   **Research assistant (1 year)** at the EC^{2}G group, in Chile.

2014 - 2017   **Research assistant (3 years)** (as Msc. student) From 2016 to 2017, project Fondecyt 1161453. From 2014 to 2015, project Fondecyt 1130627. At *Universidad Técnica Federico Santa María*. Chile.

2013 - 2016   **Teaching and laboratory assistant (140 h)** at *Universidad Técnica Federico Santa María*. Chile.

2013 - 2014   **Research assistant (6 months)** at *Universidad Técnica Federico Santa María*.

Awards

- Laureate of the Jean Bricard prize given by ASFERA, at the *34ème Congrès Français sur les Aérosols*, Paris, France 2021 (on line).

- Best Poster Award at the 24th ETH Combustion Generated Nanoparticles Conference, Zurich, Switzerland 2021 (on line).

Community Service

2014   Volunteer for 3 months in AIESEC. Fortaleza, Brazil.

2013-2014   Volunteer for 1 year in *Voluntariado USM*. Valparaíso, Chile.

E | Synthèse en français

E.1 Introduction

Comme le montre la Fig. E.1, l'étude de la formation des particules de suie, avec un accent particulier sur la morphologie, a un impact remarquable dans 4 domaines : (1) la santé humaine, (2) l'atmosphère et la qualité de l'air, (3) les matériaux carbonés industriels, (4) les mesures expérimentales. Les particules de suie ont été identifiées comme le deuxième plus grand contributeur au réchauffement climatique, juste après le dioxyde de carbone. Lorsqu'elles sont libérées dans l'atmosphère, ces particules peuvent influencer la formation des nuages et modifier les propriétés radiatives de l'atmosphère [4]. Ces particules peuvent pénétrer profondément dans les poumons et même être cancérigènes [9]. Cependant, la suie n'est pas toujours mauvaise puisque la production industrielle de ces particules se fait à raison de plusieurs tonnes par jour. La plupart des applications actuelles (∼ 70%) concernent les pigments et les renforts de pneus. La morphologie et les propriétés physico-chimiques des particules de suie ont été mises en évidence comme étant les propriétés les plus importantes et les plus prometteuses pour d'éventuelles applications futures dans le domaine de l'exploitation des énergies renouvelables, notamment la séparation du dioxyde de carbone, les supercondensateurs, les batteries et le support de catalyseur dans les piles à combustible et les cellules solaires [3]. Enfin, une meilleure compréhension de la formation, de la composition et de la morphologie des particules de suie est nécessaire pour améliorer la précision des diagnostics expérimentaux basés sur l'interaction particule-lumière [14] ou l'analyse directe par microscopie électronique [15].
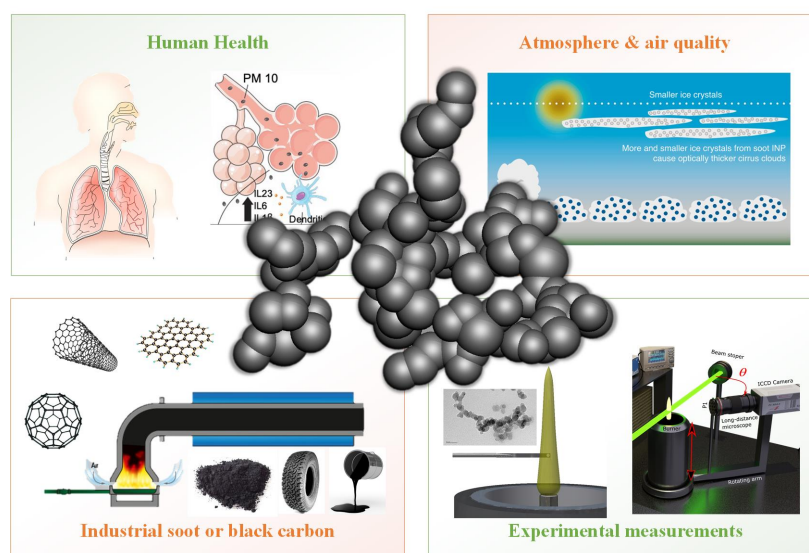

Figure E.1: Domaines d'impact des particules de suie.

L'une des propriétés les plus complexes des particules de suie est leur structure filamentaire de type fractal (voir Fig. E.1). Dans ce contexte, la plupart des codes numériques actuels basés sur le modèle

de bilan de population (Smoluchowski) négligent leur morphologie et considèrent que les particules sont sphériques. Les codes les plus avancés considèrent que les particules primaires sphériques se touchent ponctuellement et négligent la géométrie des contacts pouvant prendre la forme d'une gangue[6] et/ou d'un recouvrement[7]. Ces propriétés ont été négligées pendant longtemps dans la littérature en raison de leur faible importance apparente pour la dynamique des particules ou les taux de collision. Cependant, il existe différents phénomènes physiques très sensibles à ces propriétés, comme l'interaction particule-lumière [47]. De plus, une bonne prédiction des contacts géométriques des particules primaires est essentielle pour comprendre la fragmentation des particules et leur performance physico-chimique (réactions chimiques, transfert de chaleur et de masse). En raison des limites des modèles de bilan de population, de nouvelles approches sont nécessaires pour apporter des informations précises sur la morphologie des particules de suie et la dynamique de leur formation dans des conditions de flamme réelles. La modélisation par éléments discrets (MED), où la trajectoire de chaque particule individuelle est simulé, apparaît comme une alternative attrayante pour surmonter les limitations mentionnées avant. Les simulations MED prennent de plus en plus d'importance au fur et à mesure que des ressources informatiques plus importantes deviennent disponibles. Dans ce travail, un nouveau code MED de Monte Carlo appelé MCAC est présenté et ensuite utilisé pour étudier l'agglomération de la suie, et sa croissance de surface dans des flammes d'éthylène prémélange et diffusion.
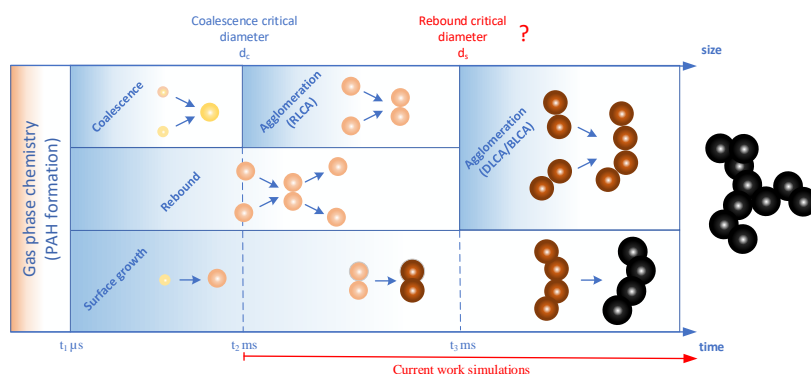
Figure E.2: Différents mécanismes et processus impliqués dans la formation de la suie dans les flammes.

Il est généralement admis de considérer les hydrocarbures aromatiques polycycliques (HAP) comme les précurseurs de la formation de suie lors d'une combustion riche en carburant. Les premiers noyaux de suie ont un diamètre d'environ 1 nm avec une morphologie sphérique, quasi liquide due à la coalescence (voir Fig. E.2). En même temps, la taille des particules augmente en raison de la croissance de surface où les molécules de HAP peuvent se condenser sur la surface des particules de suie et/ou le carbone est ajouté en même temps que l'hydrogène est evacué des particules (phénomène HACA). L'agglomération des particules peut se produire avec une probabilité donnée de collage en fonction de leur composition chimique (maturité), de leur taille, et de la température de la flamme. Les agglomérats peuvent expérimenter un changement de régime, passant d'une agglomération balistique et limitée par réaction à une agglomération proche du régime limitée par la diffusion. Enfin, ces particules peuvent être éventuellement oxydées, c'est-à-dire que des atomes de carbone dans les particules réagisent principalement avec l'oxygène et l'hydroxyle présents dans la phase gazeuse. Dans ce contexte, l'effet de changement du régime d'agglomération a reçu peu d'attention dans la littérature, et ses effets morphologiques restent incertains. L'effet de la probabilité de collage n'a pas été systématiquement étudié et le diamètre critique (d_s dans la Fig. E.2) pour considérer une probabilité de collage unitaire est actuellement inconnu. La majorité des études dans la littérature sont basées sur une description de la formation de la suie par le bilan de population qui ne prend pas en compte la morphologie des particules. L'évolution morphologique complexe des agrégats de suie dans les flammes a été étudiée par quelques travaux et une meilleure compréhension en termes d'impact sur la cinétique de croissance des particules, et la distribution de taille des particules nécessite plus de recherches. Le présent travail tente de

---

[6]*Necking* en anglais.
[7]*Overlapping* en anglais.

combler ces manques de connaissances.

E.2   Méthodes

Comme le montre la Fig. E.3, les simulations MCAC représentent l'évolution des particules de suie le long d'une ligne de courant donnée dans la flamme (ligne continue cyan). Cette ligne de courant déterminera un profil de température, la disponibilité des espèces gazeuses pour les réactions de surface, et la nucléation des particules de suie. Comme le montre la partie droite, au début de la simulation, les particules de suie sont considérées comme sphériques avec un certain degré de polydispersité en taille. Ces particules sont distribuées aléatoirement dans un domaine cubique en évitant l'intersection avec d'autres particules déjà présentes et en introduisant suffisamment de particules pour respecter une fraction volumique initiale connue. Le domaine est supposé être porté par l'écoulement, négligeant ainsi les effets d'inertie. Cette dernière est justifiée par la petite taille et la masse des particules de suie (arrivant rarement à l'ordre du micromètre). La trajectoire de chaque particule individuelle est intégrée sur la base d'un nouveau schéma de Monte Carlo (MCAC) trouvé en bon accord avec l'équation de Langevin.
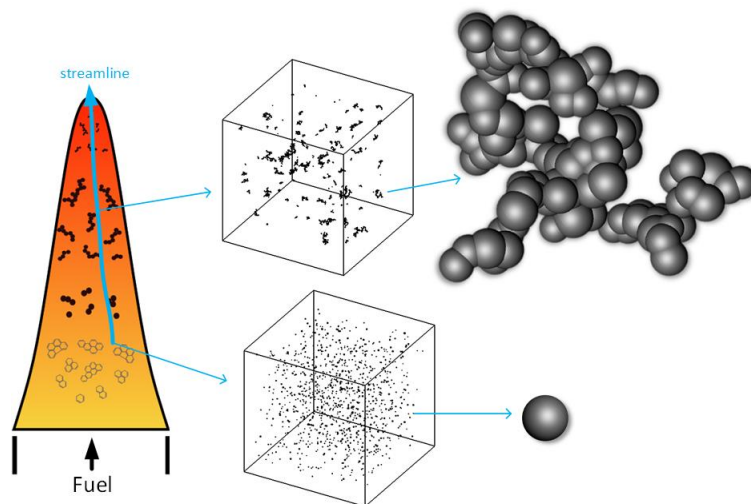

Figure E.3: Méthode de simulation MCAC.

Des conditions périodiques aux limites sont considérées. Nous laissons les particules s'agglomérer avec une probabilité de collage donnée lors des collisions. Ces dernières conduisent à la formation d'agglomérats comme celui montré dans la partie supérieure de la Figure E.3. En même temps que l'agrégation a lieu, la croissance de surface des particules de suie est prise en compte en simulant un flux de molécules qui augmentent continuellement la taille des particules primaires conduisant à leur recouvrement apparent comme observé sur cette figure.

E.2.1   Approche de Monte Carlo

Le code d'agrégation de Monte Carlo proposé (MCAC). Cette version du code est couplé avec des simulations CFD permettant la prise en compte de la nucléation, de la coagulation, de la croissance de surface et de l'oxydation des nanoparticules. Cette dernière peut conduire à la fragmentation des agrégats. Le code est décrit comme suit,

---

Code d'agrégation de Monte Carlo

Étape 1 : Au début de la simulation, les particules sont réparties de manière aléatoire dans une boîte cubique en évitant tout intersection entre elles.

Étape 2: Une particule est choisie au hasard avec une probabilité de prélèvement p.

Étape 3: La particule sélectionnée est déplacée dans une orientation aléatoire (θ) le long de sa distance persistante (λ_p) ou moins si une collision avec un voisin est détectée.

Étape 4: Si aucune collision n'est détectée, on passe à l'**Étape 5**. Dans le cas d'une collision, un nombre aléatoire (avec une distribution uniforme) $\delta \in [0,1]$ est généré et deux résultats possibles existent en fonction de la probabilité de collage q,

  Étape 4.1: Les deux particules se collent l'une à l'autre au premier point de contact lorsque $\delta \leq q$,

  Étape 4.2: Les particules rebondissent, c'est-à-dire qu'elles ne se collent pas et se heurtent élastiquement lorsque $\delta > q$.

Étape 5: La particule sélectionnée subit des réactions de surface. Cela signifie que ses particules primaires peuvent augmenter (croissance de surface) ou diminuer (oxydation) de taille. Ce dernier cas implique une vérification ultérieure de la fragmentation de l'agrégat.

  Étape 5.1: Si aucune fragmentation ne s'est produite, on passe à l'**Étape 6**.

  Étape 5.2: Sinon, l'agglomérat est fragmenté en 2 ou plusieurs petits morceaux (agrégat).

Étape 6: La nucléation, où les particules primaires sont introduites de manière aléatoire dans le domaine (en évitant l'intersection avec les voisins), peut avoir lieu.

Étape 7: Le taux de réaction de surface, le taux de nucléation, la température et la composition des particules sont mis à jour selon le couplage MCAC-CFD. Ce processus est répété de manière itérative à partir de l'**Étape 2** jusqu'à ce qu'un critère défini par l'utilisateur soit satisfait, par exemple, une limite du temps de résidence est atteinte.

Dans ce contexte, les méthodes MCAC détaillées sont,

- **Dynamique des particules** : La distance persistante des particules (λ_p) et le temps de résidence (Δt) correspondant des agrégats sont introduits,

$$\lambda_p = \sqrt{18D\tau}; \qquad \Delta t = 3\tau \tag{E.2.1}$$

où D est le coefficient de diffusion de la particule en (m^2/s), $\tau = m/f$ est le temps de relaxation de la quantité de mouvement en fonction de la masse de la particule (m) et du coefficient de friction (f). De plus, Δt est le temps mis par la particule pour parcourir la distance de persistance λ_p et simuler correctement le mouvement brownien de la particule. En outre, la probabilité de choisir la i'ème particule est,

$$p_i = \frac{\Delta t_i^{-1}}{\sum_j \Delta t_j^{-1}} \tag{E.2.2}$$

De plus, lorsque les agglomérats grandissent, ils peuvent subir un changement de régime d'écoulement, c'est-à-dire que la force de friction évolue d'une forme moléculaire libre ou d'Epstein ($f \sim R_m^2$) vers un continuum ou une forme de Stokes ($f \sim R_m$), où R_m est le rayon de mobilité et f le coefficient de friction. Ceci est pris en compte sur la base du modèle de Yon et al. [56]. Pour un agrégat constitué de $N_{p,eff}$ particules primaires,

$$f = f_p N_{p,eff}^{\Gamma/D_f} \tag{E.2.3}$$

où f_p est le coefficient de friction d'une particule primaire individuelle, D_f est la dimension fractale de l'agrégat, et Γ est une fonction dépendant du régime d'écoulement de la particule primaire. Ce dernier est déterminé par la thermodynamique du fluide et la taille de la particule primaire. Veuillez noter que lorsque les particules se recouvrent en raison de la croissance de surface, $N_{p,eff}$ est considéré comme un nombre effectif de particules primaires.

- **Probabilités de collage/collision** : Considéré comme le produit de deux probabilités.

$$q_1 = 1 - \mathrm{erf}\left(\sqrt{\widetilde{E_{bar}}}\right) + \sqrt{\widetilde{E_{bar}}}\exp\left[-\widetilde{E_{bar}}\right] \tag{E.2.4a}$$

$$q_2 = \text{erf}\left(\sqrt{\widetilde{E_{stick}}}\right) - \sqrt{\widetilde{E_{stick}}} \exp\left[-\widetilde{E_{stick}}\right] \tag{E.2.4b}$$

Où, $\text{erf}(x)$ est la fonction d'erreur d'une variable x. De plus, les E_{bar} et E_{stick} sont la barrière d'énergie électrostatique et l'énergie totale de collage (la somme de la valeur absolue du puits de potentiel et de la barrière d'énergie). La probabilité q_1 dépend de la composition chimique (maturité), de la taille et de la température des particules de suie. Et q_2 dépend des charges électriques des particules. En termes simples, une particule de suie petite et non mature (~ 2 nm de diamètre) a $q_1 \ll 1$, tandis qu'une particule mature plus grande (~ 12 nm de diamètre) a $q_1 \gg 1$. Les particules de charge égale se repoussent ($q_2 \ll 1$) tandis que la collision neutre-chargée ou neutre-neutre entraîne $q_2 \approx 1$.

- **Croissance de surface** Pendant un petit pas de temps Δt, la masse de la particule primaire augmente (Δm) en raison d'une densité de flux spécifique entrante φ en (kg/m^2/s) est,

$$\Delta m = \Delta v \rho_p = \int_S \varphi ds \cdot \Delta t \tag{E.2.5}$$

Où Δv et ρ_p sont l'augmentation du volume des particules et la masse volumique apparente, respectivement. De plus, S est la surface de la particule primaire exposée au flux entrant. Le rapport $\varphi/\rho_p = u$ est interprété comme la vitesse de croissance de surface en (m/s). En evaluant l'augmentation du volume de la particule primaire par $\Delta v = S \Delta r$, où Δr est l'augmentation de la taille de la particule primaire, on obtient l'expression suivante,

$$r(t + \Delta t) = r(t) + u \Delta t \tag{E.2.6}$$

- **Nucléation** : La naissance de particules primaires sphériques a lieu à un diamètre donné. Pour ce faire, on considère un flux de nucléation $\dot{\omega}_{nuc}$ en (kg/m^3/s) qui est multiplié par le volume de la boîte de simulation pour obtenir la masse totale à introduire, puis il est divisé par la masse des nucléi individuels pour déterminer la concentration en nombre de monomères (N) à nucléer à chaque pas de temps.

$$\frac{dN}{dt} = \frac{1}{m_{nuc}} \dot{\omega}_{nuc} \tag{E.2.7}$$

- **Oxydation** : Dans la version actuelle du code MCAC, l'oxydation est considérée comme le processus inverse de la croissance de surface et l'équation (E.2.6) est utilisée pour déterminer la taille des particules primaires lorsque le taux u est négatif. Ensuite, sur la base de la théorie des graphes, le chevauchement entre les particules primaires appartenant à un agrégat est vérifié et la fragmentation, où les agrégats sont divisés en plusieurs petits morceaux, peut avoir lieu.

E.2.2 Validation de la méthode proposée

La dynamique d'une population de particules primaires polydispersées sans interaction est en bon accord avec les simulations de Dynamique de Langevin. Cela signifie que le mouvement brownien des particules individuelles est correctement simulé et que le temps de résidence des particules individuelles est cohérent avec la méthode mentionnée. Le code est utilisé pour simuler l'agglomération de nanoparticules en suspension dans des conditions de flamme. Il est en bon accord avec la littérature en termes de noyaux de coagulation pour différents régimes d'agglomération (de balistique à diffusif). Le code est également comparé à une méthode nodale de bilan de population. Compte tenu de l'incertitude sur la morphologie des particules de cette dernière, l'accord entre les deux approches en termes de cinétique d'agglomération, de taille et de polydispersité des particules est considéré bon. Cependant, il existe de petites incertitudes liées à la prise en compte de la morphologie dans les codes de bilan de population.

La méthode proposée suppose un équilibrage thermique rapide des particules. La distance persistante proposée et le pas de temps correspondant considèrent que le mouvement des particules est toujours en équilibre thermique avec le fluide environnant. Du point de vue de la collision, cette hypothèse est valable lorsque $\tau \ll \tau_c$ où τ_c est le temps caractéristique de la collision. À chaque collision inélastique (agglomération), les

particules sont temporairement hors équilibre avec le gaz environnant et un certain temps est nécessaire pour atteindre cet équilibre. Si une collision subséquente arrive dans cette fenêtre de temps, alors l'hypothèse d'équilibre thermique dans l'approche proposée n'est pas respectée. Selon la littérature, cela ne peut devenir important que pour des fractions volumiques de particules extrêmement grandes, de l'ordre de 0.1%. Du point de vue des réactions de surface, $\tau \ll \tau_{sr}$ où τ_{sr} est le temps caractéristique des réactions de surface. Dans l'approche proposée, les particules sont déplacées et les réactions de surface ont lieu individuellement. Cela suppose intrinsèquement que les particules sont déplacées dans une échelle de temps où la mise à jour des autres voisins, et par conséquent les probabilités d'appel de particules, ne changent pas considérablement. Cette hypothèse est difficile à vérifier et, par la suite, certains tests ont été effectués en simulant la croissance de surface sur la base de réactions individuelles et de population sans trouver de différence significative. Ainsi, pour les simulations de suie dans des conditions de flamme où les fractions volumiques sont bien inférieures à la limite mentionnée précédemment, et où le temps de réaction en surface n'est pas trop rapide par rapport au temps de relaxation des particules, il n'y a pas de problème.

E.3 Résultats

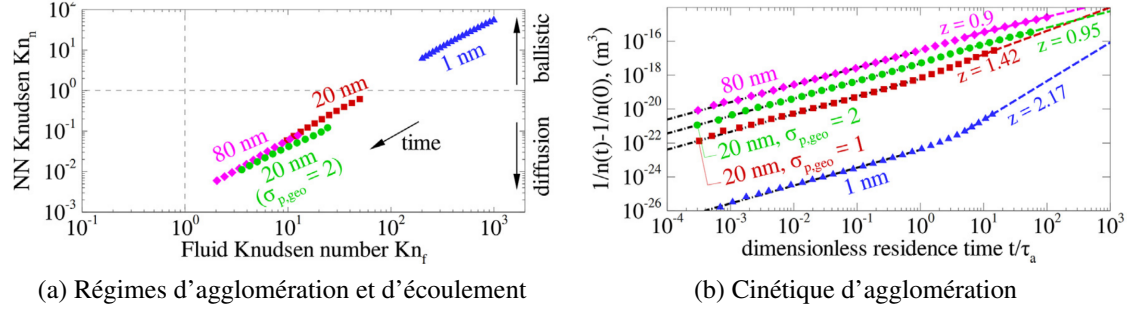### E.3.1 Agglomération de suie

E.3.1.1 Simulations

L'agglomération des particules de suie est tout d'abord considérée avec une masse volumique constante ρ_p = 1.8 g/cm³ aux conditions de flamme (pression atmosphérique et température de 1800 K). Le code décrit dans les sections précédentes est utilisé sans tenir compte des réactions de surface et la nucléation est considérée comme ayant cessé au début de ces simulations. L'agglomération a lieu lors de collisions de particules avec une probabilité de collage unitaire q = 1. Sauf indication contraire, les particules primaires sont de taille monodispersée avec un diamètre compris entre 1 et 80 nm. Ces paramètres sont représentatifs des particules de suie dans les flammes. Les particules sont considérées comme matures tout au long de la simulation et la variation temporelle de la masse volumique et des probabilités d'adhérence est négligée. Un total de 2048 particules est considéré par simulation et les résultats sont moyennés sur un total de 10 simulations pour chaque cas étudié.

E.3.1.2 Régimes et cinétique d'agglomération

La Figure E.4a présente les régimes d'agglomération (interaction particule-particule) et d'écoulement (interaction particule-gaz). Le premier est déterminé par le nombre de Knudsen des plus proches voisins $Kn_n = \lambda_p/R_n$ où $R_n \sim N^{-3}$ est la distance moyenne entre voisins, inversement proportionnelle au nombre de concentration totale de particules N. Le nombre de Knudsen du fluide $Kn_f = \lambda_f/R_m$ où λ_f est le libre parcours moyen du fluide qui est d'environ 66 nm pour l'air à température ambiante, et d'environ 498 nm pour l'air à la température de flamme. Sur cette figure, la transition simultanée des régimes d'écoulement et d'agglomération est observée pour différents diamètres et polydispersités de particules primaires. Les particules les plus petites, comme celles de 1 nm de diamètre, ont un mouvement très balistique et leur dynamique est déterminée par le régime d'écoulement moléculaire libre ou d'Epstein. Par ailleurs, les particules plus grandes, telles que celles monodispersées de 80 nm de diamètre, ont un mouvement très diffus et un régime d'écoulement proche du continuum à la température de la flamme.

La Figure E.4b, présente l'évolution de l'inverse de la concentration en nombre de particules présentant une évolution en loi de puissance avec le temps $1/N(t) \propto (t/\tau_a)^z$ où z est l'exposant cinétique, et τ_a est le temps caractéristique de l'agglomération. Au début du processus d'agglomération ($t/\tau_a \ll 1$), tous les cas montrent une évolution similaire dans le temps. Ceci s'explique par le fait que l'exposant cinétique est $z \sim 1$ pour les particules primaires sphériques et ne dépend pas fortement du régime d'agglomération. Au moment $t/\tau_a \approx 1$, une transition claire vers un processus dominé par l'agglomération est observée. À ce stade, l'exposant cinétique est déterminé par le régime d'agglomération / écoulement. L'agglomération

(a) Régimes d'agglomération et d'écoulement

(b) Cinétique d'agglomération

Figure E.4: Dynamique d'agglomération de la suie (la fraction volumique des particules est constante de 10 ppm).

moléculaire balistique / libre est très rapide et présente donc les plus grands exposants cinétiques. À l'opposé, les particules primaires plus grandes et plus lourdes (80 nm) présentent l'agglomération la plus lente avec un exposant cinétique non très différent de celui des sphères primaires.

E.3.1.3   Distribution de taille des particules

La figure E.5 présente la distribution granulométrique asymptotique ($t/\tau_a \gg 1$) des agrégats. C'est l'une des raisons pour lesquelles la simulation des agglomérats est si complexe. Comme on peut l'observer sur la figure, on trouve différentes formes de distributions pour les diamètres equivalent volume, de giration, et de mobilité. Ces distributions sont caractérisées par des écarts types géométriques et des moyennes géométriques différents selon les régimes d'agglomération et d'écoulement.
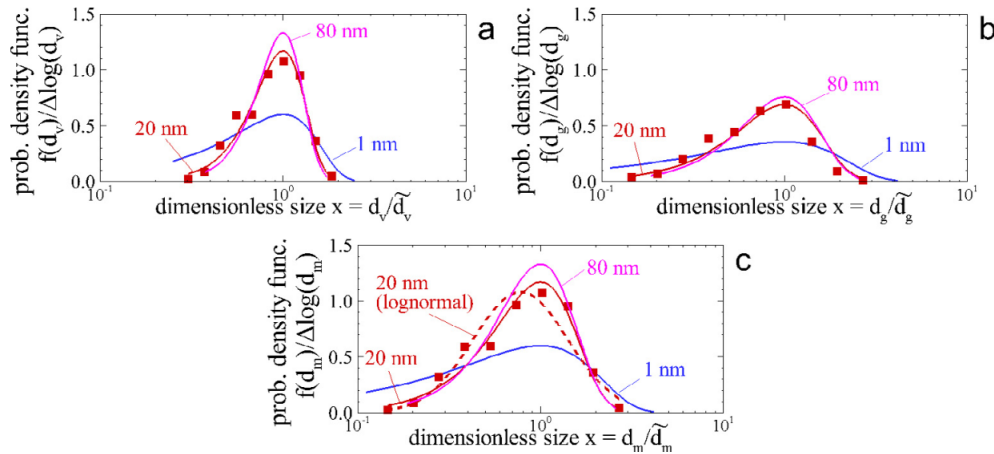
Figure E.5: Distribution asymptotique de la taille des particules exprimée en termes de (a) diamètre équivalent au volume, (b) diamètre de giration, et (c) diamètre de mobilité.

Connaître la distribution en termes d'un des diamètres mentionnés précédemment peut permettre de trouver la distribution en termes des autres diamètres, cependant il n'existe actuellement aucune méthode permettant cette conversion. Dans le présent travail, nous constatons que les différentes distributions de taille de particules suivent une distribution Gamma genéralisée,

$$f(x) = \frac{\left(p/a^d\right)}{x\Gamma(d/p)} X^{d-1} \exp\left[-\left(\frac{X}{a}\right)^p\right], \tag{E.3.8}$$

où $f(x)$ est la fonction de densité de probabilité de taille des particules. Ici, x correspond à l'un des quatre paramètres de taille considérés dans la présente étude (nombre de monomères, volume, giration, et diamètre de mobilité). Dans cette équation, $\Gamma(y) = \int_0^\infty t^{y-1} e^{-t} \, dt$ est la fonction Gamma, p est un paramètre de dimension,

$a = (1 - \lambda)^{-1/p}$, $d = p(1 - \lambda)$, et $X = x/\widetilde{x}$ est une grandeur sans dimension où $\widetilde{x} = (\overline{x^p})^{1/p}$. Ici, le paramètre clé est le coefficient d'homogénéité λ qui dépend de l'agglomération et du régime d'écoulement. La figure E.5 présente en ligne continue la distribution Gamma correspondant au régime auto-préservée. Cette dernière se trouve en meilleur accord avec les simulations qu'une distribution lognormale qui est typiquement observée dans les expériences.

E.3.1.4   Morphologie des agrégats

La morphologie des agrégats est étudiée en ajustant la loi de puissance fractale en fonction de la population de particules à chaque pas de temps de la simulation,

$$\frac{V_a}{V_p} \propto \left(\frac{D_g}{D_p}\right)^{D_f} \tag{E.3.9}$$

Où V_a et V_p sont le volume moyen de l'agrégat et de la particule primaire, respectivement. De même, D_g et D_p représentent respectivement le diamètre de giration et le diamètre moyen des particules primaires. Enfin, D_f et k_f est la dimension fractale et prefacteur, respectivement. Dans la Figure E.6, la dimension fractale asymptotique ($t/\tau_a \gg 1$) est rapportée en fonction du diamètre des particules primaires. Tout d'abord, les valeurs obtenus sont inférieures à celles classiquement rapportées pour l'agglomération limitée par des collisions balistiques (BLCA) mais aussi, elles peuvent aller en dessous de l'agglomération limitée par des collisions diffusives (DLCA) en accordance avec Meakin [286]. Cette observation est cohérente avec les particules échantillonnées expérimentalement dans différents types de colloïdes [317].
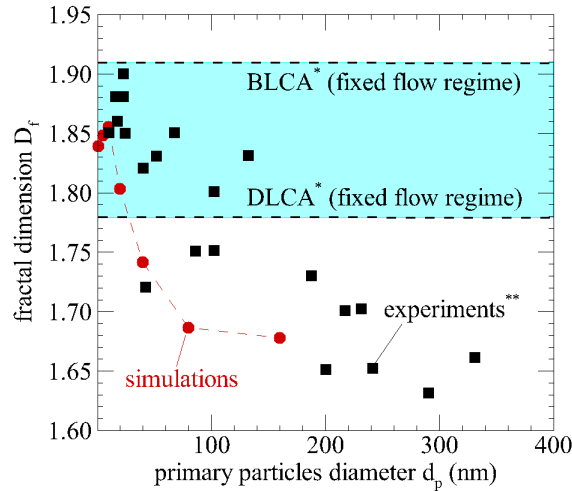
Figure E.6: Dimension fractale asymptotique en fonction du diamètre des particules primaires. Comparaison avec les limites BLCA (D_f = 1.91) et DLCA (D_f = 1.78) pour des régimes d'écoulement fixes [286] (*) et des mesures expérimentales [317] (**).

E.3.1.5   Conclusions

Le changement simultané des régimes d'écoulement et d'agglomération pour la formation de nanoparticules dans des conditions de flamme n'a pas été systématiquement étudié dans la littérature. Dans le présent travail, cette dépendance est étudiée en fonction de différentes tailles de particules primaires en considérant leur polydispersité. Ceci a un impact significatif sur la cinétique d'agglomération ; en effet, l'exposant cinétique peut augmenter d'un facteur 2 lorsque l'agglomération passe du régime diffusif au régime balistique. La distribution de taille des particules est également affectée par les régimes d'écoulement et d'agglomération.

Une expression unifiée a été proposée pour décrire la distribution de taille auto-préservée des nanoparticules telle qu'elle est atteinte pour les particules de suie sous différents régimes d'agglomération et d'écoulement. Enfin, un effet significatif sur la morphologie est également observé en fonction de la taille des particules primaires et donc de l'agglomération des particules et des régimes d'écoulement. La dimension fractale est inversement corrélée à la taille des particules primaires et des valeurs inférieures à la limite de diffusion sont ainsi déterminées.

E.3.2   Agglomération et croissance de surface de la suie

E.3.2.1   Simulations

Un environnement de flamme prémélangée d'éthylène tel qu'étudié par Harris [238] est considéré pour simuler l'agrégation et la croissance de surface simultanées des particules de suie. Dans ce contexte, une température constante de 1700 K et la pression ambiante sont considérées. Le flux de croissance de surface mesuré expérimentalement en fonction du temps est considéré comme basé sur ce travail en supposant une masse volumique de suie constante de 1.8 g/cm^3. Les cas seront référencés tout au long de ce manuscrit en termes de taux initial de croissance de surface, c'est-à-dire $u_0 = 0.4$ nm/ms correspondant à une flamme ayant un rapport C/O=0.82, et $u_0 = 0.6$ nm/ms correspondant à C/O=0.94 tel que mesuré expérimentalement par Harris [238]. Comme cas de référence, une agrégation pure sans croissance de surface est également simulée (référencés $u = 0$). En considérant les données expérimentales disponibles, les simulations couvrent la gamme $8.3 - 30$ ms en temps de résidence, correspondant approximativement à $5 - 25$ mm en termes de hauteur au-dessus du brûleur. Au temps de résidence initial (8.3 ms), l'agglomération des particules de suie peut être négligée en raison de la coalescence des particules après la collision [215]. Dans ce contexte, la distribution initiale de la taille des particules primaires est considérée comme lognormale avec une moyenne géométrique de 8 nm, et un écart type géométrique $\sigma_{p,geo} = 1.2$ en accord avec les données des flammes d'éthylène prémélangées. La fraction volumique initiale de suie est de $f_v = 0.118$ ppm pour tous les cas sauf un cas ayant $u_0 = 0.6$ nm/ms, où $f_v = 0.357$ ppm est considéré. Pour chaque cas simulé, un total de 1024 particules primaires est considéré au début de la simulation et un total de 10 simulations est effectué par condition. Les résultats rapportés ultérieurement sont moyennés sur 10 simulations. Le cas de référence ($u = 0$) a été validé avec succès par comparaison avec des simulations macroscopiques de Bilan de Population en termes de cinétique d'agrégation et de distribution de taille des particules.

E.3.2.2   Fraction volumique de la suie et cinétique d'agglomération

Comme le montre la Fig. E.7a, les fractions volumiques de suie augmentent dans le temps en raison du transfert de masse avec la phase gazeuse. L'augmentation de f_v est proportionnelle au taux de croissance de surface et ne semble pas dépendre fortement de la valeur initiale de f_v puisque les deux cas correspondant à $u_0 = 0.6$ montrent une augmentation en pourcentage presque équivalentes dans le temps. Il est important de noter que négliger la croissance de surface peut conduire à un facteur 10 dans la determination de la fraction de volume de particules. La Fig. E.7b montre l'effet de la croissance de surface sur l'inverse de la concentration en nombre d'agrégats $1/N(t)$ en fonction du temps. Pour tous les cas correspondant à $f_v = 0.118$ initial, aucune différence significative n'est observée jusqu'à un temps de résidence d'environ 15 ms, ce qui montre bien que la croissance de surface est plus forte au début, elle n'est pas capable de changer la cinétique des petits agrégats constitués de quelques monomères ou de monomères isolés. De plus, à court terme, la fraction volumique initiale des particules semble beaucoup plus importante en termes de cinétique d'agrégation. L'exposant cinétique (z) rapporté pour des temps de séjour plus avancés montre une dégradation de la cinétique d'agrégation produite par la croissance de surface.

E.3.2.3   Morphologie de suie

La Fig. E.7c montre l'évolution du nombre de coordinence moyen de la population $\overline{n_c}$ en fonction du temps. Tout d'abord, nous constatons qu'il augmente de façon monotone dans le temps pour atteindre une valeur
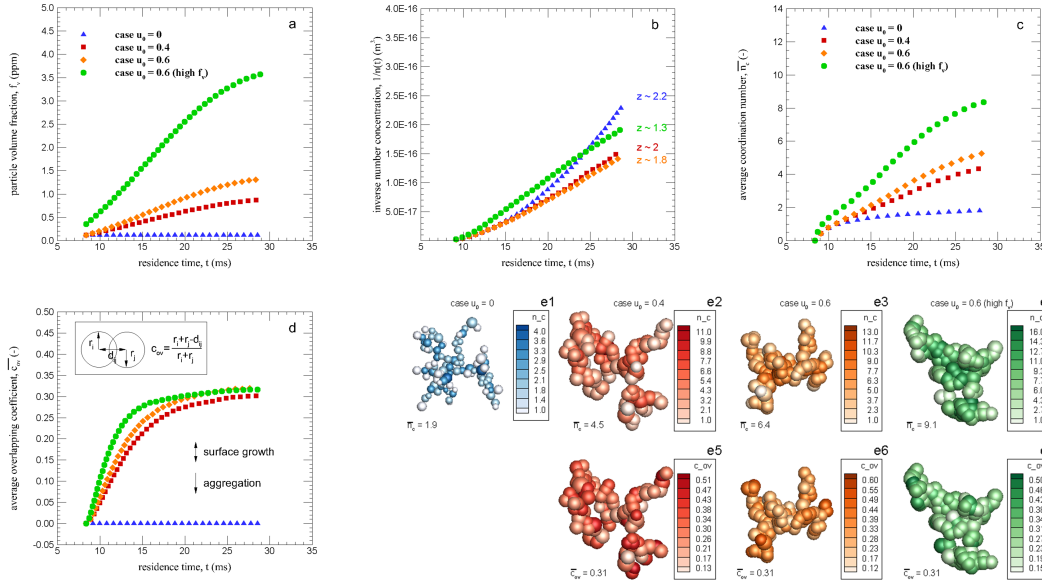
Figure E.7: Fraction volumique de la suie (a), inverse de la concentration du nombre de particules (b), nombre de coordinance moyenne (c), coefficient de recouvrement moyen (d) en fonction du temps. Nombre de coordinance locale (e1-e4), et coefficient de recouvrement local (e5-e7).

asymptotique de 2 lorsqu'il n'y a pas de croissance de surface [53]. Cependant, lorsque la croissance de surface est présente, cette valeur peut augmenter jusqu'à $3 - 8$ en fonction du taux de croissance de surface et de la fraction volumique initiale des particules. La plus grande valeur de $\overline{n_c}$ observée pour le cas $u_0 = 0.6$ (haute f_v) n'est pas liée à la morphologie des particules, elle est plutôt liée à l'amélioration de la cinétique d'agrégation qui conduit à une augmentation rapide de la taille des agrégats par rapport aux autres cas. Bien que la coordinances moyennes maximales soient compris entre 2 et 8, les valeurs locales observées sur la Fig. E.7(e1-e4) peuvent atteindre 16. Cela signifie que la croissance de surface produit une interaction très complexe entre les monomères et augmente considérablement la compacité des particules primaires.

Enfin, la Fig. E.7d rapporte l'évolution temporelle du coefficient de recouvrement moyen de la population $\overline{c_{ov}}$. Ce paramètre est mesuré comme $c_{ov} = (r_i + r_j - d_{ij})/(r_i + r_j)$, où $r_i + r_j$ est la somme des rayons des particules primaires et d_{ij} la distance entre leurs centres. Lorsque les particules ne font que s'agglomérer, elles sont en point de contact donc $d_{ij} = r_i + r_j$, et par conséquent $c_{ov} = 0$, cela correspond au cas $u = 0$ dans cette figure. Cependant, lorsque deux monomères sont totalement fusionnés, alors $d_{ij} = 0$ et $c_{ov} = 1$. Comme le temps de résidence des particules augmente, le rayon des particules primaires augmente, ce qui entraîne une augmentation continue de c_{ov}. Cependant, il est moins évident de comprendre pourquoi une valeur tout à fait asymptotique $\overline{c_{ov}} \approx 0.30$ est observée. Cela s'explique par le fait que si l'agrégation a tendance à diminuer le $\overline{c_{ov}}$, la croissance de surface rend à augmenter et diminuer le $\overline{c_{ov}}$ au même temps. En effet, comme les particules primaires croissent, leur recouvrement avec les voisins qui se touchent augmente ; cependant, de nouvelles intersections entre les monomères appartenant au même agrégat se produisent, ce qui entraîne également une diminution de $\overline{c_{ov}}$. De plus, comme on l'observe sur la Fig. E.7(e5-e7), le coefficient de recouvrement local peut être jusqu'à 2 fois supérieur au $\overline{c_{ov}}$. Les particules de suie provenant de flammes de diffusion et des flammes prémélangées présentent généralement un coefficient de recouvrement (2d determinées à partir des images TEM[8]) entre 0.11 et 0.36, ce qui est en bon accord avec nos simulations [6, 77].

La Fig. E.8 montre sous forme de symbole la fonction de l'autocorrélation de paires basée sur le volume $A(r)$ calculée pour des agrégats représentant de chaque cas simulé [53]. Les agrégats de gauche

---

[8]Abbreviation *TEM: Transmission Electron Microscopy* de l'anglais.
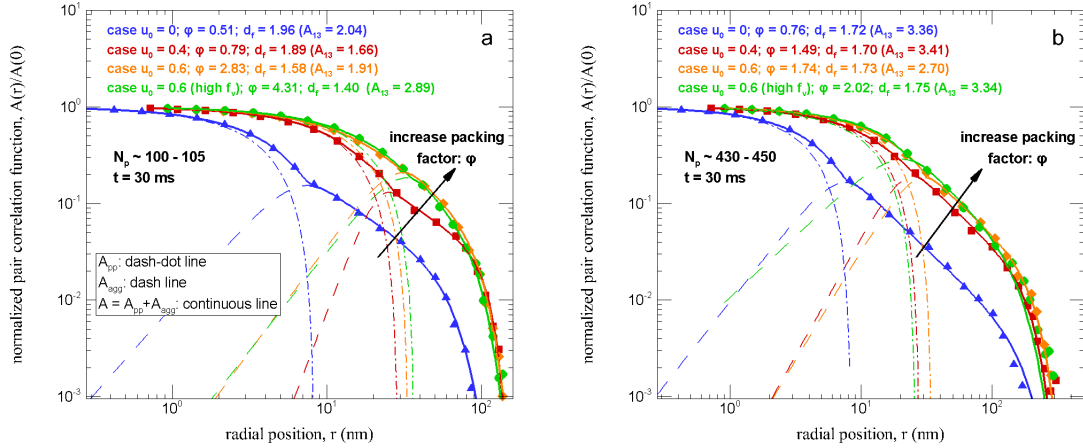
Figure E.8: Ajustement de la fonction de corrélation de paires d'agrégats sélectionnés pour chaque condition. Les symboles correspondent à la fonction de corrélation de paires normalisée d'agrégats présentant une anisotropie représentative et échantillonnés à la fin des simulations (t = 30 ms). Les agrégats constitués de $N_p \in$ [100, 105] et de $N_p \in$ [430, 450] sont présentés respectivement sur les Fig. a et b. Les lignes continues présentent le total ajusté $A(r) = A_{pp} + A_{agg}$, tandis que les deux composantes A_{pp} et A_{agg} sont la contribution des particules primaires (lignes en traitillée/pointillée) et des agrégats (lignes en pointillés), respectivement. Le coefficient d'anisotropie A_{13} et les paramètres ajustés (ϕ et $D_{f,i}$) sont indiqués dans les légendes.

correspondent à un nombre de particules primaires compris entre 100 et 105, tandis que ceux de droite correspondent à 430 − 450. Tous ces agrégats sont échantillonnés à la fin de la simulation (t = 30 ms), et sélectionnés pour avoir un coefficient d'anisotropie (A_{13}) représentatif de l'ensemble des particules du système. Le $A(r)$ calculé est ajusté sur la base d'une version modifiée du modèle proposé par Yon et al. [53] pour prendre en compte le recouvrement des particules primaires. Le taux de remplissage[9] ajusté (ϕ), représentant la compacité locale des agrégats, est indiqué pour chaque cas. Ce paramètre augmente clairement avec la croissance de surface. De même, la dimension fractale ajustée (D_f) décrivant la structure globale de l'agrégat est également indiquée pour chaque cas. Lorsque la croissance de surface est présente, des agrégats plus grands sont nécessaires pour observer une forme auto-similaire de la fonction de corrélation des paires. Ce paramètre ne dépend pas fortement du niveau de croissance de surface et les valeurs sont en bon accord avec les mesures TEM [6, 77].

E.3.2.4   Volume et surface de la suie

Une nouvelle méthode d'approximation du volume total et de la surface de la suie évoluant dans le temps est proposée. L'objectif est de fournir une méthode qui pourrait éventuellement être utilisée dans les simulations de la formation de suie par bilan de population. Dans ce contexte, les positions et les tailles exactes des particules primaires ne sont pas des informations disponibles et, par conséquent, le recouvrement des particules primaires est généralement négligé dans la littérature. Le volume total V et la surface S sont,

$$V = N\overline{v} \approx N\overline{\alpha_v}\overline{N_p}\frac{\pi}{6}\overline{D_p^3}, \tag{E.3.10a}$$

$$S = N\overline{s} \approx N\overline{\alpha_s}\overline{N_p}\pi\overline{D_p^2}, \tag{E.3.10b}$$

L'équation (E.3.10) est combinée avec des expressions supplémentaires, pour déterminer les facteurs correctifs de volume α_v et de surface α_s en fonction du coefficient moyen de recouvrement de la population,

---

[9]*Packing factor* en anglais.

ceci a été mis en œuvre dans le présent travail pour prédire l'évolution temporelle de V et S et les résultats sont présentés dans la Fig. E.9. Les valeurs calculées sont déterminées sur la base de la bibliothèque SBL [341]. Premièrement, le fait de négliger le recouvrement des particules conduit à une surestimation maximale du volume total et de la surface des particules de 91 et 218%, respectivement. Ensuite, la méthode proposée présente une erreur maximale de 0.6% pour le volume total et de 5.75% pour la surface totale, respectivement. La méthode proposée peut potentiellement être intégrée dans les simulations de bilan de population [148], Monte Carlo de bilan de population [345], et peut également améliorer les mesures expérimentales du volume et de la surface des particules basées sur l'analyse d'images TEM [77, 323, 359, 360].
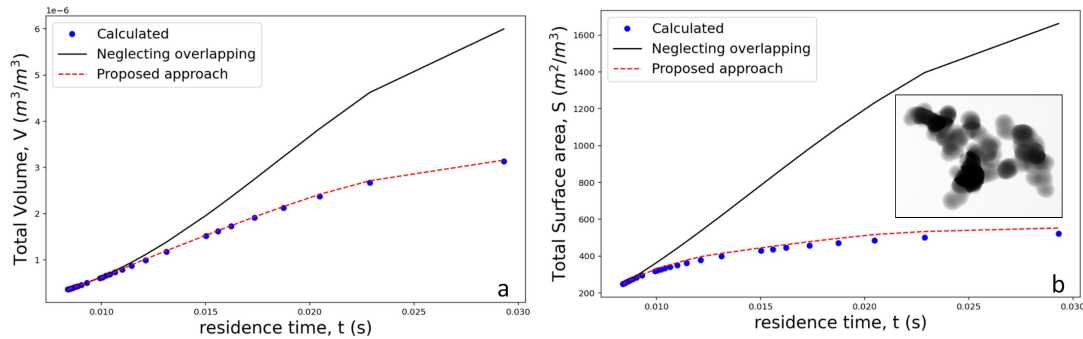

Figure E.9: Approximation du volume total et de la surface totale.

E.3.2.5 Conclusions

L'agrégation et la croissance de surface simultanées des particules de suie dans une flamme prémélangée d'éthylène conduisent à la formation d'agrégats avec une morphologie complexe. Ceux-ci consistent en des particules primaires fortement recouvertes avec des valeurs locales allant jusqu'à 60% alors que la moyenne de la population globale atteint une valeur robuste autour de 30%. De plus, le nombre de coordination local est en moyenne compris entre 4 et 8, ce qui est respectivement 2 et 4 fois supérieur aux valeurs maximales atteintes par les agglomérats formés en absence de croissance de surface. Les nombres de coordinance locaux peuvent cependant atteindre 16. La croissance de surface n'affecte pas fortement la structure globale des agrégats (dimension fractale), mais elle augmente considérablement la compacité locale telle que quantifiée par le taux de remplissage. Cela peut expliquer les valeurs elevées du préfacteur fractal des particules de suie mesurées expérimentalement. Enfin, le fait de négliger la croissance de surface sous-estime la fraction volumique de la suie d'un facteur de $8 - 10$ selon les conditions de la flamme.

E.3.3 Maturité des suies

La dynamique des particules de suie naissantes est très importante pour bien prédire la distribution de taille des particules de suie et leur morphologie dans les flammes [246]. Cependant, elle représente actuellement un grand défi. En effet, lorsque les particules de suie évoluent dans les flammes, elles subissent un evolution de maturité [242], c'est-à-dire un changement de leur composition chimique (déshydrogénation), une augmentation de la masse volumique, et une augmentation de la taille et de la masse due à la fois à l'agrégation et à la croissance de surface. En effet, les particules de suie naissantes peuvent croître dans le régime d'agrégation limité par réaction (probabilité d'adhérence $\ll 1$). Cependant, on ne sait pas actuellement à quelle vitesse se ferait la transition vers les régimes d'agrégation limités par la diffusion ou balistiques, comme on l'observe pour les suies matures (probabilité d'adhérence d'environ 1). En outre, l'influence de la maturité sur la cinétique d'agrégation, la distribution de la taille des particules et la morphologie a reçu peu d'attention dans la littérature. Ce travail vise à combler cette lacune de connaissance en se concentrant sur des particules de suie simulées numériquement et formées dans une flamme laminaire prémélangée.

E.3.3.1 Simulations

Le code Monte Carlo à éléments discrets appelé MCAC est utilisé. Dans ces simulations, les trajectoires individuelles des particules sont intégrées dans le temps. Dans cette partie de la thèse, MCAC a été adapté aux probabilités de collision et de collage non unitaires en considérant trois résultats différents pour les agrégats en interaction (voir Fig. E.10). Les particules de suie sont modélisées comme de la matière condensée, c'est-à-dire que leur composition atomique détermine leurs interactions de van der Waals et notamment leur probabilité de rebond lors d'une collision (q_1). De plus, la probabilité de collision est considérée comme dépendant des charges électrostatiques des particules de suie (q_2). Une flamme prémélangée est considérée comme cas d'étude. Afin de commencer les simulations à un temps de résidence de $t = 3.5$ ms, les taux de croissance de surface de la section précédente ont été linéairement extrapolés. Les simulations commencent avec une fraction volumique de suie de 0.002 ppm, à une pression constante (1 atm) et une température de 1700 K. La simulation se termine à un temps de résidence $t = 35$ ms. Les particules de suie jeunes ont un C/H=1.1 et $\rho_p = 1.2$ g/cm^3. En revanche, les particules de suie mature ont un C/H=10 et $\rho_p = 1.8$ g/cm^3.
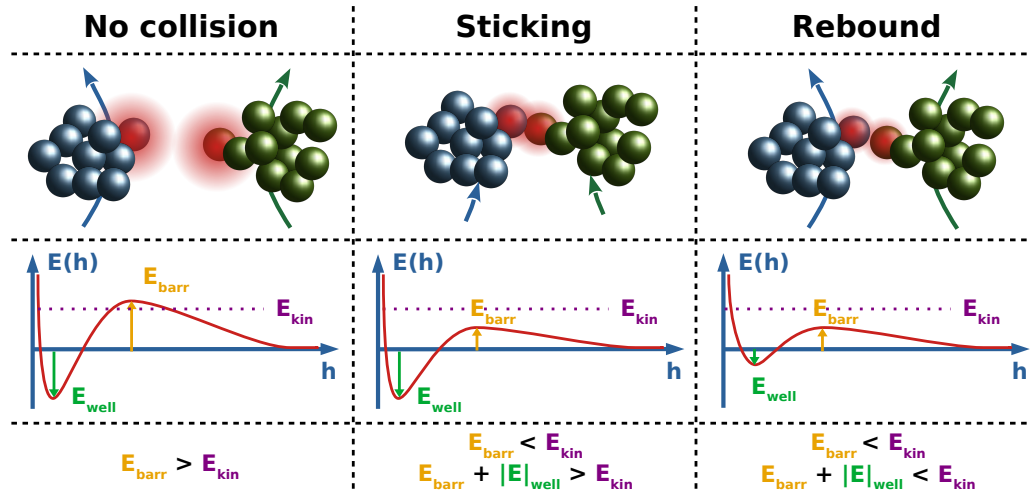

Figure E.10: Résultat détaillé de l'interaction des agrégats de suie (approche énergétique).

E.3.3.2 Cinétique d'agrégation et distribution de la taille de la suie

Comme le montre la Fig. E.11a, le noyau de coagulation monodispersé équivalent augmente dans le temps en raison de l'agglomération. Les agglomérats ont une surface de collision beaucoup plus grande que leurs particules primaires, ce qui domine la friction, et ils coagulent donc plus rapidement. Les cas impliquant une maturité totale et une maturité variable ne révèlent aucun impact important associé à la probabilité de collage (van der Waals (vdW) et électrostatique). Cependant, la suie naissante montre un impact considérable sur la fréquence de collision, comme cela est particulièrement évident au début des simulations. Dans ce cas, la comparaison de vdW avec le cas sans potentiel révèle une diminution du noyau de collision due à l'efficacité de l'adhérence de van der Waals. Les particules de suie naissantes coagulent plus rapidement que les particules matures. Ce dernier point s'explique par la masse volumique plus faible, qui fait que les particules se déplacent plus rapidement et s'agglomèrent donc plus vite. En outre, la Fig. E.11b montre l'évolution de l'inverse du nombre de concentration de particules où différents exposants cinétiques asymptotiques(z) sont observés. Une fois encore, les cas matures et les cas où la composition varie présentent un exposant cinétique similaire. Le plus grand exposant cinétique est observé pour les particules naissantes sous l'efficacité de collision vdW qui est par conséquent plus rapide que le cas sans potentiels. Ce dernier peut sembler incohérent mais il s'explique en fait par le changement de régime d'agglomération / écoulement induit par la réduction de l'efficacité de collision pour le cas sans potentiels au début de la simulation. Un comportement similaire est observé en comparant les cas mature avec / sans potentiels d'interaction.

(a) Noyaux de coagulation

(b) Cinétique d'agglomération
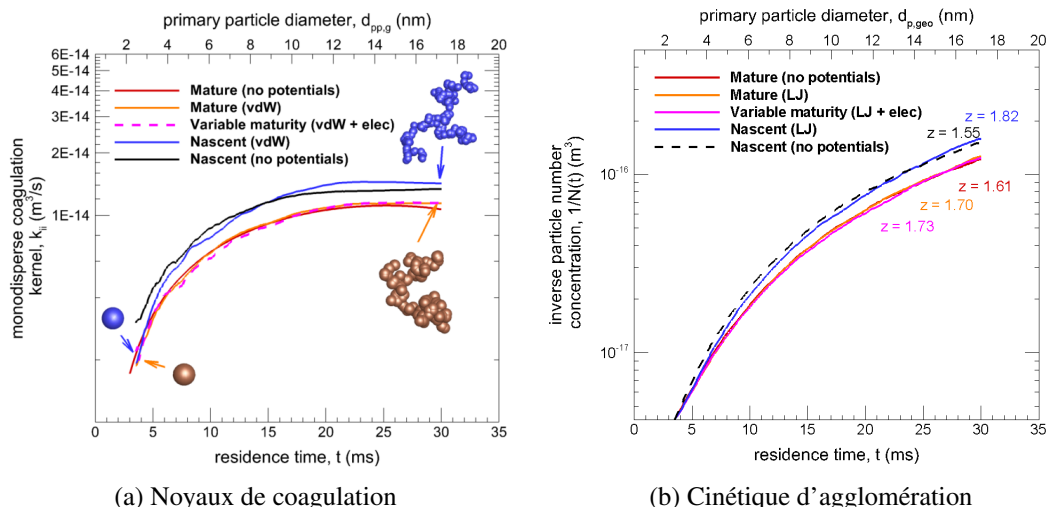
Figure E.11: Noyaux et cinétique de la coagulation des particules de suie avec et sans prise en compte de la maturité.

E.3.3.3 Conclusions

Le diamètre critique pour considérer une probabilité de collage unitaire (d_s) est évalué entre 10 et 12 nm pour les suies matures et naissantes, respectivement. La dépendance à la composition chimique est donc faible. Ce résultat est important pour la synthèse de nanomatériaux fabriqués en flamme et aussi pour les simulations de bilan de population de la formation de suies dans des systèmes industriels. Cependant, dans les conditions étudiées, la transition suie naissante-mature s'avère être très rapide (quelques millisecondes). Nous concluons que l'hypothèse d'une probabilité de collage et de collision unitaire (dans les conditions de flamme étudiées) ne produit pas de grands changements sur la cinétique d'agrégation, la distribution de taille des particules, et la morphologie. Enfin, nous avons constaté que l'évolution de la masse volumique des particules de suie liée à leur maturité joue un rôle important dans la cinétique d'agrégation et la distribution de la taille des particules. Cet aspect devrait être pris en compte dans les futures simulations de la formation de suie dans les flammes, telles que les simulations par éléments discrets, Monte Carlo ou Bilan de population.

E.3.4 Couplage CFD-MCAC

Il est utile de rappeler que l'un des principaux objectifs de cette thèse est de simuler une évolution réaliste de la morphologie des particules de suie dans des conditions de flamme. A cette fin, une approche MED de Monte Carlo (MCAC) est utilisée. Cette approche est couplée à une simulation CFD résolvant les propriétés d'écoulement de la flamme et les réactions chimiques menant à la formation, la croissance, et l'oxydation de la suie. Idéalement, cette approche de couplage nécessite une simulation CFD basée sur le suivi lagrangien des particules de suie dans la flamme comme proposé par Gallen et al. [383]. Cependant, au moment de la rédaction de cette thèse, ces simulations n'etaient pas achevées. Par conséquent, une approche lagrangienne de post-traitement basée sur les simulations de CoFlame [148] a été proposée.

E.3.4.1 Simulations CFD de flamme

La flamme de diffusion laminaire d'éthylène cible est générée par un brûleur de Gülder, le même que celui étudié expérimentalement par Yon et al. [89], où le combustible (éthylène) est injecté dans le tube central (10.9 mm et 12.7 mm de diamètre interne et externe) à un débit de 0,194 ln/min, et l'oxydant (mélange d'oxygène à 21% et d'azote à 79%) dans un tube à co-courant de 90 mm de diamètre interne à un débit de 150 ln/min. Comme mentionné dans l'introduction de ce chapitre, cette approche de couplage nécessite une simulation CFD basée sur le suivi lagrangien des particules de suie dans la flamme. Cette flamme est

simulée en utilisant CoFlame [148]. Ce code a été largement utilisé dans la littérature et validé pour étudier la formation de suie dans des flammes prémélangées [245, 389], et de diffusion [217, 292] sous différentes compositions de carburant et de gaz. Dans ce code, les équations elliptiques de conservation de la masse, de la quantité de mouvement, de l'énergie et de la fraction massique des espèces sont résolues. Ces équations sont résolues en coordonnées cylindriques bidimensionnelles (radiales r et axiales z) en profitant de la configuration axisymétrique de la flamme. La chimie de la flamme est modélisée en utilisant le mécanisme chimique développé au centre aérospatial allemand (DLR) [391] avec les modifications proposées par Dworkin et al. [392]. Un modèle HAP à 5 anneaux (A5) est utilisé pour prédire la nucléation et la condensation des particules de suie. Le domaine de calcul s'étend jusqu'à 14.342 cm dans la direction axiale, et jusqu'à 2.741 cm dans la direction radiale. Il est divisé en 202 et 92 éléments de volume non régulièrement espacés dans les directions axiale et radiale, respectivement.
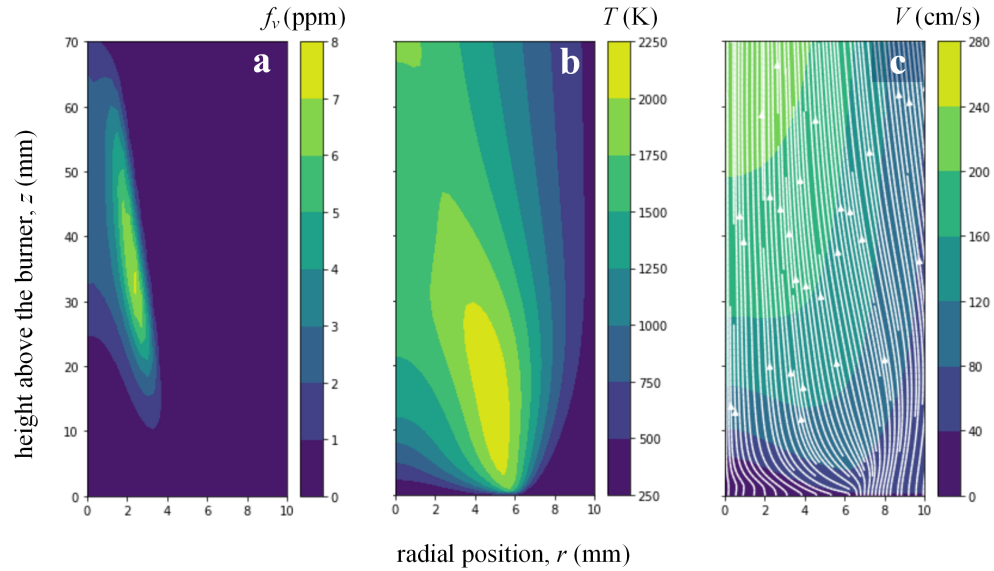
Figure E.12: Vue d'ensemble de la flamme de diffusion simulée par CFD CoFlame, (a) fraction volumique de suie, et (b) température de la flamme, (c) champ de vitesse de l'écoulement du gaz.

Les Fig. E.12a, b et Fig. E.12c présentent respectivement la fraction volumique de suie, la température de la flamme et l'amplitude (et lignes de courant) de la vitesse d'écoulement tel qui simules pqr CoFlame. En comparant avec les résultats expérimentaux disponibles, nous pouvons mettre en évidence la capacité de CoFlame à prédire la concentration globale des particules de suie et les gradients de température au sein de la flamme. De plus, les lignes de courant montrent une tendance très similaire à se rapprocher de l'axe central, ce qui est cohérent avec les expériences [387]. Cependant, la fraction volumique de la suie est toujours sous-estimé. Ceci est lié aux difficultés de CoFlame à simuler les réactions de surface et la nucléation. La température de la flamme semble être légèrement sur-estimé, mais montre globalement un bon accord avec les expériences.

E.3.4.2 Couplage CFD-MCAC

Comme le montre la Fig. E.13, le modèle CFD continu fournit deux types de paramètres d'entrée pour les simulations MCAC pour une trajectoire lagrangienne des particules dans la flamme donnée. Cela comprend la condition initiale (distribution de la taille des particules primaires et fraction volumique), et les propriétés dépendant du temps, notamment la température de la flamme, le taux massique de nucléation et le taux massique de réactions de surface. La trajectoire lagrangienne est déterminée en post-traitement en résolvant la 2ème loi de Newton sur la conservation de la quantité de mouvement linéaire pour une particule traceuse en tenant compte des forces de traînée et de thermophorèse.
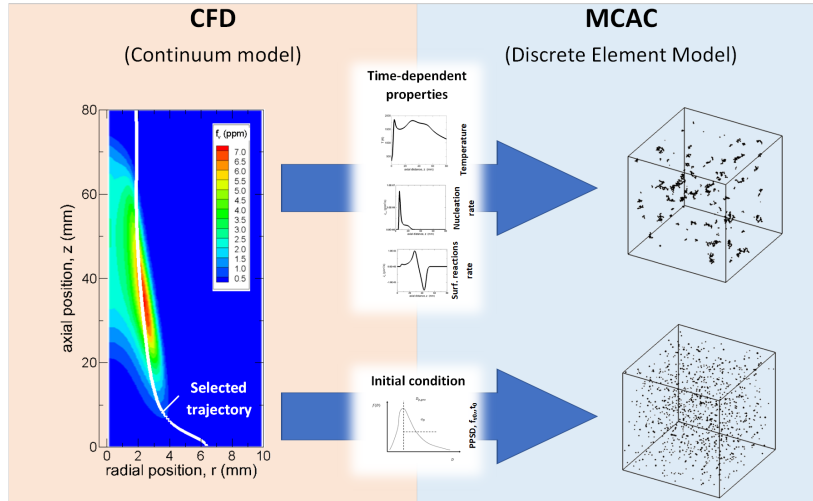
Figure E.13: Stratégie de couplage unidirectionnel CFD-MCAC.

Comme le montre la Fig. E.14a, un total de quatre trajectoires sont sélectionnées, y compris la ligne centrale, les ailes[10] de la flamme (traversant la zone de fraction volumique maximale), et deux trajectoires intermédiaires. Les propriétés dépendantes du temps, c'est-à-dire la température de la flamme, le taux massique de nucléation, les taux massique net de réaction de surface de chaque trajectoire sont rapportés dans la Fig. E.14b, c, et d, respectivement. Ces propriétés sont traitées par MCAC et utilisées pour déterminer la dynamique des particules, la nucléation et les taux de réaction de surface. Enfin, pour chaque trajectoire sélectionnée, un total de 10 simulations sont effectués et les résultats présentés dans les sections suivantes correspondent à la moyenne de ces 10 simulations pour chaque cas. Toutes les simulations commencent avec un total de 1024 particules primaires. Les particules nucléées sont monodispersées, avec un diamètre $D_p = D_c = 5$ nm, et une masse $m_{nuc} = 1.243 \cdot 10^{-22}$ kg. La méthode de réactions individuelles de surface sont considérées et le volume et la surface des particules sont mis à jour à chaque itération du code en fonction des corrections apportées au volume et à la surface. A chaque itération temporelle, la température de la flamme, les taux de nucléation et de réaction de surface sont mis à jour selon les paramètres donnés par les simulations de CoFlame. Les particules de suie sont considérées comme matures avec une masse volumique 1.9 g/cm³ et les chargées électrique des suies ne sont pas prises en compte. Cela signifie que les probabilités de collision et de collage sont supposées unitaires (voir section E.3.3). Les simulations se terminent lorsque toutes les particules ont disparu du domaine de simulation en raison de leur oxydation totale. Les simulations sont échantillonnées à partir d'une position axiale minimale $z = 10$ jusqu'à $z = 70$ mm avec un espacement de 10 mm entre les points consécutifs. Cela permet une comparaison plus directe avec les mesures expérimentales disponibles.

E.3.4.3 Résultats du couplage CFD-MCAC

Le couplage CoFlame-MCAC conduit à une taille des agrégats de suie ($\widetilde{D_g}$) en bon accord avec les données disponibles dans la littérature, en particulier pour les positions axiales intermédiaires (z entre 30 et 40 mm). Pour des positions axiales plus haut, nos simulations ont prédit un $\widetilde{D_g}$ plus faible. Cette divergence peut s'expliquer par les taux de réaction de surface sous-estimé par CoFlame ainsi que par le faible taux de croissance de surface effectif simulé dans MCAC en raison de la prise en compte plus réaliste de la surface disponible de la suie (particules primaires se recouvrent).

Comme le montre la Fig. E.16, ces simulations révèlent des signatures morphologiques très claires et marquées des agrégats formés près de la ligne centrale et de ceux formés dans les ailes de la flamme (c'est-à-dire, en passant par la région de fraction volumique maximale). La Fig. E.16a révèle des nombres

---

[10]Appelé *wings* en anglais.
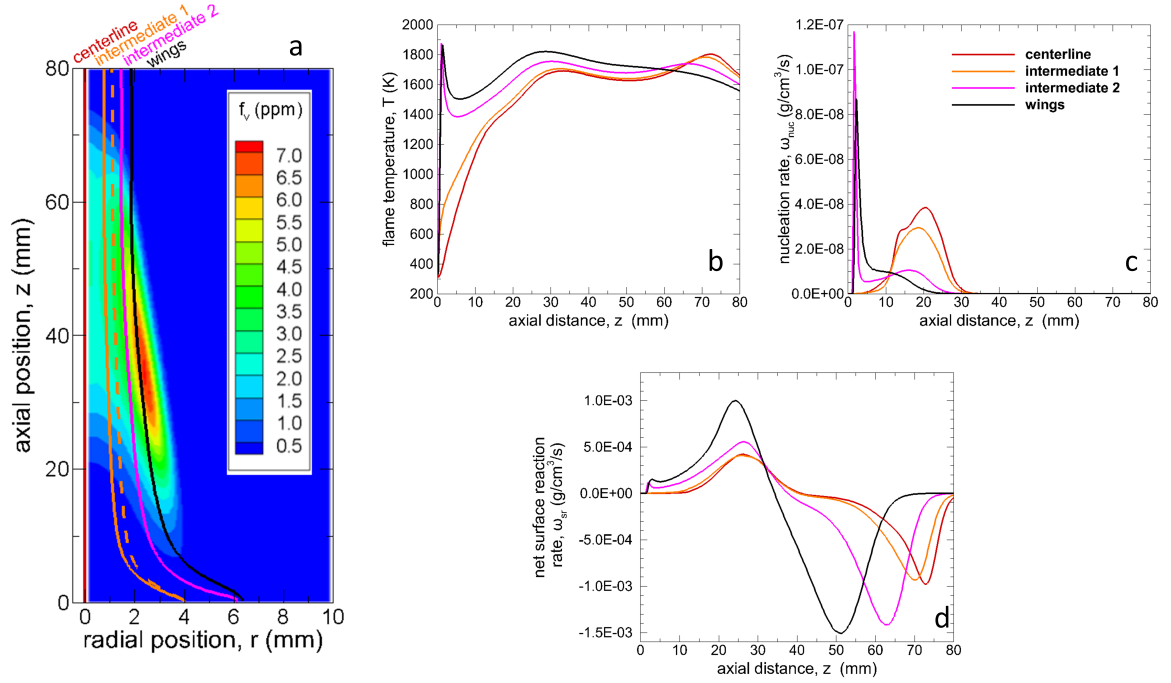
Figure E.14: Trajectoires lagrangiennes et les paramètres d'entrée pertinents correspondants pour les simulations MCAC. Les lignes continues correspondent aux valeurs déterminées en tenant compte de la force thermophorétique et les lignes en pointillés sans la prendre en compte (uniquement indiqué pour la trajectoire intermédiaire 1).
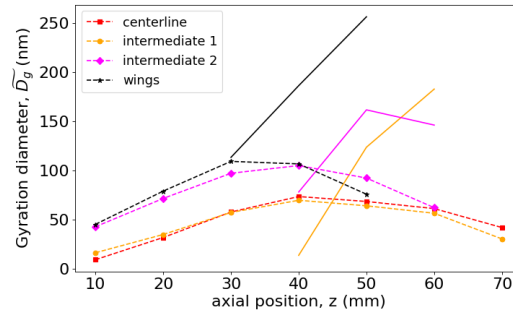
Figure E.15: Comparaison du diamètre de giration moyen d'ordre D_f entre les simulations (lignes pointillées avec symboles) et les expériences (lignes continues).

de cordinance plus grandes d'un facteur 2 pour les ailes par rapport à la ligne centrale de la flamme et des valeurs aussi élevées que 14 sont observées. En outre, les coefficients de recouvrement atteignent des valeurs maximales aussi élevées que 50% avec une importance particulière dans la trajectoire lagrangienne intermédiaire 1. En outre, les valeurs observées le long de la ligne centrale atteignent 30%, ce qui est en bon accord avec les mesures expérimentales basées sur l'analyse d'image TEM [6, 77]. Ces résultats sont cohérents avec le préfacteur fractal indiqué dans la Fig. E.16c. Les différences de morphologie entre la ligne centrale et les ailes de la flamme deviennent moins évidentes lorsque l'on compare la dimension fractale de la population D_f rapportée dans la Fig. E.16d pour $N_{p,eff} > 3$. Des dimensions fractales plus petites sont observées près pour la trajectoire intermediaire 1 où des valeurs autour de 1.7 à 1.8 sont observées. Pour les lignes de courant plus proches de la ligne centrale, des D_f plus grands sont observés avec des valeurs autour de 1.9.

(a) Nombre de coordinance

(b) Coefficient de recouvrement

(c) Préfacteur fractal

(d) Dimension fractale
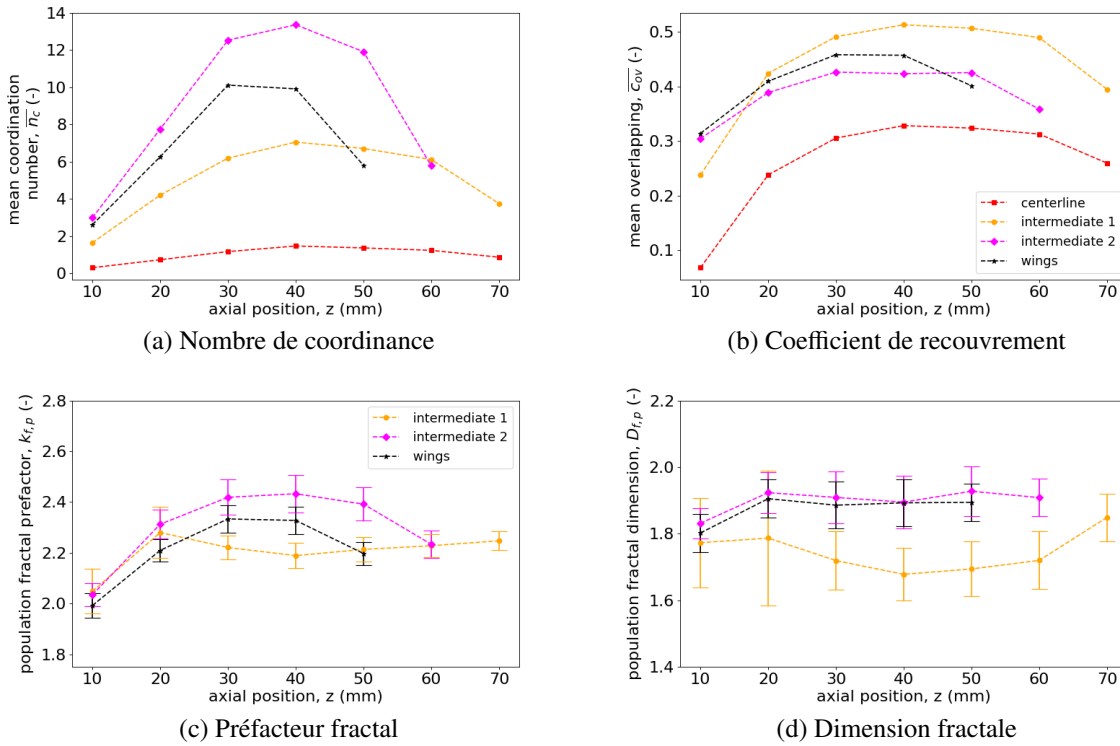
Figure E.16: Paramètres morphologiques des agrégats de suie, notamment le nombre moyen de coordinance, le recouvrement, le préfacteur fractal et la dimension fractale ($N_{\text{p,eff}} > 3$).

La Fig. E.17a montre les points d'échantillonnage dans la flamme selon les 4 trajectoires différentes en fonction de la fraction volumique de suie. Sur la partie droite de cette figure, quelques images numériques de microscopie électronique à transmission (nTEM) sont montrées. Ces images nTEM sont obtenues à partir d'un échantillon de population d'agrégats (choisis au hasard) à chaque position axiale. Toutes les images ont une taille de 1024×1024 pix^2 et la même échelle (pix/nm) comme indiqué sur la figure. La couverture de surface des images est choisie proportionnellement à la fraction volumique locale et varie de 0.05 à 0.20. Les positions des agrégats dans l'image sont choisies aléatoirement en évitant l'intersection apparent 2d entre les agrégats. Attention, cela signifie que la distance entre les agrégats dans ces images n'est pas représentative de la simulation et que la taille de l'image n'est pas liée à la taille de la boîte de simulation. Cette figure a pour but de montrer qualitativement l'aspect morphologique des particules formées sous différentes histoires thermiques et de réaction de surface lorsqu'elles sont comparées à une position axiale équivalente, comme cela est généralement fait lors de l'analyse d'images TEM expérimentales [399–402]. Des particules plus petites et plus sphériques sont observées le long de la ligne centrale et des trajectoires intermédiaires 1. A l'inverse, des agrégats beaucoup plus grands et de forme irrégulière sont observés dans les trajectoires intermédiaires 2 et dans les ailes. Bien que la figure du champ de fraction de volume de suie sur le côté gauche montre des valeurs inférieures à 1 ppm pour les différentes trajectoires, il est remarquable d'observer des particules déjà présentes sur les images nTEM. En particulier, pour les trajectoires intermédiaire 2 et des ailes, certains agrégats peuvent déjà être observés. Ceci est dû au pic de nucléation plus précoce révélé par les simulations CoFlame. En observant l'évolution du nTEM le long de la même trajectoire, les différentes étapes de la formation de la suie peuvent être observées, y compris la production de suie pour les *z* inférieurs, l'agglomération est observée lorsque l'on se deplace verticalement, dans les dernières images de chaque trajectoire, une réduction considérable de la taille des particules primaires et des agrégats est observée. Ceci est dû à l'oxydation et donc à la fragmentation qui en résulte. Enfin, comme il a été précédemment observé dans les expériences, de grandes particules primaires sont observées en présence de très petites (même au sein du même agrégat), ce qui dans les simulations actuelles, est attribué au profil de nucléation des monomères

pour chaque cas. L'observation attentive des agrégats révèle également leur morphologie complexe et le degré de recouvrement entre les particules primaires et par conséquence la difficulté de leur identification.

E.3.4.4 Conclusions

Le couplage CoFlame-MCAC est réalisé avec succès dans une flamme de diffusion d'éthylène. Un total de 4 trajectoires couvrant la ligne centrale jusqu'aux ailes de la flamme (où les fractions volumiques maximales de suie sont observées) sont réalisées. La détermination des trajectoires lagrangiennes des particules de suie présente une importante source d'incertitude dans l'approche actuelle. En particulier, l'inclusion de la force thermophorétique pour la détermination des trajectoires de suie peut jouer un rôle important comme le suggère l'approche actuelle. Cette détermination des trajectoires devient particulièrement importante à proximité des ailes de la flamme. Ceci est dû aux forts gradients de température, et principalement à un pic de nucléation trouvé près de la sortie du brûleur à l'interface entre les tubes de combustible et d'oxydant. Ceci suggère que des méthodes de suivi lagrangien plus précises telles que celles réalisées dans [383] devraient être mises en œuvre pour améliorer la précision de ces simulations.

Les agrégats de suie formés dans les ailes ont une morphologie et une taille significativement différentes de celles des agrégats formés dans la ligne centrale. Ceci est cohérent avec les observations expérimentales précédentes d'images TEM dans des flammes de diffusion [399–402]. Les agrégats formés dans les ailes sont beaucoup plus grands. Cependant, ils présentent la plus grande compacité locale exprimée par le coefficient de recouvrement des particules primaires et le nombre de coordinance. De plus, les agrégats formés dans les ailes présentent des coefficients d'anisotropie plus élevés, ce qui devrait s'expliquer par la plus grande taille des agrégats par rapport à la ligne centrale.

E.4 Conclusions générales et perspectives

- MCAC est un nouveau et puissant code, capable de simuler la formation d'agrégats de suie complexes dans des conditions de flamme. La cinétique de l'agrégation, la distribution de la taille des particules et la morphologie détaillée de la suie peuvent être étudiées. Il s'agit d'un code open-source et toutes les versions sont disponibles sur Gitlab.

- Les résultats ont montré l'importance du changement simultané des régimes d'agrégation et d'écoulement pour l'agrégation de la suie. Cela est particulièrement impactant au travers de la variation du diamètre des particules primaires qui affecte considérablement la distribution de la taille des agrégats, la cinétique de l'agrégation et la morphologie des agrégats.

- La prise en compte de la croissance de surface conduit à une morphologie réaliste des agrégats de suie. La croissance de surface n'influence pas considérablement la dimension fractale de la suie mais augmente considérablement la compacité locale des agrégats, comme le montre l'augmentation du taux de remplissage, du nombre de coordinance et du coefficient de recouvrement.

- L'évolution de la maturité de la suie a un impact modéré sur la cinétique d'agrégation et la distribution de la taille des particules (et beaucoup moins sur la morphologie). Cet effet est plus important en termes d'évolution de la masse volumique de la suie qu'en termes probabilités de collision ou de collage.

- Différentes alternatives pour améliorer la modélisation du bilan de population de la formation de suie dans les flammes sont proposées. Parmi elles, les noyaux de collision sont calculés, des équations permettant d'estimer le volume et la surface des agrégats de suie complexes constitués de particules primaires en recouvrement sont proposées.

- L'amélioration de la caractérisation de la suie par l'analyse d'images de microscopie électronique à transmission peut être obtenue grâce aux méthodes proposées et à la correction des corrélations morphologiques telles que les lois de puissance reposant sous la surface projetée et les corrélations volume / surface.

- Les simulations avec couplage CFD-MCAC sont en bon accord avec les mesures expérimentales précédentes basées sur l'extinction/émission de la lumière, et les mesures de diffusion de la lumière sur une flamme de diffusion laminaire d'éthylène [89, 242]. Ces simulations ont permis de mieux comprendre l'évolution de la morphologie de la suie le long de différentes lignes de courant. L'évolution morphologique est en bon accord avec les observations expérimentales issues de l'analyse des images TEM [6, 400].

- La perspective de ce travail de thèse est d'améliorer le couplage des simulations CFD-MCAC en condensant une approche lagrangienne plus précise comme celle proposée par Gallen et al. [383].

- Les travaux futurs pourraient impliquer la modélisation de flammes plus complexes telles que les flammes turbulentes présentant un intérêt particulier pour les applications aéronautiques. Les effets d'inertie des particules, en particulier pour les grands agrégats, pourraient être explorés dans le futur. La formation de super-agrégats de suie et la transition vers la gélification pourraient être simulées à l'avenir.

- MCAC est un code polyvalent qui peut être adapté pour simuler le transport d'agglomérats sous l'action de champs de force exterieurs tels que gravitationnels, électriques, thermophorétiques ou magnétiques. Il peut trouver de nombreuses applications dans les domaines de la combustion, de la science des aérosols, et de la technologie des poudres.
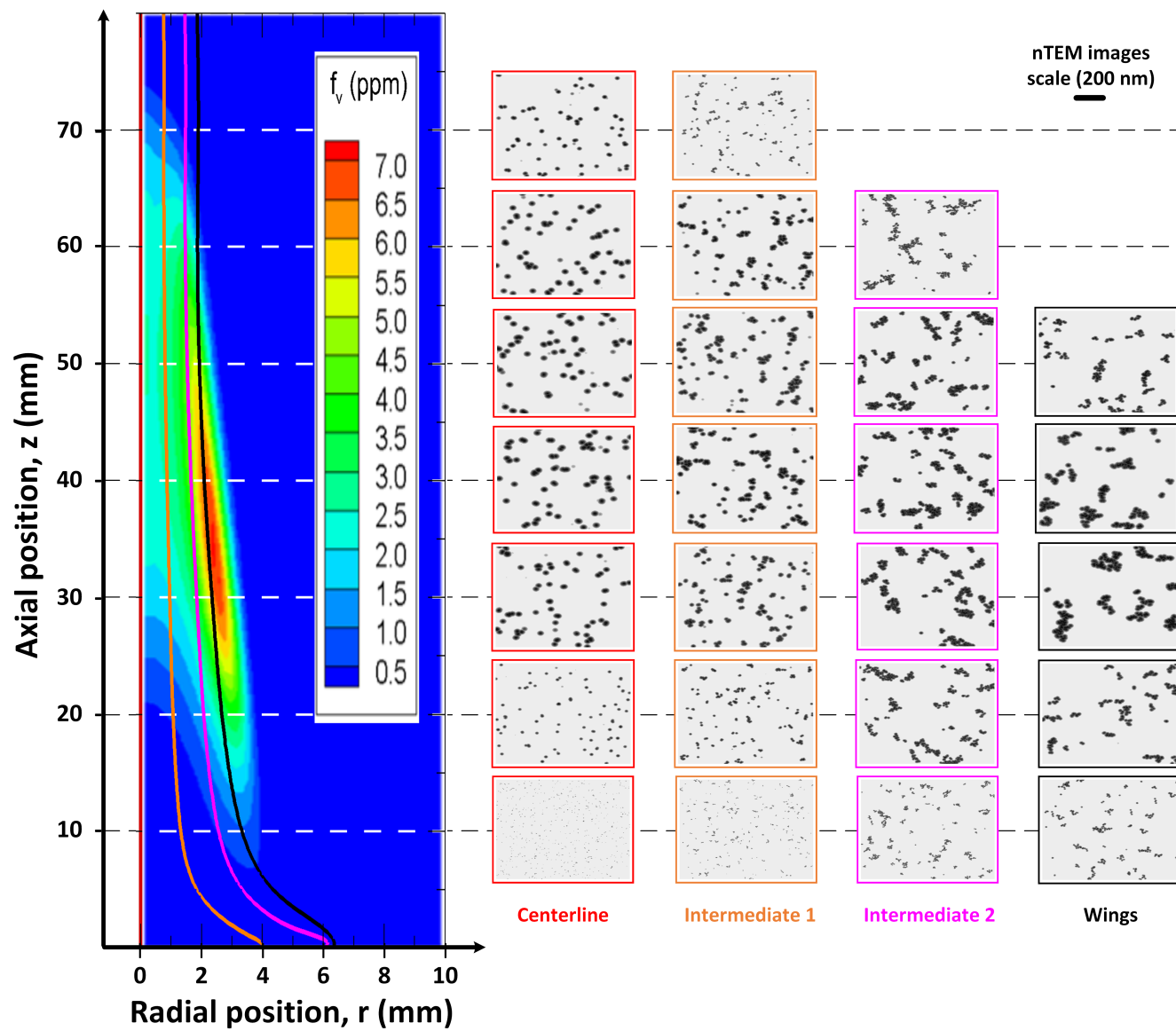
Figure E.17: Images nTEM pour les trajectoires sélectionnées.